

Journal of
Mechanics of
Materials and Structures

Volume 2, N° 5

May 2007



mathematical sciences publishers

JOURNAL OF MECHANICS OF MATERIALS AND STRUCTURES

<http://www.jomms.org>

EDITOR-IN-CHIEF Charles R. Steele
ASSOCIATE EDITOR Marie-Louise Steele
Division of Mechanics and Computation
Stanford University
Stanford, CA 94305
USA

BOARD OF EDITORS

D. BIGONI University of Trento, Italy
H. D. BUI École Polytechnique, France
J. P. CARTER University of Sydney, Australia
R. M. CHRISTENSEN Stanford University, U.S.A.
G. M. L. GLADWELL University of Waterloo, Canada
D. H. HODGES Georgia Institute of Technology, U.S.A.
J. HUTCHINSON Harvard University, U.S.A.
C. HWU National Cheng Kung University, R.O. China
IWONA JASIUK University of Illinois at Urbana-Champaign
B. L. KARIHALOO University of Wales, U.K.
Y. Y. KIM Seoul National University, Republic of Korea
Z. MROZ Academy of Science, Poland
D. PAMPLONA Universidade Católica do Rio de Janeiro, Brazil
M. B. RUBIN Technion, Haifa, Israel
Y. SHINDO Tohoku University, Japan
A. N. SHUPIKOV Ukrainian Academy of Sciences, Ukraine
T. TARNAI University Budapest, Hungary
F. Y. M. WAN University of California, Irvine, U.S.A.
P. WRIGGERS Universität Hannover, Germany
W. YANG Tsinghua University, P.R. China
F. ZIEGLER Technische Universität Wien, Austria

PRODUCTION


PAULO NEY DE SOUZA Production Manager
SHEILA NEWBERY Senior Production Editor
SILVIO LEVY Scientific Editor

See inside back cover or <http://www.jomms.org> for submission guidelines.

Regular subscription rate: \$500 a year.

Subscriptions, requests for back issues, and changes of address should be sent to Mathematical Sciences Publishers, 798 Evans Hall, Department of Mathematics, University of California, Berkeley, CA 94720-3840.

©Copyright 2007. Journal of Mechanics of Materials and Structures. All rights reserved.

 mathematical sciences publishers

TWO COMPLEMENTARY TRIOS MATERIAL MODEL AND EXPERIMENTAL SIMULATIONS OF SAE 4340 AND RHA

CHEIN-SHAN LIU, HONG-KI HONG AND YA-PO SHIAO

A two-complementary-trio material model for cyclic plasticity is proposed in this paper. In this formulation we consider a contact surface to confine the motion of contact stress. While the on-off switching criteria of plasticity are derived from the first complementary trio, the switching criteria of kinematic hardening rules are derived according to the second complementary trio. In terms of the new concept of contact stress and contact surface, it becomes easier to derive the governing rule of back stress during the contact of yield surface and bounding surface. The validity of the new model is confirmed by comparing the computational results with the experimental data for materials of SAE 4340 and RHA under uniaxial cyclic tests and biaxial cyclic tests. Even though the material constants used in the new model are parsimonious (with only 12), it is immediately recognized that the cyclic response curves described by the new model are in good agreement with the experimental data.

1. Introduction

Simulations using the conventional J_2 mixed-hardening plasticity model reveal an over-square phenomenon in the bending corners of the stress-strain curve [Liu 2004], which definitely does not match the most experimental results. This shortcoming may be attributed to the fact that in conventional plasticity the plastic modulus has the same value at all the stress points on the yield surface. In order to address this limitation, many researchers have introduced different nonlinear kinematic hardening laws [Liu 2005], in the context of single surface plasticity theory.

An elastic/plastic model with a unique yield surface has severe limitations as pointed out by Liu [2006]: (a) a discontinuous stress rate and strain rate relation is predicted, which changes abruptly when stress reaches the yield surface, (b) upon loading, the consistent condition requires the subsequent stress points to remain on the yield surface, and (c) the hysteresis loop for a partial unloading-reloading cycle, the Masing effect and the strain ratcheting phenomenon cannot be described properly.

To remedy these limitations, various unconventional constitutive models have been proposed for simulating the cyclic behavior of materials in the past few decades. In contrast to the conventional single yield-surface plasticity theory, Mróz [1967] has proposed a multisurface model with an associated kinematic hardening rule. Thereafter, while a simplified two-surface model employing a yield surface and only one subyield surface enclosing a purely elastic domain was formulated by Dafalias and Popov [1975; 1976], Krieg [1975], Mróz et al. [1979], Tseng and Lee [1983], and Hashiguchi [1988], the infinite-surface model was developed by Mróz et al. [1981], and the subloading surface model was developed by Hashiguchi [1989].

Keywords: cyclic plasticity, two complementary trios.

Two-surface theories originate from a nesting-surface model proposed by Mróz [1967]. In practical applications, there have been several versions of two-surface theories, which are in general supported by different experimental investigations. Basically, these theories aim to make the plastic modulus a more flexible mechanism to fit the experimental results, so that it can be used to predict the material behavior more appropriately.

For example, Dafalias and Popov [1975; 1976] have introduced the concept of *bounding surface* to assert that there exist three regions at which the plastic modulus first takes the value infinity as the stress point first attaches to the yield surface; then, when it pushes and moves together with the yield surface the plastic modulus decreases smoothly; and finally, the plastic modulus becomes a constant in the third region. The last region is called the bounding surface. At the same time, Krieg [1975] has proposed a two-surface theory more similar to the multisurface theory of Mróz, which assumed many nonintersecting yield surfaces. In addition to a yield surface, Krieg [1975] introduced a limiting surface to delineate the plastic modulus of material at the reversal loading direction. This theory can be viewed as a continuous version of the discrete multisurface model of Mróz.

Ohno and Wang [1991] have shown that the nonlinear kinematic hardening rule with back stress decomposed into multicomponents can be transformed into a multisurface form, and that the transformed multisurfaces are nested and obey the Mróz-type translation rule without intersecting each other.

The existence of a bounding surface has been supported by experimental work [Phillips and Sierakowski 1965; Phillips and Tang 1972; Phillips and Kasper 1973; Phillips and Moon 1977]. The plastic behavior of material is governed by two surfaces: the yield surface and the bounding surface. According to the investigations made by these authors, two important phenomena can be observed.

The first is that the behavior on the bounding surface tends to satisfy the isotropic hardening rule and the normality principle, which indicates that when the stress approaches the bounding surface, the plastic strain rate will align its direction to the normal direction of the bounding surface.

The second is that the yield surface cannot penetrate the bounding surface, and they can be in contact at most. When the yield surface is in contact with the bounding surface, the motion of yield surface must be modified to avoid the penetration of the bounding surface, and thus the motion of yield surface does not necessarily abide by Prager's kinematic hardening rule [Prager 1956].

The possibilities of intersection of yield and bounding surfaces have been examined by McDowell [1989] in the framework of two-surface plasticity theory. Intersections are undesirable from the perspectives of both computational implementation and agreement with experimental results. McDowell [1989] has shown that the intersections may occur even for the commonly employed formulations for certain loading histories. Therefore, in the development of a two-surface plasticity model it is important to avoid intersection. Recently, the multisurface plasticity models were developed and applied by Elgamal et al. [2003], Khoei and Jamali [2005], and Abdel-Karim [2005].

A correct simulation of cyclic phenomena is still one of the most difficult problems, and there are many complex constitutive models that allow one to simulate the cyclic behavior appropriately. See, for example, [Chaboche 1991; 1994; Voyiadjis and Sivakumar 1991; 1994; Hassan and Kyriakides 1992a; 1992b; Ohno and Wang 1993a; 1993b; 1994; Abdel-Karim and Ohno 2000; Ohno and Abdel-Karim 2000; Bari and Hassan 2001; 2002; Voyiadjis and Abu Al-Rub 2003; Chen and Jiao 2004; Vincent et al. 2004; Dieng et al. 2005; Chen et al. 2005; Liu 2006]. This list reflects just some of the active research dealing with the cyclic behaviors of materials, and improvements are still in progress.

Evolutions of yield surface and plastic strain increments have been investigated by Wu [2003] from the perspective of Prager's linear kinematic hardening rule, and it was found that the plastic strain increment vector is normal to the yield surface and its magnitude and direction vary as the stress path is traversed. Liu and Chang [2005] have studied the material models endowed with the anisotropic quadratic yield criteria from a noncanonical Minkowski frame to enhance the computational accuracy. However, many higher-order nonquadratic yield criteria have been proposed to simulate the distortion of yield surfaces during plastic deformation, which is an important issue in plasticity theory; see, for example, [François 2001; Chiang et al. 2002; Bron and Besson 2004; Cazacu and Barlat 2004; Kowalczyk and Gambin 2004; Vincent et al. 2004; Liu and Chang 2004; Wu et al. 2005; Yeh and Lin 2006; Christensen 2006].

For the simulation of cyclic loading phenomena and strain induced anisotropy, the present method introduces a two-complementary-trio mechanism. Usually, only one complementary-trio is employed in the conventional plasticity theory [Liu 2004]. In the following we first give the basic hypotheses underlying the new model in Section 2. A distance function is derived to control the plastic modulus. In Section 3, some demonstrations are given to rewrite the model in terms of the back stress and the eccentric stress (the center of the bounding surface). In Section 4, we discuss the weak stability criteria of the new model, where a rather detailed description about the material functions is given. According to the first complementary trio, we derive the switching criteria of plasticity in Section 5. Then, according to the second complementary trio we derive the switching criteria of kinematic hardening rules in Section 6. In Section 7, we give a procedure to determine the coefficient functions appearing in the kinematic hardening rule. In Section 8, we discuss the plastic modulus. In Sections 9 and 10, we show and discuss the experimental results of SAE 4340 and RHA. In Section 11, the comparisons between theoretical and experimental results are given. In Section 12, we prove the convexity of the distance function and derive a yield surface with a prescribed strain offset. It is shown that the two-complementary-trio model can properly account for deformation induced anisotropy, where by using an offset of strain [Wu 2005] to delineate the yield point, we can produce nonquadratic yield loci in the stress plane. Finally, some conclusions are given in Section 13.

2. The postulations

The internal variables theory has played a key role in the development of plastic constitutive equations. The internal variables widely employed are: the back stress locating the center of the yield surface in the stress space; the parameters that characterize the expansion/contraction of the yield surface; the parameters that characterize the bounding surface in multisurface plasticity theories, etc. However, these specifications of the constitutive relations may be not self-consistent, unless the specific model is so designed. In particular, we have mentioned the possible intersection of the yield surface and the bounding surface in two-surface theories. Therefore, how to develop a two-surface theory that can avoid the intersection automatically may be a significant work. Although, Ohno and Wang [1991] have solved this problem for a multisurface theory with a different approach, it is worthwhile to propose a two-surface plasticity model that does not have the intersection problem.

It is known that the complementary trio in a single-yield surface theory plays a vital role in confining the stress point to a location within the yield surface. This concept can be employed and extended to cover the two-surface theory. In addition to the first complementary trio, we can introduce the second

complementary trio to govern the motion of a newly defined "contact stress", which is the difference of the back stress (the center of the yield surface) with respect to the eccentric stress (the center of the bounding surface). Therefore, with a different approach than before, we can propose a new plastic flow rule and evolution laws of active stress and contact stress such that the intersection of yield and bounding surfaces can be avoided automatically.

We construct such a two-complementary-trio cyclic elastoplasticity model by using the following hypotheses:

$$\dot{e}_{ij} = \dot{e}_{ij}^e + \dot{e}_{ij}^p, \quad (1)$$

$$s_{ij} = s_{ij}^d + s_{ij}^c + s_{ij}^a, \quad (2)$$

$$\dot{s}_{ij} = 2G\dot{e}_{ij}^e, \quad (3)$$

$$\dot{e}_{ij}^p = \frac{3\dot{\lambda}_a}{2h_a}s_{ij}^a + \frac{3\dot{\lambda}_c}{2h_c}s_{ij}^c, \quad (4)$$

$$\dot{s}_{ij}^a = -C_1\dot{\lambda}_c s_{ij}^a - \left(\frac{2}{3}k'_a + \gamma_c C_2\right)\dot{e}_{ij}^p - C_3\dot{\lambda}_c e_{ij}^p + (1 - \gamma_c)\dot{s}_{ij} + C_4\dot{\lambda}_c s_{ij}, \quad (5)$$

$$\dot{s}_{ij}^c = -C_1\dot{\lambda}_c s_{ij}^c + \left(\frac{2}{3}k'_c + \gamma_c C_2\right)\dot{e}_{ij}^p + \gamma_c \dot{s}_{ij}, \quad (6)$$

$$f_a \leq 0, \quad (7)$$

$$\dot{\lambda}_a \geq 0, \quad (8)$$

$$\dot{\lambda}_a f_a = 0, \quad (9)$$

$$f_c \leq 0, \quad (10)$$

$$\dot{\lambda}_c \geq 0, \quad (11)$$

$$\dot{\lambda}_c f_c = 0, \quad (12)$$

in which e_{ij} , e_{ij}^e , e_{ij}^p , s_{ij}^a , s_{ij}^c , s_{ij}^d and s_{ij} are respectively the deviatoric tensors of strain, elastic strain, plastic strain, active stress, contact stress, eccentric stress and stress. Here,

$$f_a := \sqrt{\frac{3}{2}s_{ij}^a s_{ij}^a} - h_a \quad (13)$$

is the von Mises yield function, and

$$f_c := \sqrt{\frac{3}{2}s_{ij}^c s_{ij}^c} - h_c \quad (14)$$

is a corresponding contact function of the same form with f_a .

In Equations (1), (3)–(6), (8), (9), (11) and (12) the rates are obtained by taking the derivatives with respect to time. However, all the dt can be factored out to obtain an incremental form of these equations because the model is rate-independent; if we employ another time scale, say t' , with $dt'/dt > 0$, in these equations, it does not change the response.

It deserves to be noted that the plastic flow rule in Equation (4) is different from the conventional one by virtue of an extra term which is proportional to the contact stress. However, this term is active only when the yield surface is in contact with the bounding surface. Before such contact, equation (4) follows the associated flow rule.

The material functions are dependent on the equivalent plastic strain \bar{e}^p defined by

$$\bar{e}^p = \int_{t_0}^t \dot{\bar{e}}^p(\xi) d\xi, \quad \dot{\bar{e}}^p := \left(\frac{2}{3} \dot{e}_{ij}^p \dot{e}_{ij}^p \right)^{\frac{1}{2}} \geq 0. \quad (15)$$

It can be seen that \bar{e}^p is a time-like parameter because its time derivative $\dot{\bar{e}}^p$ is nonnegative, and hence is an indicator of the irreversible change of material properties.

In the above equations, $\dot{\lambda}_c$ is defined as

$$\dot{\lambda}_c := \gamma_c \dot{\bar{e}}^p, \quad (16)$$

with

$$\gamma_c := \frac{s_{ij}^c}{\sqrt{\frac{2}{3}} h_c} \frac{s_{ij}^a}{\sqrt{\frac{2}{3}} h_a} - \frac{h'_c}{k'_c}. \quad (17)$$

The above definition of γ_c will be derived in Section 6.

The material functions h'_a , k'_a , h'_c and k'_c are assumed to be related by

$$(h'_a + k'_a) \left(1 - \exp\left(a \left(\frac{\mathcal{D}}{2h_c}\right)^b\right) \right) = (h'_c - k'_c) \exp\left(a \left(\frac{\mathcal{D}}{2h_c}\right)^b\right), \quad (18)$$

where $a \geq 0$ and $b \geq 0$ are two material constants, and

$$\mathcal{D} = -\frac{(s_{ij}^a + s_{ij}^c) \dot{e}_{ij}}{\sqrt{\frac{2}{3}} \dot{e}_{mn} \dot{e}_{mn}} + \sqrt{\frac{((s_{ij}^a + s_{ij}^c) \dot{e}_{ij})^2}{\frac{2}{3} \dot{e}_{mn} \dot{e}_{mn}} + (h_a + h_c)^2 - \frac{3}{2} (s_{ij}^a + s_{ij}^c) (s_{ij}^a + s_{ij}^c)}} \quad (19)$$

is a distance function between the stress point s_{ij} and its image point on the bounding surface along the strain rate direction \dot{e}_{ij} , as shown in Figure 1. The bounding surface is a surface in the stress space with center s_{ij}^d and radius $h_a + h_c$, whereas the contact surface is a surface with center s_{ij}^d and radius h_c . When $f_a = 0$ and $f_c = 0$, the yield surface is in contact with the bounding surface. Figure 1 shows a noncontact case.

The projection of $s_{ij}^a + s_{ij}^c$ onto the unit tensor along the direction \dot{e}_{ij} is denoted by

$$d_1 = \frac{(s_{ij}^a + s_{ij}^c) \dot{e}_{ij}}{\sqrt{\frac{2}{3} \dot{e}_{mn} \dot{e}_{mn}}}. \quad (20)$$

From Figure 1 we can obtain the following relation:

$$(\mathcal{D} + d_1)^2 + d_2^2 = (h_a + h_c)^2, \quad (21)$$

where

$$d_2^2 = \frac{3}{2} (s_{ij}^a + s_{ij}^c) (s_{ij}^a + s_{ij}^c) - d_1^2. \quad (22)$$

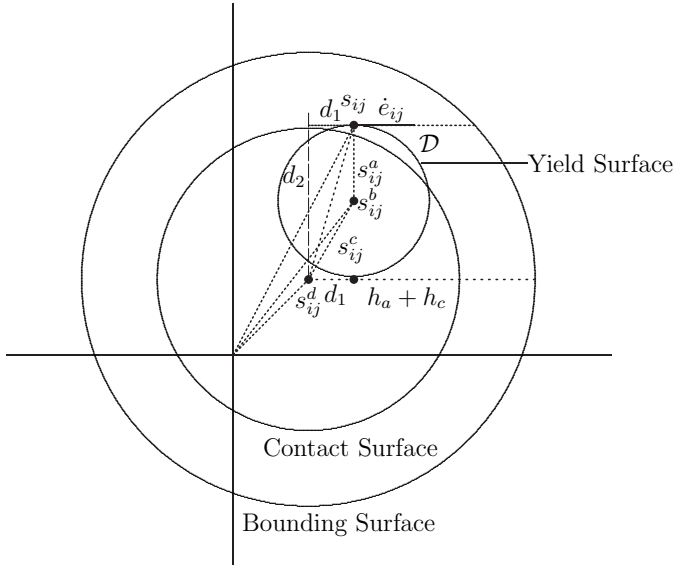


Figure 1. The distance between the current stress point and the image point on the bounding surface along a strain rate direction.

Therefore, from (20)–(22) we can derive Equation (19).

We also suppose that

$$G > 0, h_a > 0, h_c > 0, h'_c > 0, k'_c > 0. \tag{23}$$

A detailed description of these material functions is given in Section 4.

3. Comments on postulations

The evolution rules proposed for s_{ij}^a and s_{ij}^c in (5) and (6) may be replaced by the following differential equations for s_{ij}^b and s_{ij}^d :

$$\dot{s}_{ij}^b = -C_1 \dot{\lambda}_c s_{ij}^b + \left(\frac{2}{3}k'_a + \gamma_c C_2\right) \dot{e}_{ij}^p + C_3 \dot{\lambda}_c e_{ij}^p + \gamma_c \dot{s}_{ij} + (C_1 - C_4) \dot{\lambda}_c s_{ij}, \tag{24}$$

$$\dot{s}_{ij}^d = -C_1 \dot{\lambda}_c s_{ij}^d + \frac{2}{3}(k'_a - k'_c) \dot{e}_{ij}^p + C_3 \dot{\lambda}_c e_{ij}^p + (C_1 - C_4) \dot{\lambda}_c s_{ij}, \tag{25}$$

in which

$$s_{ij}^b := s_{ij}^c + s_{ij}^d$$

is called the back stress.

The above representation in terms of back stress and the center of bounding surface is schematically shown in Figure 1. It is interesting to note that both s_{ij}^d and s_{ij}^b play the role of a back stress; while s_{ij}^a is a back stress of contact surface (or bounding surface), s_{ij}^b is known to be a back stress of the yield surface. It is also interesting to note that both s_{ij}^c and s_{ij}^a play the role of a relative stress; while s_{ij}^c is a relative stress between s_{ij}^b and s_{ij}^d , s_{ij}^a is known to be a relative stress between stress s_{ij} and back stress s_{ij}^b . More frequently, s_{ij}^a is called the active stress. In the two complementary trios model, there are two

surfaces, the yield surface and the contact surface (or bounding surface); two back stresses, s_{ij}^b and s_{ij}^d ; and two relative stresses, s_{ij}^a and s_{ij}^c .

It is observed that (9) and (12) constitute the Kuhn–Tucker conditions [Rockafellar 1970] for the following constrained optimization problem: minimize $-\sigma_{ij}\dot{\epsilon}_{ij}^p$ subject to (7) and (10). In other words, the plastic-flow rule (4), the equalities $\dot{\lambda}_a f_a = 0$ and $\dot{\lambda}_c f_c = 0$, and the inequalities $\dot{\lambda}_a \geq 0$, $f_a \leq 0$ and $\dot{\lambda}_c \geq 0$, $f_c \leq 0$ are sufficient and necessary for the assertion of maximum plastic power for the set of admissible stress states. Because these conditions are the hypotheses of the new model, we have proved the assertion for the conditional *associativity/nonassociativity* of the new model. The *associativity* refers to that $\partial f/\partial\sigma_{ij} = c\partial g/\partial\sigma_{ij}$, where c is a positive real and g is a certain plastic potential function. Conversely, the *nonassociativity* refers to that $\partial f/\partial\sigma_{ij} \neq c\partial g/\partial\sigma_{ij}$ for any positive real c . In the present model the plastic flow is associated under the condition of ($f_c < 0$) or ($f_c = 0$ and $\gamma_c = 0$). Otherwise, it is nonassociated.

For the two complementary trios represented by (7)–(12), there exist two *switching criteria* that characterize the values of $\dot{\lambda}_a$ and $\dot{\lambda}_c$. The details of deriving some suitable switching criteria to control them will be given in Section 5. However, for use in the next section, we will call the one that controls $\dot{\lambda}_a$ the first switch, and that which controls $\dot{\lambda}_c$, the second switch.

As seen from (24) the present model may have a rather complex kinematic hardening rule. However, as will be discussed in Section 7, we can greatly simplify this kinematic hardening rule in view of the concept of contact stress. In addition the present model also emphasizes the isotropic hardening aspect through (13) and (14). These two material functions h_a and h_c are allowed to be functions of $\bar{\epsilon}^p$, which, as specified at the beginning in Section 2, may characterize the expansion/contraction of the yield surface. It is well known that the isotropic hardening contribution is very important for the task of modeling the cyclic behavior of materials, especially the nonproportional cyclic loading ones.

4. Weak stability criteria

The substitution of Equations (3) and (4) into the inner product of Gs_{ij}^a with (1) gives

$$Gs_{ij}^a\dot{\epsilon}_{ij} = \frac{1}{2}s_{ij}^a\dot{s}_{ij} + \frac{3G\dot{\lambda}_a}{2h_a}s_{ij}^a s_{ij}^a + \frac{3G\dot{\lambda}_c}{2h_c}s_{ij}^a s_{ij}^c. \quad (26)$$

The plastic modulus E_p is defined by [Dafalias 1984]

$$\dot{\epsilon}_{ij}^p = \frac{n_{kl}\dot{s}_{kl}}{\frac{2}{3}E_p}v_{ij}, \quad (27)$$

where v_{ij} is the unit normal direction of the plastic strain rate, and

$$n_{ij} := \frac{1}{\left\| \frac{\partial f_a}{\partial s_{ij}} \right\|} \frac{\partial f_a}{\partial s_{ij}} = \frac{1}{\sqrt{\frac{2}{3}h_a}} s_{ij}^a \quad (28)$$

is the unit normal direction of the yield surface, which can be deduced from Equation (13). Substituting (28) into (27) gives

$$\dot{\epsilon}_{ij}^p = \frac{3s_{kl}^a\dot{s}_{kl}}{2\sqrt{\frac{2}{3}E_p}h_a}v_{ij}.$$

The substitution of the above equation into (15) further leads to

$$s_{ij}^a \dot{s}_{ij} = \frac{2}{3} E_p h_a \dot{\epsilon}^p. \tag{29}$$

If both the yield and contact conditions are satisfied, by using (29) and (26) we have

$$3G s_{ij}^a \dot{\epsilon}_{ij} = E_p h_a \dot{\epsilon}^p + 3G h_a \dot{\lambda}_a + \frac{9G}{2h_c} \dot{\lambda}_c s_{ij}^a s_{ij}^c. \tag{30}$$

By inserting the plastic flow rule (4) into (15), it follows that

$$\dot{\lambda}_a^2 + \frac{3\dot{\lambda}_c s_{ij}^a s_{ij}^c}{h_a h_c} \dot{\lambda}_a + \dot{\lambda}_c^2 - (\dot{\epsilon}^p)^2 = 0.$$

Then, by using (16) and (17) we can derive the following result:

$$\dot{\lambda}_a = \gamma_a \dot{\epsilon}^p, \tag{31}$$

where

$$\gamma_a := -\gamma_c \left(\gamma_c + \frac{h'_c}{k'_c} \right) + \sqrt{\left(\gamma_c^2 + \gamma_c \frac{h'_c}{k'_c} \right)^2 + 1 - \gamma_c^2}. \tag{32}$$

If $0 \leq \gamma_c < 1$ (see below), it is easy to prove that

$$\gamma_a > 0. \tag{33}$$

If the second switch is in the *off* state, that is, $\dot{\lambda}_c = 0$, we have $\gamma_c = 0$ by Equation (16). Thus $\gamma_a = 1$ via (32), and simultaneously Equation (31) reduces to

$$\dot{\lambda}_a = \dot{\epsilon}^p. \tag{34}$$

Hence, once the term $\dot{\epsilon}^p$ in (30) is replaced by $\dot{\lambda}_a$, we can obtain

$$3G s_{ij}^a \dot{\epsilon}_{ij} = (E_p + 3G) h_a \dot{\lambda}_a. \tag{35}$$

For the case of $\dot{\lambda}_c > 0$, from Equations (30), (31), (32), (16) and (17) it follows that

$$3G s_{ij}^a \dot{\epsilon}_{ij} = \left(E_p + 3G \sqrt{\left(\gamma_c^2 + \gamma_c \frac{h'_c}{k'_c} \right)^2 + 1 - \gamma_c^2} \right) h_a \dot{\epsilon}^p, \tag{36}$$

which reduces to Equation (35), when $\gamma_c = 0$.

The following inequality can be proved:

$$\left(\gamma_c^2 + \gamma_c \frac{h'_c}{k'_c} \right)^2 - \gamma_c^2 \leq 0. \tag{37}$$

Since $s_{ij}^c / (\sqrt{\frac{2}{3}} h_c)$ and $s_{ij}^a / (\sqrt{\frac{2}{3}} h_a)$ are two unit tensors, from (17), (23), (11) and (15) it follows that

$$0 \leq \gamma_c \leq 1 - \frac{h'_c}{k'_c}, \quad \left(\gamma_c + \frac{h'_c}{k'_c} \right)^2 \leq 1. \tag{38}$$

Then, by using

$$\left(\gamma_c^2 + \gamma_c \frac{h'_c}{k'_c}\right)^2 - \gamma_c^2 = \left(\left(\gamma_c + \frac{h'_c}{k'_c}\right)^2 - 1\right)\gamma_c^2,$$

the inequality (37) is proved. From this result we have

$$E_p + 3G \sqrt{\left(\gamma_c^2 + \gamma_c \frac{h'_c}{k'_c}\right)^2 + 1 - \gamma_c^2} \leq E_p + 3G. \tag{39}$$

The above equality holds only for $\gamma_c = 0$ or $\gamma_c = 1 - h'_c/k'_c$, which, in view of (32), corresponds to $\gamma_a = 1$ or $\gamma_a = h'_c/k'_c$. For these two cases, we have $\gamma_a + \gamma_c = 1$. But from (17) with $\gamma_c = 1 - h'_c/k'_c$, we have $s_{ij}^a s_{ij}^c = 2h_a h_c/3$, which is substituted into (19), and then the use of yield and contact conditions leads to $\mathcal{D} = 0$. Thus from (18) we have $h'_c/k'_c = 1$, which makes $\gamma_c = 0$ and $\gamma_a = 1$ again. So the range of γ_c in (38) is modified to

$$0 \leq \gamma_c < 1 - \frac{h'_c}{k'_c}. \tag{40}$$

The range of γ_c can be estimated more precisely. From Equation (18) we have $k'_c \geq h'_c$ and thus, by (23),

$$0 < \frac{h'_c}{k'_c} \leq 1. \tag{41}$$

From (40) it follows that

$$0 \leq \gamma_c < 1.$$

In summary, $\gamma_a + \gamma_c = 1$ holds only under the condition $\gamma_c = 0$, and the equality in (39) holds only for the case of $\gamma_c = 0$.

For other cases with the range of γ_c specified by (40) we can prove that

$$\gamma_a + \gamma_c \geq 1. \tag{42}$$

Inserting (32) for γ_a , the above inequality means that

$$\gamma_c - \gamma_c \left(\gamma_c + \frac{h'_c}{k'_c}\right) + \sqrt{\left(\gamma_c^2 + \gamma_c \frac{h'_c}{k'_c}\right)^2 + 1 - \gamma_c^2} \geq 1.$$

Thus, we have

$$0 < 1 - \gamma_c + \gamma_c \left(\gamma_c + \frac{h'_c}{k'_c}\right) \leq \sqrt{\left(\gamma_c^2 + \gamma_c \frac{h'_c}{k'_c}\right)^2 + 1 - \gamma_c^2}. \tag{43}$$

To prove the first inequality in the above, that is,

$$\gamma_c^2 + \left(\frac{h'_c}{k'_c} - 1\right)\gamma_c + 1 > 0,$$

let us note that the above inequality holds when $\gamma_c = 0$ and that the discriminant satisfies

$$\left(\frac{h'_c}{k'_c} - 1\right)^2 - 4 < 0$$

by (41). Therefore, the first inequality in Equation (43) follows obviously.

Taking the square of both the sides and canceling the common terms of the second inequality in (43), we obtain

$$\gamma_c \left(\gamma_c + \frac{h'_c}{k'_c} - 1 \right) \leq 0.$$

It is true for γ_c in the range specified by (40). Thus the inequality in (42) is proved.

As discussed above, the equality $\gamma_a + \gamma_c = 1$ holds only under the condition $\gamma_c = 0$, and for the other cases of $\gamma_c > 0$, we always have $\gamma_a + \gamma_c > 1$, which, together with the plastic flow rule in equation (4) and (16) and (31), indicates that the plastic flow increases under the condition of contact. Indeed, $\dot{\bar{e}}^P$ is a quantity to measure the strength of plastic flow. When comparing (35) and (36) and noting the inequality (39), we can also conclude that the plastic flow under the condition of contact is stronger than that in the noncontact condition.

Under the condition $\dot{\lambda}_c = 0$, the weak stability criteria are

$$G > 0, \quad h_a > 0, \quad E_p + 3G > 0. \tag{44}$$

Otherwise, under the condition of $\dot{\lambda}_c > 0$, the weak stability criteria are

$$G > 0, \quad h_a > 0, \quad E_p + 3G \sqrt{\left(\gamma_c^2 + \gamma_c \frac{h'_c}{k'_c} \right)^2 + 1 - \gamma_c^2} > 0. \tag{45}$$

If $f_a = 0$, the consistency condition reads as

$$\frac{\partial f_a}{\partial s_{ij}^a} \dot{s}_{ij}^a + \frac{\partial f_a}{\partial \bar{e}^P} \dot{\bar{e}}^P = 0,$$

or by Equation (13), further reads as

$$s_{ij}^a \dot{s}_{ij}^a = \frac{2}{3} h_a h'_a \dot{\bar{e}}^P. \tag{46}$$

Then, taking the inner product of both the sides of (4) with s_{ij}^a with the help of (31), (16) and (17) leads to

$$s_{ij}^a \dot{e}_{ij}^P = \left(\gamma_a + \gamma_c \left(\gamma_c + \frac{h'_c}{k'_c} \right) \right) h_a \dot{\bar{e}}^P. \tag{47}$$

This equation is to be used later.

5. Switch of plastic irreversibility

The first complementary trio (7)–(9) enables the model to possess a switch of plastic irreversibility, whose *on/off* conditions are derived below.

We first consider the case of $\dot{\lambda}_c = 0$. If the yield condition $f_a = 0$ and the consistency condition $\dot{f}_a = 0$ are satisfied, but the contact condition is unsatisfied, that is, $f_c < 0$ and thus $\dot{\lambda}_c = 0$ by (12), then (35) can be used. Because of (44) for the weak stability criteria of the case of $\dot{\lambda}_c = 0$, from Equation (35) it follows that

$$\text{if } f_a = 0, \quad \text{then } s_{ij}^a \dot{e}_{ij} > 0 \iff \dot{\lambda}_a > 0. \tag{48}$$

Thus, we have

$$f_a = 0 \quad \text{and} \quad s_{ij}^a \dot{e}_{ij} > 0 \implies \dot{\lambda}_a > 0. \tag{49}$$

On the other hand, if $\dot{\lambda}_a > 0$, (9) ensures $f_a = 0$, which, together with (48), asserts that

$$\dot{\lambda}_a > 0 \Rightarrow f_a = 0 \quad \text{and} \quad s_{ij}^a \dot{e}_{ij} > 0. \quad (50)$$

Therefore, from (49) and (50) we conclude that the yield condition $f_a = 0$ and the straining condition $s_{ij}^a \dot{e}_{ij} > 0$ are sufficient and necessary for plastic irreversibility with $\dot{\lambda}_a > 0$. Considering this and Equation (7), we thus possess the following switching criteria of plastic irreversibility:

$$\dot{\lambda}_a \begin{cases} > 0, & \text{if } f_a = 0 \quad \text{and} \quad s_{ij}^a \dot{e}_{ij} > 0, \\ = 0, & \text{if } f_a < 0 \quad \text{or} \quad s_{ij}^a \dot{e}_{ij} \leq 0, \end{cases} \quad (51)$$

or, due to Equations (31) and (33),

$$\dot{e}^p \begin{cases} > 0, & \text{if } f_a = 0 \quad \text{and} \quad s_{ij}^a \dot{e}_{ij} > 0, \\ = 0, & \text{if } f_a < 0 \quad \text{or} \quad s_{ij}^a \dot{e}_{ij} \leq 0. \end{cases} \quad (52)$$

Next, we consider the case of $\dot{\lambda}_c > 0$, from which we have (36). Because of (45) for the weak stability criteria of the case of $\dot{\lambda}_c > 0$, from (36) it follows that

$$\text{if } f_a = 0, \quad \text{then} \quad s_{ij}^a \dot{e}_{ij} > 0 \iff \dot{e}^p > 0. \quad (53)$$

Thus,

$$f_a = 0 \quad \text{and} \quad s_{ij}^a \dot{e}_{ij} > 0 \Rightarrow \dot{e}^p > 0. \quad (54)$$

On the other hand, if $\dot{e}^p > 0$, then $\dot{\lambda}_a > 0$ by (31) and (33), and then (9) assures $f_a = 0$, which, together with (36), asserts that

$$\dot{e}^p > 0 \Rightarrow f_a = 0 \quad \text{and} \quad s_{ij}^a \dot{e}_{ij} > 0.$$

Therefore, from Equations (53) and (54) we conclude that the yield condition $f_a = 0$ and the straining condition $s_{ij}^a \dot{e}_{ij} > 0$ are sufficient and necessary for the plastic irreversibility with $\dot{e}^p > 0$. For this case, we thus possess the same switching criteria of plastic irreversibility as that given by Equation (52).

In the *on* state of the switch, $\dot{\lambda}_a > 0$ and $\dot{e}^p > 0$, the mechanism of plastic irreversibility is working and the material exhibits elastoplastic behavior, while in the *off* state of the switch, $\dot{\lambda}_a = 0$ and $\dot{e}^p = 0$, the material is reversible and elastic. According to the complementary trio (7)–(9), there are two states: (i) $\dot{\lambda}_a > 0$ and $f_a = 0$, and (ii) $\dot{\lambda}_a = 0$ and $f_a \leq 0$. From the switch (51) it is clear that (i) corresponds to the *on* state whereas (ii) corresponds to the *off* state.

6. Switch of kinematic hardening rules

The following discussion is under the condition of $\dot{e}^p > 0$ in the plastic state. The second complementary trio (10)–(12) enables the model to possess a switch of kinematic hardening rules, the *on/off* conditions of which are derived below.

If the contact condition $f_c = 0$ is not satisfied, that is, $f_c < 0$, then by Equation (12) we have $\dot{\lambda}_c = 0$ and then $\gamma_c = 0$ by (16). Thus, before the occurrence of contact from (6) we have

$$\dot{s}_{ij}^c = \frac{2}{3} k'_c \dot{e}_{ij}^p. \quad (55)$$

Continuously moving under the above governing law of contact stress, the contact may happen, that is, $f_c = 0$, because of $k'_c > 0$ by (23), and at the moment of contact, if $\dot{f}_c > 0$, there will eventually occur a penetration to violate the contact condition. From (14) and (55) the penetration condition can be derived as follows:

$$k'_c s_{ij}^c \dot{e}_{ij}^p - h_c h'_c \dot{e}^p > 0.$$

The substitution of (4) and (34) into the above equation gives

$$\left(\frac{3}{2h_a} k'_c s_{ij}^c s_{ij}^a - h_c h'_c \right) \dot{e}^p > 0.$$

Due to (23), dividing the above equation by $h_c k'_c > 0$, leads to

$$\left(\frac{s_{ij}^c}{\sqrt{\frac{2}{3}}h_c} \frac{s_{ij}^a}{\sqrt{\frac{2}{3}}h_a} - \frac{h'_c}{k'_c} \right) \dot{e}^p = \gamma_c \dot{e}^p > 0,$$

where the definition given in Equation (17) is used. Using the definition (16) the penetration condition now reads as

$$f_c = 0 \quad \text{and} \quad \dot{\lambda}_c > 0. \tag{56}$$

Therefore, upon happening the contact we cannot continuously use (55) to avoid the penetration, and the contact law must be switched to (6).

Considering this and (10), we thus possess the following switching criteria of kinematic hardening rules:

$$\dot{\lambda}_c \begin{cases} > 0, & \text{if } f_c = 0 \quad \text{and} \quad \gamma_c > 0, \\ = 0, & \text{if } f_c < 0 \quad \text{or} \quad \gamma_c = 0. \end{cases} \tag{57}$$

In the *on* state of the switch, $\dot{\lambda}_c > 0$, the mechanism of kinematic hardening is working according to (24), while in the *off* state of the switch, $\dot{\lambda}_c = 0$, the kinematic hardening rule is still governed by (24) but with $\dot{\lambda}_c = 0$ and $\gamma_c = 0$, that is, the Prager kinematic hardening rule:

$$\dot{s}_{ij}^b = \frac{2}{3} k'_a \dot{e}_{ij}^p. \tag{58}$$

According to the complementary trio (10)–(12), there are two states of the kinematic hardening: (i) $\dot{\lambda}_c > 0$ and $f_c = 0$, and (ii) $\dot{\lambda}_c = 0$ and $f_c \leq 0$. From the switch (57) it is clear that (i) corresponds to the *on* state whereas (ii) to the *off* state.

7. The coefficient functions

The existence of contact surface will affect the motion of yield surface, and thus the kinematic hardening rules must be modified to abide the contact rule. In contrast to the penetration condition as given in (56), the nonpenetration condition is

$$(f_c < 0) \quad \text{or} \quad (f_c = 0 \quad \text{and} \quad \dot{f}_c \leq 0). \tag{59}$$

The condition of $f_c < 0$ corresponds to the *off* state of the second switch. In the rest of this section, we will consider the case of *on* state of the switch of (57), that is, $\dot{\lambda}_c > 0$. By Equation (14), the conditions

of $f_c = 0$ and $\dot{f}_c \leq 0$ in the above can be written as

$$\frac{3}{2}s_{ij}^c s_{ij}^c = h_c^2, \quad \frac{3}{2}s_{ij}^c \dot{s}_{ij}^c - h_c h_c' \dot{e}^p \leq 0. \tag{60}$$

This indeed supplies a constraint on the contact rule (6) in the case of $\dot{\lambda}_c > 0$.

Substitution of (6) into the latter one of (60) and the use of the former one lead to

$$-C_1 \dot{\lambda}_c h_c^2 + \left(k'_c + \frac{3}{2}\gamma_c C_2\right) s_{ij}^c \dot{e}_{ij}^p + \frac{3}{2}\gamma_c s_{ij}^c \dot{s}_{ij} \leq h_c h_c' \dot{e}^p. \tag{61}$$

Inserting

$$\gamma_c C_2 = -\frac{2}{3}k'_c \tag{62}$$

into (61), which, dividing by $\dot{\lambda}_c h_c^2$ and then using (23), (16) and $\dot{\lambda}_c > 0$, gives the following inequality

$$C_1 \geq \frac{3s_{ij}^c \dot{s}_{ij}}{2h_c^2 \dot{e}^p} - \frac{h'_c}{\gamma_c h_c}.$$

So we let

$$C_1 = \frac{3s_{ij}^c \dot{s}_{ij}}{2h_c^2 \dot{e}^p} - \frac{h'_c}{\gamma_c h_c} \tag{63}$$

to guarantee that the contact can be continued to avoid the penetration. By using (63) and (62) for C_1 and C_2 , Equation (6) can be simplified to

$$\dot{s}_{ij}^c = \frac{h'_c \dot{e}^p}{h_c} s_{ij}^c + \gamma_c \left(\dot{s}_{ij} - \frac{3\dot{s}_{mn} s_{mn}^c}{2h_c^2} s_{ij}^c \right). \tag{64}$$

Substituting Equations (5) and (62) into (46) leads to

$$-C_1 \dot{\lambda}_c s_{ij}^a s_{ij}^a - \frac{2}{3}(k'_a - k'_c) s_{ij}^a \dot{e}_{ij}^p - C_3 \dot{\lambda}_c s_{ij}^a e_{ij}^p + (1 - \gamma_c) s_{ij}^a \dot{s}_{ij} + C_4 \dot{\lambda}_c s_{ij}^a s_{ij} = \frac{2}{3} h_a h'_a \dot{e}^p. \tag{65}$$

From Equations (16), (29), (47) and $f_a = 0$, the final form of the above equation can be obtained,

$$\begin{aligned} \gamma_c C_3 s_{ij}^a e_{ij}^p &= \frac{2}{3} E_p h_a (1 - \gamma_c) - \frac{2}{3} h_a \left\{ h'_a + (k'_a - k'_c) \left(\gamma_a + \gamma_c \left(\gamma_c + \frac{h'_c}{k'_c} \right) \right) \right\} \\ &+ \gamma_c C_4 s_{ij}^a s_{ij} - \gamma_c C_1 \frac{2h_a^2}{3}. \end{aligned} \tag{66}$$

Up to now, there have been three equations (62), (63) and (66) to determine the four unknown coefficients C_1 , C_2 , C_3 and C_4 . For simplicity, the remaining one is assumed to be

$$C_4 = \frac{-C_3}{2G}. \tag{67}$$

Substituting Equation (67) into (66) leads to

$$\gamma_c C_3 s_{ij}^a \left[e_{ij}^p + \frac{1}{2G} s_{ij} \right] = \frac{2}{3} E_p h_a (1 - \gamma_c) - \gamma_c C_1 \frac{2h_a^2}{3} - \frac{2}{3} h_a \left(h'_a + (k'_a - k'_c) \left(\gamma_a + \gamma_c \left(\gamma_c + \frac{h'_c}{k'_c} \right) \right) \right). \tag{68}$$

This equation can be used to determine C_3 .

In summary, the procedures to obtain the coefficient functions are:

$$C_1 \text{ given by (63)} \longrightarrow C_3 \text{ from (68)} \longrightarrow C_4 \text{ from (67)} \longrightarrow C_2 \text{ from (62)}.$$

Under the noncontact condition, the governing equations of back stress and contact stress as presented by (58) and (55), respectively, have the same simpler form. However, under the contact condition, the governing equation of back stress becomes very complex, as shown by (24) with the above coefficient functions C_1, \dots, C_4 , whereas we can appreciate the neatness of the governing equation for the contact stress as shown by (64). Therefore, in terms of the concept of contact stress we can more precisely derive the contact condition and its switching criteria.

8. Plastic modulus

The equality of $\gamma_c = 0$ can happen for $\dot{\lambda}_c = 0$ in the *off* state of the switch (57), or for a state of which the yield surface is in contact with the bounding surface and stress is impinging simultaneously on the both surfaces. In this latter case the two unit tensors in (17) are in parallel, and thus, one has

$$\frac{s_{ij}^c}{\sqrt{\frac{2}{3}}h_c} \frac{s_{ij}^a}{\sqrt{\frac{2}{3}}h_a} = 1 \Rightarrow \gamma_c = 1 - \frac{h'_c}{k'_c}. \tag{69}$$

From (19) it is also $\mathcal{D} = 0$ for this case, and hence we have $h'_c/k'_c = 1$ in view of (18). So γ_c is zero by (69), and then $\dot{\lambda}_c = 0$ by (16). Therefore we have the same kinematic hardening rule as the one that is using before the occurrence of contact.

For the case of $\mathcal{D} = 0$ the plastic modulus $E_p = h'_a + k'_a$ is the slope of the stress-plastic strain curve in the uniaxial tension test after the intersection of the yield curve and the bounding curve. On the other hand, for the case of $\mathcal{D} > 0$ the plastic modulus $E_p = h'_a + k'_a$ is a function of $h'_0, k'_0, h_c = h_0 - h_a$ and \mathcal{D} , the last term of which is the distance between the current stress point and its image point on the bounding surface as shown by (19), and h'_0, k'_0, h_0, h_a are material functions, such that

$$E_p = h'_a + k'_a = (h'_0 + k'_0) \exp\left(a\left(\frac{\mathcal{D}}{2h_c}\right)^b\right). \tag{70}$$

The contact stress bound is given by $h_c = h_0 - h_a$ and the kinematic modulus of contact surface is given by $k'_c = k'_a - k'_0$. They are consistent with (18). It means that (70) is a direct result of (18) by inserting $h'_c = h'_0 - h'_a$ and $k'_c = k'_a - k'_0$.

The substitution of (70) into (35) gives

$$\dot{\bar{e}}^p = \frac{3Gs_{ij}^a \dot{e}_{ij}}{h_a \left((h'_0 + k'_0) \exp\left(a\left(\frac{\mathcal{D}}{2h_c}\right)^b\right) + 3G \right)}, \tag{71}$$

from which the amount of $\dot{\bar{e}}^p$ can be greatly reduced for a larger $\mathcal{D} > 0$. This result can be compared with that demonstrated in Section 4, where the plastic flow increases under the condition of contact.

When the yield surface is in contact with the bounding surface and stress stands on both surfaces, we have $\mathcal{D} = 0$, and thus from (70) we have $h'_a + k'_a = h'_0 + k'_0$, which guarantees the continuity of plastic modulus.

9. Experimental tests of SAE 4340 and RHA

In this section the materials SAE 4340 and RHA (rolling homogeneous armory) under various loadings in an MTS axial-torsional test system are investigated. The investigation includes loading, unloading, reverse loading, and cyclic loading for uniaxial and biaxial conditions. The related basic material functions used in the constitutive laws are identified based on the experimental data.

The conventional method to obtain the material functions in the classic plasticity models is to perform the uniaxial tension/compression or torsional test. These techniques seem to be sufficient to fit the material functions of mixed-hardening model only, and not enough to fit the material functions needed in the constitutive equations of the present paper for a more powerful cyclic model. The other drawback of a simple test is that the range of equivalent plastic strain $\bar{\epsilon}^p$ is too small (about 10 percent), such that the material functions obtained from that test may not be appropriate for the cyclic loading conditions, because the value of $\bar{\epsilon}^p$ may reach over 100% in a typical cyclic loading test.

9.1. Experimental method.

Experimental apparatus and method. For the uniaxial tension/compression cyclic test the results can be used to determine the material functions used in the constitutive equations. For this purpose a uniaxial cyclic test is designed, which is conducted in the MTS test system under strain control.

The biaxial cyclic loading test was conducted with an MTS 458.20 Axial-Torsional test machine of the College of Engineering of the National Taiwan University. This machine can be feedback controlled simultaneously for axial and torsional directions by either stroke, load or strain control.

In this series of tests the strain control mode was selected, which is the most stable control method. The measurement of strain was performed by the MTS 632.80C-04 biaxial extensometer.

A thin-walled tube was adopted as the test specimen. When the ratio of outside diameter to thickness is large enough (about 8/1), the stress (σ_{11}, σ_{12}) can be viewed as uniformly distributed in the axial parallel portion of the specimen.

Size and material of specimen. We chose two metallic materials to be tested, the chemical compositions of which are shown in Table 1.

The size of the specimen for the uniaxial test was of total length 12 cm, the end parts with length 4 cm and diameter 16 mm, and the parallel portion with length greater than 3 cm and diameter 8 mm. The uniaxial extensometer MTS 623.11C-20 was used to measure strain.

The gauge length of the biaxial extensometer MTS 632.80C-04 was 25 mm. Therefore, the outside diameter of the parallel portion of the specimen was restricted to 25 mm, and the end part was 46 mm. The inside diameter of the parallel part of the specimen was chosen to be 23 mm, so the outside diameter/thickness ratio was less than 8/1 to avoid the buckling of the specimen under compression.

	C	Mn	P	S	Si	Cr	Ni	Mo	Al
SAE 4340	0.3746	0.6196	0.0177	0.0168	0.2116	0.6344	1.592	0.1584	0.0256
RHA	0.2413	0.2128	0.0114	0.0140	0.2171	1.160	2.851	0.2499	0.0197

Table 1. Chemical compositions of tested materials.

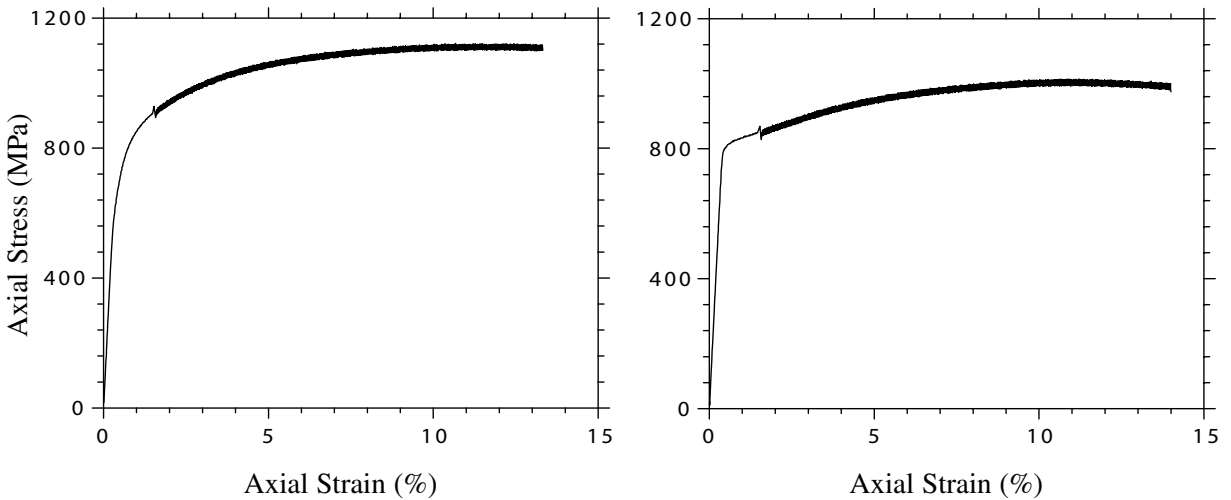


Figure 2. Experimental results of (left) SAE 4340 and (right) RHA under monotonic axial strain.

9.2. Experimental path design. Metallic materials in general exhibit hardening and then softening in the stress-strain curve for the uniaxial monotonic loading test. Because the stress control experiment cannot be conducted in the range of softening, the experiments are all of the strain-controlled tests in this paper. Hence, the ratcheting effects which can be revealed only in the stress-controlled tests were not studied in this paper.

The following strain paths likely to occur with a typical structure during repeated loadings were chosen:

(1) Uniaxial experiments:

(a) Monotonic axial loading from $\epsilon_{11} = 0$ to $\epsilon_{11} = 15\%$: Figure 2.

(b) Cyclic loading

(i) mean strain 0 and strain amplitude 1.5%: Figure 3.

(ii) mean strain 1.5% and strain amplitude 1.5%: Figure 4.

(iii) initial mean strain equals zero and initial strain amplitude equals 0.6%, and mean strain and strain amplitude are increased cyclically both with the amounts of 0.3% per each cycle up to the values of 1.8% for mean strain and 2.4% for strain amplitude: Figure 5.

(iv) initial mean strain equals zero and initial strain amplitude equals 0.5%, and strain amplitude is increased cyclically with the amount of 0.5% per each cycle: Figure 6.

(2) Biaxial experiments:

(a) Proportional cyclic loadings with different ratios: Figures 7 and 8.

(b) Non-proportional cyclic loading with phase lags of 0° , 45° , 90° and 135° : Figures 9 and 10.

(c) Square paths: Figures 11 and 12.

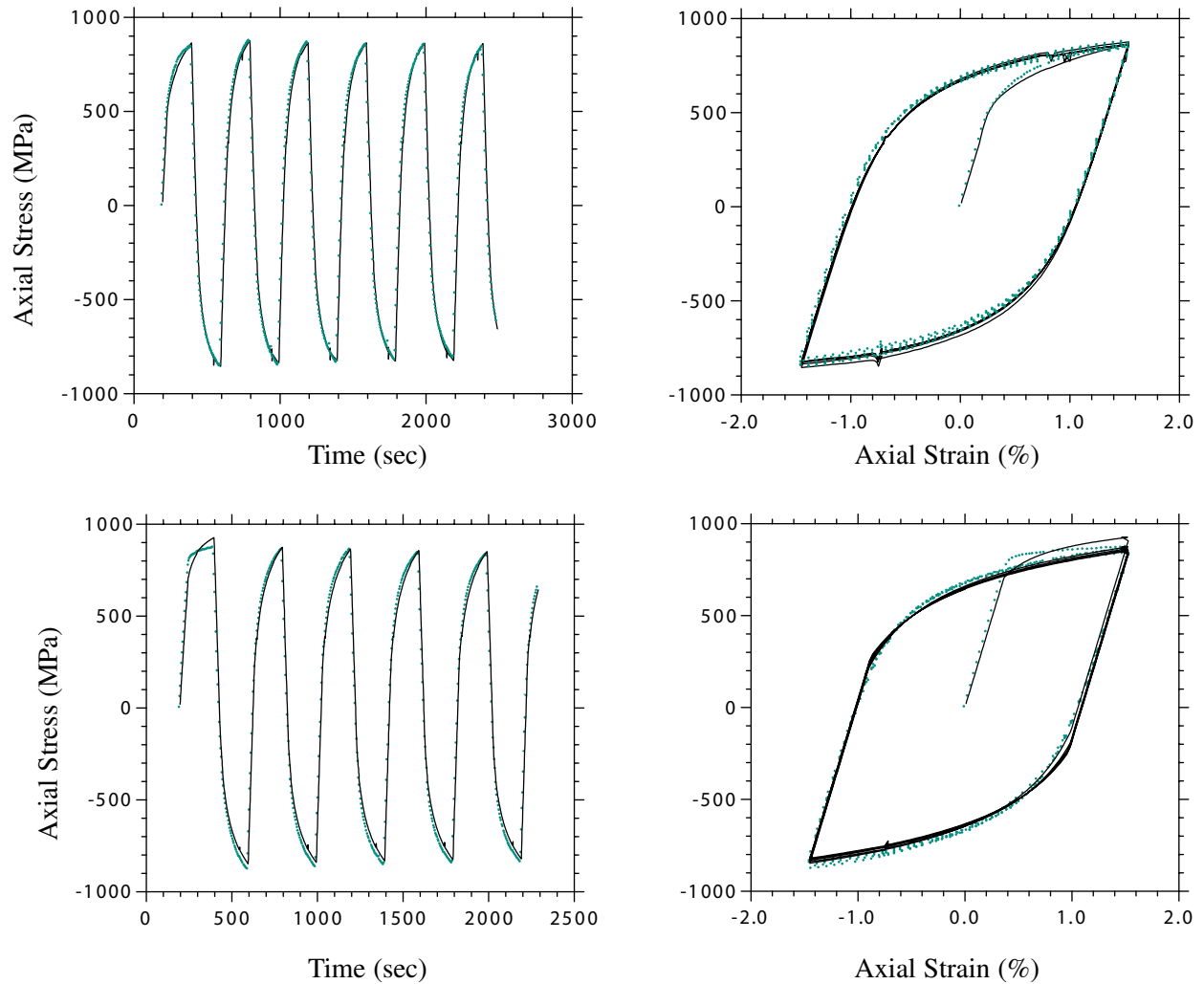


Figure 3. Experimental and simulated results for (top) SAE 4340 and (bottom) RHA under cyclic axial strain with amplitude 1.5% and zero mean. Left: time history of axial stress; right: axial stress versus axial strain. Green dots represent experimental values, solid lines represent the theory.

In the biaxial tests, each subpart was carried out for five cycles. All the tests were conducted at room temperature under a nearly quasistatic process (the axial strain rate was about 10^{-4}s^{-1} and the shear strain rate was about $1.732 \times 10^{-4}\text{s}^{-1}$). Thus the thermal effect and the rate effect were excluded.

All the stress-strain curves that appear in this paper were plotted by the computer from the acquired data without any data smoothing effort; some irregular bursts presented in the figures may be attributed to the electrical and hydraulic instability of the test machine. The discussions of the test results are given below.

9.3. Experimental results.

Uniaxial experiments. Figure 2 displays the stress-strain relation of SAE 4340 and RHA. The Young's modulus of SAE 4340 is about 200 GPa, and the yield point is detected at about 870 MPa. At a strain of 12%, SAE 4340 is hardened to 1100 MPa. The Young's modulus of RHA is about 200 GPa, and the yield point is detected at about 800 MPa. At a strain of 12%, RHA is hardened to 1000 MPa.

From Figure 3 it can be seen that the initial yield of SAE 4340 occurred at a stress equal to 600 MPa. When the reverse loading was applied up to the plastic range again the yield stress was reduced to -400 MPa, which is much less than the tensile stress. This phenomenon is known as the Bauschinger effect. After the second cycle, SAE 4340 displayed a cyclic softening and tended to saturation rather fast. Eventually, the maximum tensile stress 900 MPa and maximum compressive stress -850 MPa were reached with the strain amplitude of 1.5%. From this fact we know that the cyclic stress response is drastically different from the simple loading test. At this test, the Bauschinger and Masing effects are apparent. From Figure 3, it appears that the cyclic behavior of RHA is similar to that of SAE 4340.

Figure 4 shows the test results with mean strain different from zero. Since the mean of strain is not zero, the cyclic stress-strain curve shows a shift in the positive strain direction. Basically, the experimental result is similar to the above case, but in this case the stabilization of the cyclic curve is quicker than that of the previous loading case. This phenomenon may be attributed to the fact that the accumulated plastic strain is larger than that in Figure 3 before the cyclic loading is executed.

The purpose of the tests shown in Figure 5 is to investigate both the effects of strain amplitude and mean stress on the cyclic stress-strain curve. Both materials tested exhibited a mixed-hardening behavior. The right panels in these figures show the results due to the interaction of amplitude and mean, in which the elastic range is increased gradually, that is, the isotropic hardening increased with increasing amplitude and mean. In addition, the kinematic hardening seems saturated. It seems that the effect of the memory of maximum plastic strain can be investigated from this test.

The test results shown in Figure 6 can be used to investigate the influence of increasing strain amplitude. The expansion and contraction of the elastic range can be investigated, which means that the isotropic hardening and then softening occur in this test; on the other hand the kinematic hardening tends to saturation as shown in the right-hand panes of the figure. Due to the large strain amplitudes imposed in this test, it can be seen that the material hardens immensely, then softens slightly and then reaches towards a final failure only within a few cycles.

Biaxial experiments. The results of the biaxial experiments are shown in Figures 7 and 8, which plot the results of proportional loading tests with different ratios of axial strain amplitudes and shear strain amplitudes. In the first five cycles of the strain path with a zero shear strain, the stress-strain relations are similar to the results obtained from a uniaxial cyclic test. In the second stage the shear strain is raised by a ratio of half the amplitude of the axial strain. The hysteresis loop of axial stress-axial strain in this stage becomes smaller than that of the previous one due to the reduction of axial strain. In this stage the hysteresis loop seems saturated very soon to a stable shape. In the third stage the ratio of axial strain amplitude to shear strain amplitude is $2 : \sqrt{3}$, and the size of axial hysteresis loop becomes much smaller. At the fourth stage a pure shear imposed, the size of shear hysteresis loop increases and the axial stress relaxes. The fifth and sixth stages are the same as that of the third and second stages with only the axial strains being now inversed to a compressive one. In the last two stages further hardening is detected.

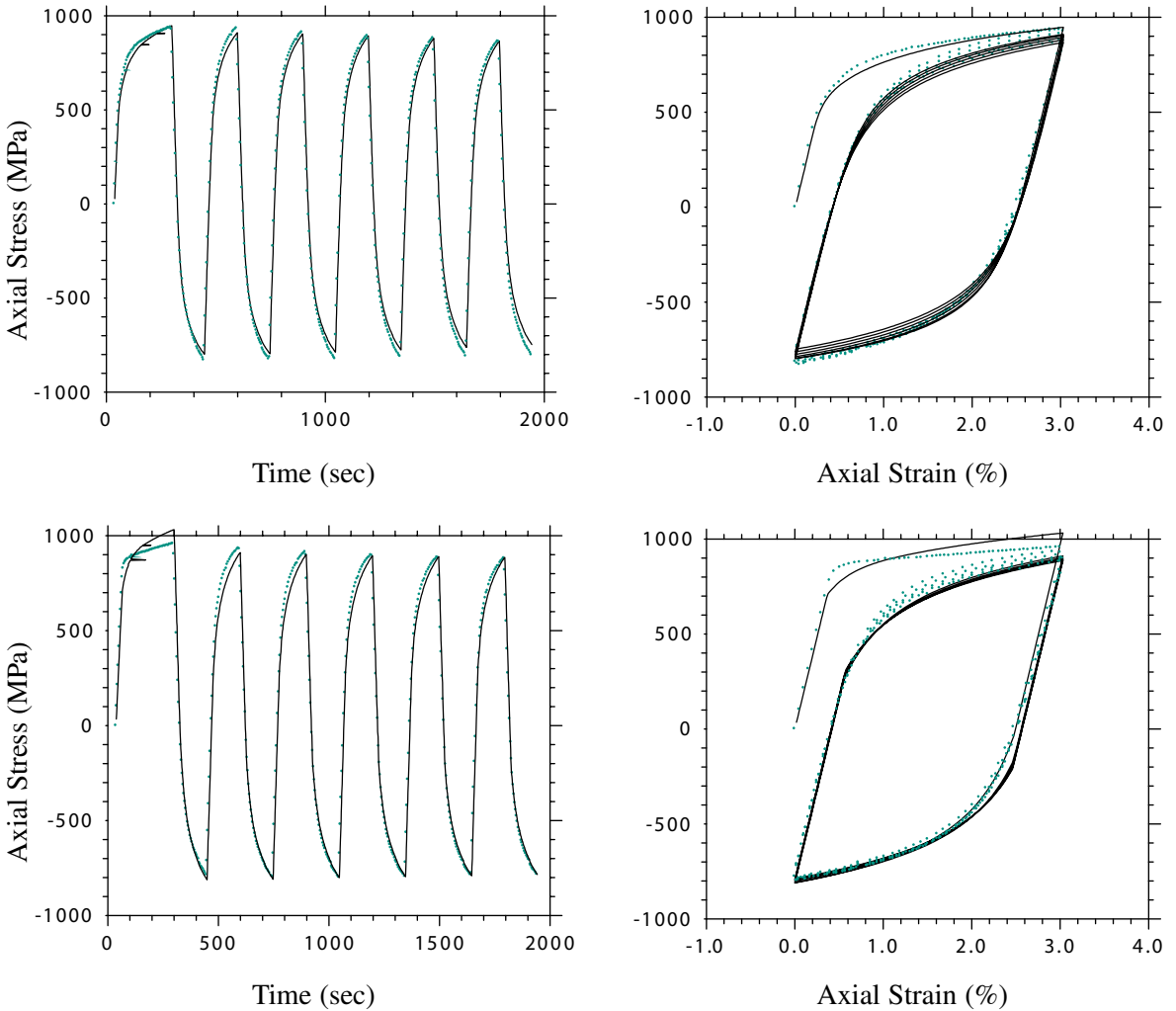


Figure 4. Experimental and simulated results of (top) SAE 4340 and (bottom) RHA under cyclic axial strain with amplitude 1.5% and mean 1.5%. Left: time history of axial stress; right: axial stress versus axial strain. Green dots represent experimental values, solid lines represent the theory.

Figures 9 and 10 show and compare the test results of nonproportional loadings with phase lags of 0° , 45° , 90° and 135° , respectively. In the first stage it is a proportional biaxial loading, in which the stress is reduced slightly as compared with the uniaxial test. In the second stage a 45° phase lag biaxial loading is applied. The hysteresis loops reveal a great distortion and hardening, and the stress path is displayed as an ellipse. The phase lag is increased to 90° in the third stage. More hardening phenomenon can be seen, the hysteresis loop looks like an ellipse, and the stress path looks like a circle. In the fourth stage the phase lag is 135° . The stress-strain diagrams are similar to the results in the previous stage with the roles of the two axes interchanged. No further hardening exists in this stage.

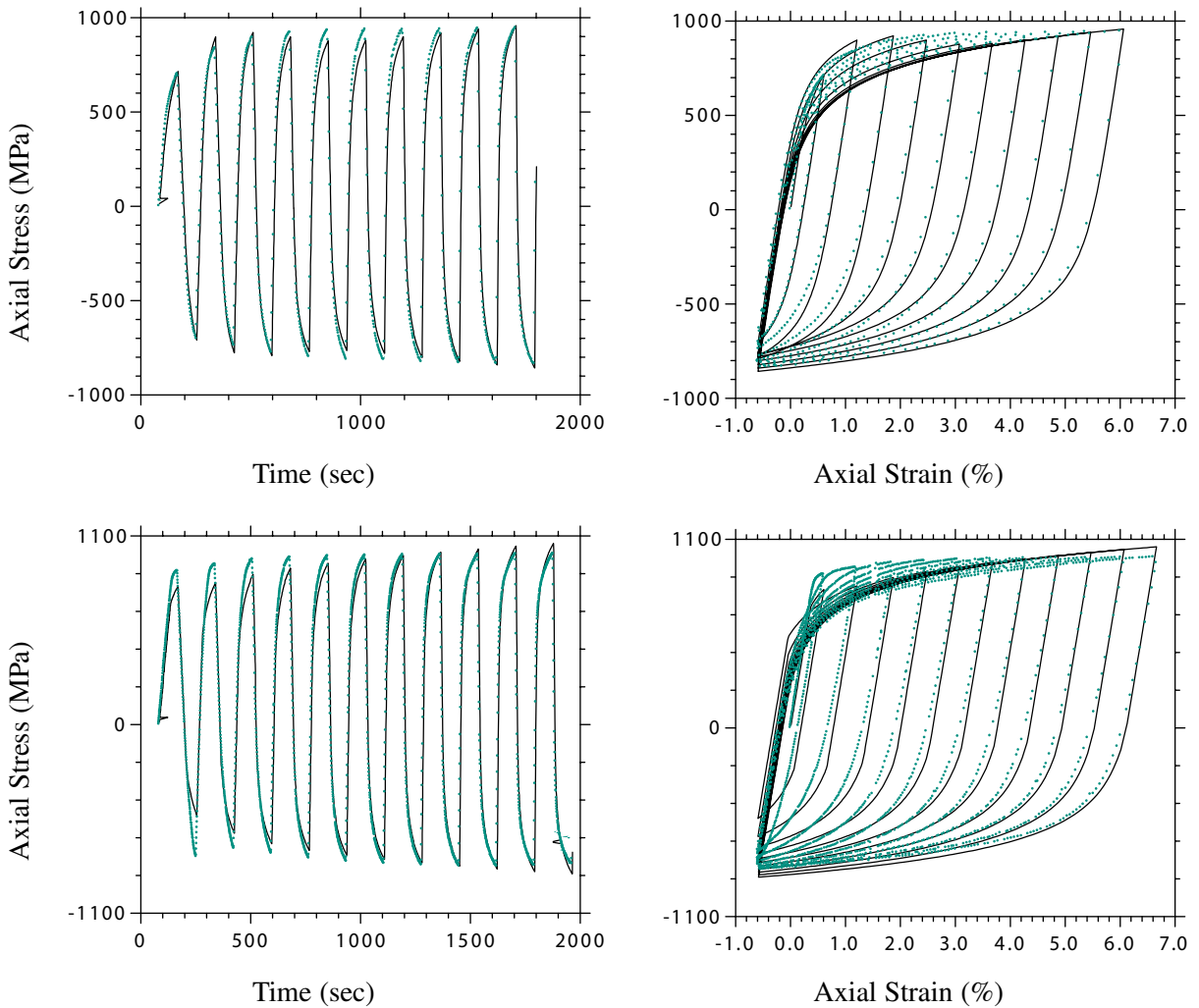


Figure 5. Experimental and simulated results for (top) SAE 4340 and (bottom) RHA under cyclic axial strain with increasing amplitude 0.6% per cycle and fixed compressive strain -0.6% . Left: time history of axial stress; right: axial stress versus axial strain. Green dots represent experimental values, solid lines represent the theory.

The experimental results given in Figures 11 and 12 are used to evaluate the alternative loading-unloading effects on the two materials tested. In the first stage which starts from a shear strain loading, an upper yield point can be seen. The strain hardening is apparent in this test. The stress relaxation to zero value and stabilization appear when the strain is held in one direction. In the second stage, an over hardening phenomenon can be seen.

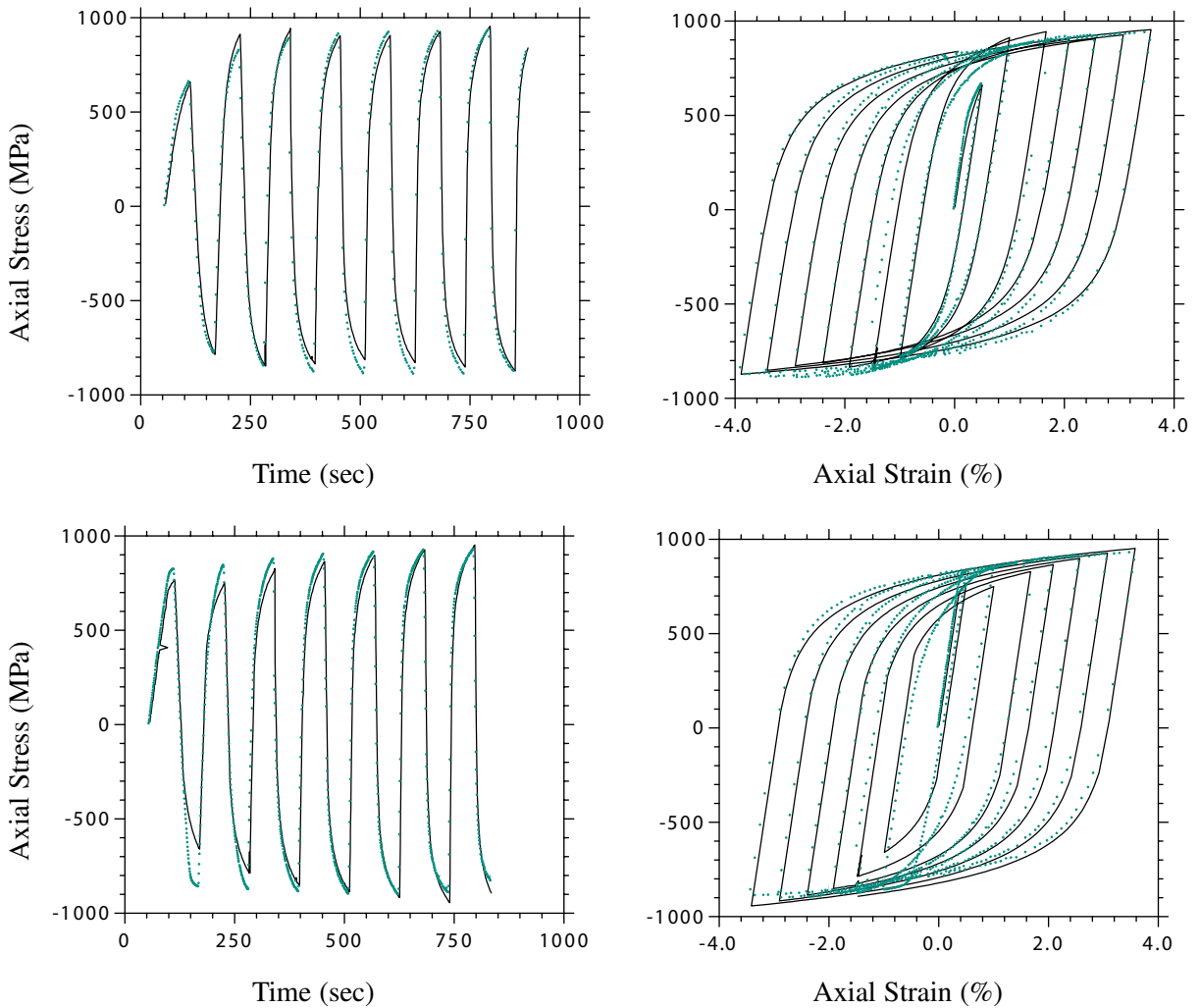


Figure 6. The experimental and simulated results of (top) SAE 4340 and (bottom) RHA under cyclic axial strain with increasing amplitude 0.5% per cycle but with zero mean. Left: time history of axial stress; right: axial stress versus axial strain. Green dots represent experimental values, solid lines represent the theory.

10. Discussion

In this experimental study, SAE 4340 and RHA were investigated under various uniaxial and biaxial cyclic loadings under strain control. Accordingly, the following results can be summarized.

- (1) Precluding the thermal and rate effects, the reverse loading path abides the mixed hardening rules. In all tests the Bauschinger and Masing effects are apparent.

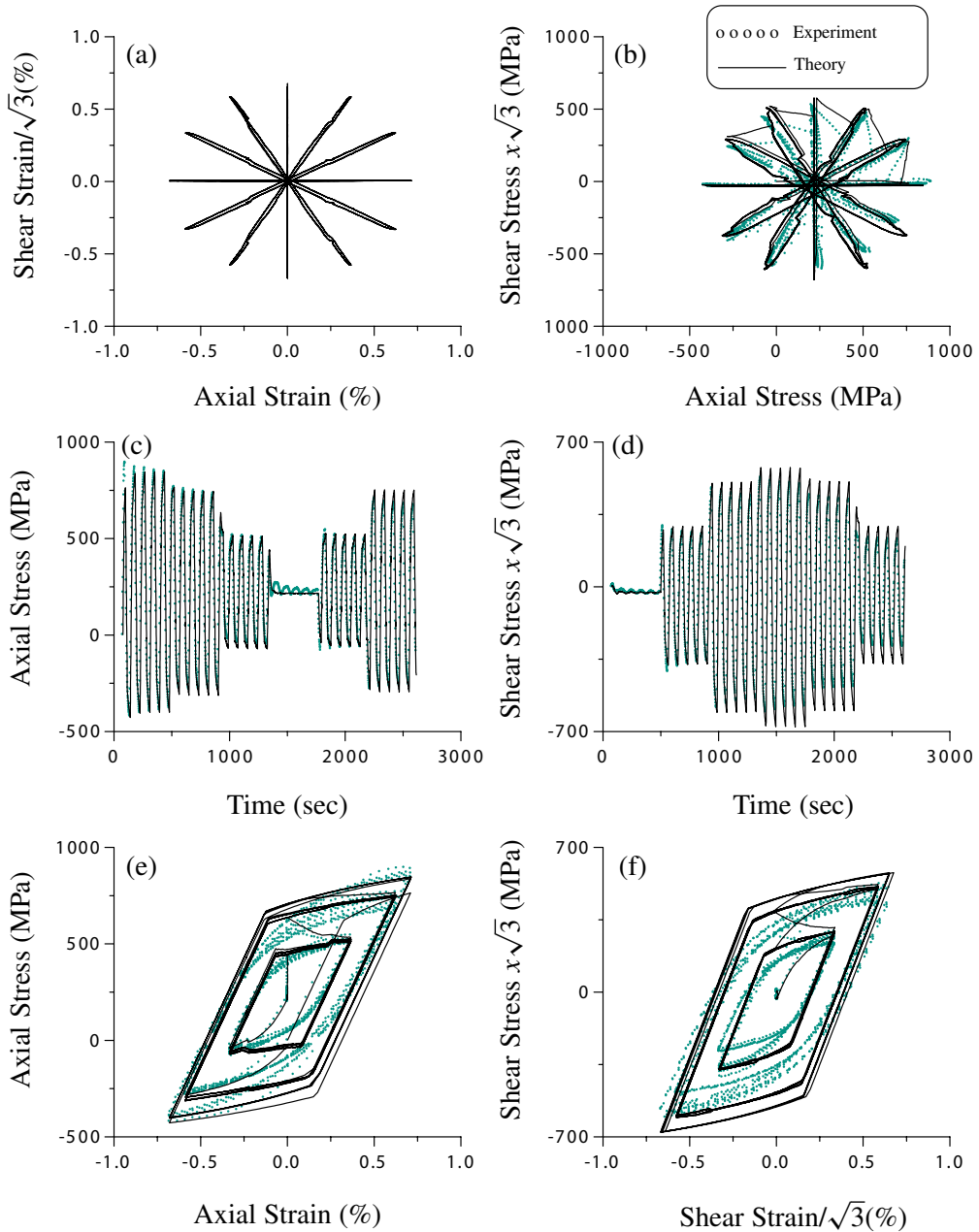


Figure 7. The experimental and simulated results of SAE 4340 under cyclic biaxial strain with input given in (a), and (b) the corresponding biaxial stress path, (c) time history of axial stress, (d) time history of shear stress, (e) axial stress versus axial strain, (f) shear stress versus shear strain.

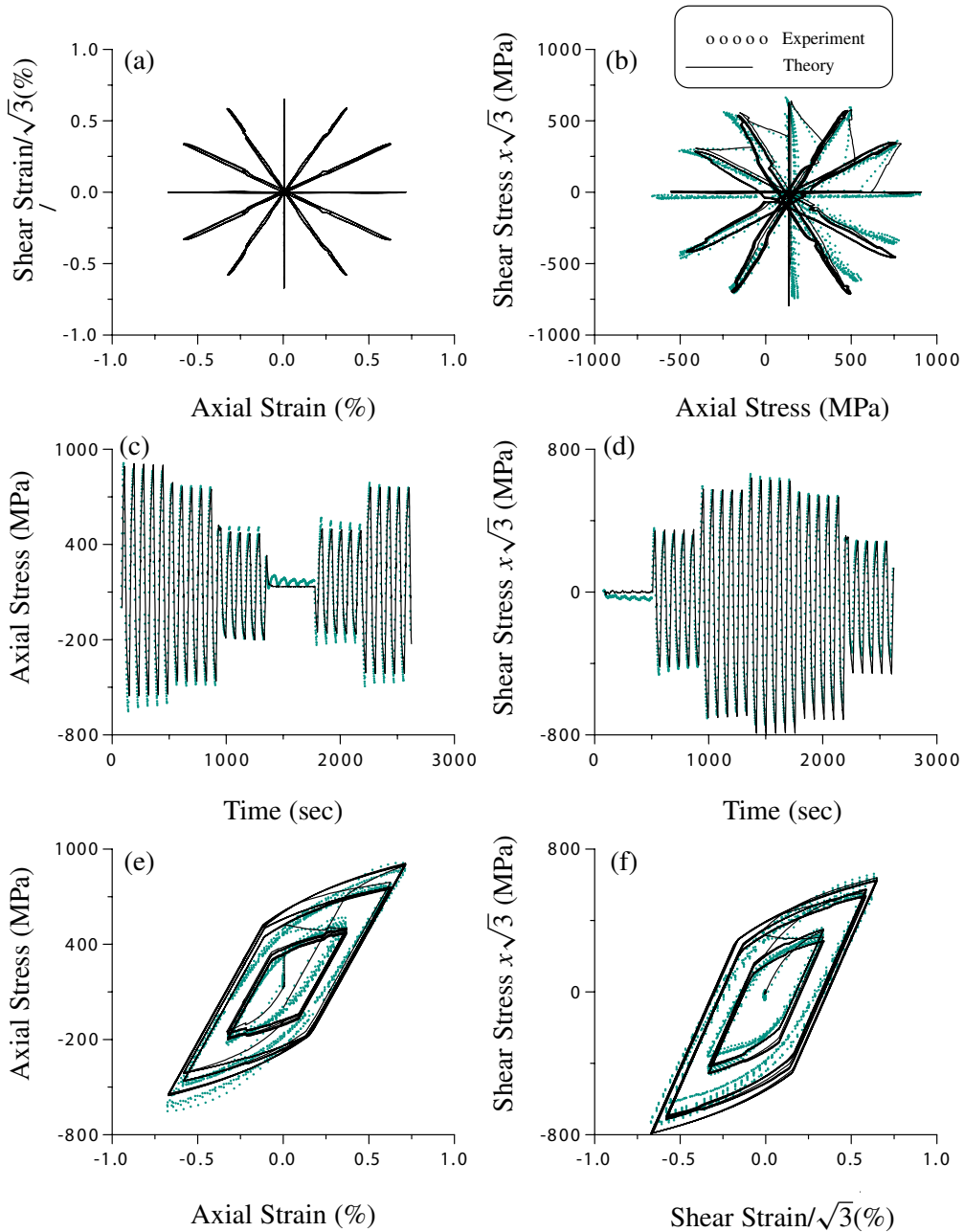


Figure 8. The experimental and simulated results of RHA under cyclic biaxial strain with input given in (a), and (b) the corresponding biaxial stress path, (c) time history of axial stress, (d) time history of shear stress, (e) axial stress versus axial strain, (f) shear stress versus shear strain.

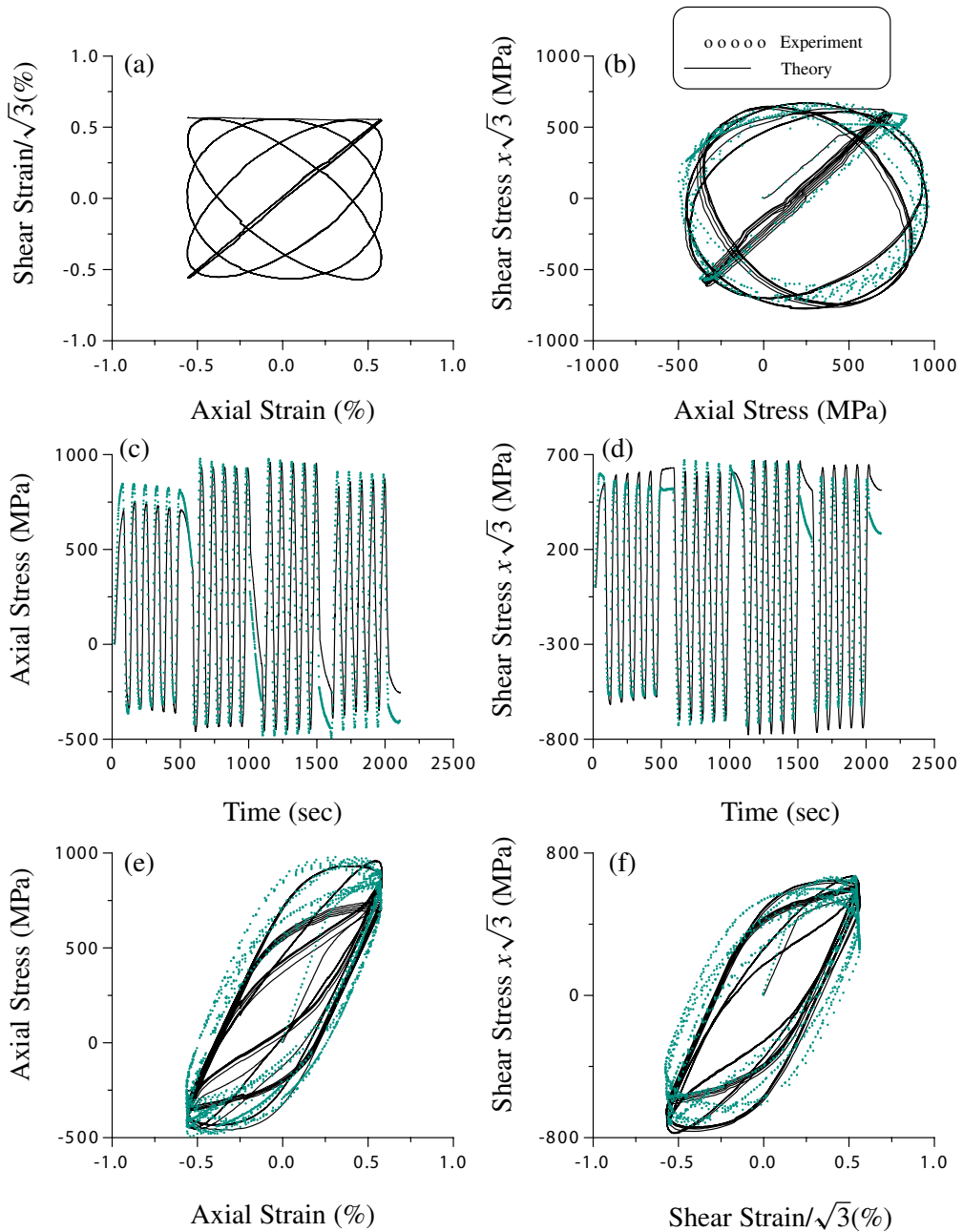


Figure 9. The experimental and simulated results of SAE 4340 under cyclic biaxial strain with input given in (a), and (b) the corresponding biaxial stress path, (c) time history of axial stress, (d) time history of shear stress, (e) axial stress versus axial strain, (f) shear stress versus shear strain.

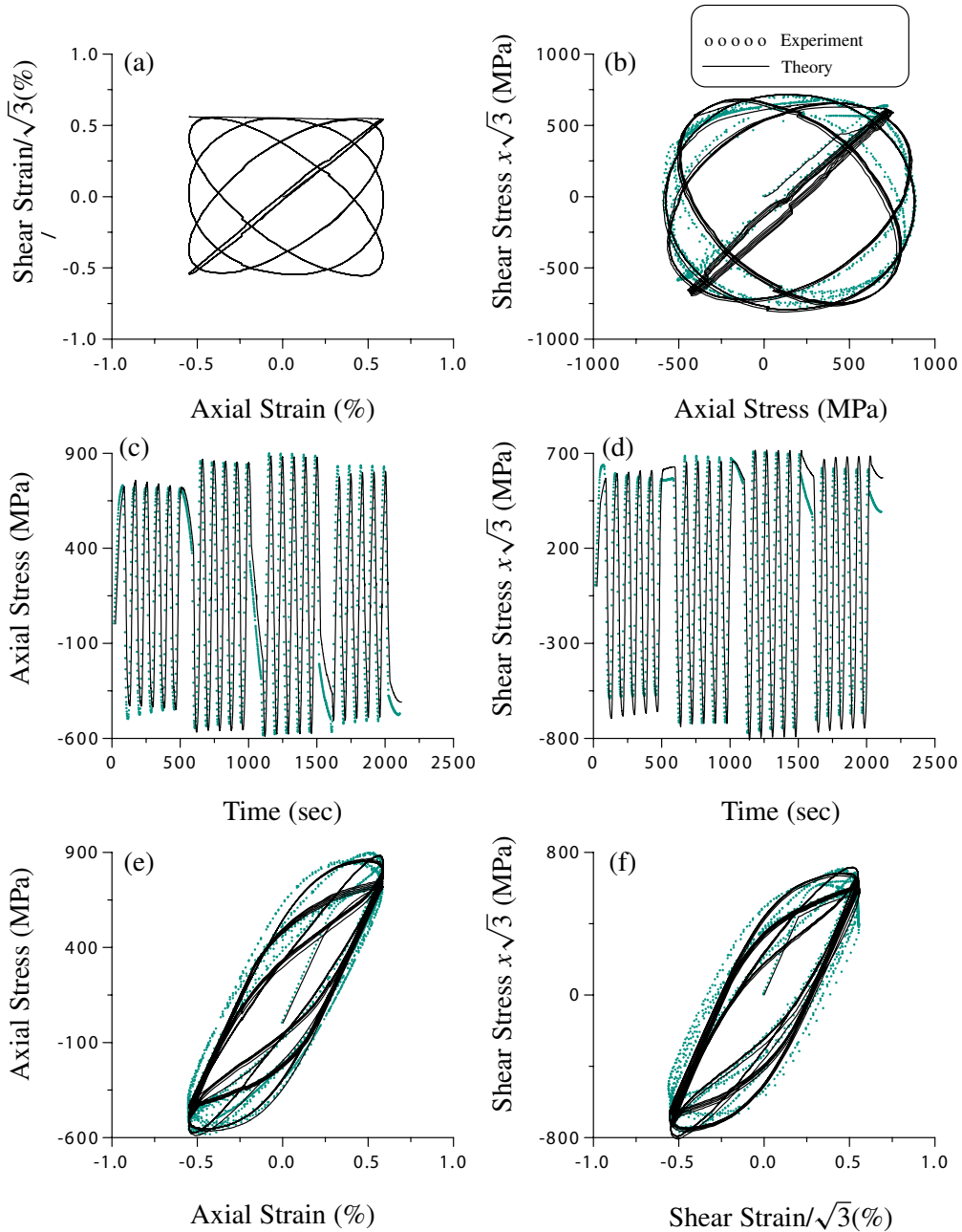


Figure 10. The experimental and simulated results of RHA under cyclic biaxial strain with input given in (a), and (b) the corresponding biaxial stress path, (c) time history of axial stress, (d) time history of shear stress, (e) axial stress versus axial strain, (f) shear stress versus shear strain.

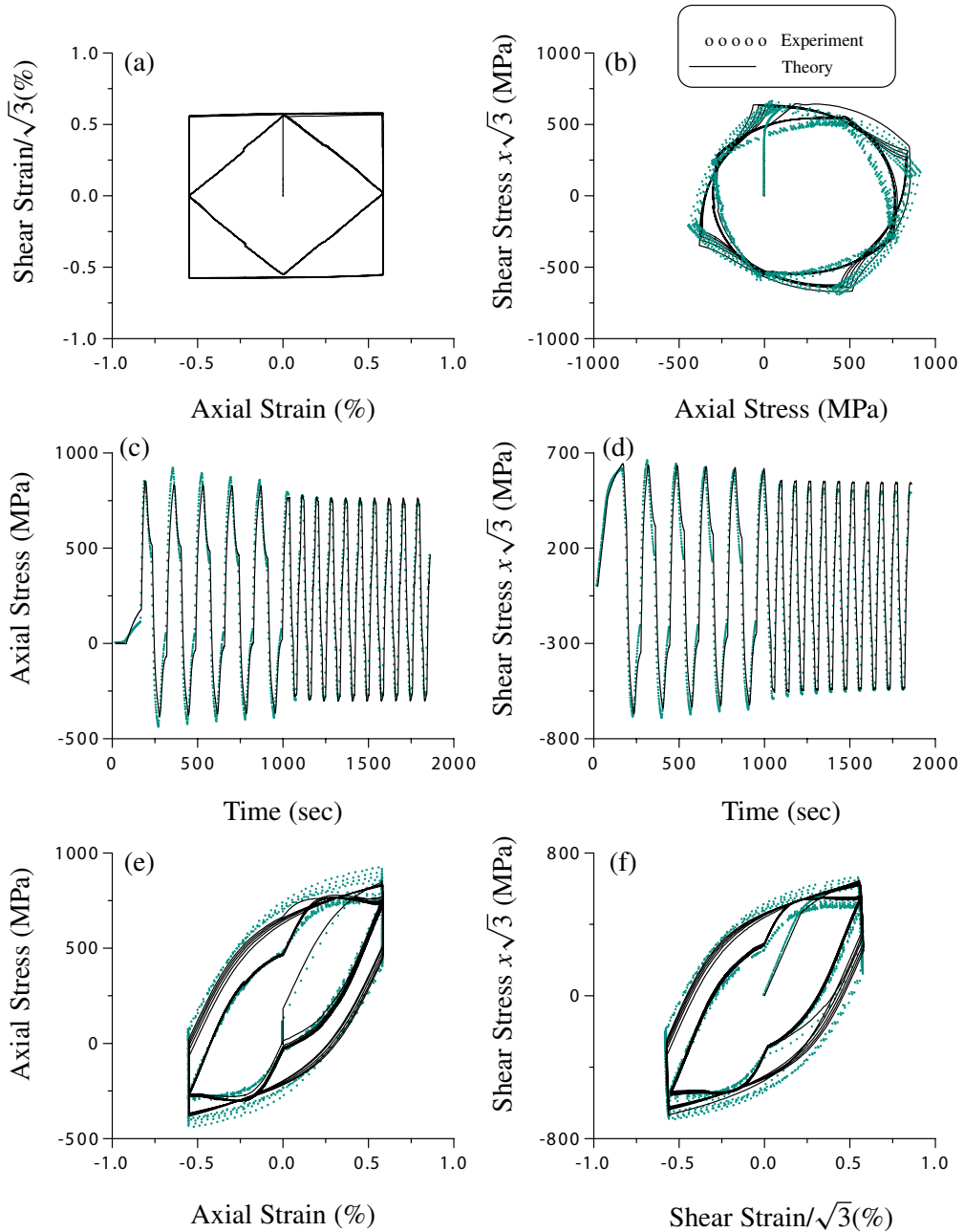


Figure 11. The experimental and simulated results of SAE 4340 under cyclic biaxial strain with input given in (a), and (b) the corresponding biaxial stress path, (c) time history of axial stress, (d) time history of shear stress, (e) axial stress versus axial strain, (f) shear stress versus shear strain.

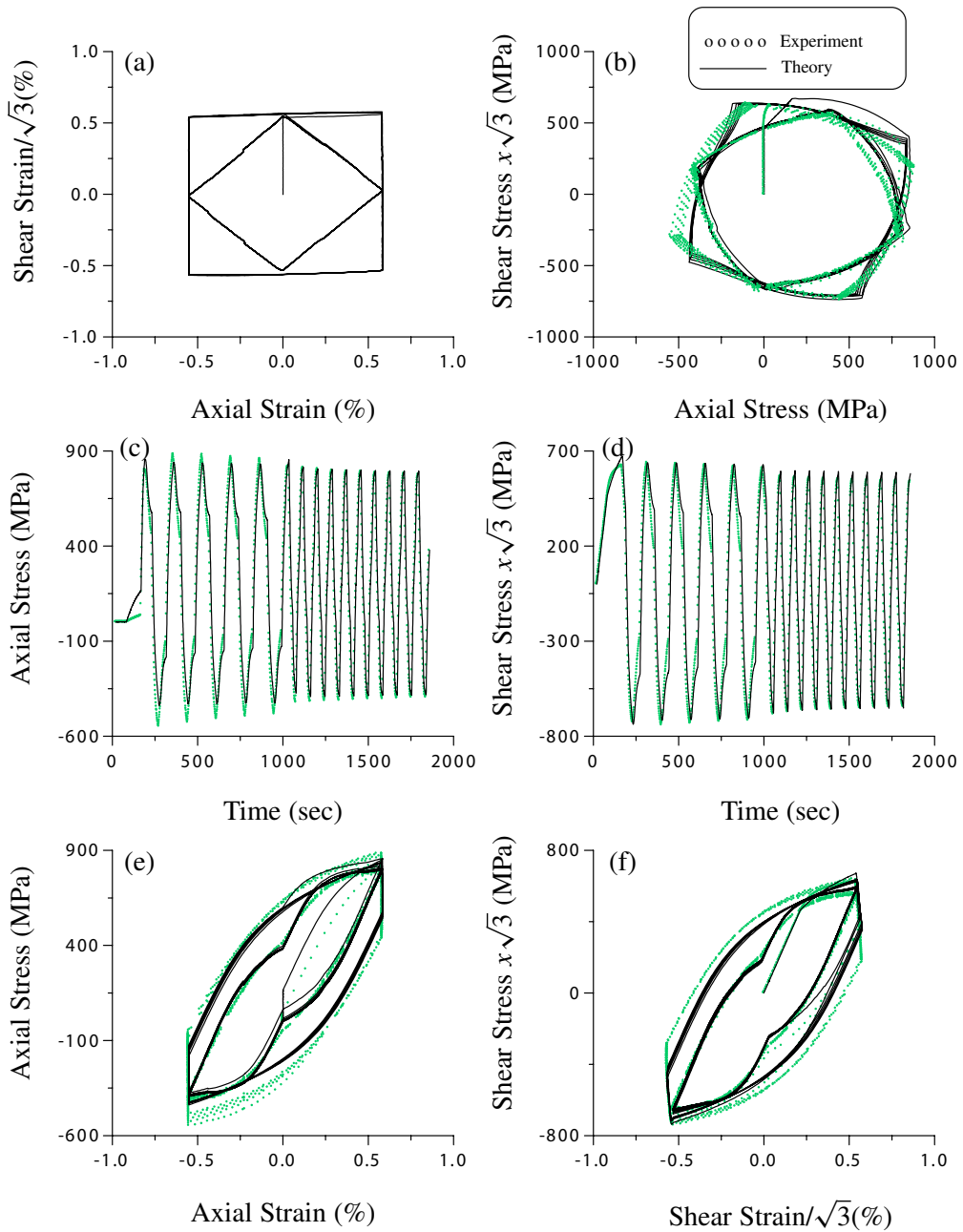


Figure 12. The experimental and simulated results of RHA under cyclic biaxial strain with input given in (a), and (b) the corresponding biaxial stress path, (c) time history of axial stress, (d) time history of shear stress, (e) axial stress versus axial strain, (f) shear stress versus shear strain.

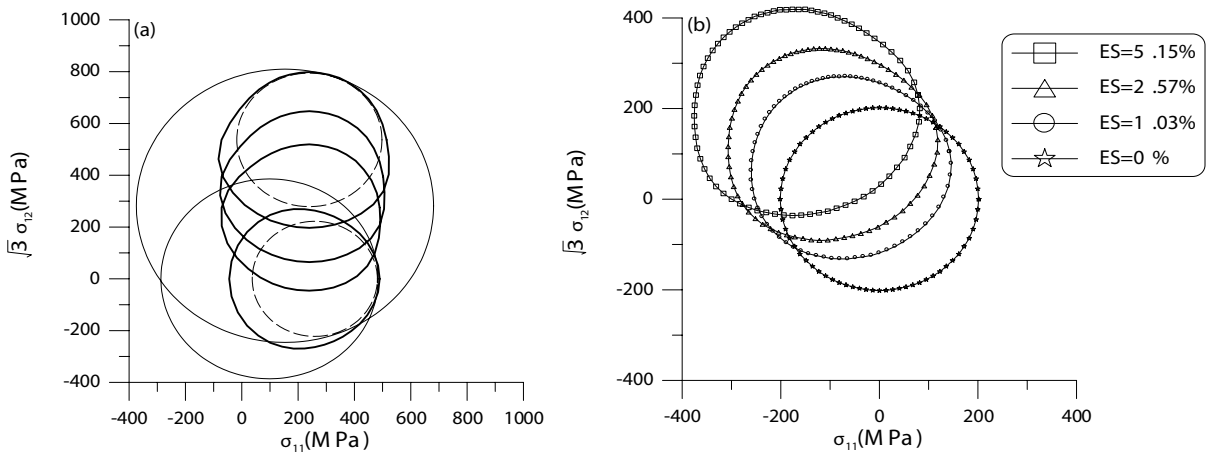


Figure 13. A theoretical prediction of yield surfaces with an equivalent strain offset with 0.001.

- (2) For SAE 4340 and RHA, in the uniaxial cyclic tests subjected to a constant strain amplitude the cyclic stress-strain behavior tends to a steady state in the early stage of the test, and results in a stable hysteresis loop.
- (3) For RHA in the uniaxial cyclic tests as shown in Figures 3 and 4, bottom, it behaves as an elastic-perfectly plastic material at the beginning of the yielding. According to the interpretation by Abdul-Latif [1996] for Waspaloy, a similar behavior of this sort is governed by a competition between softening (due to the isotropic softening) and the hardening (due to the kinematic hardening).
- (4) The effect of mean strain for the constant strain amplitude tests seems less to affect the shape of the hysteresis loop.
- (5) The cube type strain path may induce the stress relaxation in each direction. The relaxation in the axial direction is more significant.
- (6) The effect of nonproportional strain paths is very pronounced in the biaxial cyclic tests of these two materials. Proportional loading results in a hysteresis loop which has the same shape as that for the uniaxial test. The highest stress response is obtained for a 90° out-of-phase loading. Complicated shapes of the hysteresis loops arise for both tensile and shear stresses in the nonproportional cyclic tests.
- (7) In Figures 9c and 9d for the time histories of axial and shear stresses for SAE 4340, and in Figures 10c and 10d for the time histories of axial and shear stresses for RHA, an obvious softening cyclic phenomenon appears governed by the reduction in the loading path complexity, which changes from a 90° out-of-phase loading path to a 135° out-of-phase loading path. In a micromechanical view, this change leads to decreasing the number of activated slip systems in each plastified grain.

11. Numerical simulations

The conventional plasticity model may fail to simulate cyclic behavior properly, because the material functions used are only dependent on $\bar{\epsilon}^p$ alone. In cyclic loading conditions, $\bar{\epsilon}^p$ may be increased to a

large value. So the difficulty may arise when one wants to fit the material functions used in the cyclic response curves by using the data from a simple test.

In contrast, in the current two-complementary-trio model there exists a more flexible mechanism to control the increment of \bar{e}^p through (71), of which the increasing of \bar{e}^p can be reduced largely when the stress point is inside the bounding surface. In order to illustrate the proposed model response, the numerical simulations are presented below. The uniaxial cyclic strain paths and biaxial cyclic paths were designed to investigate the cyclic behaviors of SAE 4340 and RHA, including two tests in constant strain amplitude of 1.5% with the means of zero and 1.5%, a test with increasing amplitude and mean, the amplitudes of which start from 0.6% to 6% by adding 0.6% per cycle and with -0.6% fixed in the compression direction, and a cyclic test with increasing amplitude 0.5% per cycle but with mean zero.

The material functions used in this model have the following forms:

$$h_0(\bar{e}^p) = a_1 - a_2 e^{-a_3 \bar{e}^p} \text{ (MPa),}$$

$$h_a(\bar{e}^p) = a_4 - a_5 e^{-a_6 \bar{e}^p} \text{ (MPa),}$$

$$k'_0 = a_7 - a_8 e^{-a_9 \bar{e}^p} \text{ (MPa),}$$

$$k'_a = (h'_0 + k'_0) \exp\left(a_{10} \left(\frac{\mathcal{D}}{2(h_0 - h_a)}\right)^{a_{11}}\right) - h'_a \text{ (MPa),}$$

$$G = a_{12} \text{ (MPa).}$$

The other two material functions are given by $h_c = h_0 - h_a$ and $k'_c = k'_a - k'_0$. There are 12 material constants to be specified, one of which is the shear modulus of material. Table 2 lists the material constants for numerical simulations.

Figures 3–12, comparing numerical and experimental results, suggest that the overall behavior of these two materials SAE 4340 and RHA, as detected in this study, can be described very well. Phenomena covered by the description include the Bauschinger and Masing effects, cyclical hardening, saturation of stress, and out-of-phase hardening. Note that the material functions for each material used to simulate all four uniaxial tests and three biaxial tests are the same; no fine-tuning of the material functions was required in the simulations. Even for the long-term (20–30 cycles) prediction of this model, it still provides very good simulation results.

The comparisons of the biaxial cyclic test data and the numerical results calculated indeed provide very good prediction of the behavior of these two materials under nonproportional cyclic loading. Especially,

	G	a_1	a_2	a_3	a_4	a_5	a_6	a_7	a_8	a_9	a_{10}	a_{11}
unit	MPa	MPa	MPa	-	MPa	MPa	-	MPa	MPa	-	-	-
SAE 4340	72500	1453.8	3.2	34.8	100.2	-1.2	40	410	0.2	40	12.5	0.8
RHA	72500	1321	21	9.8	550	25	10	450	-50	10	8	0.8

Table 2. Material constants used in the numerical simulations.

the overhardening phenomena resulting from the nonradiality of the input strain path can be described very well by the proposed model.

12. Convexity of the distance function and yield surface with strain offset

For the linear path with $\dot{e}_{ij} = c_{ij}$ the switched-on time t_i for plasticity can be calculated by

$$t_i = \frac{\sqrt{2h_a^2/3}}{2G\sqrt{c_{mn}c_{mn}}}. \tag{72}$$

The integration of (3) with $\dot{e}_{ij}^p = 0$ from 0 to t_i gives

$$s_{ij}(t_i) = 2Ge_{ij}(t_i). \tag{73}$$

During this period of time, we have $s_{ij}^b(t_i) = s_{ij}^b(0)$ and

$$s_{ij}^a(t_i) = 2Ge_{ij}(t_i). \tag{74}$$

The substitution of the above equation and (72) into $s_{ij}^a(t_i)c_{ij}$ yields

$$s_{ij}^a(t_i)c_{ij} = \sqrt{2h_a^2c_{mn}c_{mn}/3}. \tag{75}$$

From these equations the distance function is found to be

$$\mathcal{D} = -h_a - \frac{s_{ij}^c c_{ij}}{\sqrt{\frac{2}{3}c_{mn}c_{mn}}} + \sqrt{\frac{3(s_{ij}^c c_{ij})^2}{2c_{mn}c_{mn}} + h_a^2 + \frac{3}{2}s_{ij}^c s_{ij}^c}. \tag{76}$$

Assuming that the normalized condition $\frac{2}{3}c_{mn}c_{mn} = 1$ holds, we have

$$\mathcal{D} = -h_a - s_{ij}^c c_{ij} + \sqrt{(s_{ij}^c c_{ij})^2 + h_a^2 + \frac{3}{2}s_{ij}^c s_{ij}^c}. \tag{77}$$

Because of

$$\frac{\partial^2 \mathcal{D}}{\partial c_{ts} \partial c_{mn}} = \frac{h_a^2 + 3s_{ij}^c s_{ij}^c / 2}{[(s_{kl}^c c_{kl})^2 + h_a^2 + 3s_{kl}^c s_{kl}^c / 2]^{3/2}} s_{ts}^c s_{mn}^c, \tag{78}$$

the Hessian matrix of \mathcal{D} is positive definite, and thus we have proved that the distance function \mathcal{D} is strictly convex with respect to c_{ij} .

Consider a two dimensional strain path with $\dot{e}_{11} = \cos \theta$ and $\dot{e}_{12} = \sin \theta$. The distance function reads as

$$\mathcal{D} = -h_a - \|s_{ij}^c\| \cos(\theta - \beta) + \sqrt{[\|s_{ij}^c\| \cos(\theta - \beta)]^2 + h_0^2 - \|s_{ij}^c\|^2}, \tag{79}$$

where

$$\|s_{ij}^c\| := \sqrt{\frac{3}{2}s_{ij}^c s_{ij}^c}, \quad \beta := \arccos \frac{s_{11}^b - s_{11}^d}{\|s_{ij}^c\|}.$$

It is easy to check that \mathcal{D} as a function of θ is strictly convex.

For each linear path specified by $\dot{e}_{11} = \cos \theta$ and $\dot{e}_{12} = \sin \theta$, the increment of active stress and back stress before contact can be obtained, respectively, from (5) and (24):

$$\begin{aligned}\delta s_{ij}^a &= 2G\delta e_{ij} - \left(2G + \frac{2}{3}k'_a\right) \frac{3\delta\bar{e}^p}{2h_a} s_{ij}^a, \\ \delta s_{ij}^b &= \frac{k'_a\delta\bar{e}^p}{h_a} s_{ij}^a.\end{aligned}$$

Accordingly, we have

$$\begin{aligned}\|\delta s_{ij}^a\| &= \frac{3Gh'_a\|\delta e_{ij}\|}{3G + h'_a + k'_a}, \\ \|\delta s_{ij}^b\| &= \frac{3Gk'_a\|\delta e_{ij}\|}{3G + h'_a + k'_a},\end{aligned}$$

in which

$$\|\delta s_{ij}^a\| := \sqrt{\frac{3}{2}\delta s_{ij}^a\delta s_{ij}^a}, \quad \|\delta s_{ij}^b\| := \sqrt{\frac{3}{2}\delta s_{ij}^b\delta s_{ij}^b}, \quad \|\delta e_{ij}\| := \sqrt{\frac{2}{3}\delta e_{ij}\delta e_{ij}}.$$

The quantity $\|\delta e_{ij}\|$ is a prescribed offset of equivalent strain along the radial path, and $\|\delta s_{ij}^a\| + \|\delta s_{ij}^b\|$ is the corresponding stress increment induced by $\|\delta e_{ij}\|$. Consequently, the yield surface determined by the offset is given by

$$f(\theta) := h_a + \|\delta s_{ij}^a\| + \|\delta s_{ij}^b\| = h_a + \frac{3G\|\delta e_{ij}\|(h'_a + k'_a)}{3G + h'_a + k'_a},$$

From (70) and (79) the function $f(\theta)$ can be written as

$$f(\theta) = h_a + \frac{3G\|\delta e_{ij}\|(h'_0 + k'_0) \exp\left(a\left(\frac{\mathfrak{D}}{2h_c}\right)^b\right)}{3G + (h'_0 + k'_0) \exp\left(a\left(\frac{\mathfrak{D}}{2h_c}\right)^b\right)}. \quad (80)$$

For a prestrain of certain values of \bar{e}^p and s_{ij}^c with a prescribed offset $\|\delta e_{ij}\|$, the above yield function can be determined.

Let us consider the following material functions:

$$h_0(\bar{e}^p) = 630 - 340e^{-7\bar{e}^p} \text{ (MPa)},$$

$$h_a(\bar{e}^p) = 290 - 90e^{-6\bar{e}^p} \text{ (MPa)},$$

$$k'_0 = 2500 - 500e^{-15\bar{e}^p} \text{ (MPa)},$$

$$k'_a = (h'_0 + k'_0) \exp\left(14\left(\frac{\mathfrak{D}}{2(h_0 - h_a)}\right)^{1.5}\right) - h'_a \text{ (MPa)},$$

$$G = 27255.6 \text{ (MPa)}.$$

A theoretical prediction of the yield surfaces with a strain offset with 0.001 derived from Equations (80) and (79) is plotted in Figure 13a. We first apply a prestress to $\sigma_{11} = 481$ MPa, and then an elastic unloading to $\sigma_{11} = 228$ MPa. The first yield surface is plotted with thick black line, while the bounding

surface is plotted with a thin black line and the dashed line presents the surface of active stress s_{ij}^a . Consecutively, we plot the other three yield surfaces where the axial and shear stress are, respectively, $(\sigma_{11}, \sigma_{12}) = (306, 562)$ MPa, $(\sigma_{11}, \sigma_{12}) = (306, 687)$ MPa, and $(\sigma_{11}, \sigma_{12}) = (306, 837)$ MPa. The last bounding surface is also plotted with a thin black line and the dashed line is used to present the surface of active stress s_{ij}^a . It can be seen that the yield surfaces are gradually distorted from a circle to a convex curve with a front sharp and a rear flat. By the same token, in Figure 13b we plot the four yield surfaces along the 135° direction at the four different equivalent strains (ES) with $ES = 0\%$, 1.03% , 2.57% , 5.15% . Similarly, the yield surfaces are gradually distorted from a circle to a convex curve with a front sharp and a rear flat.

The plastic deformation induced anisotropy was explicitly shown through the motion and distortion of the yield surface. The expansion in size, translation, distortion, and rotation of the yield surface strongly depend on the loading paths as shown in Figure 13, which reflect that the present model can simulate the strain-induced anisotropy of materials.

13. Concluding remarks

To effectively simulate the cyclic behavior of materials, a more tractable method to adjust the plastic modulus in the complex loading situation is needed. The combination of J_2 theory and the two-complementary-trio theory provides a good method to predict the material behaviors under cyclic loading conditions. For this model, we have demonstrated that the kinematic hardening rule is of the Prager type before contact or $\mathcal{D} = 0$. In the plasticity stage, before the contact of yield surface and bounding surface, the plastic flow is weak because $\mathcal{D} > 0$ in Equation (71), which renders the increment of \bar{e}^p small. In order to avoid penetration, we have derived a contact rule about the motion of the contact surface. During the period of contact, the kinematic hardening rule is more complex and the plastic flow is large. The validity and accuracy of the new model were confirmed by comparing the numerical results with the experimental data for SAE 4340 and RHA materials under four uniaxial cyclic testings and three biaxial cyclic testings. Only 12 material constants were required in the new model, and it can be seen that the cyclic response curves described by the new model were in good agreement with the experimental data.

References

- [Abdel-Karim 2005] M. Abdel-Karim, "Numerical integration method for kinematic hardening rules with partial activation of dynamic recovery term", *Int. J. Plast.* **21**:7 (2005), 1303–1321.
- [Abdel-Karim and Ohno 2000] M. Abdel-Karim and N. Ohno, "Kinematic hardening model suitable for ratchetting with steady-state", *Int. J. Plast.* **16**:3-4 (2000), 225–240.
- [Abdul-Latif 1996] A. Abdul-Latif, "Constitutive equations for cyclic plasticity of Waspaloy", *Int. J. Plast.* **12**:8 (1996), 967–985.
- [Bari and Hassan 2001] S. Bari and T. Hassan, "Kinematic hardening rules in uncoupled modeling for multiaxial ratcheting simulation", *Int. J. Plast.* **17**:7 (2001), 885–905.
- [Bari and Hassan 2002] S. Bari and T. Hassan, "An advancement in cyclic plasticity modeling for multiaxial ratcheting simulation", *Int. J. Plast.* **18**:7 (2002), 873–894.
- [Bron and Besson 2004] F. Bron and J. Besson, "A yield function for anisotropic materials application to aluminum alloys", *Int. J. Plast.* **20**:4-5 (2004), 937–963.

- [Cazacu and Barlat 2004] O. Cazacu and F. Barlat, “A criterion for description of anisotropy and yield differential effects in pressure-insensitive metals”, *Int. J. Plast.* **20**:11 (2004), 2027–2045.
- [Chaboche 1991] J. L. Chaboche, “On some modifications of kinematic hardening to improve the description of ratchetting effects”, *Int. J. Plast.* **7**:7 (1991), 661–678.
- [Chaboche 1994] J. L. Chaboche, “Modeling of ratchetting: evaluation of various approaches”, *Eur. J. Mech. A Solids* **13** (1994), 501–518.
- [Chen and Jiao 2004] X. Chen and R. Jiao, “Modified kinematic hardening rule for multiaxial ratcheting prediction”, *Int. J. Plast.* **20**:4-5 (2004), 871–898.
- [Chen et al. 2005] X. Chen, R. Jiao, and K. S. Kim, “On the Ohno–Wang kinematic hardening rules for multiaxial ratcheting modeling of medium carbon steel”, *Int. J. Plast.* **21**:1 (2005), 161–184.
- [Chiang et al. 2002] D.-Y. Chiang, K.-H. Su, and C.-H. Liao, “A study on subsequent yield surface based on the distributed-element model”, *Int. J. Plast.* **18**:1 (2002), 51–70.
- [Christensen 2006] R. M. Christensen, “Yield functions and plastic potentials for BCC metals and possibly other materials”, *J. Mech. Mat. Struct.* **1**:1 (2006), 183–204.
- [Dafalias 1984] Y. F. Dafalias, “Modelling cyclic plasticity: simplicity versus sophistication”, pp. 153–178 in *Mechanics of engineering materials*, edited by C. S. Desai and R. H. Gallagher, John Wiley & Sons, New York, 1984.
- [Dafalias and Popov 1975] Y. F. Dafalias and E. P. Popov, “A model of nonlinearly hardening materials for complex loading”, *Acta Mech.* **21**:3 (1975), 173–192.
- [Dafalias and Popov 1976] Y. F. Dafalias and E. P. Popov, “Plastic internal variables formalism of cyclic plasticity”, *J. Appl. Mech. (Trans. ASME)* **98** (1976), 645–651.
- [Dieng et al. 2005] L. Dieng, A. Abdul-Latif, M. Haboussi, and C. Cunat, “Cyclic plasticity modeling with the distribution of non-linear relaxations approach”, *Int. J. Plast.* **21**:2 (2005), 353–379.
- [Elgamal et al. 2003] A. Elgamal, Z. Yang, E. Parra, and A. Ragheb, “Modeling of cyclic mobility in saturated cohesionless soils”, *Int. J. Plast.* **19**:6 (2003), 883–905.
- [François 2001] M. François, “A plasticity model with yield surface distortion for non proportional loading”, *Int. J. Plast.* **17**:5 (2001), 703–717.
- [Hashiguchi 1988] K. Hashiguchi, “A mathematical modification of two surface model formulation in plasticity”, *Int. J. Solids Struct.* **24**:10 (1988), 987–1001.
- [Hashiguchi 1989] K. Hashiguchi, “Subloading surface model in unconventional plasticity”, *Int. J. Solids Struct.* **25**:8 (1989), 917–945.
- [Hassan and Kyriakides 1992a] T. Hassan and S. Kyriakides, “Ratcheting in cyclic plasticity, I: uniaxial behavior”, *Int. J. Plast.* **8**:1 (1992), 91–146.
- [Hassan and Kyriakides 1992b] T. Hassan and S. Kyriakides, “Ratcheting in cyclic plasticity, II: multiaxial behavior”, *Int. J. Plast.* **8**:1 (1992), 91–146.
- [Khoei and Jamali 2005] A. R. Khoei and N. Jamali, “On the implementation of a multi-surface kinematic hardening plasticity and its applications”, *Int. J. Plast.* **21**:9 (2005), 1741–1770.
- [Kowalczyk and Gambin 2004] K. Kowalczyk and W. Gambin, “Model of plastic anisotropy evolution with texture-dependent yield surface”, *Int. J. Plast.* **20**:1 (2004), 19–54.
- [Krieg 1975] R. D. Krieg, “A practical two surface plasticity theory”, *J. Appl. Mech. (Trans. ASME)* **42** (1975), 641–646.
- [Liu 2004] C.-S. Liu, “A consistent numerical scheme for the von Mises mixed-hardening constitutive equations”, *Int. J. Plast.* **20**:4-5 (2004), 663–704.
- [Liu 2005] C.-S. Liu, “Computational applications of the Poincaré group on the elastoplasticity with kinematic hardening”, *Comput. Model. Eng. Sci.* **8**:3 (2005), 231–258.

- [Liu 2006] C.-S. Liu, “Reconcile the perfectly elastoplastic model to simulate the cyclic behavior and ratcheting”, *Int. J. Solids Struct.* **43**:2 (2006), 222–253.
- [Liu and Chang 2004] C.-S. Liu and C.-W. Chang, “Lie group symmetry applied to the computation of convex plasticity constitutive equation”, *Comput. Model. Eng. Sci.* **6**:3 (2004), 277–294.
- [Liu and Chang 2005] C.-S. Liu and C.-W. Chang, “Non-canonical Minkowski and pseudo-Riemann frames of plasticity models with anisotropic quadratic yield criteria”, *Int. J. Solids Struct.* **42**:9-10 (2005), 2851–2882.
- [McDowell 1989] D. L. McDowell, “Evaluation of intersection conditions for two-surface plasticity theory”, *Int. J. Plast.* **5**:1 (1989), 29–50.
- [Mróz 1967] Z. Mróz, “On the description of anisotropic workhardening”, *J. Mech. Phys. Solids* **15**:3 (1967), 163–175.
- [Mróz et al. 1979] Z. Mróz, V. A. Norris, and O. C. Zienkiewicz, “Application of an anisotropic hardening model in the analysis of elasto-plastic deformation of soils”, *Geotechnique* **29** (1979), 1–34.
- [Mróz et al. 1981] Z. Mróz, V. A. Norris, and O. C. Zienkiewicz, “An anisotropic, critical state model for soils subjected to cyclic loading”, *Geotechnique* **31** (1981), 451–469.
- [Ohno and Abdel-Karim 2000] N. Ohno and M. Abdel-Karim, “Uniaxial ratchetting of 316FR steel at room temperature, II: constitutive modeling and simulation”, *J. Eng. Mater. Technol. (Trans. ASME)* **122**:1 (2000), 35–41.
- [Ohno and Wang 1991] N. Ohno and J.-D. Wang, “Transformation of a nonlinear kinematic hardening rule to a multisurface form under isothermal and nonisothermal conditions”, *Int. J. Plast.* **7**:8 (1991), 879–891.
- [Ohno and Wang 1993a] N. Ohno and J.-D. Wang, “Kinematic hardening rules with critical state of dynamic recovery, I: formulation and basic features for ratchetting behavior”, *Int. J. Plast.* **9**:3 (1993), 375–403.
- [Ohno and Wang 1993b] N. Ohno and J.-D. Wang, “Kinematic hardening rules with critical state of dynamic recovery, II: application to experiments of ratchetting behavior”, *Int. J. Plast.* **9**:3 (1993), 375–403.
- [Ohno and Wang 1994] N. Ohno and J.-D. Wang, “Kinematic hardening rules for simulation of ratchetting behavior”, *Eur. J. Mech. A Solids* **13** (1994), 519–531.
- [Phillips and Kasper 1973] A. Phillips and R. Kasper, “On the foundations of thermoplasticity — an experimental investigation”, *J. Appl. Mech. (Trans. ASME)* **40** (1973), 891–896.
- [Phillips and Moon 1977] A. Phillips and H. Moon, “An experimental investigation concerning yield surfaces and loading surfaces”, *Acta Mech.* **27**:1-4 (1977), 91–102.
- [Phillips and Sierakowski 1965] A. Phillips and R. L. Sierakowski, “On the concept of the yield surface”, *Acta Mech.* **1**:1 (1965), 29–35.
- [Phillips and Tang 1972] A. Phillips and J. L. Tang, “The effect of loading path on the yield surface at elevated temperatures”, *Int. J. Solids Struct.* **8**:4 (1972), 463–474.
- [Prager 1956] W. Prager, “A new method of analyzing stresses and strains in work-hardening plastic solids”, *J. Appl. Mech. (Trans. ASME)* **23** (1956), 493–496.
- [Rockafellar 1970] R. T. Rockafellar, *Convex analysis*, Princeton University, New Jersey, 1970.
- [Tseng and Lee 1983] N. T. Tseng and G. C. Lee, “Simple plasticity model of two-surface type”, *J. Eng. Mech. ASCE* **109** (1983), 795–810.
- [Vincent et al. 2004] L. Vincent, S. Calloch, and D. Marquis, “A general cyclic plasticity model taking into account yield surface distortion for multiaxial ratchetting”, *Int. J. Plast.* **20**:10 (2004), 1817–1850.
- [Voyiadjis and Abu Al-Rub 2003] G. Z. Voyiadjis and R. K. Abu Al-Rub, “Thermodynamic based model for the evolution equation of the backstress in cyclic plasticity”, *Int. J. Plast.* **19**:12 (2003), 2121–2147.
- [Voyiadjis and Sivakumar 1991] G. Z. Voyiadjis and S. M. Sivakumar, “A robust kinematic hardening rule for cyclic plasticity with ratchetting effects, I. theoretical formulation”, *Acta Mech.* **90**:1-4 (1991), 105–123.
- [Voyiadjis and Sivakumar 1994] G. Z. Voyiadjis and S. M. Sivakumar, “A robust kinematic hardening rule for cyclic plasticity with ratchetting effects, II: application to nonproportional loading cases”, *Acta Mech.* **107**:1-4 (1994), 117–136.

- [Wu 2003] H. C. Wu, “Effect of loading-path on the evolution of yield surface for anisotropic metals subjected to large pre-strain”, *Int. J. Plast.* **19**:10 (2003), 1773–1800.
- [Wu 2005] H. C. Wu, *Continuum mechanics and plasticity*, Chapman & Hall/CRC, New York, 2005.
- [Wu et al. 2005] P. D. Wu, S. R. MacEwen, D. J. Lloyd, M. Jain, P. Tugcu, and K. W. Neale, “On pre-straining and the evolution of material anisotropy in sheet metals”, *Int. J. Plast.* **21**:4 (2005), 723–739.
- [Yeh and Lin 2006] W.-C. Yeh and H.-Y. Lin, “An endochronic model of yield surface accounting for deformation induced anisotropy”, *Int. J. Plast.* **22**:1 (2006), 16–38.

Received 26 Jun 2006. Accepted 9 Oct 2006.

CHEIN-SHAN LIU: csliu@mail.ntou.edu.tw

Department of Mechanical and Mechatronic Engineering, No.2, Beining Road, Taiwan Ocean University, Keelung 202-24, Taiwan

HONG-KI HONG: hkhong@ntu.edu.tw

Department of Civil Engineering, No.1, Sec. 4, Roosevelt Road, Taiwan University, Taipei 106-17, Taiwan

YA-PO SHIAO: ypshiao@mdu.edu.tw

Department of Computer Science and Information Engineering, Mingdao University, Changhua, Taiwan

GEOMETRICALLY NONLINEAR EFFECTS IN THE FLEXURAL RESPONSE OF MASONRY WALLS STRENGTHENED WITH COMPOSITE MATERIALS

EHAB HAMED AND ODED RABINOVITCH

The geometrically nonlinear effects in the out-of-plane flexural response of unreinforced masonry walls strengthened with externally bonded composite materials are analytically investigated. The investigation aims to explore the stabilizing or destabilizing influence of the arching action formed under realistic supporting conditions (restricted longitudinal deformations) of the wall, and to quantify the contribution of the strengthening system to improving the stability characteristics of the wall. The localized buckling effects associated with the development of compressive stresses in the FRP strip are also examined. Variational principles, large displacements kinematics, compatibility conditions between the structural components (masonry units, mortar joints, FRP strips, and adhesive layers), and the assumption of one-way flexural action are used for the formulation of the nonlinear analytical model. The cracking of the mortar joints, which is essential to the development of the arching action, and the formation of debonded zones are also considered. A numerical example that highlights the geometrically nonlinear effects in the response of the strengthened wall and examines the influence of the slenderness ratio is presented. The results quantify the potential increase of the limit point load and deflection due to the externally bonded composite system. They also quantitatively reveal the wrinkling phenomenon of the compressed FRP strip and the shear and peeling stress concentrations that develop in the vicinity of the cracked mortar joints, the debonded regions, and the wrinkled FRP layer. The paper closes with concluding remarks.

Introduction

Unreinforced masonry structures are found in almost every modern or historic building environment all over the world. With the advantages of this classical building technique, come critical deficiencies, namely the vulnerability of masonry structures to lateral (out-of-plane) loads, and especially to wind and seismic loads. This deficiency may result in considerable damage to the masonry structure, loss of functionality, or even injury to the occupants.

Many strengthening and upgrading techniques have been proposed in attempt to improve the strength and stability of unreinforced masonry (URM) walls. Recently, the use of externally bonded composite materials in the form of fiber reinforced polymer (FRP) laminates and fabrics has gained widespread acceptance. The behavior of URM walls strengthened with composite materials and subjected to out-of-plane loading was examined in many experimental studies [Gilstrap and Dolan 1998; Velazquez-Dimas et al. 2000; Albert et al. 2001; Hamilton and Dolan 2001; Hamoush et al. 2002; Kiss et al. 2002; Kuzik et al. 2003; Ghobarah and El Mandooh Galal 2004; Tan and Patoary 2004]. These studies reveal that the use of the externally bonded FRP system leads to an increase of 10–50 times the strength of the masonry

Keywords: arching, buckling, composite materials, cracking, debonding, masonry, nonlinear analysis, strengthening, wrinkling.

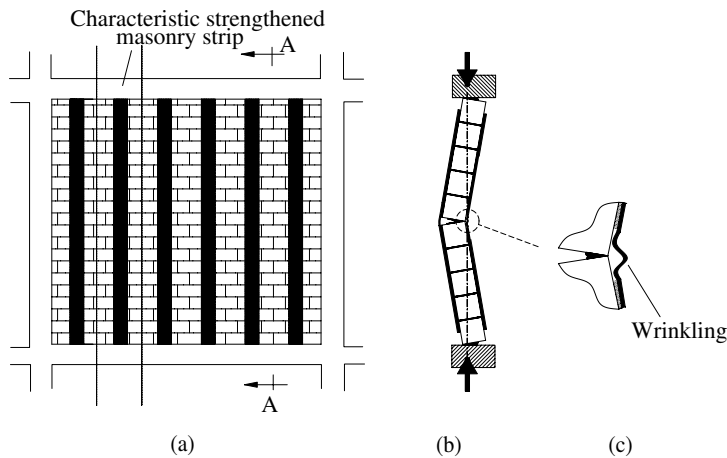


Figure 1. Out-of-plane flexural response of strengthened masonry walls: (a) a one-way strengthening system of FRP strips; (b) section A-A: formation of arching action; (c) localized wrinkling.

wall. However, the majority of the experimental studies focused on ideal boundary conditions, in which the masonry wall is simply supported with no restraint of its in-plane longitudinal deformations.

In practice, masonry walls are usually built within a surrounding frame that restrains the in-plane deformations of the wall's edges (see Figure 1a). These types of supporting conditions, along with the cracking pattern of the wall, lead to the development of eccentric membrane thrust forces and to the formation of the *arching action* (see Figure 1b) [McDowell et al. 1956; Anderson 1984; Dafnis et al. 2002; Griffith et al. 2004]. Under relatively low levels of lateral load (yet beyond the cracking point), the thrust forces increase the compressive stresses in the masonry wall, restraining the cracking in the joints, and forming an eccentric force couple that balances the external bending moment. In this sense the arching action has a stabilizing or strengthening effect on the behavior of the wall. Under higher levels of load, and particularly for slender walls, the geometric nonlinear effect of the compressive forces has a destabilizing effect that may lead to loss of stability and total collapse of the wall. Hence, in the common case of longitudinally constrained masonry walls, and especially for slender walls, the analysis must account for the geometrically nonlinear effects associated with the arching action (see the British standard BS5628 and [Hasetline and Moore 1981]).

The restriction of the longitudinal deformations and the formation of the thrust forces may induce compressive stresses in the externally bonded FRP reinforcement, along with the global geometrically nonlinear effects. These forces may trigger localized geometrically nonlinear effects in the form of localized buckling or wrinkling of the FRP layer (see Figure 1c and [Rabinovitch 2004b; [UBC 1991, pp. 227–232]; Deuring 1993]). Hence, the analysis of the strengthened wall must also account for the geometrically nonlinear effects on the localized scale.

A comparatively small number of research projects focus on the out-of-plane behavior of strengthened walls with realistically constrained edges, in contrast to the vast amount of research on unconstrained

masonry walls strengthened with composite materials. [Tumialan et al. 2000; Tumialan et al. 2003] presented results of field tests conducted on existing URM walls. These studies showed that the capacity of the strengthened wall is only about 1.4 times higher than the unstrengthened one. This strengthening ratio is much smaller than the ones obtained using ideal, simply supported and longitudinally unconstrained edges. Based on experimental observations, [Galati et al. 2002] indicated that strengthened URM walls, with longitudinally constrained edges, may undergo two failure mechanisms that include flexural failure (masonry crushing and FRP rupture) or shear-compression failure at the supports. The latter mode is directly attributed to the formation of the arching thrust forces. The experimental study of [Davidson et al. 2005] focused on the behavior of strengthened URM walls subjected to blast loadings. It was found that the wall-frame gap, and thus the level of development of the arching action, affects the behavior of the wall and its failure mechanisms.

In terms of theoretical models, [Tumialan et al. 2003] proposed a linear model for the evaluation of the peak load and deflection of strengthened URM walls subjected to out-of-plane loading. This model considers cracking of the mortar joints at midspan and at the supports only, and is based on the displacement pattern of three hinged rigid bodies. At the section level, the strain compatibility approach was adopted. This geometrically linear model provides an acceptable prediction of the ultimate load in cases of crushing failure of the masonry units under relatively low levels of load. However, the consideration of the geometrically nonlinear destabilizing effects of the arching action and the consideration of the wrinkling and buckling of the compressed FRP strip near the mortar joints are beyond the scope of this model. [Davidson et al. 2005] used nonlinear FE models for the analysis of strengthened masonry walls subjected to blast loadings. This type of analysis accounts for the stability aspects. However, the different length scales (thickness of the adhesive layer and the FRP strip with respect to the thickness of the masonry unit), the differences in the mechanical properties of the materials, and the singularities and stress concentrations at critical points, make the application of the FE method for the nonlinear analysis of strengthened masonry walls computational effort consuming.

In this paper, the global and local geometrically nonlinear effects are investigated. The objectives of this paper are to gain insight into the geometrically nonlinear effects in the out-of-plane flexural response of URM walls strengthened with composite materials, and to provide a theoretical approach for the nonlinear analysis of the strengthened wall. In particular, the paper focuses on exploring and quantifying the stabilizing/destabilizing influence of the arching effect; the contribution of the strengthening system to the improvement of the stability characteristics of the wall; and the localized buckling/wrinkling of the compressed FRP strip near the mortar joints. The analytical model assumes a one-way flexural response of the strengthened wall. Although in some cases two-way out-of-plane flexural action is possible, in most practical cases, the boundary conditions of the existing wall (which usually consist of only two opposite supported edges) and the use of strengthening system with one-way FRP strips (which is generally easier to install) yield an overall one-way action of the strengthened wall [Davidson et al. 2005]. It is also assumed that the stress and deformation fields are uniform through the width of the FRP strips and the adhesive layers, as well as through the active width of the masonry strip, as seen in Figure 1a,b [Davidson et al. 2005; Hamilton and Dolan 2001].

The geometrically nonlinear effects are considered through the large displacements, moderate rotations, and small strain kinematic relations. Variational principles, static equilibrium, and compatibility requirements between the masonry units, mortar joints, FRP strips, and the adhesive layers, are also

flexural rigidity of the strengthened section. In the mortar joint section, the increased longitudinal strains that develop in the FRP strips bridging over the cracked mortar joint result in a failure of the adhesive material that may still be attached to the debonded FRP strip. Thus, the longitudinal rigidity of the adhesive is neglected in this region as well.

Figure 2a shows that the strengthened strip may consist of regions strengthened on two sides and regions that are not strengthened through the height of the wall. In other cases, strengthening on one side of the wall may also be considered. For the sake of generality, the formulation presented next focuses on walls externally strengthened on both sides. Figure 2b shows that the two-side strengthened region may include two types of subregions. The first one is a *fully bonded* sub-region in which the FRP strip is firmly attached through the adhesive layer (section I-I in Figure 2b). The second sub-region is a debonded one in which one of the interfaces loses its ability to transfer shear stresses (sections II-II and III-III in Figure 2b). Such debonded regions may result from improper fastening of the bonded system, unlevelled faces of the masonry wall, gaps near the mortar joints, or, most likely, from cracking of the mortar joints. While the debonded interface cannot resist shear stresses, it can transfer out-of-plane normal compressive stresses where contact exists. Hence, the model further distinguishes between debonded subregions with contact and debonded subregions without contact.

The field equations and the boundary/continuity conditions for the fully bonded region and for the two types of debonded subregions are derived using the variational principle of virtual work:

$$\delta(U + V) = 0; \tag{1}$$

where U is the strain energy, V is the potential of the external loads, and δ is the variational operator. The first variation of the strain energy is

$$\begin{aligned} \delta U = & \sum_1^{N_{mu}} \int_{V_{mu}} (\sigma_{xx}^{mu} \delta \varepsilon_{xx}^{mu} + \tau_{xz}^{mu} \delta \gamma_{xz}^{mu}) dv_{mu} + \sum_1^{N_{mj}} \int_{V_{mj}} (\sigma_{xx}^{mj} \delta \varepsilon_{xx}^{mj} + \tau_{xz}^{mj} \delta \gamma_{xz}^{mj}) dv_{mj} \\ & + \int_{V_{frp1}} (\sigma_{xx}^{frp1} \delta \varepsilon_{xx}^{frp1} + \tau_{xz}^{frp1} \delta \gamma_{xz}^{frp1}) dv_{frp1} + \int_{V_{frp2}} (\sigma_{xx}^{frp2} \delta \varepsilon_{xx}^{frp2} + \tau_{xz}^{frp2} \delta \gamma_{xz}^{frp2}) dv_{frp2} \\ & + \int_{V_{a1}} (\tau_{xz}^{a1} \delta \gamma_{xz}^{a1} + \sigma_{zz}^{a1} \delta \varepsilon_{zz}^{a1}) dv_{a1} + \int_{V_{a2}} (\tau_{xz}^{a2} \delta \gamma_{xz}^{a2} + \sigma_{zz}^{a2} \delta \varepsilon_{zz}^{a2}) dv_{a2}; \tag{2} \end{aligned}$$

where the notations ‘mu’, ‘mj’, ‘frp1’, ‘frp2’, ‘a1’ and ‘a2’ refer to the masonry unit, mortar, inner FRP strip, outer FRP strip, inner adhesive layer, and the outer adhesive layer, respectively; σ_{xx}^i and ε_{xx}^i are the in-plane normal stress and strain in the masonry unit ($i = mu$), the mortar joint ($i = mj$), and the FRP strips ($i = frp1$ or $i = frp2$); τ_{xz}^i and γ_{xz}^i ($i = mu, mj, frp1, frp2$) are the shear stress and shear angle in the masonry unit, the mortar joint, the FRP strips, respectively; σ_{zz}^{aj} and ε_{zz}^{aj} ($j = 1, 2$) are the out-of-plane normal stresses and strains in the inner and the outer adhesive layers, respectively; τ_{xz}^{aj} and γ_{xz}^{aj} ($j = 1, 2$) are the shear stress and shear angle in the adhesive layers; and N_{mu} and N_{mj} are the number of the masonry units and the mortar joints, respectively.

The nonlinear kinematic relations for the masonry units, the mortar joints, and the FRP strips follow the first order shear deformation theory and the assumption of large displacements, moderate rotations,

and small strains as follows:

$$w_i(x, z_i) = w_i(x); \quad (3a)$$

$$u_i(x, z_i) = u_{oi}(x) - z_i\phi_i(x); \quad (3b)$$

$$\gamma_{xz}^i(x, z_i) = w_{i,x}(x) - \phi_i(x); \quad (3c)$$

$$\varepsilon_{xx}^i(x, z_i) = u_{oi,x}(x) + \frac{1}{2}(w_{i,x}(x))^2 - z_i\phi_{i,x}(x); \quad (3d)$$

where $w_i(x)$, $u_{oi}(x)$ and $\phi_i(x)$ are the out-of-plane displacement, the in-plane displacement, and the rotation of the reference line of the masonry unit ($i = \text{mu}$), the mortar joint ($i = \text{mj}$), and the FRP strips ($i = \text{frp1}, \text{frp2}$), respectively, z_i is measured from the reference line of each component inwards (the reference lines are arbitrarily located at the middle plane of each component, see Figure 2d), and $(\)_{,x}$ denotes a derivative with respect to x . Since both the masonry units and the mortar joints are modeled using the same kinematic assumptions and differ in their constitutive model only, the superscripts mu and mj are replaced with c . Thus, $c = \text{mu}$ refers to the masonry unit regions (sections I-I and II-II in Figure 2b), and $c = \text{mj}$ refers to the mortar regions (section III-III in Figure 2b).

The kinematic relations for the adhesive are:

$$\varepsilon_{zz}^{aj}(x, z_{aj}) = w_{aj,z}(x, z_{aj}); \quad (4a)$$

$$\gamma_{xz}^{aj}(x, z_{aj}) = u_{aj,z}(x, z_{aj}) + w_{aj,x}(x, z_{aj}) \quad (j = 1, 2); \quad (4b)$$

where w_{aj} and u_{aj} are the out-of-plane and in-plane displacements of the inner ($j = 1$) and outer ($j = 2$) adhesive layers, respectively.

The loads are exerted at the masonry wall only. Thus, the first variation of the potential of the external loads equals:

$$\delta V = - \int_{x=0}^{x=H} (q_z \delta w_c + n_x \delta u_{oc} + m_y \delta \phi_c) dx - \sum_{k=1}^{NC} \int_{x=0}^{x=H} (P_k \delta w_c(x_k) + N_k \delta u_{oc}(x_k) + M_k \delta \phi_c(x_k)) \delta_D(x - x_k) dx; \quad (5)$$

where q_z , n_x , and m_y are distributed loads and bending moments, respectively, P_k , N_k , and M_k are concentrated loads and bending moments at $x = x_k$ (see Figure 2a), δ_D is the Dirac function, and NC is the number of the concentrated loads and moments.

Compatibility and debonding conditions. In the fully bonded subregions, the compatibility conditions at the adhesive-masonry, adhesive-mortar, and adhesive-FRP interfaces read:

$$w_{a1}(x, z_{a1} = 0) = w_c(x); \quad (6a)$$

$$u_{a1}(x, z_{a1} = 0) = u_{oc}(x) - \frac{d_c}{2} \phi_c(x); \quad (6b)$$

$$w_{a1}(x, z_{a1} = c_{a1}) = w_{frp1}(x); \tag{7a}$$

$$u_{a1}(x, z_{a1} = c_{a1}) = u_{ofrp1}(x) + \frac{d_{frp1}}{2} \phi_{frp1}(x); \tag{7b}$$

$$w_{a2}(x, z_{a2} = 0) = w_{frp2}(x); \tag{8a}$$

$$u_{a2}(x, z_{a2} = 0) = u_{ofrp2}(x) - \frac{d_{frp2}}{2} \phi_{frp2}(x); \tag{8b}$$

$$w_{a2}(x, z_{a2} = c_{a2}) = w_c(x); \tag{9a}$$

$$u_{a2}(x, z_{a2} = c_{a2}) = u_{oc}(x) + \frac{d_c}{2} \phi_c(x); \tag{9b}$$

where $d_c (= d_{mu}$ or $d_{mj})$, d_{frp1} and d_{frp2} are the thicknesses of the masonry unit, the mortar joint, and the FRP strips, respectively; c_{a1} and c_{a2} are the thicknesses of the inner and outer adhesive layers, respectively; and $z_{aj} (j = 1, 2)$ are measured from the outer interface of each adhesive layer inwards; see Figure 2d.

In the debonded subregions, the interfaces are free of shear and may slip with respect to each other. Hence, the condition of compatible longitudinal deformations is replaced with the condition of shear free interface. For example, in case the inner adhesive-masonry interface is debonded, Equation (6b) is replaced with:

$$\tau_{xz}^{a1}(x, z_{a1} = 0) = 0. \tag{10}$$

If the debonded interfaces are in contact, the condition of compatible out-of-plane deformations holds. If out-of-plane contact does not exist, the compatibility condition is replaced with the null normal stress condition. In the case mentioned above, Equation (6a) is replaced with:

$$\sigma_{zz}^{a1}(x, z_{a1} = 0) = 0. \tag{11}$$

Nonlinear field equations. The nonlinear field (equilibrium) equations for the strengthened (bonded or debonded) regions are formulated using the variational principle (Equations (1), (2), (5)), along with the kinematic relations (Equations (3a)–d, (4)) and the compatibility requirements (Equations (6)–(11)). The field equations take the following form:

$$N_{xx,x}^{frp1}(x) - \alpha_1^{frp} b_{frp1} \tau_{xz}^{a1}(x, z_{a1} = c_{a1}) = 0; \tag{12}$$

$$N_{xx,x}^c(x) - \alpha_2^c b_{frp2} \tau_{xz}^{a2}(x, z_{a2} = c_{a2}) + \alpha_1^c b_{frp1} \tau_{xz}^{a1}(x, z_{a1} = 0) = -n_x(x); \tag{13}$$

$$N_{xx,x}^{frp2}(x) + \alpha_2^{frp} b_{frp2} \tau_{xz}^{a2}(x, z_{a2} = 0) = 0; \tag{14}$$

$$V_{xz,x}^{frp1}(x) + (N_{xx}^{frp1}(x)w_{frp1,x}(x))_{,x} - \beta_1^{frp} b_{frp1} \sigma_{zz}^{a1}(x, z_{a1} = c_{a1}) = 0; \tag{15}$$

$$V_{xz,x}^c(x) + (N_{xx}^c(x)w_{c,x}(x))_{,x} + \beta_1^c b_{frp1} \sigma_{zz}^{a1}(x, z_{a1} = 0) - \beta_2^c b_{frp2} \sigma_{zz}^{a2}(x, z_{a2} = c_{a2}) = -q_z(x); \tag{16}$$

$$V_{xz,x}^{frp2}(x) + (N_{xx}^{frp2}(x)w_{frp2,x}(x))_{,x} + \beta_2^{frp} b_{frp2} \sigma_{zz}^{a2}(x, z_{a2} = 0) = 0; \tag{17}$$

$$M_{xx,x}^{frp1}(x) - V_{xz}^{frp1}(x) + \alpha_1^{frp} b_{frp1} \frac{d_{frp1}}{2} \tau_{xz}^{a1}(x, z_{a1} = c_{a1}) = 0; \tag{18}$$

$$M_{xx,x}^c(x) - V_{xz}^c(x) + \alpha_1^c b_{frp1} \frac{d_c}{2} \tau_{xz}^{a1}(x, z_{a1} = 0) + \alpha_2^c b_{frp2} \frac{d_c}{2} \tau_{xz}^{a2}(x, z_{a2} = c_{a2}) = m_y(x); \tag{19}$$

$$M_{xx,x}^{frp2}(x) - V_{xz}^{frp2}(x) + \alpha_2^{frp} b_{frp2} \frac{d_{frp2}}{2} \tau_{xz}^{a2}(x, z_{a2} = 0) = 0; \tag{20}$$

$$\tau_{xz,x}^{a1}(x, z_{a1}) + \sigma_{zz,z}^{a1}(x, z_{a1}) = 0; \tag{21}$$

$$\tau_{xz,z}^{a1}(x, z_{a1}) = 0; \tag{22}$$

$$\tau_{xz,x}^{a2}(x, z_{a2}) + \sigma_{zz,z}^{a2}(x, z_{a2}) = 0; \tag{23}$$

$$\tau_{xz,z}^{a2}(x, z_{a2}) = 0; \tag{24}$$

where N_{xx}^i , V_{xz}^i , and M_{xx}^i ($i = c, frp1, frp2$) are the in-plane, shear, and the bending moment stress resultants, respectively, in the masonry unit, the mortar joint, and the FRP strips; b_i ($i = frp1, frp2$) is the width of the inner and outer FRP strips; α_m^n is a flag that equals 0 for a debonded interface or equals 1 for a bonded one ($m = 1$ for the inner adhesive layer and $m = 2$ for the outer adhesive layer; $n = frp$ for the adhesive-FRP interface and $n = c$ for the adhesive-masonry/mortar interface, see Figure 2d); β_m^n is also a flag that equals 0 for debonding without contact or equals 1 for debonding with contact, with the above notation for m and n . Note that Equations (12)–(24) are valid for both the masonry regions ($c = mu$) and the mortar regions ($c = mj$), whereas the distinction between the two cases is achieved through the constitutive relations.

Boundary and continuity conditions. The boundary conditions at the edges of the masonry panel and the FRP strips are:

$$\psi N_{xx}^i = \vartheta N_k \quad \text{or} \quad u_{oi} = \bar{u}_{oi}; \tag{25}$$

$$-\psi M_{xx}^i = \vartheta M_k \quad \text{or} \quad \phi_i = \bar{\phi}_i; \tag{26}$$

$$\psi (V_{xz}^i + N_{xx}^i w_{i,x}) = \vartheta P_k \quad \text{or} \quad w_i = \bar{w}_i; \tag{27}$$

where P_k , N_k and M_k are external loads and bending moments at $x_k = 0$ or $x_k = H$; \bar{u}_{oi} , \bar{w}_i and $\bar{\phi}_i$ ($i = c, frp1, frp2$) are prescribed deformations and rotations; $\psi = 1$ where $x = H$; $\psi = -1$ where $x = 0$; $\vartheta = 1$ for the boundary conditions of the masonry units or the mortar joints; and $\vartheta = 0$ for the boundary conditions of the FRP strips.

The boundary conditions at the edges of the adhesive layers are:

$$\tau_{xz}^{aj}(z_{aj}) = 0 \quad \text{or} \quad w_{aj}(z_{aj}) = \bar{w}_{aj}(z_{aj}); \tag{28}$$

where $\bar{w}_{aj}(z_{aj})$ ($j = 1, 2$) are prescribed deformation distributions through the thicknesses of the adhesive layers.

The continuity conditions at any point $x = x_k$ within the fully bonded sub-region are $i = c, \text{frp1}, \text{frp2}; j = 1, 2$

$$u_{oi}^{(-)} = u_{oi}^{(+)}; \quad w_i^{(-)} = w_i^{(+)}; \quad \phi_i^{(-)} = \phi_i^{(+)}; \quad (29)$$

$$N_{xx}^{i(-)} - N_{xx}^{i(+)} = \vartheta N_k; \quad -M_{xx}^{i(-)} + M_{xx}^{i(+)} = \vartheta M_k; \quad (30)$$

$$V_{xz}^{i(-)} + N_{xx}^{i(-)} w_{i,x}^{(-)} - V_{xz}^{i(+)} - N_{xx}^{i(+)} w_{i,x}^{(+)} = \vartheta P_k; \quad (31)$$

$$\tau_{xz}^{aj(-)}(z_{aj}) = \tau_{xz}^{aj(+)}(z_{aj}); \quad w_{aj}^{(-)}(z_{aj}) = w_{aj}^{(+)}(z_{aj}); \quad (32)$$

where the superscripts $(-)$ and $(+)$ denote quantities left and right to the point $x = x_k$, respectively.

Constitutive relations. The cracking of the mortar joints is a critical condition for the development of the arching action. Hence, the analysis must account for this type of physical nonlinear constitutive behavior. Based on the experimental observations of [Velazquez-Dimas et al. 2000] and [Hamilton and Dolan 2001], it is assumed that cracking is limited to the mortar joints. Hence, the constitutive relations for the masonry units assume linear elastic behavior, whereas the constitutive model for the mortar assumes a linear elastic behavior in compression and a brittle cracking behavior in tension. (Note that the constitutive model for the mortar can be extended to include a nonlinear behavior in compression. However, these effects are beyond the scope of this paper and are not considered here). The material point level constitutive relation for the normal stresses in the mortar is:

$$\sigma_{xx}^{\text{mj}} = \begin{cases} E_{\text{mj}} \varepsilon_{xx}^{\text{mj}}, & \text{if } \varepsilon_{xx}^{\text{mj}} \leq \varepsilon_t^{\text{mj}} \\ 0, & \text{if } \varepsilon_{xx}^{\text{mj}} > \varepsilon_t^{\text{mj}} \end{cases}, \quad (33)$$

where E_{mj} is the modulus of elasticity of the mortar, and $\varepsilon_t^{\text{mj}}$ is its the ultimate tensile or bond strain. The generalized (cross-sectional) constitutive relations for the masonry units and the mortar joints are:

$$N_{xx}^c = \int_{A_c} \sigma_{xx}^c(z_c) dA_c = A_{11}^c \left(u_{oc,x} + \frac{1}{2} (w_{c,x})^2 \right) - B_{11}^c \phi_{c,x} \quad (c = \text{mu or mj}); \quad (34)$$

$$M_{xx}^c = \int_{A_c} \sigma_{xx}^c(z_c) z_c dA_c = B_{11}^c \left(u_{oc,x} + \frac{1}{2} (w_{c,x})^2 \right) - D_{11}^c \phi_{c,x} \quad (c = \text{mu or mj}); \quad (35)$$

$$V_{xx}^c = \int_{A_c} \tau_{xz}^c(z_c) dA_c = A_{55}^c (w_{c,x} - \phi_c) \quad (c = \text{mu or mj}); \quad (36)$$

where A_{11}^c , B_{11}^c , D_{11}^c and A_{55}^c are the extensional, coupling, flexural, and shear rigidities of the masonry unit ($c = \text{mu}$) or the mortar joint ($c = \text{mj}$), multiplied by b_c , which is the width of the examined strengthened masonry strip.

Due to the assumed linear elastic behavior of the masonry unit material, the equivalent rigidities of the masonry units reduce to the traditional extensional, flexural and shear rigidities of the elastic section:

$$A_{11}^{mu} = \int_{-d_{mu}/2}^{d_{mu}/2} b_{mu} E_{mu} dz_{mu} = EA_{mu}; \tag{37a}$$

$$B_{11}^{mu} = \int_{-d_{mu}/2}^{d_{mu}/2} b_{mu} E_{mu} z_{mu} dz_{mu} = 0; \tag{37b}$$

$$D_{11}^{mu} = \int_{-d_{mu}/2}^{d_{mu}/2} b_{mu} E_{mu} z_{mu}^2 dz_{mu} = EI_{mu}; \tag{37c}$$

$$A_{55}^{mu} = \int_{-d_{mu}/2}^{d_{mu}/2} b_{mu} G_{mu} dz_{mu} = \kappa GA_{mu}; \tag{37d}$$

where E_{mu} and G_{mu} are the elastic and shear moduli of the masonry unit, EA_{mu} , EI_{mu} and GA_{mu} are the extensional, flexural and shear stiffnesses of the masonry unit section, respectively, $b_{mu} = b_c$, and κ is the shear correction constant.

In the mortar joint, the nonlinear constitutive law and the combined in-plane and bending tractions require special consideration. The general stress and strain distributions under various combined tractions appear in Figure 3a–c. In case the tensile strains are lower than the ultimate tensile/bond strain ϵ_t^{mj} (Figure 3a), the mortar joint is *uncracked* and it exhibits a linear elastic behavior. Therefore, the equivalent rigidities are given by Equation (37)a–d with the subscript/superscript mj instead of mu . In case the tensile strains exceed ϵ_t^{mj} (Figure 3b), the mortar joint is *cracked* and the equivalent rigidities take the following form:

$$A_{11}^{mj} = \int_{-d_{mj}/2}^{z_{act}^{mj}} b_{mj} E_{mj} dz_{mj} = E_{mj} b_{mj} \left(\frac{d_{mj}}{2} + \varphi z_{act}^{mj} \right); \tag{38a}$$

$$B_{11}^{mj} = \int_{-d_{mj}/2}^{z_{act}^{mj}} b_{mj} E_{mj} z_{mj} dz_{mj} = -\varphi \frac{E_{mj} b_{mj}}{2} \left(\left(\frac{d_{mj}}{2} \right)^2 - (z_{act}^{mj})^2 \right); \tag{38b}$$

$$D_{11}^{mj} = \int_{-d_{mj}/2}^{z_{act}^{mj}} b_{mj} E_{mj} z_{mj}^2 dz_{mj} = \frac{E_{mj} b_{mj}}{3} \left(\left(\frac{d_{mj}}{2} \right)^3 + \varphi (z_{act}^{mj})^3 \right); \tag{38c}$$

$$A_{55}^{mj} = \int_{-d_{mj}/2}^{z_{act}^{mj}} b_{mj} G_{mj} dz_{mj} = \kappa G_{mj} b_{mj} \left(\frac{d_{mj}}{2} + \varphi z_{act}^{mj} \right); \tag{38d}$$

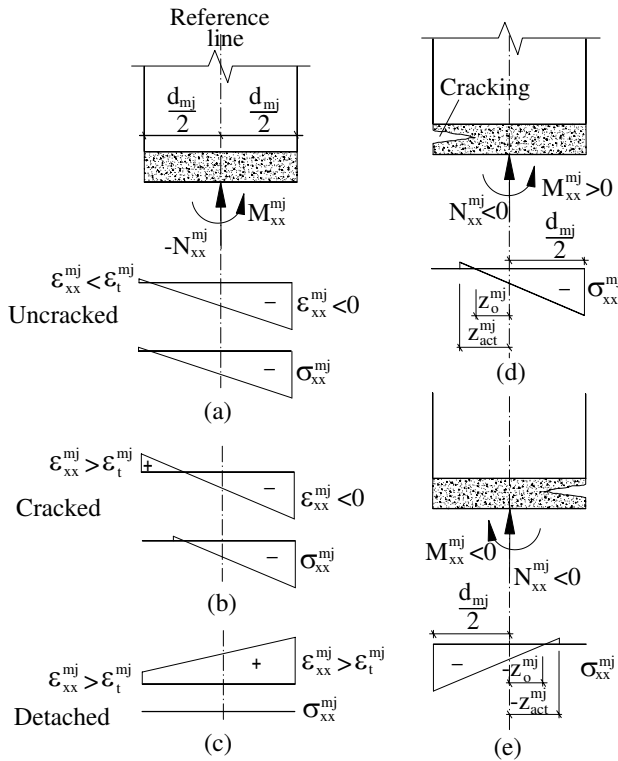


Figure 3. Stress distributions through the mortar joint: (a) uncracked joint; (b) cracked joint; (c) detached joint; (d) stress distribution under positive moment and compressive force; (e) stress distribution under negative moment and compressive force.

where according to Figure 3, b_{mj} and z_{act}^{mj} define the width and the depth of the active zone in the mortar cross section, $\varphi = 1$ in case the mortar section is locally subjected to in-plane compression combined with a positive bending moment (Figure 3d), $\varphi = -1$ if the in-plane compression is combined with a negative bending moment (Figure 3e) and G_{mj} is the shear modulus of the mortar. In case the mortar joint is fully detached (Figure 3c), its rigidities are zero and the functionality of the strengthened wall depends on the FRP strips only. In most practical cases, the contribution of the tensioned mortar to the stiffness of the cracked cross section is negligible, and thus z_{act}^{mj} can be replaced with z_o^{mj} , which is the height of the neutral axis; see Figure 3.

The constitutive relations of the FRP strips follow the classical lamination theory and use Equations (33)–(35) with the superscripts/subscripts frp1 or frp2 instead of c . In this case, A_{11}^i , B_{11}^i , D_{11}^i and A_{55}^i ($i = \text{frp1, frp2}$) are the extensional, coupling, flexural, and shear rigidities of the inner and outer FRP strips, respectively [Vinson and Sierakowski 1986], multiplied by the width of the strip. Note that the shear rigidity of the FRP strip may be one or two orders of magnitude smaller than its extensional rigidity, which may affect the localized buckling characteristics of the FRP strip [Sheinman and Adan 1987].

The constitutive relations for the adhesive material assume linear-elastic behavior, and read

$$\sigma_{zz}^{aj} = E_{aj}\varepsilon_{zz}^{aj}, \quad \tau_{xz}^{aj} = G_{aj}\gamma_{xz}^{aj}, \quad (j = 1, 2), \tag{39}$$

where E_{aj} and G_{aj} ($j = 1, 2$) are the modulus of elasticity and the shear modulus of the adhesive material, respectively. Note that in some cases, the material behavior of the adhesive may exhibit some nonlinear or inelastic characteristics. These effects, and especially their influence on the localized stress concentrations in the adhesive layer in externally strengthened reinforced concrete beams, are studied in [Rabinovitch 2005]. For brevity, and in order to focus on the geometrically nonlinear effects, they are not studied here.

Adhesive layers—stress and displacement fields. The stress and displacement fields of the adhesive layers follow the high-order approach [Rabinovitch and Frostig 2000], and are derived using Equations (21)–(24), along with the compatibility requirements/debonding conditions (Equations (6)–(11)) and the kinematic and constitutive relations (Equations (4), (39)). In the fully bonded regions they take the following form:

$$\tau_{xz}^{aj}(x, z_{aj}) = \tau_{xz}^{aj}(x) = \tau_{aj}; \tag{40}$$

$$\sigma_{zz}^{aj}(x, z_{aj}) = -\frac{2z_{aj} - c_{aj}}{2}\tau_{aj,x} + \frac{\lambda E_{aj}(w_i - w_c)}{c_{aj}}; \tag{41}$$

$$w_{aj}(x, z_{aj}) = -\frac{z_{aj}^2 - c_{aj}z_{aj}}{2E_{aj}}\tau_{aj,x} + \frac{\lambda(w_i - w_c)z_{aj}}{c_{aj}} + \frac{(1 + \lambda)}{2}w_c + \frac{(1 - \lambda)}{2}w_{frp2}; \tag{42}$$

$$u_{aj}(x, z_{aj}) = \frac{\tau_{aj}z_{aj}}{G_{aj}} + \frac{\tau_{aj,xx}}{2E_{aj}}\left(\frac{z_{aj}^3}{3} - c_{aj}\frac{z_{aj}^2}{2}\right) - \frac{\lambda(w_{i,x} - w_{c,x})z_{aj}^2}{2c_{aj}} - \frac{(\lambda + 1)}{2}\left(w_{c,x}z_{a1} - u_{oc} + \frac{d_c}{2}\phi_c\right) + \frac{(\lambda - 1)}{2}\left(w_{frp2,x}z_{a2} - u_{oc} + \frac{d_{frp2}}{2}\phi_{frp2}\right); \tag{43}$$

where $\lambda = 1$ for $j = 1$ and $i = frp1$, and $\lambda = -1$ for $j = 2$ and $i = frp2$. The stress fields in the debonded subregions (with or without contact) are:

$$\tau_{xz}^{aj}(x, z_{aj}) = \tau_{xz}^{aj}(x) = \tau_{aj} = 0; \tag{44}$$

$$\sigma_{zz}^{aj}(x, z_{aj}) = \frac{\beta_j \lambda E_{aj}(w_i - w_c)}{c_{aj}}; \tag{45}$$

where $\beta_j = \beta_j^c \cdot \beta_j^{frp}$.

Nonlinear governing equations. The nonlinear governing equations for the strengthened regions (fully bonded or debonded) are derived using Equations (12)–(20), the constitutive relations (Equations (34)–(39)), the compatibility requirements, Equations (7b), (9b) (in the bonded case), and the stress and deformation fields of the adhesive layers (Equations (40)–(45)). The governing equations are stated in terms of the unknown displacements and rotations, $(w_c, w_{frp1}, w_{frp2}, u_{oc}, u_{o\ frp1}, u_{o\ frp2}, \phi_c, \phi_{frp1}, \phi_{frp2})$,

and the unknown shear stresses (τ_{a1} and τ_{a2}), and read:

$$A_{11}^{\text{frp1}}(u_{o\text{frp1},xx} + w_{\text{frp1},x}w_{\text{frp1},xx}) - B_{11}^{\text{frp1}}\phi_{\text{frp1},xx} - \alpha_1^{\text{frp}}\alpha_1^c b_{\text{frp1}}\tau_{a1} = 0; \quad (46)$$

$$A_{11}^c(u_{oc,xx} + w_{c,x}w_{c,xx}) - B_{11}^c\phi_{c,xx} - \alpha_2^{\text{frp}}\alpha_2^c b_{\text{frp2}}\tau_{a2} + \alpha_1^{\text{frp}}\alpha_1^c b_{\text{frp1}}\tau_{a1} = -n_x; \quad (47)$$

$$A_{11}^{\text{frp2}}(u_{o\text{frp2},xx} + w_{\text{frp2},x}w_{\text{frp2},xx}) - B_{11}^{\text{frp2}}\phi_{\text{frp2},xx} + \alpha_2^{\text{frp}}\alpha_2^c b_{\text{frp2}}\tau_{a2} = 0; \quad (48)$$

$$A_{55}^{\text{frp1}}(w_{\text{frp1},xx} - \phi_{\text{frp1},x}) + A_{11}^{\text{frp1}}\left((w_{\text{frp1},x}u_{o\text{frp1},x})_{,x} + \frac{3}{2}w_{\text{frp1},xx}(w_{\text{frp1},x})^2\right) - B_{11}^{\text{frp1}}(w_{\text{frp1},x}\phi_{\text{frp1},x})_{,x} + \frac{\alpha_1^{\text{frp}}\alpha_1^c b_{\text{frp1}}c_{a1}}{2}\tau_{a1,x} - \beta_1\frac{b_{\text{frp1}}E_{a1}}{c_{a1}}(w_{\text{frp1}} - w_c) = 0; \quad (49)$$

$$A_{55}^c(w_{c,xx} - \phi_{c,x}) + A_{11}^c\left((w_{c,x}u_{oc,x})_{,x} + \frac{3}{2}w_{c,xx}(w_{c,x})^2\right) - B_{11}^c(w_{c,x}\phi_{c,x})_{,x} + \frac{\alpha_2^{\text{frp}}\alpha_2^c b_{\text{frp2}}c_{a2}}{2}\tau_{a2,x} + \frac{\alpha_1^{\text{frp}}\alpha_1^c b_{\text{frp1}}c_{a1}}{2}\tau_{a1,x} + \beta_2\frac{b_{\text{frp2}}E_{a2}}{c_{a2}}(w_{\text{frp2}} - w_c) + \beta_1\frac{b_{\text{frp1}}E_{a1}}{c_{a1}}(w_{\text{frp1}} - w_c) = -q_z; \quad (50)$$

$$A_{55}^{\text{frp2}}(w_{\text{frp2},xx} - \phi_{\text{frp2},x}) + A_{11}^{\text{frp2}}\left((w_{\text{frp2},x}u_{o\text{frp2},x})_{,x} + \frac{3}{2}w_{\text{frp2},xx}(w_{\text{frp2},x})^2\right) - B_{11}^{\text{frp2}}(w_{\text{frp2},x}\phi_{\text{frp2},x})_{,x} + \alpha_2^{\text{frp}}\alpha_2^c b_{\text{frp2}}c_{a2}\tau_{a2,x} - \beta_2\frac{b_{\text{frp2}}E_{a2}}{c_{a2}}(w_{\text{frp2}} - w_c) = 0; \quad (51)$$

$$D_{11}^{\text{frp1}}\phi_{\text{frp1},xx} - B_{11}^{\text{frp1}}(u_{o\text{frp1},xx} + w_{\text{frp1},x}w_{\text{frp1},xx}) + A_{55}^{\text{frp1}}(w_{\text{frp1},x} - \phi_{\text{frp1}}) - \alpha_1^{\text{frp}}\alpha_1^c b_{\text{frp1}}\frac{d_{\text{frp1}}}{2}\tau_{a1} = 0; \quad (52)$$

$$D_{11}^c\phi_{c,xx} - B_{11}^c(u_{oc,xx} + w_{c,x}w_{c,xx}) + A_{55}^c(w_{c,x} - \phi_c) - \alpha_2^{\text{frp}}\alpha_2^c b_{\text{frp2}}\frac{d_c}{2}\tau_{a2} - \alpha_1^{\text{frp}}\alpha_1^c b_{\text{frp1}}\frac{d_c}{2}\tau_{a1} = -m_y; \quad (53)$$

$$D_{11}^{\text{frp2}}\phi_{\text{frp2},xx} - B_{11}^{\text{frp2}}(u_{o\text{frp2},xx} + w_{\text{frp2},x}w_{\text{frp2},xx}) + A_{55}^{\text{frp2}}(w_{\text{frp2},x} - \phi_{\text{frp2}}) - \alpha_2^{\text{frp}}\alpha_2^c b_{\text{frp2}}\frac{d_{\text{frp2}}}{2}\tau_{a2} = 0; \quad (54)$$

$$\alpha_1^{\text{frp}}\alpha_1^c\left(u_{oc} - u_{o\text{frp1}} - \frac{c_{a1}}{2}(w_{\text{frp1},x} + w_{c,x}) + \frac{\tau_{a1}c_{a1}}{G_{a1}} - \frac{\tau_{a1,xx}c_{a1}^3}{12E_{a1}} - \frac{d_{\text{frp1}}}{2}\phi_{\text{frp1}} - \frac{d_c}{2}\phi_c\right) = 0; \quad (55)$$

$$\alpha_2^{\text{frp}}\alpha_2^c\left(u_{o\text{frp2}} - u_{oc} - \frac{c_{a2}}{2}(w_{\text{frp2},x} + w_{c,x}) + \frac{\tau_{a2}c_{a2}}{G_{a2}} - \frac{\tau_{a2,xx}c_{a2}^3}{12E_{a2}} - \frac{d_{\text{frp2}}}{2}\phi_{\text{frp2}} - \frac{d_c}{2}\phi_c\right) = 0. \quad (56)$$

In the debonded subregions, the shear stresses τ_{a1} , τ_{a2} , or both vanish. Correspondingly, Equation (55), Equation (56), or both, which result from the requirement of compatible longitudinal deformation, also vanish.

The nonlinear governing equations and the corresponding boundary and continuity conditions are numerically solved using the Nonlinear Multiple Shooting method [Stoer and Bulirsch 1993]. Along with the geometrical nonlinearity, the model is associated with further nonlinearities due to the unknown type of debonded subregions (with or without out-of-plane contact), and due to the cracking of the mortar joints. The determination of the type of debonded subregions is conducted iteratively. Namely, one type is assumed and verified through the results of the analysis. If the results contradict the assumption, the assumed type of the debonded region is switched and the structure is reanalyzed. The nonlinearity associated with the cracking of the mortar joints is considered through the following iterative procedure.

Step 1: initial guess. All mortar joints are assumed uncracked.

Step 2: analysis of the structure. Using the rigidities calculated in the initial guess or in the previous iteration, the nonlinear governing equations are numerically solved using the multiple shooting method [Stoer and Bulirsch 1993].

Step 3: analysis of the mortar joints cross-section. Based on the solution obtained in Step 2, the location of the cracked mortar joints and the depth of the compression zone in each cracked joint are determined as follows.

- (i) The strain distribution in each mortar joint is determined through Equation (3a). If the maximum tensile strain plus the initial compressive strain due to the self-weight exceeds the ultimate tensile/bond strain of the mortar, the joint is considered cracked.
- (ii) In each cracked joint, the depth of the active zone is determined as:

$$z_{act}^{mj} = \frac{u_{o\,mj,x} + \frac{1}{2}(w_{mj,x})^2}{\phi_{mj,x}} - \frac{\varepsilon_t^{mj}}{\phi_{mj,x}}; \quad (57)$$

where $u_{o\,mj,x}$, $w_{mj,x}$ and $\phi_{mj,x}$ are obtained in Step 2.

- (iii) Once z_{act}^{mj} is determined, the rigidities of each joint are evaluated using Equations (38)a–d. Due to the relatively small height of the joints (with respect to the height of the wall), it is assumed that the rigidities are uniform through the height of each joint.

Step 4: convergence criterion. If the norm of the relative difference between the magnitudes of the equivalent rigidities of the mortar joints in two successive iterations is sufficiently small, the iterative procedure is stopped. Otherwise, the procedure returns to Step 2 with the updated rigidities determined in Step 3.

Numerical study

The numerical study focuses on the geometrically nonlinear effects in the bending behavior of a masonry wall strengthened with externally bonded FRP strips. In many practical cases, masonry walls are strengthened to carry sign-reversing loads and the FRP strengthening system is applied on both faces of the wall. This type of strengthening scheme is examined as follows. The geometry of the wall, the strengthening scheme, the mechanical properties of the materials, and the static load pattern appear in Figure 4. The FRP strips are assumed to be fully bonded in the uncracked stage. However, once the joint is cracked, it is assumed that the crack opening, the extensive longitudinal strains in the FRP strip bridging over the crack, and the inability of the cracked faces to transfer shear stresses trigger the formation of a debonded region along the cracked joint. Studies on externally strengthened concrete beams [Rabinovitch and Frostig 2000; Rabinovitch and Frostig 2001; Teng et al. 2002] and preceding studies on the geometrically linear response of strengthened masonry walls [Hamed and Rabinovitch 2005] revealed that the characteristic length scale of the peeling stress concentrations near the edge of the FRP strip, near cracks, or near the mortar joint is about the thickness of the adhesive layer. (The peeling stress concentration decays within a distance of about 2 to 3 times the thickness of the adhesive

layer). Hence, it is assumed that the height of each debonded region equals the height of the mortar joint plus twice the thickness of the adhesive layer (Figure 4d). In order to examine the role of the assumed height of the debonded region, the influence of this parameter is parametrically studied over a range of zero to three times the thickness of the adhesive layer. The effect of the existence of debonded regions in *all* mortar joints, which may result from imperfect placement of the adhesive or from preloading of the strengthened wall, is also investigated. Finally, the effect of the slenderness ratio is examined.

The load-deflection curves (equilibrium paths) and the in-plane thrust force (the *arching force*) versus the out-of-plane deflection curves of the strengthened and the unstrengthened masonry walls appear in Figure 5. In order to highlight the geometrically nonlinear effects, the results of a geometrically linear, but physically nonlinear (cracking) analysis of the strengthened wall also appear in Figure 5. The results show that both the unstrengthened wall and the strengthened wall are characterized by a limit point and a snap-through type of behavior [Simitzes 1986]. Due to the ability of the strengthened wall to carry bending moments through tensile stresses in the FRP strip and compressive stresses in the masonry panel, the post-limit-point slope of the equilibrium path and the magnitudes of the arching force in the strengthened wall are lower than those in the unstrengthened one (see Figure 5b). The latter observation is in qualitative agreement with the experimental findings of [Galati et al. 2002], which revealed a reduction in the magnitude of the thrust force with the increase of the width (and cross sectional area) of the

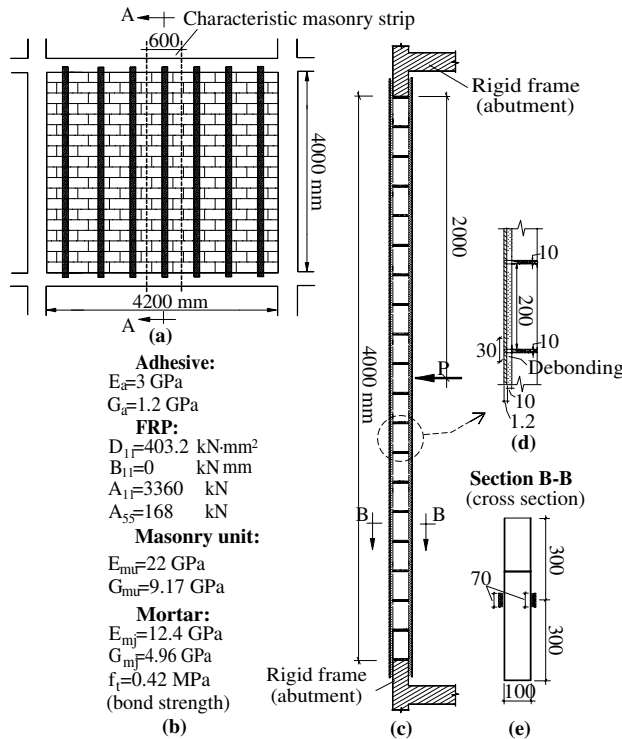


Figure 4. Geometry, material properties, and loading: (a) geometry; (b) material properties; (c) section A-A: geometry and loading; (d) cracked mortar joint and debonded regions; (e) section B-B (cross section).

strengthening system. The comparison between the nonlinear results and the linear ones clearly indicates that the decrease in the overall flexural rigidity of the strengthened wall along its equilibrium path results from the destabilizing nonlinear effects of the arching action, and not from the progressive cracking of the mortar joints. Note that the load-deflection curve in the geometrically linear case is almost linear due to the early cracking of the mortar joints under very low load levels.

In quantitative terms, Figure 5a shows that the limit point load and deflection of the unstrengthened masonry wall are about 25.4 kN and 40 mm, respectively, while those of the strengthened wall are about 36 kN and 55.5 mm, respectively. Thus, the use of the bonded FRP strips improves the stability characteristics of the wall (both the limit point load and the limit point deflection) by a factor of about 1.4. A similar *improvement factor* of the limit point load was detected in the experimental study of [Tumialan et al. 2003]. Yet, this value is much smaller than the factors experimentally detected for strengthened simply supported and longitudinally unconstrained walls [Gilstrap and Dolan 1998; Albert et al. 2001; Hamilton and Dolan 2001; Hamoush et al. 2002].

The response of the strengthened and the unstrengthened masonry walls under a displacement level of 20 mm at midspan and load levels of about 24 kN and 20 kN, respectively, is studied in Figure 6. The out-of-plane and the in-plane deflections appear in Figure 6 a,b. These figures reveal that due to the progressive cracking of the critical mortar joints at the edges and at midspan, the deformation of the wall is governed by a system of three hinged rigid bodies. A level of elastic curvature, which is slightly more prominent in the strengthened wall, is also observed due to localized bending of the masonry units (Figure 6a). Figure 6b further reveals the *jumps* in the distribution of the longitudinal deformations due to cracking of the critical joints. The distributions of the bending moments, the in-plane forces, and the shear forces appear in Figures 6c–e, respectively, and reveal the localized effects in the vicinity of the cracked mortar joints. These effects result from the prominent change in stiffness between the masonry unit section and the cracked mortar joint section. In the masonry unit section, the considerable flexural stiffness of the masonry unit allows a larger portion of the global bending moment to be carried by the masonry unit itself. As a result, the part of the global moment carried in the form of tensile forces in the

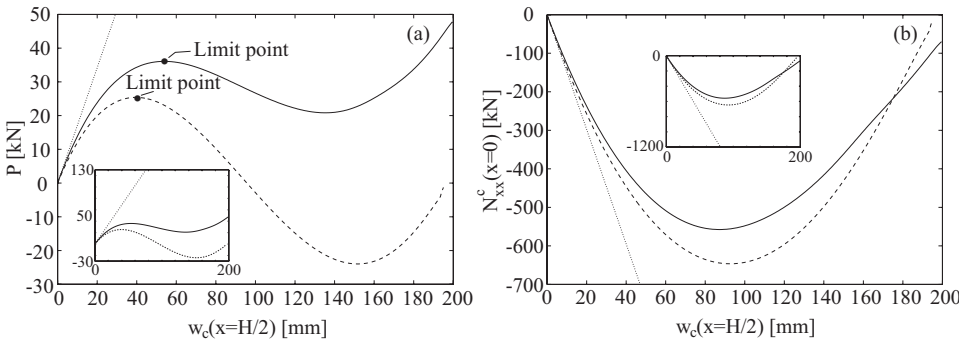


Figure 5. Response of strengthened and unstrengthened masonry wall: (a) equilibrium paths (load versus deflection); (b) “thrust force” versus deflection. (Legend: — strengthened wall (nonlinear analysis); - - - unstrengthened wall (nonlinear analysis); ··· strengthened wall (linear analysis).)

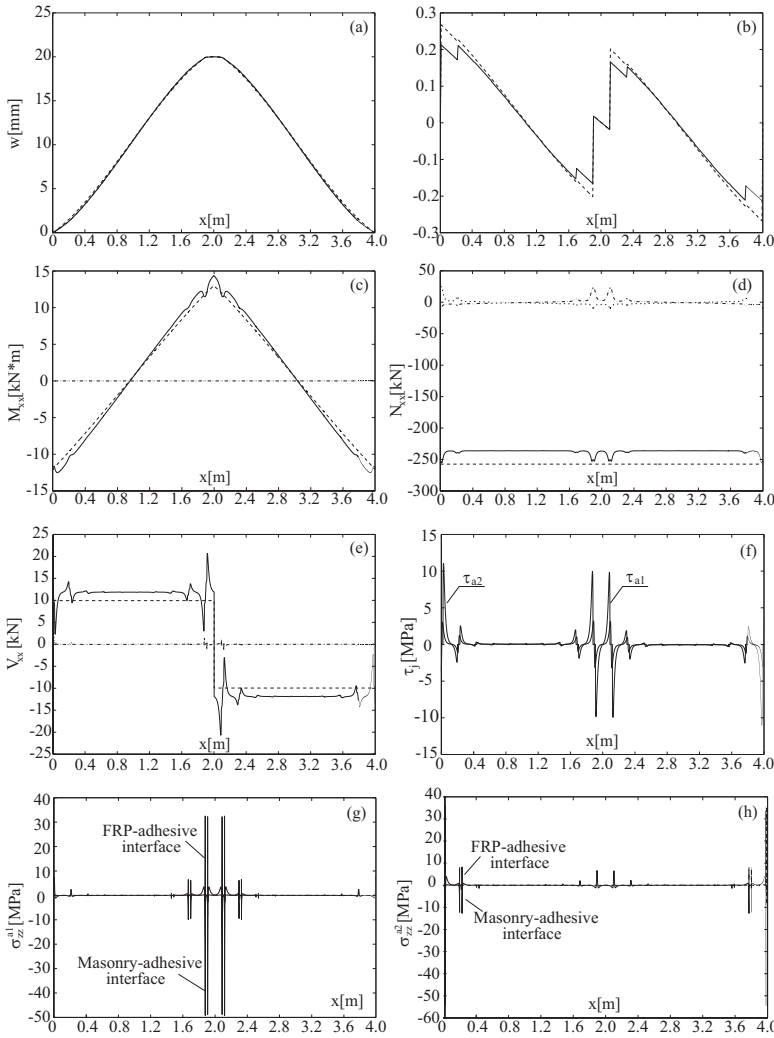


Figure 6. Response under midspan displacement of 20 mm: (a) out-of-plane deflections; (b) in-plane deformations; (c) bending moments; (d) axial forces; (e) shear forces; (f) adhesive shear stresses; (g) out-of-plane normal stresses, inner adhesive layer; (h) out-of-plane normal stresses, outer adhesive layer. (Legend: — strengthened wall; - - - unstrengthened wall; - - - - inner FRP strip; ··· outer FRP strip).

FRP strip and compressive force in the wall (the *composite action* moment) is much smaller than in the cracked mortar joint section. The variation of the tensile force in the FRP strip from the cracked joint section to the masonry unit section yields the shear stress concentrations observed in Figure 6f. Figures 6d and 6e also reveal locally increased shear and compressive forces in the masonry panel. These effects

may lead to the shear-compression crushing failure experimentally observed by Tumialan et al., [2000; 2003] and Galati et al. [2002].

The localized effects near the cracked joints and especially the rapid variation in the shear stresses (Figure 6f) also trigger the development of out-of-plane normal (peeling) stress concentrations (see Figures 6g, 6h and Equation (41)). Note that in the inner adhesive layer, the stress concentrations develop due to crack opening at the inner face of the mortar joints near midspan. In the outer adhesive layer, they develop due to crack opening at the outer face of the edge joints. These stress concentrations quantify and explain the debonding mechanisms experimentally observed by Hamilton and Dolan [2001], Carney and Myers [2005] and others.

Effect of debonded regions and local buckling. In many cases, the development of debonded regions is not limited to the vicinity of the cracked joints, but may also form due to imperfect placement of the adhesive or to preloading of the strengthened wall. The influence of the existence of debonded regions near all mortar joints is studied in Figure 7. Figure 7a shows that the overall equilibrium path (load-deflection curve) of the strengthened wall is only slightly affected by the existence of the debonded regions near all mortar joints (as compared to the case debonded regions are formed near the cracked joints only). On the other hand, the response in terms of the longitudinal normal stresses at the inner and outer faces of the compressed FRP strip near midspan (Figure 7b) reveals significant differences between

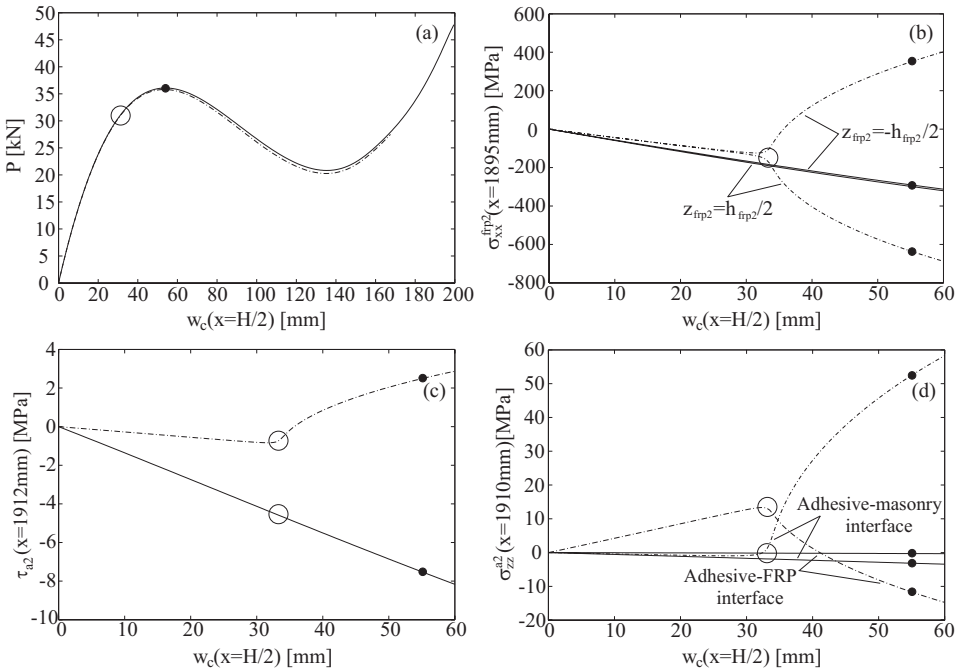


Figure 7. Equilibrium paths and stresses in the FRP strip and the adhesive versus midspan deflection: (a) equilibrium paths; (b) longitudinal stresses in the outer FRP strip; (c) shear stresses in the adhesive; (d) out-of-plane normal stresses in the adhesive. (Legend: — debonding in the cracked joints only; ---- debonding in all joints; • limit point; o wrinkling).

the two cases. In case the FRP strip is fully bonded, the two faces are subjected to an almost equal level of compressive stresses, and the effect of the local bending moment is minor. In the debonded case, starting from a load level of about 31.3 kN (and a displacement level of about 32 mm), the local bending moment significantly affects the in-plane normal stresses. This bending moment is a direct result of the local buckling (wrinkling) of the compressed FRP.

The effect of the localized buckling and wrinkling phenomena on the shear and the out-of-plane normal stresses in the adhesive at the edges of the debonded region near midspan is studied in Figures 7c and 7d, respectively. These curves show that once the compressed FRP has buckled, the shear stresses and, particularly, the out-of-plane normal stresses are significantly increased. Furthermore, while the adhesive-masonry interface is in compression in the prebuckling stage, beyond the local buckling point it is subjected to tensile stresses. Due to the brittleness and the low out-of-plane tensile strength of the masonry material, this may trigger the growth of the debonded region, and may lead to total failure of the strengthening system. The results presented here in terms of stress fields in relation to this effect can be used for the quantitative evaluation of a fracture-mechanics based criterion for the growth of the debonded regions [Rabinovitch and Frostig 2001; 2006; Rabinovitch 2004a]. The results also show that the local buckling of the FRP strip occurs at a load level that is lower than the limit point load. Hence, in this case, the localized stability effects are expected to be more dominant than the global ones.

The out-of-plane deflections and the in-plane normal stresses in the FRP strip under load levels of 28.5 kN and 33.5 kN appear in Figure 8 and clearly show the wrinkling of the FRP strip within the debonded region (Figure 8a). Figure 8b reveals the considerable amplification of the in-plane normal stresses in the inner and outer faces of the FRP strip. Also there, is the direct result of the bending moments that develop due to the local buckling of the FRP strips.

Effect of the height of the debonded regions (h_{deb}). The influence of the height of debonded regions on the local and global behavior of the strengthened wall (in case debonded regions are formed near all joints) is parametrically studied in Figure 9. The results show that the height of the debonded regions does not qualitatively affect the general pattern of the nonlinear behavior of the strengthened wall. However, Figures 9 a, c, d show that the limit point loads and the limit point displacements detected with very

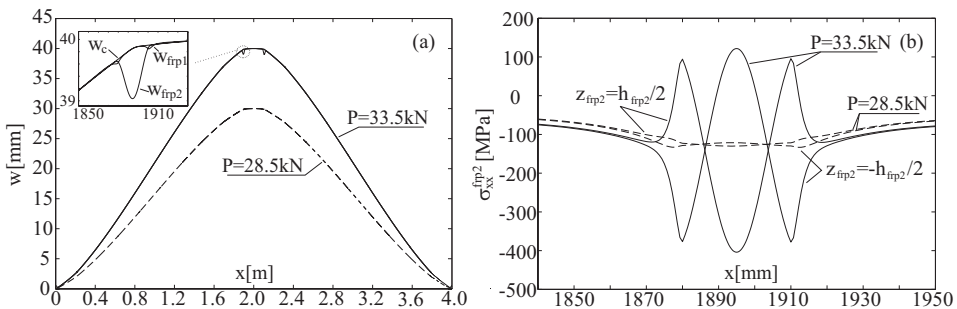


Figure 8. Response of the strengthened wall with debonded regions in all joints: (a) out-of-plane deflections along the wall; (b) longitudinal stresses in the faces of the outer FRP strip. (Legend: — response under $P = 33.5\text{ kN}$ ($w_{c,max} = 40\text{ mm}$); - - - response under $P = 28.5\text{ kN}$ ($w_{c,max} = 30\text{ mm}$)).

short debonded regions ($h_{deb} \rightarrow 0$) are notably higher than the ones detected with the higher (up to 70 mm) ones. In other words, the results show that the height of the debonded regions affects the limit point load and the limit point deflection *improvement factors* of the strengthening system (that is, the ratios of the limit point load or deflection of the strengthened wall over those of the original wall). These factors range from about 1.65 for the short debonded regions to only about 1.2 for the longer debonded regions. Figures 9b and 9d further show that, as expected, the magnitudes of the wrinkling load of the compressed FRP strip significantly decrease with the increase of the height of the debonded regions. Note that in the case of debonded region shorter than 20 mm, wrinkling of the FRP strip does not occur. The results observed in Figure 9 clarify that the height of the debonded region quantitatively affects the global nonlinear behavior of the wall and critically governs the localized response (wrinkling) near the cracked joint. Furthermore, the results highlight the necessity of a fracture mechanics approach to the debonding growth mechanism [Rabinovitch and Frostig 2001; 2006; Rabinovitch 2004a]. This approach can be applied based on the stress and displacement fields detected here.

Effect of the slenderness ratio. Four strengthened URM walls with different slenderness ratios, ($H/h_c = 21.1, 31.6, 40, \text{ and } 52.6$) are examined. The dimensions of the masonry units and the mortar joints are the same for all walls, while the slenderness ratio is controlled by modifying the number of the masonry units. The *normalized* load-deflection curves (equilibrium paths) for the four unstrengthened walls, the

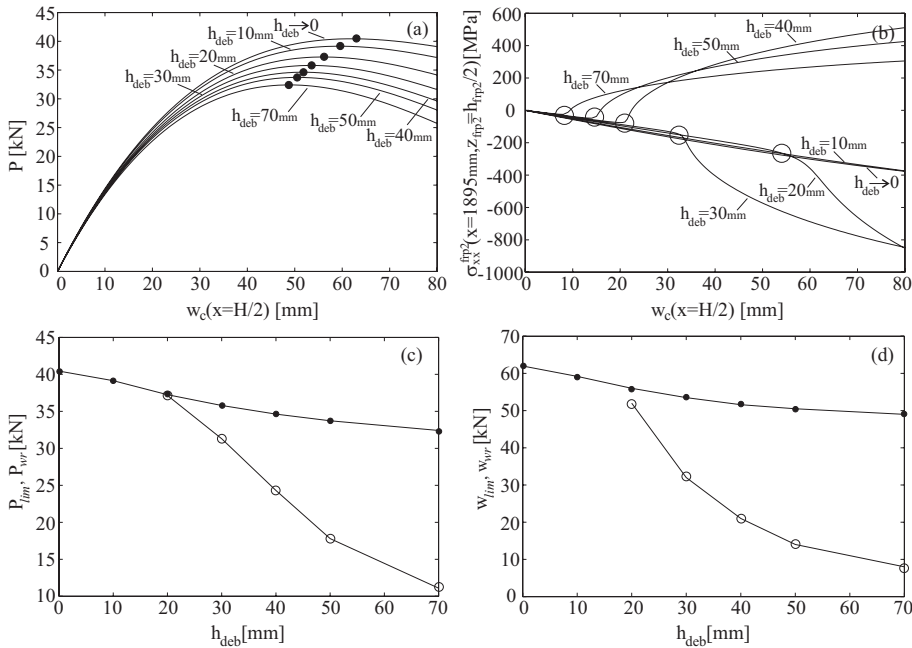


Figure 9. Influence of the height of debonded regions (h_{deb}): (a) equilibrium paths; (b) longitudinal stresses in the outer FRP strip; (c) critical (limit point, wrinkling) load versus h_{deb} ; (d) critical (limit point, wrinkling) displacement versus h_{deb} . (Legend: ● limit point; ○ wrinkling point).

strengthened walls with debonded regions near the cracked joints only, and the strengthened walls with debonded regions near all joints appear in Figure 10. (Note that in some cases, numerical convergence was not achieved and the deep post-limit-point response, which is of less practical importance, was not detected). The *normalized* results show that walls with different slenderness ratios exhibit a qualitatively similar nonlinear behavior with a limit point and a snap through. Considering the *limit point load improvement factor* of the strengthening system it is seen that for the configuration studied here (with $h_{deb} = 30$ mm), this normalized factor is about 1.4 for all slenderness ratios. The results further show that the strengthening system modifies the limit point deflection and increases it from about $0.4h_c$ in the unstrengthened walls to about $0.55h_c$ in the strengthened ones. Also, the *limit point deflection improvement factor* equals about 1.4 for all slenderness ratios.

In quantitative terms, the critical limit point load drops down from 223 kN in the strengthened stubby wall to about 29 kN in the most slender one. Yet, the critical limit point deflection is about 55 mm in all cases. The reduction in the critical load (limit point loads, P_{lim} , or wrinkling load, P_{wr}) with the increase of the slenderness ratio is quantitatively studied in Figure 11. These results emphasize that in the high slenderness ratios ($H/h_c = 40, 52.6$), the geometrically destabilizing effects may lead to loss of stability before exceeding the ultimate strength of the materials [Carney and Myers 2005]. The ability to explore and quantify these geometrically nonlinear effects is essential for the design and use of the strengthened wall.

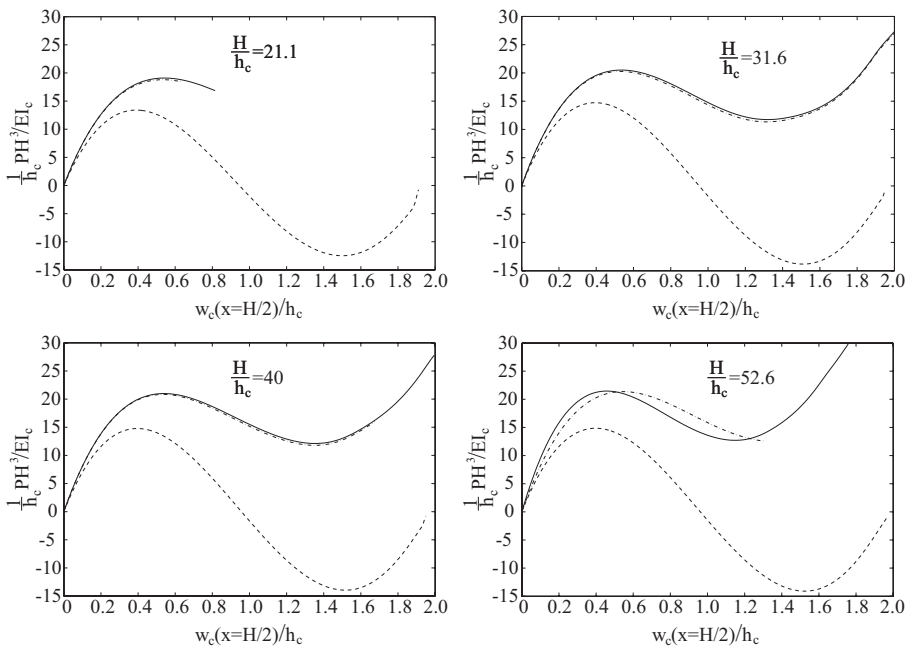


Figure 10. Normalized equilibrium paths for different slenderness ratios. (Legend: — strengthened wall with debonded regions near the cracked joints only; ---- strengthened wall with debonded regions near all joints; - - - unstrengthened wall).

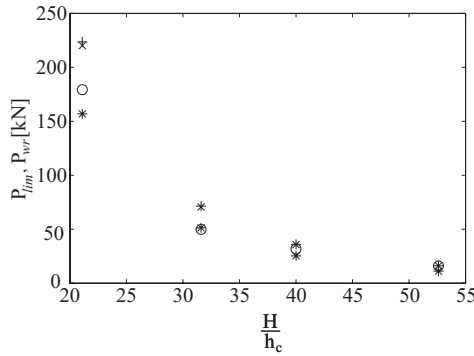


Figure 11. Critical loads (limit point load, wrinkling load) versus slenderness ratio. (Legend: * unstrengthened wall limit point; + strengthened wall limit point; · strengthened wall with debonded regions in all joints—limit point; o wrinkling load).

Comparison to finite element analysis

In this section, the results obtained through the nonlinear theoretical model developed here are compared to finite element analysis (FEA), using the commercial package ANSYS. The geometry of two blocks specimen, the mechanical properties of the materials, and the 2D finite element model appear in Figure 12. The analytical model assumes that debonded regions develop at the mortar joints in case of imperfect placement of the adhesive, or in case of cracking of the joint. Correspondingly, the same assumption

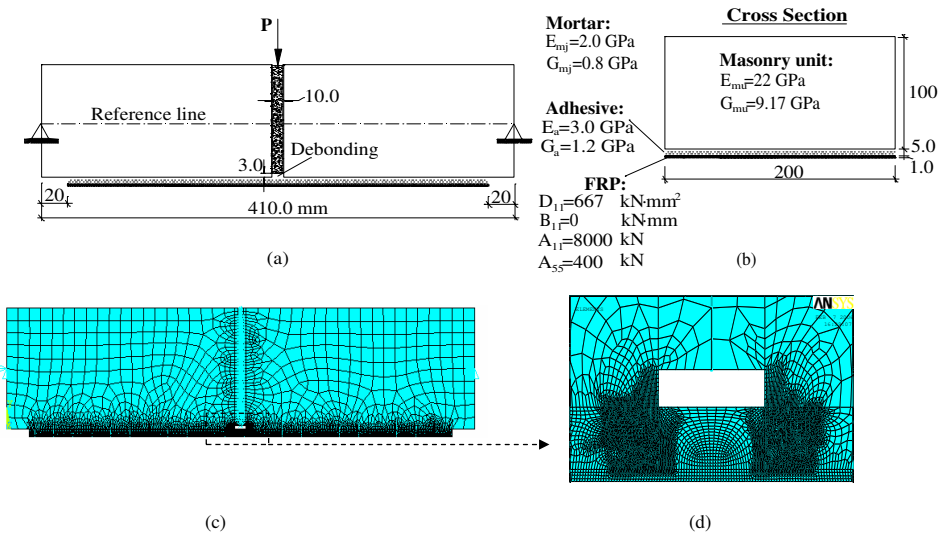


Figure 12. Geometry, material properties, and load pattern for masonry specimens: (a) geometry and load; (b) cross section and material properties; (c) finite element mesh; (d) zoom on the mortar joint.

is made in the FE model and a 3.0 mm deep and 10.0 mm high gap is assumed between the mortar and the adhesive (see Figure 12a). The nonlinear effect of mortar joint cracking is considered as a contact problem, using contact and target surface elements located at midspan. The masonry, the mortar, the FRP strip, and the adhesive are modeled using 4 node elements, and they are assumed to be linear elastic. Yet, due to the extensive longitudinal strains and the probable cracking or yielding of the adhesive fillet that is attached to the debonded FRP strip within the cracked mortar joint, it is assumed that its longitudinal rigidity is significantly smaller than its out-of-plane normal rigidity. The number of elements used through the thin adhesive layer varies from 5 to 15 at the critical locations. The number of elements used through the thickness of the FRP strip is 4, and the number of elements through the depth of the masonry block is about 15. The total number of elements used in the nonlinear FEA of the two masonry units specimen is as large as 21588. This huge number of elements is required, due to the different length scales of the structure components and due to the singular points near the debonded region and near the edges of the FRP strip (also see the FE model in [Davidson et al. 2005]). Two point supports that restrict the longitudinal and the vertical displacements are located at the edges of the specimen at midheight.

The nonlinear equilibrium paths of the strengthened and the unstrengthened specimens obtained by the theoretical and the FE models appear in Figure 13. The results reveal fair agreement between the numerical and the theoretical curves. In the strengthened wall, good agreement is observed at relatively low and medium load levels. Under higher loads, the results of the FE model deviate from the equilibrium path obtained by the theoretical model. This is mainly attributed to the localized effects observed near the supports in the FE model (stress concentrations and localized deformations), and the different modeling of the cracking at the mortar joint (critical section cracking in the FE model compared with cracking of the entire length of the mortar joint in the theoretical model). The different modeling of the effect of shear deformation (first order beam theory versus 2D elasticity) may also contribute to the differences observed; however, this effect is probably secondary to other contributing factors mentioned above. Figure 13 also shows that the theoretical model predicts the limit point behavior of the strengthened masonry specimen, whereas the FE model diverges under a displacement level that is 3% higher than the limit

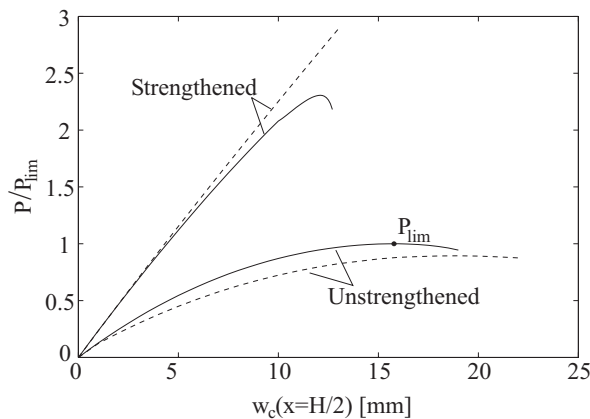


Figure 13. Equilibrium paths of strengthened and unstrengthened specimens. (Legend: — theoretical model; - - - FE model).

point displacement predicted by the theoretical model. At that point, the load predicted by the FE model is about 25% higher than the limit point load determined by the theoretical model. In the unstrengthened wall, the FE model succeeds in describing the limit point behavior and predicts a limit point load that is about 10% lower than the one predicted by the theoretical model.

The distributions of the normalized axial force in the FRP strip and the shear and peeling stresses in the adhesive are described in Figure 14. It is seen that the results of the FE analysis and those of the theoretical model are in good agreement. Figure 14a shows that the FEA also predicts that the axial force in the FRP strip is almost constant through the length of the debonded region at the mortar joint. This is due to the negligible shear stresses in the adhesive within the debonded region (Figure 14b). In the theoretical model these stresses totally vanish (Figure 14b), and the axial force in the FRP strip is uniform within the debonded region (Figure 14a). The distribution of the peeling stresses at the interfaces of the adhesive layer near the cracked mortar joint appears in Figure 14c, and also reveals an impressive agreement between the numerical and the theoretical models.

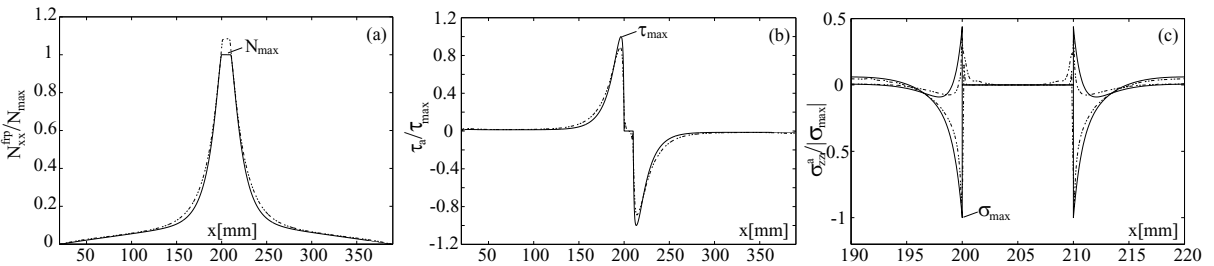


Figure 14. Response of the strengthened masonry specimen under a midspan displacement of 4 mm: (a) normalized axial forces in the FRP; (b) shear stresses in the adhesive; (c) peeling stresses in the adhesive near the joint. (Legend: — theoretical model; - - - FE model).

Opposed to the analytical stress fields used in the theoretical model (Equations (40)–(45)), the FEA is strongly affected by the singular character of the stresses near the edges of the debonded region. As a result, it is sensitive to the mesh characteristics in this region. The convergence of the FE peak shear and normal stresses in the adhesive, with the refinement of the mesh, is studied in Figure 15 (note that in both analyses, the same debonded region is assumed). The results are normalized and the ratios of the peak stresses computed by the FE model (τ_{FE} and σ_{FE}^{zz}) over the peak stresses obtained by the theoretical model (τ_{Th} and σ_{Th}^{zz}) are presented. The results in Figure 15 indicate that the numerical FE results converge towards the theoretical values with the refinement of the mesh. This trend is most notable in terms of the peak normal stresses, which are more affected by the singularity at the edges of the debonded region. This observation indicates that for cases in which the mesh of the FE model is not as fine as required, the FE model could underestimate the critical stresses in the adhesive. Due to the critical importance of these stresses, the results presented here highlight one of the most problematic aspects of the FEA of the strengthened wall and emphasize the advantages of the theoretical model.

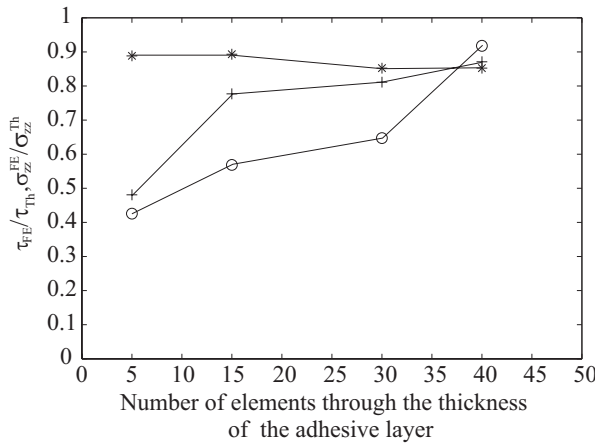


Figure 15. Convergence of the peak shear and peeling stresses near the mortar joint with mesh refinement. (Legend: * shear stresses; + peeling stresses at the adhesive-FRP interface; o peeling stresses at the adhesive-masonry interface).

Concluding remarks

The geometrically nonlinear effects of the out-of-plane flexural response of URM walls strengthened with composite materials have been investigated. A general theoretical approach and a nonlinear analytical model for the geometrically nonlinear analysis of the strengthened masonry wall have been presented. The analytical model and the numerical study have revealed a global limit-point and snap-through type of behavior that is governed by the destabilizing influence of the arching action as well as localized wrinkling effects in the compressed FRP strip. The results have also shown that the use of the bonded FRP system can potentially improve the global stability characteristics of the wall and increases its limit point load and deflection by a factor of 1.2–1.65.

The effect of the formation of debonded regions in the vicinity of the mortar joints has been examined. It has been shown that the formation of debonded regions promotes the development of wrinkling or local buckling of the compressed FRP strip. This phenomenon significantly magnifies the normal stresses in the FRP strip as well as the shear and peeling stresses in the adhesive. Thus, it may trigger an overall debonding failure of the strengthening system. In addition, it has been quantitatively shown that the increase in the height of the debonded regions affects the global nonlinear behavior of the strengthened wall and reduces the magnitude of the local wrinkling load as well as the effectiveness of the strengthening system.

The study of the influence of the slenderness ratio has shown that strengthened walls of different slenderness ratios exhibit a qualitatively similar nonlinear behavior. Quantitatively, the investigation has characterized the reduction in the global limit point load with the increase of the slenderness ratio and has highlighted the role of the geometrically nonlinear effects in the response of the slender strengthened walls.

In conclusion, the analytical model and the numerical study presented have shed some light on the global (limit-point and snap through behavior) and localized (wrinkling) geometrically nonlinear effects

in the out-of-plane behavior of URM walls strengthened with composite materials. Due to their critical influence on the structural response of the strengthened wall, these geometrically and physically nonlinear effects must be carefully considered in order to assure the effective design and the safe use of the strengthened wall.

References

- [Albert et al. 2001] M. L. Albert, A. E. Elwi, and J. J. R. Cheng, “Strengthening of unreinforced masonry walls using FRPs”, *J. Compos. Constr.* **5**:2 (2001), 76–84.
- [Anderson 1984] C. Anderson, “Arching action in transverse laterally loaded masonry wall panels”, *The Structural Engineer* **62B**:1 (1984), 12–23.
- [Carney and Myers 2005] P. Carney and J. J. Myers, “Out-of-plane static and blast resistance of unreinforced masonry wall connections strengthened with FRP”, pp. 229–248 in *Fiber-reinforced polymer (FRP) reinforcement for concrete structures: 7th international symposium* (Kansas City, MO, 2005), edited by C. K. Shield et al., American Concrete Institute, Farmington Hills, MI, 2005.
- [Dafnis et al. 2002] A. Dafnis, H. Kolsch, and H. Reimerdes, “Arching in masonry walls subjected to earthquake motions”, *J. Struct. Eng.* **128**:2 (2002), 153–159.
- [Davidson et al. 2005] J. S. Davidson, J. W. Fisher, M. I. Hammons, J. R. Porter, and R. J. Dinan, “Failure mechanisms of polymer-reinforced concrete masonry walls subjected to blast”, *J. Struct. Eng.* **131**:8 (2005), 1194–1205.
- [Deuring 1993] M. Deuring, “Verstärken von Stahlbeton mit gespannten Faserverbundwerkstoffen”, EMPA Research report 224, Swiss federal laboratories for material testing and research, Dübendorf, 1993.
- [Galati et al. 2002] N. Galati, J. G. Tumialan, A. La Tegola, and A. Nanni, “Influence of arching mechanism in masonry walls strengthened with FRP laminates”, in *Third international conference on composites in infrastructure*, San Francisco, 2002.
- [Ghobarah and El Mandooh Galal 2004] A. Ghobarah and K. El Mandooh Galal, “Out-of-plane strengthening of unreinforced masonry walls with openings”, *J. Compos. Constr.* **8**:4 (2004), 298–305.
- [Gilstrap and Dolan 1998] J. M. Gilstrap and C. W. Dolan, “Out-of-plane bending of FRP-reinforced masonry walls”, *Compos. Sci. Technol.* **58**:8 (1998), 1277–1284.
- [Griffith et al. 2004] M. C. Griffith, N. T. K. Lam, J. L. Wilson, and K. Doherty, “Experimental investigation of unreinforced brick masonry walls in flexure”, *J. Struct. Eng.* **130**:3 (2004), 423–432.
- [Hamed and Rabinovitch 2005] E. Hamed and O. Rabinovitch, “Out-of-plane bending of URM walls strengthened with FRP strips — modeling and analysis”, pp. 249–268 in *Proceedings of the 7th international symposium on fiber reinforced polymer (FRP) reinforcement for concrete structures*, edited by C. K. Shield et al., Kansas City, MO., November 6–9 2005.
- [Hamilton and Dolan 2001] H. R. Hamilton and C. W. Dolan, “Flexural capacity of glass FRP strengthened concrete masonry walls”, *J. Compos. Constr.* **5**:3 (2001), 170–178.
- [Hamoush et al. 2002] S. A. Hamoush, M. W. McGinley, P. Mlakar, and M. J. Terro, “Out-of-plane behavior of surface-reinforced masonry walls”, *Constr. Build. Mater.* **16**:6 (2002), 341–351.
- [Hasetline and Moore 1981] B. A. Hasetline and J. F. A. Moore, *Handbook to BS5628: structural use of masonry, 1: unreinforced masonry*, Brick Development Association, Windsor, UK, 1981.
- [Kiss et al. 2002] R. M. Kiss, L. P. Kollar, J. Jai, and H. Krawinkler, “Masonry strengthened with FRP subjected to combined bending and compression, II: test results and model predictions”, *J. Compos. Mater.* **36**:9 (2002), 1049–1063.
- [Kuzik et al. 2003] M. D. Kuzik, A. E. Elwi, and J. J. R. Cheng, “Cyclic flexure tests of masonry walls reinforced with glass fiber reinforced polymer sheets”, *J. Compos. Constr.* **7**:1 (2003), 20–30.
- [McDowell et al. 1956] E. L. McDowell, K. E. Mckee, and E. Sevin, “Arching action theory of masonry walls”, *J. Struct. Div.* **82**:ST2 (1956), 915–1: 915–18.
- [Rabinovitch 2004a] O. Rabinovitch, “Fracture-mechanics failure criteria for RC beams strengthened with FRP strips – a simplified approach”, *Compos. Struct.* **64**:3–4 (2004), 479–492.

- [Rabinovitch 2004b] O. Rabinovitch, “Nonlinear (buckling) effects in RC beams strengthened with composite materials subjected to compression”, *Int. J. Solids Struct.* **41**:20 (2004), 5677–5695.
- [Rabinovitch 2005] O. Rabinovitch, “Bending behavior of reinforced concrete beams strengthened with composite materials using inelastic and nonlinear adhesives”, *J. Struct. Eng.* **131**:10 (2005), 1580–1592.
- [Rabinovitch and Frostig 2000] O. Rabinovitch and Y. Frostig, “Closed-form high-order analysis of RC beams strengthened with FRP strips”, *J. Compos. Constr.* **4**:2 (2000), 65–74.
- [Rabinovitch and Frostig 2001] O. Rabinovitch and Y. Frostig, “Delamination failure of RC beams strengthened with FRP strips — a closed-form high-order and fracture mechanics approach”, *J. Eng. Mech.* **127**:8 (2001), 852–861.
- [Rabinovitch and Frostig 2006] O. Rabinovitch and Y. Frostig, “Fracture mechanics approach to geometrically nonlinear debonding problems in RC beams strengthened with composite materials”, *Adv. Struct. Eng.* **9**:6 (2006), 765–777.
- [Sheinman and Adan 1987] I. Sheinman and M. Adan, “The effect of shear deformation on post-buckling behavior of laminated beams”, *J. Appl. Mech. (Trans. ASME)* **54**:3 (1987), 558–562.
- [Simitzes 1986] G. J. Simitzes, *An introduction to the elastic stability of structures*, Krieger, Malabar, FL, 1986.
- [Stoer and Bulirsch 1993] J. Stoer and R. Bulirsch, *Introduction to numerical analysis*, Springer, New York, 1993.
- [Tan and Patoary 2004] K. H. Tan and M. K. H. Patoary, “Strengthening of masonry walls against out-of-plane loads using fiber-reinforced polymer reinforcement”, *J. Compos. Constr.* **8**:1 (2004), 79–87.
- [Teng et al. 2002] J. G. Teng, J. W. Zhang, and S. T. Smith, “Interfacial stresses in reinforced concrete beams bonded with a soffit plate: a finite element study”, *Constr. Build. Mater.* **16**:1 (2002), 1–14.
- [Timoshenko and Goodier 1970] S. Timoshenko and J. N. Goodier, *Theory of elasticity*, 3rd ed., McGraw-Hill, New York, 1970.
- [Tumialan et al. 2000] G. Tumialan, D. Tinazzi, J. J. Myers, and A. Nanni, “Field evaluation of unreinforced masonry walls strengthened with FRP composites subjected to out-of-plane loading”, in *ASCE Structures Congress*, edited by M. Elgaaly, Philadelphia, 2000. CD version.
- [Tumialan et al. 2003] J. G. Tumialan, N. Galati, and A. Nanni, “Field assessment of unreinforced masonry walls strengthened with fiber reinforced polymer laminates”, *J. Struct. Eng.* **129**:8 (2003), 1047–1056.
- [UBC 1991] UBC, *Uniform building code*, International conference of building officials, Whittier, CA, 1991.
- [Velazquez-Dimas et al. 2000] J. I. Velazquez-Dimas, M. R. Ehsani, and H. Saadatmanesh, “Out-of-plane behavior of brick masonry walls strengthened with fiber composites”, *ACI Struct. J.* **97**:3 (2000), 377–387.
- [Vinson and Sierakowski 1986] J. R. Vinson and R. L. Sierakowski, *The behavior of structures composed of composite materials*, Martinus-Nijhoff, Dordrecht, 1986.

Received 3 Apr 2006. Accepted 23 Sep 2006.

EHAB HAMED: ehab@tx.technion.ac.il

Faculty of Civil and Environmental Engineering, Technion — Israel Institute of Technology, Technion City, Haifa 32000, Israel

ODED RABINOVITCH: cvoded@tx.technion.ac.il

Faculty of Civil and Environmental Engineering, Technion — Israel Institute of Technology, Technion City, Haifa 32000, Israel

A MARCHING PROCEDURE FOR FORM-FINDING FOR TENSEGRITY STRUCTURES

ANDREA MICHELETTI AND WILLIAM O. WILLIAMS

We give an algorithm for solving the *form-finding* problem, that is, for finding stable placements of a given tensegrity structure. The method starts with a known stable placement and alters edge lengths in a way that preserves the equilibrium equations. We then characterize the manifold to which classical tensegrity systems belong, which gives insight into the form-finding process. After describing several special cases, we show the results of a successful test of our algorithm on a large system.

1. Introduction

Tensegrity structures, popularized by Buckminster Fuller following sculptures by Kenneth Snelson, have become familiar to most structural engineers and architects through their applications, in particular, to lightweight domes and to decorative structures [Pellegrino 1992; Snelson 1996]. These structures consist of a combination of rigid bars, which carry tension or compression, and inextensible cables, which can carry no compression. Pin joints connect the elements at their ends.¹ The engineering studies of trusses by Möbius and Maxwell, as well as Cauchy's analysis of the rigidity of polygonal frames, only considered traditional pinned-bar structures [Cauchy 1813; Möbius 1837; Maxwell 1869]. Calladine and Pellegrino (in the engineering literature) and Roth et al. (in the mathematical literature) extended these results to tensegrity structures [Calladine 1978; Pellegrino and Calladine 1986; Calladine and Pellegrino 1991; Roth and Whiteley 1981]. Extensive bibliographies and more recent results appear in [Connelly and Whiteley 1996; Skelton et al. 2001; Motro 2003; Williams 2003; Tibert and Pellegrino 2003; Masic et al. 2006; So and Ye 2006].

We are interested in the *form-finding problem*: given the graph of a structure, along with the relative positions of crossing elements if the graph is not planar, find which physical placements in space will result in a stable structure. Several methods which have been used to attack the form-finding problem are outlined in [Tibert and Pellegrino 2003]. Motro [1984] employed dynamic relaxation, an algorithm first introduced in [Day 1965], which has been reliably applied to tensile structures [Barnes 1999] and many other nonlinear problems. Pellegrino [1986] formulated an equivalent constrained minimization problem, and, since 1994, Burkhardt has been making extensive use of techniques from nonlinear programming [2006]. Connelly and Back [1998] applied group representation theory to discover numerous symmetric placements. Vassart and Motro [1999] employed the force density method, which was first introduced

Keywords: tensegrity structures, stability analysis, rank-deficiency manifold, marching processes, limit placements.

The research presented in this paper was partly conducted during Micheletti's 2004 visit to the Department of Mathematical Sciences of Carnegie Mellon University. Financial support from the Center of Nonlinear Analysis is gratefully acknowledged.

¹Without essential change in the computations, one may also introduce elements called *struts*, which are unpinned bars that admit no tension. We do not consider struts, as they are of less practical interest.

in [Linkwitz and Schek 1971] for form-finding of tensile structures, according to Schek [1974]. Skelton et al. [2002] presented an algebraic approach specialized to structures with noncontiguous bars, and Paul et al. [2005] used genetic algorithms. Most recently, Zhang and Ohsaki [2005] and Estrada et al. [2006] developed new numerical methods using a force density formulation, and Zhang et al. [2006] employed a refined dynamic relaxation procedure.

The form-finding problem has no complete solution, although many authors have examined sufficient conditions. The most convenient sufficient condition, which we use here, is the second-order stress test. This test is stronger than the minimal-energy condition, but equivalent to it in most common situations. More precisely, it is not a necessary condition for stability, since there can be stable structures for which it is not satisfied, but it is a necessary and sufficient condition in order to have a structure possessing first-order positive stiffness. Since we model bars as rigid and cables as inextensible, local or global buckling instabilities must be considered separately, depending on the material properties of the elements in the structure; see [Ohsaki and Zhang 2006].

Unfortunately, the known stability conditions, including the second-order test, are descriptive rather than prescriptive. That is, they are easily applied to test a given placement of the structure, but are difficult to exploit for the discovery of exact or approximate stable placements. We propose, instead, a practical algorithm for the form-finding problem which is based on setting up a system of differential equations. This system can be solved numerically to obtain a family of stable placements. The trajectory of these solutions must start at a stable placement, so the process requires we have a beginning point which is a stable structure. However, the literature offers many examples of such placements; see, for example, [Nishimura 2000; Murakami and Nishimura 2001; Sultan et al. 2001; Micheletti 2003]. Often, their high degree of symmetry enables analytic construction.

Our method has practical relevance in all those applications in the lengths of elements are changed continuously in order to pass from one configuration to another. This includes foldable, deployable, or variable-geometry structures. Furuya [1992] and Hanaor [1993] pioneered the analysis and design of tensegrity structures with these characteristics. More recent studies include [Oppenheim and Williams 1997; Bouderbala and Motro 1998; Sultan and Skelton 1998; Tibert 2002; Aldrich et al. 2003; Defossez 2003; El Smaili et al. 2004; Fest et al. 2004; Paul et al. 2006; Schenk et al. 2007].

Here is an outline of our paper. After introducing notation and concepts in Section 2, we summarize some general results on tensegrity structures in Section 3. Most of these results are scattered throughout the mathematical and engineering literature, so a coherent summary facilitates discussion of the use and limitations of the form-finding process. We also present several example structures that illustrate the limitations of these results. In Section 4, we characterize the sets of placements to which our method applies: the rank-deficient manifolds. We briefly illustrate singular cases within the characterization. Finally, in Section 5, we describe our algorithm, and give examples of its application.

2. Structural analysis of trusses

Figure 1 shows an example of a truss (we give examples in two dimensions, to keep the diagrams simple). Trusses have a graph structure in which the edges are bars, and the nodes are the pin joints which connect the bars. The symbol A denotes the *structural matrix*, also known as the *equilibrium matrix*. The vector \mathbb{f} of externally applied forces is indexed by the nodes of the structure, and the vector τ of forces in the

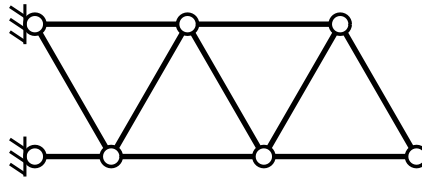


Figure 1. A simple two-dimensional truss.

edges of the structure is indexed by edge. There is a linear relationship between these two vectors:

$$\mathbb{f} = \mathbf{A}\boldsymbol{\tau}. \tag{1}$$

Dual to this is the relation between \mathbf{v} , the vector of node velocities (or, in engineering terms, infinitesimal motions), and $\boldsymbol{\delta}$, the vector of rates of change of the edge lengths:

$$\boldsymbol{\delta} = \mathbf{A}^T \mathbf{v}. \tag{2}$$

We will consider a variant of this model which is more convenient for calculations. Consider a structure in three dimensions, with n pins, located at the placement

$$\mathbb{p} := (\mathbf{p}_1, \dots, \mathbf{p}_n), \quad \mathbf{p}_r \in \mathbb{R}^3. \tag{3}$$

An edge is notated by its set of end nodes: $\{ij\}$. Let E be the set of all k edges in the structure. Next, we construct the so-called *geometric matrix* Π by specifying its column vectors, one per edge:

$$\boldsymbol{\pi}_{ij}(\mathbb{p}) = \begin{bmatrix} \mathbf{0} \\ \vdots \\ \mathbf{0} \\ \mathbf{p}_i - \mathbf{p}_j \\ \mathbf{0} \\ \vdots \\ \mathbf{0} \\ \mathbf{p}_j - \mathbf{p}_i \\ \mathbf{0} \\ \vdots \\ \mathbf{0} \end{bmatrix} \in \mathbb{R}^{3n}. \tag{4}$$

Here the entries, indexed by the list of nodes, are values in \mathbb{R}^3 . The nonzero entries in (4) are in the i -th and j -th rows, respectively. To change this matrix into the corresponding equilibrium matrix \mathbf{A} , one divides each column vector $\boldsymbol{\pi}_{ij}$ by the length of the corresponding edge.

Using this formulation, the balance of forces at each node is expressed as

$$\mathbb{f} = \Pi\boldsymbol{\omega}, \tag{5}$$

in which \mathbb{f} is the force vector of external forces applied to the nodes, and the *stress vector* $\boldsymbol{\omega}$ for the placement is a vector in \mathbb{R}^k whose ij entry is the scalar force in the edge ij divided by the length of

the edge.² Physically, one pictures an applied set of nodal forces generating stresses in the structure to support them. If the structure is redundant (has an “excess” number of edges), it may admit a self-equilibrating stress or *self stress* ω satisfying

$$\Pi\omega = \mathbf{0}. \tag{6}$$

Next, we turn to kinematics. We consider a velocity \mathbf{v} , as before. Then Π associates to \mathbf{v} a rate of change of the length of each edge in the structure, which is given by

$$\epsilon = \Pi^T \mathbf{v}, \quad \text{or} \quad \epsilon_{ij} = \boldsymbol{\pi}_{ij} \cdot \mathbf{v} = (\mathbf{p}_i - \mathbf{p}_j) \cdot (\mathbf{v}_i - \mathbf{v}_j), \tag{7}$$

in which ϵ_{ij} is the rate of change of the length of edge ij , times the length of the edge. Physically, we picture a velocity imposed on each node, which lengthens or shortens the edges.

We choose to consider only *constrained* structures, that is, structures in which several nodes are fixed to the earth. This means that these nodes only admit zero velocities. Also, we only consider cases in which enough nodes are fixed that there can be no rigid-body motions of the entire structure.³ For such a structure, a velocity which leaves all edge lengths unchanged is a flexibility in the structure. If $\mathbf{v} \neq \mathbf{0}$ and

$$\Pi^T \mathbf{v} = \mathbf{0}, \tag{8}$$

we call \mathbf{v} a flexure or a *mechanism*.

The nullspace of Π is the set of all self stresses. This space is a subspace of \mathbb{R}^k . We call its dimension s the *number of self stresses*. Likewise, we call the dimension m of the nullspace of Π^T the *number of mechanisms*.

Finally, we discuss stability. A *motion* of a structure is a time-parameterized family of placements $\mathbf{q}(t)$. The time derivative at $t = 0$, $\dot{\mathbf{q}}(0)$, is a velocity for the placement $\mathfrak{p} = \mathbf{q}(0)$. An *admissible* motion of the structure leaves edge lengths unchanged. Since our assumptions rule out rigid-body motions, any admissible motion represents a mode of collapse of the structure. The initial velocity of a collapsing motion is a mechanism, and hence one can avoid collapse by ensuring that no mechanisms occur. However, the existence of a mechanism does not imply that there is a collapsing motion.

Our nomenclature reflects the distinction between these two possibilities. A placement of the structure is said to be *stable* if admits no admissible motions away from that placement, and the structure is said to be *rigid* in that placement if it admits no mechanisms.⁴ Thus, rigidity implies stability, but the converse is false, in general. The converse may be true in specific cases: Asimow and Roth [1979] show that it holds if the present placement produces a local maximum in rank for the geometric matrix.

3. Tensegrity structures

Figure 2 shows an example of a tensegrity structure. These structures have a more restrictive definition than arbitrary trusses. First, the stress in a cable edge must be nonnegative (that is, a tension). We call a

²The literature often refers to ω_{ij} as the *force density* of the element ij .

³When a node is fixed to earth, the corresponding entry in \mathfrak{p} carries a fixed value; in computations we may choose to reduce the size of the matrix Π by omitting rows which correspond to such fixed nodes. Likewise, we may remove any “edge” which consists of two fixed nodes.

⁴Geometricians term by “rigidity” what we call stability, by “first-order rigidity” what we call rigidity. Our usage is closer to standard engineering terminology.

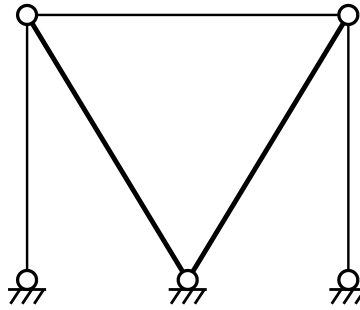


Figure 2. A two-dimensional tensegrity structure.

stress vector ω that assigns a nonnegative tension to each cable *proper*; if that tension is strictly positive for all cables, we call it *strict*. Second, we must broaden the definition of admissible motion to allow some cables to shorten, although no bar may change length and no cable may lengthen. Correspondingly, the set of admissible velocities for a tensegrity structure will include not only all mechanisms, but also all velocities v which satisfy

$$\pi_{ij} \cdot v \leq 0 \tag{9}$$

for all cables, and

$$\pi_{ij} \cdot v = 0 \tag{10}$$

for all bars.

3.1. Expanded kinematics and kinematic criteria for stability. To formulate our stability conditions, we must consider motions in more detail. It can be shown that if a motion can occur, one may assume it is real analytic [Glück 1975]. Thus, we can calculate not only its initial velocity v , but also all higher-order derivatives. We follow [Connelly and Whiteley 1996; Alexandrov 2001; Williams 2003] in the calculation of the lengths of edges caused by a motion. Such computations for bar structures date back to Koiter [1984] and Tarnai [1984], who considered the question of higher-order mechanisms. See also the development in terms of elastic energies in [Salerno 1992] and expansions similar to those below [Vassart et al. 2000].

To formulate the length measure in a convenient way, note that from (4), the edge vector π_{ij} (i.e. the column vector of Π) is a linear function of the placement vector p . (11) formalizes this relationship:

$$\pi_{ij}(p) = B_{ij}p. \tag{11}$$

It is easy to see that each operator B_{ij} is symmetric. The quantity

$$\lambda_{ij} = B_{ij}p \cdot p = \|p_i - p_j\|^2 \tag{12}$$

is the squared length of the edge ij .

We now expand a motion from p

$$q(t) = \sum_{n=0}^{\infty} t^n q_n, \tag{13}$$

with coefficients q_n and with $q_0 = \mathbb{p}$. For each edge ij , we calculate

$$\lambda_{ij}(t) = B_{ij} \left(\sum_{r=0}^{\infty} t^r q_r \right) \cdot \left(\sum_{p=0}^{\infty} t^p q_p \right) = \sum_{r,p=0}^{\infty} t^{r+p} B_{ij} q_r \cdot q_p. \tag{14}$$

Let $n = r + p$, so that $p = n - r \geq 0$ and $r \leq n$. The previous expression becomes

$$\sum_{r,p=0}^{\infty} t^{r+p} B_{ij} q_r \cdot q_p = \sum_{n=0}^{\infty} \left(\sum_{r=0}^n B_{ij} q_r \cdot q_{n-r} \right) t^n. \tag{15}$$

For $n = 0$, the first term of the sum is

$$B_{ij} q_0 \cdot q_0 = \lambda_{ij}(\mathbb{p}),$$

and we have

$$\lambda_{ij}(t) = \lambda_{ij}(\mathbb{p}) + \sum_{n=1}^{\infty} \left(\sum_{r=0}^n B_{ij} q_r \cdot q_{n-r} \right) t^n. \tag{16}$$

First, consider a bar. To be admissible, a motion must satisfy $\dot{\lambda}_{ij} = 0$, or

$$\sum_{r=0}^n B_{ij} q_r \cdot q_{n-r} = 0, \quad n = 1, 2, \dots \tag{17}$$

Since $B_{ij} q_0 = \pi_{ij}$ and B_{ij} is symmetric, we have the recurrence

$$2\pi_{ij} \cdot q_n = - \sum_{r=1}^{n-1} B_{ij} q_r \cdot q_{n-r}, \quad n = 1, 2, \dots \tag{18}$$

The first few terms of the recurrence are

$$\begin{aligned} 2\pi_{ij} \cdot q_1 &= 0, \\ 2\pi_{ij} \cdot q_2 &= -B_{ij} q_1 \cdot q_1, \\ 2\pi_{ij} \cdot q_3 &= -2 B_{ij} q_2 \cdot q_1, \\ 2\pi_{ij} \cdot q_4 &= -2 B_{ij} q_1 \cdot q_3 - B_{ij} q_2 \cdot q_2. \end{aligned} \tag{19}$$

Recall that we abbreviate $\pi_{ij}(\mathbb{p})$ as π_{ij} . The conditions could also be written in the shorter form

$$\begin{aligned} 2\pi_{ij} \cdot q_1 &= 0, \\ 2\pi_{ij} \cdot q_2 &= -\pi_{ij}(q_1) \cdot q_1, \\ &\text{etc.} \end{aligned} \tag{20}$$

Furthermore, if all edges are unchanged in length, we can write them as

$$\begin{aligned} 2\Pi^T q_1 &= 0, \\ 2\Pi^T q_2 &= -\Pi(q_1)^T \cdot q_1, \\ &\text{etc.} \end{aligned} \tag{21}$$

This formalism will be useful below.

For a cable the recurrence is similar, but may terminate after a finite number of terms. The conditions are

$$\sum_{r=0}^n B_{ij} q_r \cdot q_{n-r} \leq 0, \quad n = 1, 2, \dots, \tag{22}$$

which yields the recurrence

$$2\pi_{ij} \cdot q_n \leq - \sum_{r=1}^{n-1} B_{ij} q_r \cdot q_{n-r}, \quad n = 1, 2, \dots, \tag{23}$$

with the understanding that the recurrence terminates at the first n for which the inequality is satisfied.

Thus, the algorithm for a cable is

- (1) If $2\pi_{ij} \cdot q_1 < 0$ holds, then the motion is admissible for that component with no further testing needed.
- (2) If $2\pi_{ij} \cdot q_1 = 0$ but $2\pi_{ij} \cdot q_2 < -B_{ij} q_1 \cdot q_1$, then the motion is admissible for that component with no further testing needed.
- (3) If $2\pi_{ij} \cdot q_1 = 0$ and $2\pi_{ij} \cdot q_2 = -B_{ij} q_1 \cdot q_1$ but $2\pi_{ij} \cdot q_3 < -2 B_{ij} q_2 \cdot q_1$, then the motion is admissible for that component with no further testing needed, etc.

The simplest way to ensure stability is to rule out expansions of the sort outlined above. Note that the $n = 1$ case from each of (17) and (23) combine to require that q_1 is an admissible velocity. Moreover, if all coefficients in the expansion (13) are zero up to the p -th term, then q_p satisfies the condition to be an admissible velocity. We denote this coefficient as $v = q_p$; then it is appropriate to set $q = q_{2p}$, $\dot{q} = q_{3p}$. This gives us Criterion 1:

Criterion 1 (Kinematic Test 1). If there is no nonzero admissible velocity v for a placement, then the structure is stable in that placement.

The second-order test of Connelly and Whiteley occurs at the next step. If the first nonzero coefficient in the expansion is v and $\pi_{ij} \cdot v = 0$, then the next term q must satisfy

$$2\pi_{ij} \cdot q \leq -B_{ij} v \cdot v. \tag{24}$$

Equality is required if the edge is a bar. For a cable, if $\pi_{ij} \cdot v < 0$, then there is no second-order requirement. Formally, this gives us Criterion 2:

Criterion 2 (Kinematic Test 2). Given a placement, suppose for any admissible velocity v there is no admissible acceleration, i.e., no q such that

$$2\pi_{ij} \cdot q = -B_{ij} v \cdot v \quad \text{for each bar} \tag{25}$$

and, for each cable for which $\pi_{ij} \cdot v = 0$,

$$2\pi_{ij} \cdot q \leq -B_{ij} v \cdot v. \tag{26}$$

Then the structure is stable in that placement.

The next test is similar. If the first two nonzero coefficients are admissible, then we look at the next. This gives us Criterion 3:

Criterion 3 (Kinematic Test 3). Given a placement, suppose for any admissible velocity \mathbf{v} and acceleration \mathbf{a} , there is no \mathbf{j} such that

$$2\boldsymbol{\pi}_{ij} \cdot \mathbf{j} = -2B_{ij}\mathbf{a} \cdot \mathbf{v} \tag{27}$$

for each bar, and

$$2\boldsymbol{\pi}_{ij} \cdot \mathbf{j} \leq -2B_{ij}\mathbf{a} \cdot \mathbf{v} \tag{28}$$

for each cable for which $\boldsymbol{\pi}_{ij} \cdot \mathbf{v} = 0$ and $2\boldsymbol{\pi}_{ij} \cdot \mathbf{a} = -B_{ij}\mathbf{v} \cdot \mathbf{v}$. Then the structure is stable in that placement.

The extension to higher orders is straightforward.

Alexandrov’s more elaborate conditions [2001] for bar structures can also be extended to tensegrity structures.

3.2. Stress tests. The direct tests of the last section are not easy to implement; here we discuss simpler tests.

First, consider the simplest form of a stress test. Given a placement \mathfrak{p} , suppose that there is a mechanism \mathbf{v} , and we want to see whether there is a continued second-order term which conserves edge lengths. Equations (25) and (26) seek a solution \mathbf{a} to

$$2\Pi(\mathfrak{p})^T \mathbf{a} = -\Pi(\mathbf{v})^T \mathbf{v}. \tag{29}$$

By a standard argument in linear algebra, there is a solution if and only if the right-hand side is perpendicular to all solutions of the homogeneous equation $\Pi(\mathfrak{p})\boldsymbol{\omega} = \mathbf{0}$. Thus (29) has a solution if and only if, for all self stresses,

$$\boldsymbol{\omega} \cdot \Pi(\mathbf{v})^T \mathbf{v} = \Pi(\mathbf{v})\boldsymbol{\omega} \cdot \mathbf{v} = 0. \tag{30}$$

If for some self stress this does not hold, the expansion of the motion cannot be continued beyond the first order.

The generalization of this result to tensegrity structures depends on the following extension of the orthogonality test, which relates convex sets rather than subspaces:

Proposition 1. Given a placement and some $\boldsymbol{\epsilon} \in \mathbb{R}^k$, there exists a velocity \mathbf{w} such that, for every bar,

$$\boldsymbol{\pi}_{ij} \cdot \mathbf{w} = \epsilon_{ij}, \tag{31}$$

and for every cable,

$$\boldsymbol{\pi}_{ij} \cdot \mathbf{w} \leq \epsilon_{ij}, \tag{32}$$

if and only if, for every proper self stress $\boldsymbol{\omega}$,

$$\boldsymbol{\omega} \cdot \boldsymbol{\epsilon} \geq 0. \tag{33}$$

A proof of this can be found in [Williams 2003; Connelly and Whiteley 1996].

A useful corollary of this is the *zero-self stress condition* due to Roth and Whiteley [1981]: there is an admissible velocity which shortens a particular cable if and only if all self stresses leave that cable unstressed.

From (33), replacing ϵ_{ij} by $-B_{ij} \mathbf{v} \cdot \mathbf{v}$, we deduce a criterion for continuing an expansion past the first term \mathbf{v} . Namely, for all self stresses $\boldsymbol{\omega}$,

$$\boldsymbol{\omega} \cdot \Pi(\mathbf{v})^T \mathbf{v} = \Pi(\mathbf{v})\boldsymbol{\omega} \cdot \mathbf{v} \leq 0. \tag{34}$$

This leads to:

Criterion 4 (Second-order stress test). Given a placement, if for each admissible velocity \mathbf{v} there is a self stress $\boldsymbol{\omega}$ such that

$$\Pi(\mathbf{v})\boldsymbol{\omega} \cdot \mathbf{v} > 0, \tag{35}$$

then the structure is stable in that placement.

A cleaner form of the above computation is given if we define the so-called *stress operator*. This operator is the basis of the force density method. For a given stress vector $\boldsymbol{\omega}$, the self-equilibrium equation (6) becomes

$$\sum \omega_{ij} B_{ij} \mathbf{p} = \Omega \mathbf{p} = 0,$$

and can be regarded as a condition to be satisfied by the nodal coordinates. Due to the form of the operator B_{ij} , this condition is invariant under affine transformations of the nodal coordinates [Connelly and Whiteley 1996; Williams 2003]. We have

$$\Omega := \sum_{\text{edges}} \omega_{ij} B_{ij}, \tag{36}$$

so that

$$\Pi(\mathbf{v})\boldsymbol{\omega} \cdot \mathbf{v} = \Omega \mathbf{v} \cdot \mathbf{v}. \tag{37}$$

A simple computation then gives the following useful form for (35):

$$\Omega \mathbf{v} \cdot \mathbf{v} = \sum_{\text{edges}} \omega_{ij} (\mathbf{v}_i - \mathbf{v}_j)^2 > 0. \tag{38}$$

Calladine and Pellegrino [1991] give a physical motivation for this criterion. If the admissible velocity \mathbf{v} is regarded as an infinitesimal perturbation of \mathbf{p} , the perturbed geometric matrix is

$$\Pi(\mathbf{p} + \mathbf{v}) = [\dots \boldsymbol{\pi}_{ij}(\mathbf{p}) + \boldsymbol{\pi}_{ij}(\mathbf{v}) \dots] = \Pi(\mathbf{p}) + \Pi(\mathbf{v}). \tag{39}$$

Here, $\boldsymbol{\omega}$ is a prestress for \mathbf{p} but not necessarily one for the placement $\mathbf{p} + \mathbf{v}$. The force which would be required to maintain $\boldsymbol{\omega}$ in the new placement, that is, the so-called *geometric load vector*, would be

$$\mathbb{f} = \Pi(\mathbf{p} + \mathbf{v})\boldsymbol{\omega} = \Pi(\mathbf{v})\boldsymbol{\omega} = \sum \omega_{ij} B_{ij} \mathbf{v}. \tag{40}$$

Given that, (35) can be interpreted as

$$\mathbb{f} \cdot \mathbf{v} > 0. \tag{41}$$

This states that positive work must be done to move the structure from its original placement. In other words, the structure possesses first-order positive stiffness.

If the second-order stress test is not satisfied, we can pass to higher-order tests. The next few are (see [Williams 2003])

$$\begin{aligned}
 & \sum \omega_{ij} B_{ij} q_1 \cdot q_2 > 0, \\
 2 \sum \omega_{ij} B_{ij} q_1 \cdot q_3 + \sum \omega_{ij} B_{ij} q_2 \cdot q_2 > 0, \\
 & \sum \omega_{ij} B_{ij} q_1 \cdot q_4 + \sum \omega_{ij} B_{ij} q_2 \cdot q_3 > 0.
 \end{aligned}
 \tag{42}$$

A final result, due to Roth and Whiteley [1981], is proved by different methods (see [Williams 2003], for instance). It says that when $\Pi(p)$ satisfies the condition of maximal independence of column vectors, that is, when the evaluation at p produces a local maximum for the span of each subset of its column vectors (in their terms, when p is a *general placement*), the placement is stable if and only if it admits no admissible velocity. The argument is that under these conditions an admissible velocity always can be extended to a motion. We may refer to this as the **maximal-independence test**. Note, in particular, that the criterion is satisfied when the set of all column vectors is linearly independent.

3.3. Example. An instructive example is shown in Figure 3. In placement (a), if all edges are bars, the

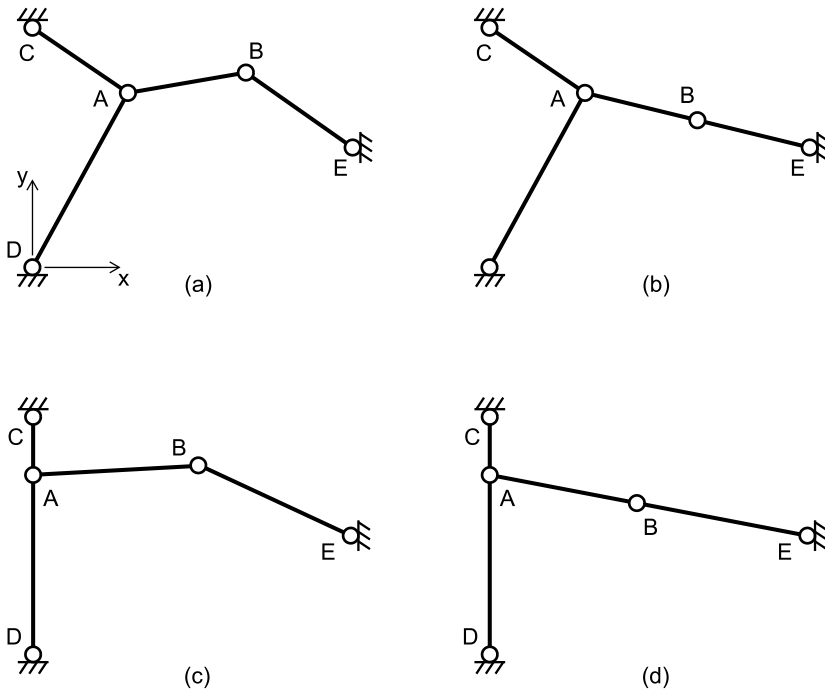


Figure 3. A four-edge example.

placement is stable and unstressed. To verify this, note that the geometric matrix is square:

$$\Pi(\mathbf{q}) = \begin{bmatrix} AC & AD & AB & BE \\ \mathbf{q}_A - \mathbf{q}_C & \mathbf{q}_A - \mathbf{q}_D & \mathbf{q}_A - \mathbf{q}_B & \mathbf{0} \\ \mathbf{0} & \mathbf{0} & \mathbf{q}_B - \mathbf{q}_A & \mathbf{q}_B - \mathbf{q}_E \end{bmatrix} \begin{matrix} A \\ B \end{matrix} \quad (43)$$

and, with the placement as illustrated, it is clear that the column vectors must be linearly independent, so the matrix is of full rank and admits neither self stress nor mechanism.

But, in the position shown, or any other in which no edges are collinear, if any of the edges is a cable, the structure is unstable. Physically, this is obvious; analytically, we note that since the placement admits no self stress, by the zero-self stress condition there is an admissible velocity which shortens the cable, and since the edge vectors are linearly independent, the maximal-independence test ensures that the structure is unstable.

If we adjust vertex B as in (b), rendering the edges AB and BE collinear, then the rank of the geometric matrix drops to three, so that both a self stress and a mechanism exist. The mechanism assigns velocity zero to node A , and a nonzero velocity, normal to the $AB - BE$ line, to node B . It is easy to see that all components of the self stress are of the same sign; we may choose them positive in order to use (35) to deduce stability. Any or all of the elements may be converted to cables and stability still is ensured.

Repositioning A as in placement (c), making AC and AD vertical and hence collinear, a different situation obtains, with only AC and AD stressable, regardless of the position of B . In this case there is a mechanism, moving both free nodes, but the stability analysis above still holds with AC and AD that can be converted to cables.

A final variation is placement (d), with AC and AD vertical and AB and BE collinear. In this placement, again we can stress only AC and AD . If AB and BE are bars, then the only mechanism affects only B , with motion of A occurring at the second order (zero velocity, nonzero acceleration). The interesting computation is that (38) now reveals the second-order stress test to fail. If we calculate the acceleration $\mathbf{0}$ as in (24) (with equality), it is easy to use the next test (42) to discover the stability of this placement. On the other hand, if either AB or BE is a cable, then there is another admissible velocity, which is not a mechanism: A can begin to move horizontally while the cable shortens. Again, one can calculate that the placement is stable in this case.

As noted earlier, the second-order test is not a necessary condition for stability, as shown for placement (d), while it is necessary and sufficient for placements possessing first-order positive stiffness, like those in (b) and (c).

4. Sets of stable placements and the rank-deficiency manifold

We have seen that simple rules based only on the topology of a structure cannot generate a generic placement that ensures the stability of a tensegrity structure. This suggests that geometric information is also needed in order to solve the form-finding problem. In this section we consider the structure of some collections of placements, emphasizing the differences between bar structures and tensegrity structures. The characterizations are incomplete, but can serve for prescribing evolution of structures between stable placements. In particular, we focus on the rank-deficient manifold of classical tensegrity structures and

describe differential equations which hold for paths on the manifold. Section 5 then describes a numerical algorithm for solving these equations.

4.1. Case 1: $\Pi(\mathfrak{p})$ has maximal rank. First, consider placements in which the $k \times 3n$ geometric matrix is over-square (i.e., $k > 2n$ for two-dimensional structures, and $k > 3n$ for three-dimensional structures) and the rank is maximal. There are self stresses, but there can be no mechanisms. In this case the structure always is stable if it is a bar structure, but if it includes cables it may be unstable. For example, consider the solid-line structure in Figure 3 (a) with an edge AE added, and suppose one of AB or BE a cable. However, if the placement admits a strict proper self stress then the structure is guaranteed to be rigid and hence is stable.

The set of maximal-rank placements is open, since it is the nonzero set of a determinant. Within this set, the set with strict proper self stresses is open.

Next, suppose that $k \leq 3n$ (in the three-dimensional case, or $k \leq 2n$ in the two-dimensional case), and the matrix is of rank k . For a bar structure, there are two cases. If $k = 3n$, then there is no mechanism, and hence the structure is stable. If $k < 3n$ there is a mechanism and because the matrix is maximum rank this means the placement is unstable. For a tensegrity structure, in either case, the absence of a self stress ensures that there is an admissible velocity. Since the rank is maximum it follows that the placement is unstable.

4.2. Case 2: $\Pi(\mathfrak{p})$ has less than maximal rank. The rank-deficiency manifold. This is the more subtle and interesting case. Recall that m denotes the number of mechanisms and s the number of self stresses, so that

$$k - s = 3n - m. \tag{44}$$

For a given structure, consider placements in which the rank of Π is r . It is easy to see that the collection of all these placements form a smooth manifold in \mathbb{R}^{3n} . (As we verify below, it can happen that the manifold intersects itself.) However, it is a little more difficult to show that at each point on the manifold, the tangent plane consists of the vectors normal to

$$\mathfrak{n} := \sum \omega_{ij} B_{ij} \mathfrak{v} = \Pi(\mathfrak{v}) \boldsymbol{\omega} = \Omega \mathfrak{v}, \tag{45}$$

for all choices of self stress $\boldsymbol{\omega}$ and mechanisms \mathfrak{v} at the point (see [Williams 2003]). The set of all the normal vectors⁵ (45) span a subspace which we will denote as \mathbb{N} .

We consider a placement on the manifold at which the second-order stress test holds. There are three subspaces of interest of \mathbb{R}^{3n} :

- $\mathbb{V} = \text{Nullspace}(\Pi(\mathfrak{p})^T)$, the subspace of mechanisms;
- $\mathbb{N} = \Omega(\mathfrak{p})\mathbb{V}$, the subspace of normal vectors;
- $\mathbb{P} := \text{Range}(\Pi(\mathfrak{p})) = \text{span}\{\boldsymbol{\pi}_{ij}(\mathfrak{p})\}$.

Since the second-order test ensures that $\Omega \mathfrak{v} \cdot \mathfrak{v} \neq 0$ for all $\mathfrak{v} \in \mathbb{V}$, it follows that the nullspace of Ω does not intersect \mathbb{V} . Thus,

$$\dim(\mathbb{N}) = \dim(\mathbb{V}) = 3n - \dim(\mathbb{P}). \tag{46}$$

⁵Notice that this is the geometric load vector of (40).

However, the test also implies that \mathbb{N} and \mathbb{P} share only the zero vector. Otherwise, if $\mathfrak{n} = \Omega \mathfrak{v}$ were in both, we would need $\mathfrak{v} \cdot \Omega \mathfrak{v} = 0$. Hence \mathbb{N} and \mathbb{P} are complementary subspaces, although in general not orthogonal. It follows that the orthogonal projection of \mathbb{P} onto the tangent space of the manifold along \mathbb{N} is the entire tangent space.

Next, note that (11) and (12) imply that $2\boldsymbol{\pi}_{ij}$ is the gradient vector of λ_{ij} . Our argument shows that when these edge vectors are projected onto the tangent space, they span that space. By assumption, they are linearly dependent; we may extract a linearly independent subset which will form a basis for the tangent space. This means that the corresponding edge lengths form a local coordinate system on the manifold. We will use this observation to prescribe paths traversing the manifold.

4.3. An example of self-intersection. Consider the structure in Figure 3. For a simple computation we set

$$\mathfrak{p}_D = (0, 0), \quad \mathfrak{p}_C = (0, 2), \quad \mathfrak{p}_E = (3, 1), \quad \mathfrak{p}_A = (x_A, y_A), \quad \mathfrak{p}_B = (x_B, y_B). \quad (47)$$

The matrix Π is square, so that the rank-deficient placements are found from $\det \Pi = 0$. The latter may be written explicitly as

$$x_A (x_B + x_A y_B - x_A - x_B y_A - 3y_B + 3y_A) = 0. \quad (48)$$

Thus $x_A = 0$ describes one manifold segment, which may be parameterized by y_A, x_B, y_B . Another manifold segment is

$$y_B = (x_B y_A - x_B + x_A - 3y_A)/(x_A - 3), \quad (49)$$

which can be parameterized by x_A, y_A, x_B . These two three-dimensional manifolds (in \mathbb{R}^4) meet in a two-dimensional manifold and clearly are not parallel at the intersection. The placement at this intersection is that shown in Figure 3 (d); it can be parameterized by y_A and x_B .

At points on the two-dimensional intersection manifold, the normal vector calculation (45) yields only null vectors, but nonetheless it is possible to traverse through the point on one of the branches of the manifold since the normals continue smoothly on either side of the intersection.

4.4. Paths traversing the manifold. The only case which is simple to treat is that of one mode of self stress (that is, $s=1$), so we consider only that case. We continue to assume that we have a placement \mathfrak{p} at which the second-order stress test is satisfied. Starting from this placement on the manifold, by the continuity of the nullspaces, there is a neighborhood on the manifold where the second-order test is satisfied and $s = 1$. Hence, the placements are stable. We consider how to construct paths on the manifold which stay within this neighborhood.

The first condition will ensure that the path $\mathfrak{q}(t)$ is on the manifold. We require that, for each normal vector \mathfrak{n} at the placement $\mathfrak{q}(t)$,

$$\dot{\mathfrak{q}} \cdot \mathfrak{n} = 0. \quad (50)$$

Recall that $\dot{\mathfrak{q}}$ denotes the nodal velocities when we are moving from one placement to another, and \mathfrak{v} denotes a mechanism in a given placement. The rate of change in each edge length as we move is

$$\boldsymbol{\pi}_{ij}(\mathfrak{q}(t)) \cdot \dot{\mathfrak{q}} = \epsilon_{ij}. \quad (51)$$

Since a selection of the edge lengths serves as a coordinate system, we may vary those at will by choosing the appropriate ϵ_{ij} in (51). Then, adding condition (50) we obtain a system of $3n = \dim(\mathbb{P}) +$

$\dim(\mathbb{N})$ differential equations for $q(t)$, whose solution allows us to compute the other edge lengths using (12). In the next section we detail this process.

Using the stress vector at $q(t)$, we have

$$\sum \omega_{ij} \boldsymbol{\pi}_{ij}(q(t)) = 0. \tag{52}$$

Taking an inner product results in

$$\sum \omega_{ij} \boldsymbol{\pi}_{ij} \cdot \dot{q} = 0, \tag{53}$$

which means that the edge lengths obey

$$\sum \omega_{ij} \dot{\lambda}_{ij} = 2 \sum \omega_{ij} \epsilon_{ij} = 0. \tag{54}$$

This condition restricts the relative change of the edge lengths at each point along the path. Recall that $\omega_{ij} = \tau_{ij}/\ell_{ij}$ and $\epsilon_{ij} = \ell_{ij} \dot{\ell}_{ij}$, with ℓ_{ij} being the length of the edge ij . Therefore, this condition takes the form $\sum \tau_{ij} \dot{\ell}_{ij} = 0$, meaning that the internal forces spend no power on the path.

Since the self stress vector also represents the vector of incompatible lengthenings (see [Pellegrino and Calladine 1986]), that is, those which do not preserve the connectivity of the structure, (54) can be seen as the orthogonality condition between $\boldsymbol{\epsilon}$ and the incompatible lengthenings. It is identically satisfied if (50) holds.

5. The marching procedure

In this section, we describe how to create a path along the rank-deficiency manifold. As before, we restrict ourselves to the case $k \leq 3n$ and $s = 1$, and assume that we are proceeding from a placement which satisfies the second-order stress test. The path on the manifold $q(t)$ is determined as the solution of the system of differential equations (50) and (51).

5.1. The system of equations. Since the dimension of the subspace of self stresses is one, we write $\dim(\mathbb{P}) = k - 1$ equations, assigning to each of $k - 1$ edge vectors the derivative of its length. By the complementarity of \mathbb{N} and \mathbb{P} , we can complete the differential system with the normal conditions between \dot{q} and the $3n - k + 1 = \dim(\mathbb{N})$ independent normal vectors.

The simplest marching process involves changing the length of only two edges, say ab and cd . To move away from the starting placement, we change the length of ab at a designated rate ϵ_{ab} . For a generic edge $hk \neq ab, cd$, the length derivative is set equal to zero. For this process, we solve for $q(t)$ the system

$$\left\{ \begin{array}{l} \boldsymbol{\pi}_{ab} \cdot \dot{q} = \epsilon_{ab} \\ \boldsymbol{\pi}_{hk} \cdot \dot{q} = 0 \quad \forall hk \neq ab, cd \\ \boldsymbol{n} \cdot \dot{q} = 0 \quad \forall \boldsymbol{n} \in \mathbb{N} \end{array} \right\}, \tag{55}$$

and then calculate the change in length of the other chosen edge, cd .

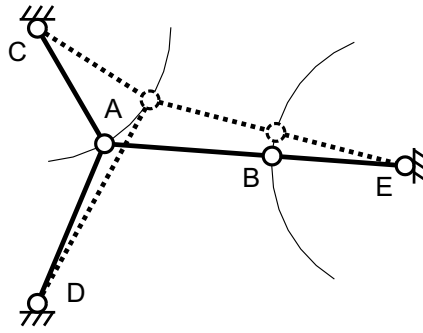


Figure 4. Moving from one placement to another.

As an example, consider the solid-line placement in Figure 4 for which we change the lengths of AB and CD , with $\epsilon_{AB} < 0$. The change of length of AD is determined by the solution to the system

$$\left\{ \begin{array}{l} \boldsymbol{\pi}_{AB} \cdot \dot{\mathbf{q}} = \epsilon_{AB} \\ \boldsymbol{\pi}_{AC} \cdot \dot{\mathbf{q}} = 0 \\ \boldsymbol{\pi}_{BE} \cdot \dot{\mathbf{q}} = 0 \\ \mathbf{n} \cdot \dot{\mathbf{q}} = 0 \end{array} \right\}. \quad (56)$$

With these settings the nodes A and B follow the thin solid-line circular trajectories; the normal condition ensures that AB and BE remain collinear and AD is lengthened accordingly, as shown by the dotted-line placement.

Often it is desirable to change the lengths of many edges at the same time, for example in order to preserve some symmetry. In such a case, we might choose two disjoint subsets $\mathcal{E}_1, \mathcal{E}_2$, of k_1, k_2 edges respectively, and assign the same changes in length, ϵ_1 and ϵ_2 respectively, to each edge in each group. In this case we have the system

$$\left\{ \begin{array}{ll} \boldsymbol{\pi}_{ij} \cdot \dot{\mathbf{q}} = \epsilon_1 & \forall ij \in \mathcal{E}_1 \\ \boldsymbol{\pi}_{hk} \cdot \dot{\mathbf{q}} = 0 & \forall hk \in \mathcal{E} \setminus \{\mathcal{E}_1 \cup \mathcal{E}_2\} \\ (\boldsymbol{\pi}_{fg} - \boldsymbol{\pi}_{lm}) \cdot \dot{\mathbf{q}} = 0 & \forall fg, lm \in \mathcal{E}_2 \\ \mathbf{n} \cdot \dot{\mathbf{q}} = 0 & \forall \mathbf{n} \in \mathbb{N} \end{array} \right\}. \quad (57)$$

The unknown change in length ϵ_2 is then obtained from the solution of this system.

Analogously, for general cases, we can choose different length derivatives, within each subset \mathcal{E}_1 and \mathcal{E}_2 , setting those in \mathcal{E}_1 directly, and those in \mathcal{E}_2 to be proportional to an assigned vector $\boldsymbol{\epsilon}_2 = \alpha \bar{\boldsymbol{\epsilon}}$. Thus we write for these edges the $k_2 - 1$ independent equations of the form

$$(\boldsymbol{\pi}_{fg} - \frac{\bar{\boldsymbol{\epsilon}}_{fg}}{\bar{\boldsymbol{\epsilon}}_{lm}} \boldsymbol{\pi}_{lm}) \cdot \dot{\mathbf{q}} = 0. \quad (58)$$

As before, the unknown parameter α is obtained from the solution of the differential system.

5.2. Limiting placements. Next, we consider possible difficulties which arise when one deals with the differential system (55), choosing to vary only two lengths. In the previous example in Figure 4 it

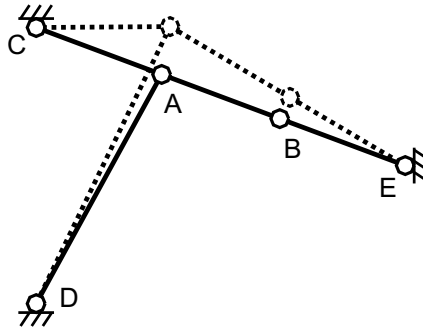


Figure 5. Moving from a limit placement.

is not possible to shorten AB indefinitely, because its length can reach a minimum value. This value corresponds to the *limit placement* represented by the solid-line in Figure 5, where the three edges AC , AB and BE are collinear. It is easy to see that this limit placement occurs at a smooth point of the rank-3 manifold, so this does not represent a break in the manifold.

Moreover, starting from the limit placement and lengthening the edge AB , there exist two possible paths on the manifold, advancing toward either the dotted-line placement in Figure 4 or that in Figure 5.

The important fact is that the edge AD is unstressed in the limiting placement. Calling the subsystem composed of all stressed edges a *minimal subsystem*, we discover that we cannot arbitrarily assign the lengthenings of all edges belonging to such a subsystem. Indeed, from (53) or (54), we have

$$0 = \omega_{AD} \boldsymbol{\pi}_{AD} \cdot \dot{\mathbf{q}} + \omega_{AB} \boldsymbol{\pi}_{AB} \cdot \dot{\mathbf{q}} = \omega_{AD} \epsilon_{AD} + \omega_{AB} \epsilon_{AB}, \tag{59}$$

since the edges AC and BE do not change in length. This relation shows that, since in the limit placement $\omega_{AD} = 0$ and $\omega_{AB} \neq 0$, the lengthening of AB must be zero. This example illustrates the role that stresses play while moving along the rank-deficiency manifold. When the edges that change their lengths have stresses of the same sign, one edge shortens and the other lengthens (see Figure 4); when the stresses are of opposite sign, they both lengthen or shorten (see Figure 5).

As a second example, consider the structure in Figure 6. We assign a positive lengthening to AD and zero lengthening to AB and BE , while the lengthening of AC is to be determined. The normal condition requires that AC and AD remain aligned. Following these rules we arrive at the dotted-line limit placement: AD cannot be further lengthened since AB and BE are aligned. In this case, both ω_{AB} and ω_{BE} are zero throughout the process.

This is a different type of limit placement in that, as noted earlier, it belongs to the intersection of two rank-deficiency manifolds. The tangent space is undefined on this intersection and the computation of the normal vector gives a null vector as a result. Progress from this placement requires a commitment to one branch or the other of the manifold, and the corresponding normals must be selected as the limit of those from adjacent placements.

5.3. Implementation in MATLAB. The MATLAB programming package has been employed for numerical computations, for both the stability analysis and the marching process.

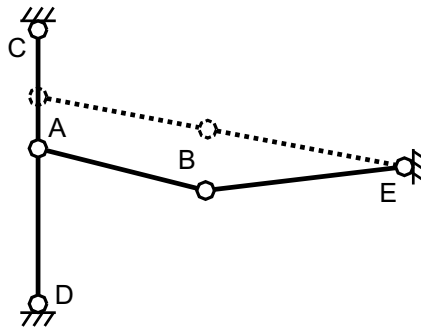


Figure 6. Another limit placement.

Figure 7 shows the flowchart that summarizes our analysis on a given system. Here is the sequence of steps:

- In Step 1, the collection of nodes and edges is assigned, and some of the nodes are constrained to fixed locations. Here n represents the number of free nodes. The vector \mathfrak{p} contains all (free and fixed) nodal coordinates, so that any vector representing velocities or higher order derivatives contains zeros as fixed entries.
- In Step 2, we construct the matrix $\Pi(\cdot)$ as a function that can be evaluated at any nodal placement.
- In Step 3, the rank of the geometric matrix $\Pi(\mathfrak{p})$ is computed; this gives also the dimensions s and m of the nullspaces of self stresses and mechanisms.
- With this information we can pass through tests from step 4 to step 7 to identify the system type. For a full-rank geometric matrix (tests 4–6), we have three cases:
 - For a square matrix, the system is stable if and only if there are no cables;
 - For $s > 0$, the system is stable if and only if there is a positive self stress in all cables;
 - For $m > 0$ the system is unstable.

The last test checks for a submaximal rank with $s = 1$; this is to exclude more complicated situations, whose methodology of analysis will be outlined in a later paper.

- In Step 8, we compute the quantity $\Omega \mathfrak{v} \cdot \mathfrak{v}$ from the self stress and the mechanisms of the system.
- In Step 9, we perform the second-order test to be ready for the marching process. To this end, it is sufficient to test the positivity of a reduced matrix $\hat{\Omega}$ whose (h, k) entry is the scalar product of the h -th independent normal vector with the k -th independent mechanism.
- If the test fails, then we perform Step 10: If $\hat{\Omega}$ is positive semidefinite we need a higher-order analysis. Otherwise the system is definitely unstable.
- We now can choose the two subsets of edges \mathcal{E}_1 and \mathcal{E}_2 in Step 11 and assign their lengthenings (Step 12).
- In step 13, we check that the chosen set of prescribed lengthenings $\mathcal{E} \setminus \mathcal{E}_2$ is not a minimal subsystem, otherwise we need to modify our choice in step 11.

- Finally, in step 14, we solve the system of differential equations. Recall that the stability of the placements on the resulting path is ensured only in a neighborhood of the starting placement, hence, it is ensured only for sufficiently small changes of the length of the elements.

The MATLAB built-in function `ode45` can be used to solve the differential system numerically. This function employs the Runge–Kutta method and solves systems of the form

$$\mathbf{M}(\mathbf{q}, t)\dot{\mathbf{q}} = \mathbf{f}(\mathbf{q}, t),$$

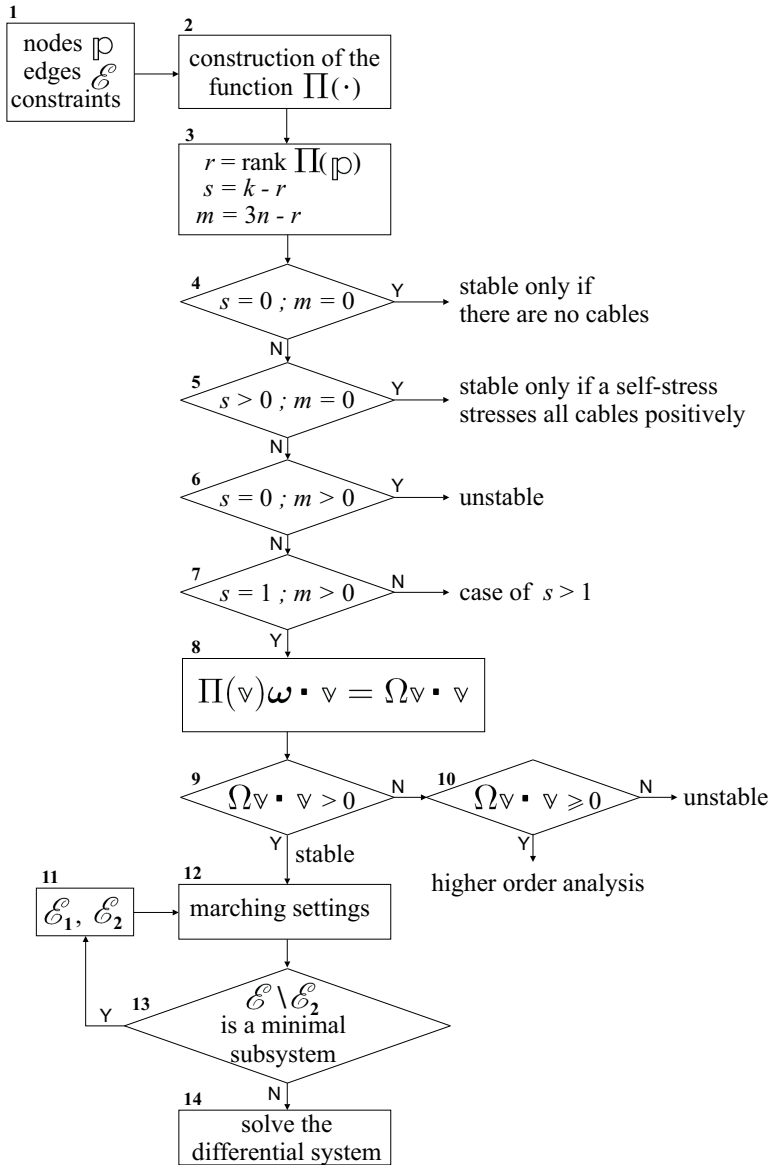


Figure 7. Flowchart for the algorithm.

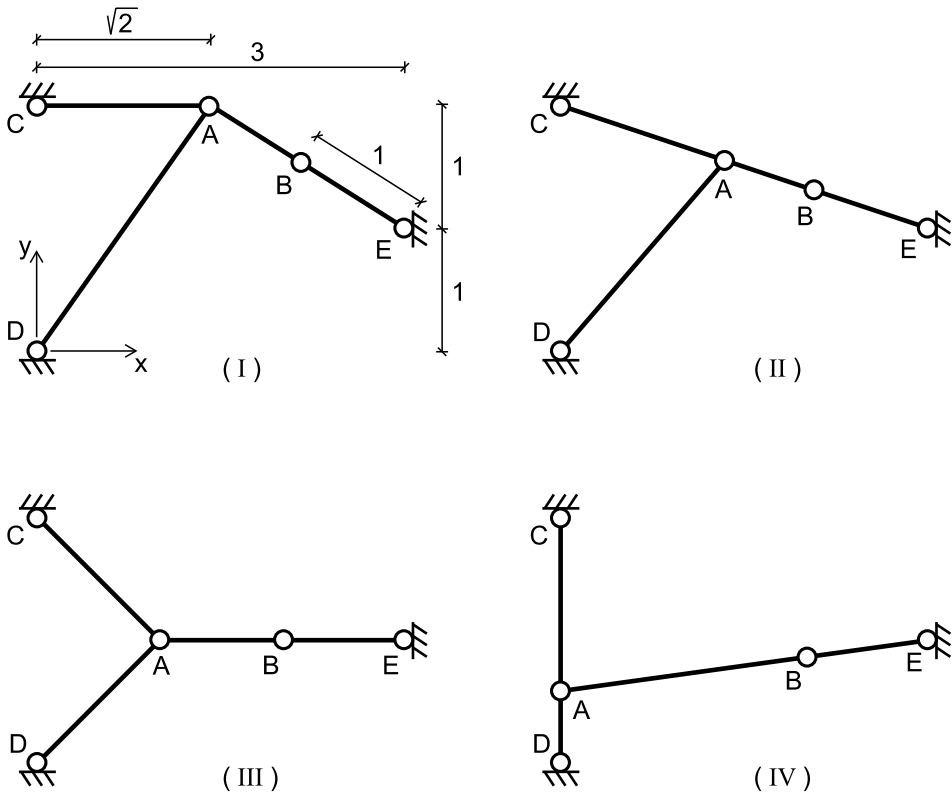


Figure 8. Sample calculations.

in which \mathbf{M} is the so-called mass matrix and \mathbf{f} is the vector of known terms. According to (57) and (58), here the rows of \mathbf{M} are the edge vectors, the linear combinations of them and the normal vectors; the entries of \mathbf{f} are the corresponding lengthenings and zeros.

In step 3 and during step 14, the rank of the geometric matrix and the associated nullspaces are computed using the singular value decomposition, through the MATLAB function `svd` (see [Pellegrino 1993]). This function gives the sets of singular vectors and the (positive) singular values in decreasing order. The singular values that are close to zero correspond to the corank $\min(3n, k) - r$ of the geometric matrix; the singular values then represent a measure of how close the placement is to the rank-deficiency manifold. For analytically determined rank-deficient placements, these values are of the order of 10^{-14} or lower. During the resolution of the differential system ($s = 1$) the unique value close to zero may grow but it is found that the ratio with the previous one remains at least of the order 10^{-3} . Usually this ratio grows excessively when the marching process requires the system to pass through a limit placement.

5.4. Numerical computations. We present some results for the example of Figure 3. The coordinates of constrained nodes are given as in Section 4.3; edges AC and BE have fixed length equal to $\sqrt{2}$ and 1 respectively.

Initial-final placement	Independent nonnull lengthening	Maximum error on final coordinates $\Delta x_P = x_{P,num} - x_{P,an}$	Singular values ratio
I-II	$\epsilon_{AB} < 0$	$ \Delta y_A \simeq 3 \cdot 10^{-3}$	10^{-10}
I-II	$\epsilon_{AD} < 0$	$ \Delta x_B \simeq 4 \cdot 10^{-12}$	10^{-12}
I-III	$\epsilon_{AD} < 0$	$ \Delta y_B \simeq 3 \cdot 10^{-9}$	10^{-10}
III-I	$\epsilon_{AD} > 0$	$ \Delta x_B \simeq 10^{-9}$	10^{-9}
II-III	$\epsilon_{AD} < 0$	$ \Delta x_A \simeq 2 \cdot 10^{-10}$	10^{-11}
III-II	$\epsilon_{AB} < 0$	$ \Delta y_A \simeq 3 \cdot 10^{-3}$	10^{-9}
III-II	$\epsilon_{AD} > 0$	$ \Delta x_A \simeq 4 \cdot 10^{-11}$	10^{-11}
I-IV	$\epsilon_{AD} < 0$	$ \Delta x_A \simeq 2 \cdot 10^{-3}$	10^{-8}
II-IV	$\epsilon_{AD} < 0$	$ \Delta x_A \simeq 2 \cdot 10^{-3}$	10^{-8}
III-IV	$\epsilon_{AD} < 0$	$ \Delta x_A \simeq 10^{-3}$	10^{-10}
III-IV	$\epsilon_{AB} > 0$	$ \Delta y_B \simeq 5 \cdot 10^{-3}$	10^{-7}

Table 1. Numerical results.

Figure 8 shows four different placements; we pass from one to another of these placements by changing the lengths of AD and AB . The last placement lies on the self-intersection of the manifold, while the other three belong to the part of the manifold represented by (49). In particular, in the first position (I) the edge AC is horizontal; the second position (II) correspond to the first kind of limit placement discussed in 5.1; in the third position (III) edges AB and BE are aligned horizontally. Edges AC and BE are fixed in length and their corresponding independent lengthening are zero. The last independent lengthening can be assigned to AD or AB by using the relation

$$\epsilon_{ij} \Delta t = \frac{1}{2}(\ell_{ij,fin}^2 - \ell_{ij,in}^2), \tag{60}$$

which is obtained by integrating the equation

$$\ell_{ij} \dot{\ell}_{ij} = \text{const} = \epsilon_{ij},$$

and relating the initial and final length of an element with its lengthening during an interval of time. For processes starting from (or passing through) position II, we are forced to assign the lengthening of AD , because we cannot fix all the lengthenings of the minimal subsystem $\{AC, AB, BE\}$. Recall that if we want to start a process from placement IV, we need to provide the initial normal vector.

Table 1 shows some results for different marching processes between the placements; the result are obtained by the MATLAB solver with default settings. For each process we report the maximum difference between analytically and numerically computed final nodal coordinates. We also report the order of the ratio between the last two singular values of the geometric matrix in the final placement; this ratio is of the order of 10^{-17} at the beginning of each process. If the final placement is the limit placement II (processes I-II and III-II), when the independent lengthening is that of AB , then the error on the coordinates may grow up to 10^{-3} : the limiting placement cannot be reached as accurately since the independent length reaches a minimum value. This is also the case of processes that end in the limit placement IV with

independent lengthening of AD . The last case III-IV with independent lengthening of AB gives worse results, this is due to the nonexistence of the normal vector in placement IV.

We end by showing an application of the method to a large three-dimensional structure. We applied the marching procedure to a tensegrity tower, the kind of decorative structure often realized by Snelson. Figure 9 shows an arch-shaped structure obtained from the tower by lengthening (shortening) the cables on the upper (lower) side of the arch. A simplified analytical solution for the form-finding problem of this kind of towers is given in [Micheletti 2003]. It is used to construct the starting placement. For the tower in question, the ratio between the last two singular values is of the order of 10^{-14} . The choice of the edge lengthenings ϵ_{ij} is crucial in order to avoid limiting placements; in some cases we reached the arch-shaped placement but we found this ratio to grow excessively, up to 10^{-2} , and the self stress to take values close to zero in most of the elements. For a careful choice of the process, this ratio can be of the order of 10^{-5} or lower at the final placement; the self stress results then are uniform along the arch and nonzero in each edge.

6. Discussion

We have presented a method for finding one-parameter families of stable placements for tensegrity structures, starting from a known initial stable placement. The method applies to the set of rank-deficient placements which is characterized within a general classification of tensegrity structures. This classification is obtained from an ordered collection of known results which were previously scattered through the mathematical and engineering literature.

After having discussed the case of a full-rank geometric matrix, we have given the characterization of the rank-deficiency manifold through the identification of its normal, (45). We proved that a subset of the edge lengths can be chosen as a local coordinate system on the manifold, Then we have focused on the simple case of a single state of self stress. The kinematic equations (51) relating the nodal velocities $\dot{\mathbf{q}}$ to the lengthenings ϵ_{ij} of the chosen coordinate system have been used to prescribe a path on the manifold, together with the prescription (50), that the nodal velocities must belong to its tangent space. The resulting differential system was implemented and solved using various MATLAB routines.

The characterization of the manifold is a key feature of the method. It appears to be not known in the literature while some of the existing form-finding methods might benefit of its application. A main advantage, with respect to other approaches, is that the lengths of the elements are directly controlled. This feature makes the method well suited for the rapid analysis of variable geometry structures, such as deployable or tendon controlled systems.

The method can be applied reliably to large structures, in general with multiple mechanisms ($m \geq 1$). The last $(m + 1)$ singular values of the geometric matrix serve to measure the accuracy of the placements on the manifold. The accuracy decays as a limit placement is approached.

Condition (54) gives insight into the marching process. It not only establishes the relation between the signs of stresses and lengthenings during a process but also justifies the definition of limit placement and minimal subsystem.

We have shown that the final placement is stable in a neighborhood of a starting stable placement, however in the simulations it is possible to reach stable placements which are very far from the initial

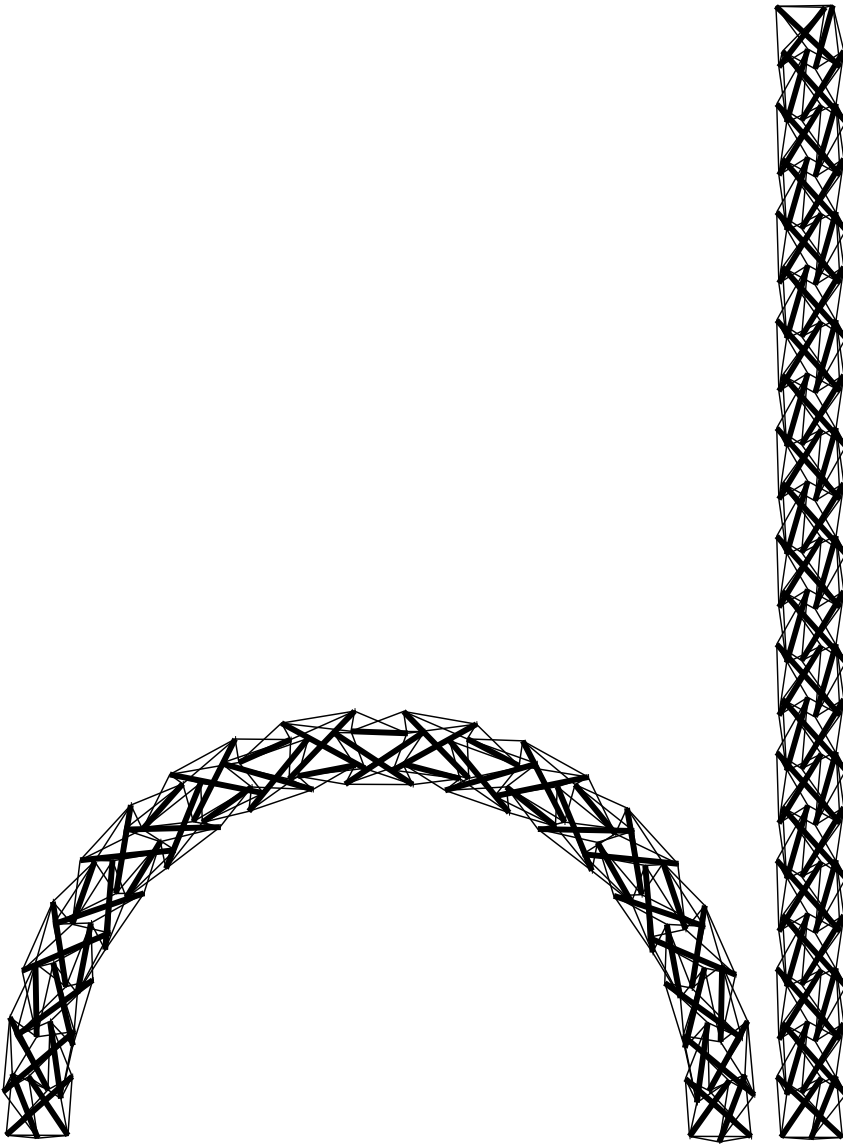


Figure 9. The algorithm was used to transform the tower into this arch.

one. For complicated cases, it can be necessary to test for stability each point of the path to avoid the occurrence of unstable portions.

We remark again that our model considers only rigid bars and inextensible cables connected by pin-joints, so that the material properties of the elements in a corresponding physical structure are not necessary for the form-finding process. On the other hand, local or global buckling instabilities, which depend on the material employed, on the magnitude of the self stress and on magnitude of the external loads, have to be considered separately. However, the stability of a physical realization of a structure satisfying

the second-order stress test can still be ensured by limiting the magnitude of the self stress and/or of the external loads. Regarding the problem of cable-slackening, it is important to avoid placements with an high ratio between the stress in bars and cables.

Concerning future improvements, some aspects are important which are not covered in this paper. A first and straightforward improvement consists in including geometry constraints. They can be easily written in the form $\mathbf{c} \cdot \dot{\mathbf{q}} = 0$, with \mathbf{c} a constant or time dependent vector characterizing the constraint. A second and more difficult task would be the extension of the method to include stress control of some edges. Lastly, a necessary step for forthcoming studies is the development of a procedure in case of multiple states of self stress. In regard to this, we remark that the characterization of the rank-deficiency manifold still holds but the details of such a procedure remain to be outlined.

7. Conclusions

Our procedure offers a simpler approach for discovering the range of feasible geometries for a given topology of a tensegrity structure, given an initial stable placement. It applies to the set of rank-deficient placements. The method is independent of the material properties of the structures. It is especially useful for the development of variable-geometry applications, since it employs the edge lengths as control parameters for movement on a continuous path of stable placements. The characterization of the rank-deficiency manifold provides more insight into the form-finding process than existing approaches. The method can be accurately applied to large structures, and it can be extended to the more complicated case of multiple states of self stress.

Acknowledgements

We thank the reviewers for several useful suggestions.

References

- [Aldrich et al. 2003] J. B. Aldrich, R. E. Skelton, and K. Kreutz-Delgado, "Control synthesis for a class of light and agile robotic tensegrity structures", pp. 5245–5251 in *Proceedings of the IEEE American Control Conference, Denver, Colorado*, 2003.
- [Alexandrov 2001] V. Alexandrov, "Implicit function theorem for systems of polynomial equations with vanishing jacobian and its application to flexible polyhedra and frameworks", *Monatsh. Math.* **132**:4 (2001), 269–288.
- [Asimow and Roth 1979] L. Asimow and B. Roth, "The rigidity of graphs, II", *J. Math. Anal. Appl.* **68**:1 (1979), 171–190.
- [Barnes 1999] M. R. Barnes, "Form finding and analysis of tension structures by dynamic relaxation", *Int. J. Space Struct.* **14**:2 (1999), 89–104.
- [Bouderbala and Motro 1998] M. Bouderbala and R. Motro, "Folding tensegrity systems", pp. 5245–5251 in *Proceedings of IUTAM/IASS Symposium on Deployable Structures: Theory and Applications, Cambridge, U.K.*, 1998.
- [Burkhardt 2006] R. W. Burkhardt, *A practical guide to tensegrity design*, Second ed., Tensegrity Solutions, Cambridge, Massachusetts, 2006.
- [Calladine 1978] C. R. Calladine, "Buckminster Fuller's 'tensegrity' structures and Clerk Maxwell's rules for the construction of stiff frames", *Int. J. Solids Struct.* **14**:2 (1978), 161–172.
- [Calladine and Pellegrino 1991] C. R. Calladine and S. Pellegrino, "First-order infinitesimal mechanisms", *Int. J. Solids Struct.* **27**:4 (1991), 505–515.

- [Cauchy 1813] A. L. Cauchy, “Sur les polygones et les polyédres”, *J. de l'École Polytechnique, XVIe Cahier* **9** (1813), 87–89.
- [Connelly and Back 1998] R. Connelly and A. Back, “Mathematics and tensegrity”, *Am. Sci.* **86**:2 (1998), 142–151.
- [Connelly and Whiteley 1996] R. Connelly and W. Whiteley, “Second-order rigidity and prestress stability for tensegrity frameworks”, *SIAM J. Discrete Math.* **9**:3 (1996), 453–491.
- [Day 1965] A. S. Day, “An introduction to dynamic relaxation”, *The Engineer* **219** (1965), 218–221.
- [Defossez 2003] M. Defossez, “Shape memory effect in tensegrity structures”, *Mech. Res. Commun.* **30**:4 (2003), 311–316.
- [El Smaili et al. 2004] A. El Smaili, R. Motro, and V. Raducanu, “New concept for deployable tensegrity systems, structural mechanics activated by shear force”, pp. 318–319 in *Proceedings of IASS04, Int. Association for Shell and Spatial Structures* (Montpellier, France), 2004.
- [Estrada et al. 2006] G. G. Estrada, H. J. Bungartz, and C. Mohrdieck, “Numerical form-finding of tensegrity structures”, *Int. J. Solids Struct.* **43**:22-23 (2006), 6855–6868.
- [Fest et al. 2004] E. Fest, K. Shea, and I. F. C. Smith, “Active tensegrity structure”, *J. Struct. Eng.* **130**:10 (2004), 1454–1465.
- [Furuya 1992] H. Furuya, “Concept of deployable tensegrity structures in space applications”, *Int. J. Space Struct.* **7**:2 (1992), 143–151.
- [Glück 1975] H. Glück, “Almost all simply connected closed surfaces are rigid”, *Lect. Notes Math.* **438** (1975), 225–239.
- [Hanaor 1993] A. Hanaor, “Double-layer tensegrity grids as deployable structures”, *Int. J. Space Struct.* **8**:1–2 (1993), 135–143.
- [Koiter 1984] W. T. Koiter, “On Tarnai’s conjecture with reference to both statically and kinematically indeterminate structures”, Technical Report 788, Laboratory for Engineering Mechanics, Delft, The Netherlands, 1984.
- [Linkwitz and Schek 1971] K. Linkwitz and H. J. Schek, “Einige Bemerkungen zur Berechnung von Vorgespannten Seilnetzkonstruktionen”, *Ing. Arch.* **40**:3 (1971), 145–158.
- [Masic et al. 2006] M. Masic, R. E. Skelton, and P. E. Gill, “Optimization of tensegrity structures”, *Int. J. Solids Struct.* **43**:16 (2006), 4687–4703.
- [Maxwell 1869] J. C. Maxwell, “On reciprocal diagrams, frames and diagrams of forces”, *T. Roy. Soc. Edin.* **26** (1869), 1–40.
- [Micheletti 2003] A. Micheletti, “The indeterminacy condition for tensegrity towers”, *Rev. Eur. de Génie Civil* **7**:3 (2003), 329–342.
- [Möbius 1837] A. F. Möbius, *Lehrbuch der statik vol. 2*, Göschen, 1837.
- [Motro 1984] R. Motro, “Forms and forces in tensegrity systems”, pp. 180–185 in *Proceedings of 3rd International Conference on Space Structures* (Amsterdam), 1984.
- [Motro 2003] R. Motro, *Tensegrity: structural systems for the future*, Kogan Page Science, London, U.K., 2003.
- [Murakami and Nishimura 2001] H. Murakami and Y. Nishimura, “Static and dynamic characterization of regular truncated icosahedral and dodecahedral tensegrity modules”, *Int. J. Solids Struct.* **38**:50–51 (2001), 9359–9381.
- [Nishimura 2000] Y. Nishimura, *Static and dynamic analyses of tensegrity structures*, Ph.D. thesis, University of California at San Diego, La Jolla, California, 2000.
- [Ohsaki and Zhang 2006] M. Ohsaki and J. Y. Zhang, “Stability conditions of prestressed pin-jointed structures”, *Int. J. Non-Linear Mech.* **41** (December 2006), 1109–1117.
- [Oppenheim and Williams 1997] I. J. Oppenheim and W. O. Williams, “Tensegrity prisms as adaptive structures”, *Adapt. Struct. Mater. Syst. ASME* **54** (1997), 113–120.
- [Paul et al. 2005] C. Paul, H. Lipson, and F. J. V. Cuevas, “Evolutionary form-finding of tensegrity structures”, in *Proceedings of the 2005 Genetic and Evolutionary Computation Conference* (Washington, D.C.), 2005.
- [Paul et al. 2006] C. Paul, F. J. V. Cuevas, and H. Lipson, “Design and control of tensegrity robots for locomotion”, *IEEE T. Robot.* **22**:5 (2006), 944–957.

- [Pellegrino 1986] S. Pellegrino, *Mechanics of kinematically indeterminate structures*, Ph.D. thesis, University of Cambridge, U.K., 1986.
- [Pellegrino 1992] S. Pellegrino, "A class of tensegrity domes", *Int. J. Space Struct.* **7** (1992), 127–142.
- [Pellegrino 1993] S. Pellegrino, "Structural computations with the singular value decomposition of the equilibrium matrix", *Int. J. Solids Struct.* **30**:21 (1993), 3025–3035.
- [Pellegrino and Calladine 1986] S. Pellegrino and C. R. Calladine, "Matrix analysis of statically and kinematically indeterminate frameworks", *Int. J. Solid Struct.* **22**:4 (1986), 409–428.
- [Roth and Whiteley 1981] B. Roth and W. Whiteley, "Tensegrity frameworks", *T. Am. Math. Soc.* **265** (1981), 419–446.
- [Salerno 1992] G. Salerno, "How to recognize the order of infinitesimal mechanisms: a numerical approach", *Int. J. Numer. Methods Eng.* **35**:7 (1992), 1351–1395.
- [Schek 1974] H. J. Schek, "The force density method for form finding and computation of general networks", *Comput. Methods Appl. Mech. Eng.* **3**:1 (1974), 115–134.
- [Schenk et al. 2007] M. Schenk, J. L. Herder, and S. D. Guest, "Zero stiffness tensegrity structures", *Int. J. Solids Struct.* (2007). In press.
- [Skelton et al. 2001] R. E. Skelton, J. W. Helton, R. Adhikari, J. P. Pinaud, and W. Chan, *The mechanical systems design handbook: modeling, measurement and control*, Chapter An introduction to the mechanics of tensegrity structures, pp. 316–386, CRC Press, London, 2001.
- [Skelton et al. 2002] R. E. Skelton, D. Williamson, and J. Han, "Equilibrium conditions of a class I tensegrity structure", *Adv. Astronaut. Sci.* **112**:2 (2002), 927–950.
- [Snelson 1996] K. D. Snelson, "Snelson on the tensegrity invention", *Int. J. Space Struct.* **11** (1996), 43–48.
- [So and Ye 2006] A. M. So and Y. Ye, "A semidefinite programming approach to tensegrity theory and realizability of graphs", pp. 766–775 in *Proceedings of the 17th Annual ACM-SIAM Symposium on Discrete Algorithms* (Miami, Florida), 2006.
- [Sultan and Skelton 1998] C. Sultan and R. E. Skelton, "Tendon control deployment of tensegrity Structures", in *Proceeding of SPIE, 5th International Symposium on Smart Structures and Materials* (San Diego), 1998.
- [Sultan et al. 2001] C. Sultan, M. Corless, and R. E. Skelton, "The prestressability problem of tensegrity structures: some analytical solutions", *Int. J. Solids Struct.* **38**:30-31 (2001), 5223–5252.
- [Tarnai 1984] T. Tarnai, "Comments on Koiter's classification of infinitesimal mechanisms", Technical report, Hung. Inst. Build. Sci., Budapest, Hungary, 1984.
- [Tibert 2002] G. Tibert, *Deployable tensegrity structures for space applications*, Ph.D. thesis, Royal Institute of Technology, Stockholm, Sweden, 2002, Available at <http://www.diva-portal.org/kth/abstract.xsql?dbid=3317>.
- [Tibert and Pellegrino 2003] A. G. Tibert and S. Pellegrino, "Review of form-finding methods for tensegrity structures", *Int. J. Space Struct.* **18**:4 (2003), 209–223.
- [Vassart and Motro 1999] N. Vassart and R. Motro, "Multiparametered formfinding method: application to tensegrity systems", *Int. J. Space Struct.* **14**:2 (1999), 147–154.
- [Vassart et al. 2000] N. Vassart, R. Laporte, and R. Motro, "Determination of mechanism's order for kinematically and statically indetermined systems", *Int. J. Solids Struct.* **37**:28 (2000), 3807–3839.
- [Williams 2003] W. O. Williams, "A primer on the mechanics of tensegrity structures", Technical report, Center for Nonlinear Analysis, Department of Mathematical Sciences, Carnegie Mellon University, Pittsburgh, Pennsylvania, 2003, Available at <http://www.math.cmu.edu/users/wow/papers/newprimer.pdf>.
- [Zhang and Ohsaki 2005] J. Y. Zhang and M. Ohsaki, "Form-finding of self-stressed structures by an extended force density method", pp. 159–166 in *Proceedings of IASS05, Int. Association for Shell and Spatial Structures* (Bucharest), 2005.
- [Zhang et al. 2006] L. Zhang, B. Maurin, and R. Motro, "Form-finding of nonregular tensegrity systems", *J. Struct. Eng.* **132**:9 (2006), 1435–1440.

Received 9 May 2006. Accepted 9 Oct 2006.

ANDREA MICHELETTI: micheletti@ing.uniroma2.it

Dipartimento di Ingegneria Civile, Università di Roma Tor Vergata, Via Politecnico 1, 00133 Rome, Italy

WILLIAM O. WILLIAMS: wow@cmu.edu

William O. Williams, Department of Mathematical Sciences, Carnegie Mellon University, Pittsburgh, PA 15213-3890, United States

<http://www.math.cmu.edu/~wow/williams>

ELEMENT STACKING METHOD FOR TOPOLOGY OPTIMIZATION WITH MATERIAL-DEPENDENT BOUNDARY AND LOADING CONDITIONS

GIL HO YOON, YONG KEUN PARK AND YOON YOUNG KIM

A new topology optimization scheme, called the element stacking method, is developed to better handle design optimization involving material-dependent boundary conditions and selection of elements of different types. If these problems are solved by existing standard approaches, complicated finite element models or topology optimization reformulation may be necessary. The key idea of the proposed method is to stack multiple elements on the same discretization pixel and select a single or no element. In this method, stacked elements on the same pixel have the same coordinates but may have independent degrees of freedom. Some test problems are considered to check the effectiveness of the proposed stacking method

1. Introduction

This investigation is concerned with solving some class of topology optimization problems for which current formulations or modeling techniques are not easy to apply. When material-dependent boundary conditions need to be considered, current multimaterial approaches [Bendsøe and Kikuchi 1988; Stegmann and Lund 2005; Bendsøe and Sigmund 2003; Sigmund 2001; Yin and Ananthasuresh 2002; Mei and Wang 2004] may be difficult to apply directly. These problems may arise when only a particular material among a group of given materials is allowed along some specific boundaries because of assembly or mechanical/thermal impedance matching requirements.

Another difficult class of problems is to select not only material property but also element types governed by different field equations. For instance, one can consider design-dependent pressure load problems. These problems were solved by several approaches [Hammer and Olhoff 2000; Sigmund and Clausen 2007; Yoon et al. 2006], but a straightforward and easy-to-implement method may be useful.

In this investigation, we aim to develop an alternative method capable of dealing with the above-mentioned problems efficiently. The key idea in the proposed method is to stack multiple elements on the same discretization pixel. The number of the stacked elements at the same discretization pixel is the same as the number of candidate materials or material types. Though the nodes of stacked elements have exactly the same spatial coordinates, the nodal degrees of freedom need not to be the same. Consequently, elements of different types having different boundary or loading conditions can be stacked. When nonlinear elements are to be stacked, the element connectivity parameterization formulation [Yoon and Kim 2005a; 2005b] can be incorporated, but no nonlinear elements were considered in this work.

Keywords: element stacking, topology optimization, material-dependent boundary conditions.

For this research, the first author was supported by the Korea Research Foundation Grant funded by the Korean Government (MOEHRD, Basic Research Promotion Fund) (KRF-2004-214-M01-2004-000-20114-0).

After presenting the detailed modeling and implementation procedure of the proposed element stacking method, several verification problems are considered.

2. Element stacking method

2.1. Underlying concept and optimization formulation. Figure 1 compares multimaterial models by standard methods such as those of Stegmann and Lund 2005 and Yin and Ananthasuresh 2002, and by the proposed element stacking method. Unlike standard approaches using a single finite element, the element stacking method selects a finite element among elements satisfying different governing equations, or having different material properties subjected to different boundary conditions. Thus, more than one element is juxtaposed on the same pixel in the element stacking method. If only material selection is concerned, the element stacking method is basically the same as the standard multimaterial method.

To select only one finite element or a void from multiple elements, an element selection scheme should be used. Formulations for standard material selection can be used for element selection [Bendsøe and Sigmund 1999; Yin and Ananthasuresh 2002; Bendsøe and Sigmund 2003; Mei and Wang 2004; Stegmann and Lund 2005]. In this work, the following formulation by Stegmann and Lund 2005 will be modified for element selection needed in the stacking method:

$$C^e = \sum_{i=1}^{N_m} \left[(\gamma_i^e)^p \prod_{j=1}^{N_m} [1 - (\gamma_{j \neq i}^e)^q] \right] \bar{C}_i. \tag{1}$$

In Equation (1), the material property of the e th element is interpolated by those of available N_m materials. The design variable is γ_i^e ($0 < \gamma_i^e \leq 1$) to indicate the selection of the i th material at the e th element (if selected, $\gamma_i^e = 1$). The symbols (p, q) denote the penalty exponents. The actual material property of the i th material, such as Young’s modulus or thermal conductivity, is denoted by \bar{C}_i , and the corresponding material property for the e th element is denoted by C^e . The symbol Π in Equation (1) denotes a multiplication operator. For instance, if two materials, \bar{C}_1 and \bar{C}_2 , are considered, the following

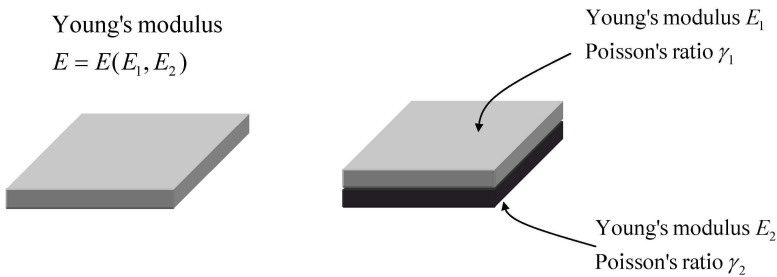


Figure 1. Left: multimaterial models by standard approaches using a single finite element. Right: the proposed element stacking method. Using the element stacking method, elements of different types and material-dependent boundary conditions can be handled. Without these conditions, the proposed method becomes identical to the standard multimaterial topology optimization.

interpolations are used:

$$C^e = \bar{C}_1(\gamma_1^e)^p(1 - (\gamma_2^e)^q) + \bar{C}_2(\gamma_2^e)^p(1 - (\gamma_1^e)^q) \quad (w_k = 1). \tag{2}$$

The interpolation formulation in Equation (1) is slightly modified so as to select the stiffness matrix \mathbf{k}^e of the e th pixel having N_m stacked finite elements, as

$$\mathbf{k}^e(\boldsymbol{\gamma}^e) = \mathbf{A}_{i=1}^{N_m} \mathbf{k}_i^e(\boldsymbol{\gamma}^e) = \mathbf{A}_{i=1}^{N_m} \phi_i^e(\boldsymbol{\gamma}^e) \bar{\mathbf{k}}_i^e = \mathbf{A}_{i=1}^{N_m} \underbrace{\left[(\gamma_i^e)^p \prod_{\substack{j=1 \\ j \neq i}}^{N_m} [1 - (\gamma_j^e)^q] \right]}_{\phi_i^e(\boldsymbol{\gamma}^e)} \bar{\mathbf{k}}_i^e, \tag{3}$$

where γ_i^e and ϕ_i^e denote the design variable and the participation factor of the i th element stiffness to the interpolated stiffness of the e th pixel, respectively. While the stiffness matrix $\mathbf{k}_i^e(\boldsymbol{\gamma}^e)$ depends on the set of design variables $\boldsymbol{\gamma}^e = \{\gamma_i^e, \gamma_i^e, \dots, \gamma_{N_m}^e\}^T$, the stiffness matrix $\bar{\mathbf{k}}_i^e(\gamma_i^e = 1, \text{ other } \gamma_{j,i \neq j}^e = 0)$ is a design variable-independent matrix. The pixel-level assembly operator of the element stiffness matrices \mathbf{k}_i^e is denoted by $\mathbf{A}_{i=1}^{N_m}$.

The main difference between formulas (1) and (3) is that the summation operator $\sum_{i=1}^{N_m}$ is replaced by the assembly operator $\mathbf{A}_{i=1}^{N_m}$. The stacked elements defined on the same pixel can have independent nodal degrees of freedom because a different boundary should be allowed to each of the stacked elements. Moreover, it is also possible to stack the differently formulated elements having same degrees of freedom. Therefore, the summation operator in (1) must be replaced by the element assembly operator in (3). In (3), two penalty parameters p and q are also used to improve solution convergence.

Notice that this element stacking method should have the identical effectiveness and numerical efficiency of the existing multimaterial design methods such as schemes presented in [Stegmann and Lund 2005] or [Yin and Ananthasuresh 2002] without the conditions presented in Figure 2. In other words, if only multiple-material problems are considered, there is no difference between the assembly operator $\mathbf{A}_{i=1}^{N_m}$ and the summation operator $\sum_{i=1}^{N_m}$. Thus, the same performance should be obtained between two methods which have the same interpolation functions.

For the case of compliance minimization, the following optimization setting is used while the interpolation formulation (3) is employed to implement the element stacking method:

$$\min_{\boldsymbol{\gamma}} F = \mathbf{u}^T \mathbf{f} \tag{4a}$$

$$\text{subject to } \mathbf{K}(\boldsymbol{\gamma})\mathbf{u} = \mathbf{f} \tag{4b}$$

$$m_i = \sum_{e=1}^{N_p} \gamma_i^e v^e \leq \bar{m}_i \quad \text{for } k = 1, \dots, N_m, \tag{4c}$$

where

$$\mathbf{K}(\boldsymbol{\gamma}) = \mathbf{A} \sum_{e=1}^{N_p} \mathbf{k}^e(\boldsymbol{\gamma}^e), \tag{4d}$$

$$\boldsymbol{\gamma} = \{\gamma^1, \gamma^2, \dots, \gamma^{N_p}\}, \quad \boldsymbol{\gamma}^e = \{\gamma_1^e, \gamma_2^e, \dots, \gamma_{N_m}^e\}, \tag{4e}$$

$$10^{-4} = \gamma_{\min} \leq \gamma_i^e \leq 1 \quad \text{for } i = 1, 2, \dots, N_m, \quad e = 1, 2, \dots, N_p. \tag{4f}$$

In Equation (4a), \mathbf{u} and \mathbf{f} are the nodal displacement vector and the nodal force vector, respectively. The global stiffness matrix is denoted by $\mathbf{K}(\boldsymbol{\gamma})$. The total number of discretizing pixels is N_p . The area or the volume of the e th pixel is denoted by v^e . Equation (4c) imposes the mass of the i th material to be bounded by \bar{m}_i . Thus, N_m mass constraints are used to constrain each of N_m materials.

To solve Equation (4) numerically, the method of moving asymptotes (MMA)¹ is employed [Svanberg 1987]. The sensitivity of the objective function $F(\boldsymbol{\gamma})$ with respect to the design variable γ_i^e can be written

$$\frac{\partial F}{\partial \gamma_k^e} = -(\mathbf{u}^e)^T \frac{\partial \mathbf{k}^e(\boldsymbol{\gamma}^e)}{\partial \gamma_k^e} \mathbf{u}^e, \tag{5}$$

where \mathbf{u}^e is the nodal displacement vector of the stacked finite elements defined on the e th pixel. The partial derivative $\partial \mathbf{k}^e(\boldsymbol{\gamma}^e)/\partial \gamma_k^e$ can be calculated explicitly from Equation (3) as

$$\begin{aligned} \frac{\partial \mathbf{k}^e(\boldsymbol{\gamma}^e)}{\partial \gamma_k^e} &= p(\gamma_k^e)^{p-1} \prod_{\substack{j=1 \\ j \neq k}}^{N_m} [1 - (\gamma_j^e)^q] \bar{\mathbf{k}}_k^e - q(\gamma_k^e)^{q-1} \mathbf{A} \sum_{\substack{i=1 \\ i \neq k}}^{N_m} \left[(\gamma_i^e)^p \prod_{\substack{j=1 \\ j \neq i, j \neq k}}^{N_m} [1 - (\gamma_j^e)^q] \right] \bar{\mathbf{k}}_i^e, \\ &= \frac{p}{\gamma_k^e} \phi_k^e(\boldsymbol{\gamma}^e) \bar{\mathbf{k}}_k^e - \frac{q(\gamma_k^e)^{q-1}}{1 - (\gamma_k^e)^q} \mathbf{A} \sum_{\substack{i=1 \\ i \neq k}}^{N_m} \phi_i^e(\boldsymbol{\gamma}^e) \bar{\mathbf{k}}_i^e. \end{aligned} \tag{6}$$

Substituting Equation (6) into (5) yields

$$\frac{\partial F}{\partial \gamma_k^e} = -\frac{p}{\gamma_k^e} (\mathbf{u}_k^e)^T \mathbf{k}_k^e(\boldsymbol{\gamma}^e) \mathbf{u}_k^e + \frac{q(\gamma_k^e)^{q-1}}{1 - (\gamma_k^e)^q} \mathbf{A} \sum_{\substack{i=1 \\ i \neq k}}^{N_m} (\mathbf{u}_i^e)^T \mathbf{k}_i^e(\boldsymbol{\gamma}^e) (\mathbf{u}_i^e), \tag{7}$$

where \mathbf{u}_k^e is the subset vector for \mathbf{k}_k^e from \mathbf{u}^e . The accuracy of the driven sensitivity is checked though the finite difference. Because the sensitivities of the constraint equations (4c) are trivial to derive, they will not be given here explicitly.

Because the problem under consideration is not a convex problem, the use of a gradient-based optimizer would yield local optima depending on different initial conditions and values of the penalty parameters. In numerical problems below, the best results are presented, not necessarily the global optima. Design variable filtering was also used. Specifically, the filtering radius is two times the element size.

2.2. Problems solved by element stacking method. Two classes of problems will be solved by the proposed element stacking method. When the element stacking method is applied to problems solved by existing methods, it can be used as an alternative and easy-to-implement method.

¹The authors thank Prof. Svanberg for providing his MMA code.

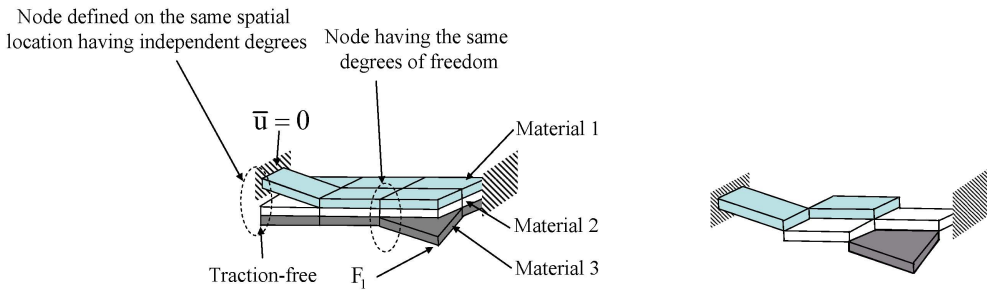


Figure 2. Element stacking modeling. Left: prescription of material-dependent boundary/loading conditions. Right: an optimized layout after topology optimization.

Class 1: Multiple materials and material-dependent boundary conditions. When material selection under material-independent boundary conditions is considered, the proposed element stacking formulation becomes virtually the same as the standard multimaterial selection formulation. Figure 2 (left) illustrates the case where material-dependent boundary conditions are prescribed, and Figure 2 (right) shows an optimal layout that may be obtained by the element stacking formulation. To deal with material-dependent conditions, the degrees of the nodes defined on the same spatial location are forced to be independent. Otherwise, they have the same degrees of freedom.

Class 2: Selection of elements of different types. An interesting application of the element stacking formulation is to select an element among a group of different elements, such as a solid elastic element and an incompressible fluid element. This may be solved as a material-selection problem, as demonstrated by Sigmund and Clausen 2007 and Yoon et al. 2006 for pressure-loaded structural design. Here, we will demonstrate that element stacking can be a simple and efficient alternative to solve the pressure-loaded structural design problem as well. For the element connectivity parameterization, the incompressible fluid is modeled by one element type (a mixed displacement-pressure element), and the solid by another (a nonconforming element). Example 4 presented in the next section deals with this problem.

3. Numerical results

In this section, four design examples are considered. Where applicable, results of the standard multimaterial approach are compared with those obtained with the stacking approach.

Example 1: Material-dependent boundary condition — compliance minimization case 1. To compare the element stacking method with the existing multimaterial design, the compliance minimization problem with simple material dependent boundary condition as shown in Figure 3 is considered. At the left-bottom and right-bottom sides, clamp boundary conditions are imposed only for the weak material and strong material, respectively. Though the problem involves material-dependent boundary conditions, one may consider using the existing multimaterial modeling technique depicted in Figure 4 (top).² Because

²The comparison of the existing multimaterial formulation with the element stacking method has been suggested by an anonymous reviewer.

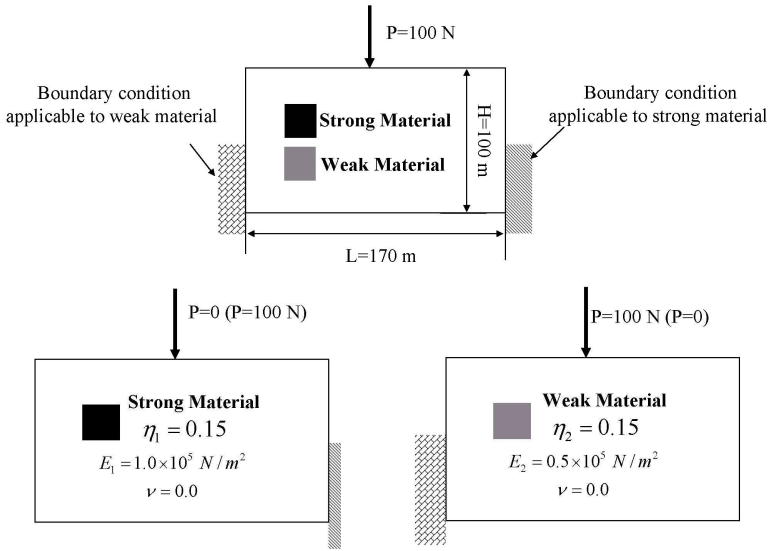


Figure 3. Compliance minimization problem involving material-dependent boundary conditions. Overall problem description (170 by 100 discretization) (top), conditions for Material 1 (strong material) (bottom left), and conditions for Material 2 (weak material) (bottom right). The permitted mass usage of Material i having Young’s modulus of E_i ($i = 1, 2$) is expressed by $\eta_i = \bar{m}_i/M$ where M is the mass of the material occupying the given design domain.

only Material 1 (strong material) is allowed to appear along the right lower side, $\gamma_2 = 0$ is used in the elements adjacent to the side. Similar modeling is used in the elements adjacent to the left lower side. When the element stacking method is used, two elements having materials 1 and 2 are juxtaposed on every pixel. Thus two layers of elements are placed on the design domain. In this modeling, only the nodes along the left and right lower sides with material-dependent boundary conditions have independent degrees of freedom. Thus, the system matrix size by the element stacking formulation is slightly larger than that of the standard multimaterial formulation. (Because the design domain is discretized by 171×101 elements, the size increases from $2 \times 171 \times 101$ to $2 \times 171 \times 101 + 2 \times 101$.)

The optimized layouts and the values of the objective function are shown in Figure 4.³ Because a gradient-based optimizer is used, optimal solutions tend to be affected by initial conditions. Therefore, presetting γ_i along the left and right lower sides in the existing multimaterial formulation tends to yield a local optimum having a poor objective function value. On the other hand, because the element stacking method does not preset γ_i along the sides, it appears easier for the local optimizer to find a better optimal solution. Although the result by the stacking method is also a local optimum (as evident from the presence of a small stiff material in the lower left part), Figure 4 indicates the advantage of using the element stacking formulation.

³To plot the results, we render the gray level of an optimized image proportional to $E_1 \times \gamma_1^e \times (1 - \gamma_2^e) + E_2 \times \gamma_2^e \times (1 - \gamma_1^e)$.

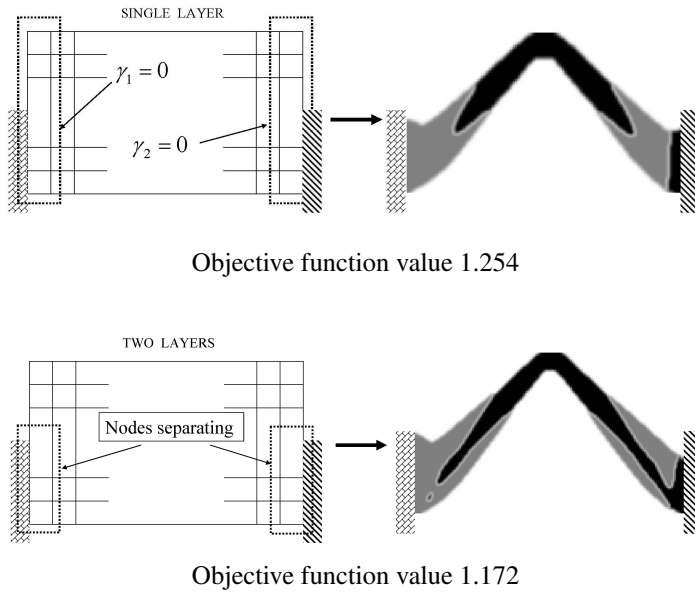


Figure 4. Top: optimization results for the problem design in Figure 3 by the standard multimaterial design method (where symbols γ_1 and γ_2 denote the design variables associated with strong and weak materials, respectively). Bottom: the element stacking method ($p = 5, q = 1$). A better result was obtained by the element stacking method.

Example 2: Material-dependent boundary condition — compliance minimization case 2. Figure 5 (top) shows another design problem involving complex material-dependent boundary conditions. The right lower boundary side constrains vertical displacement if strong material (Material 1) appears and horizontal displacement if weak material (Material 2) appears. This problem is made to demonstrate the potential use of the element stacking method because it is nearly impossible to solve by the existing multimaterial formulation. However, this problem is easy to handle with the proposed element stacking method. A similar problem having different boundary conditions is also considered in Figure 5 (bottom). Good convergence was observed in the optimal layout shown in Figure 5 (top).

Example 3: Two-material heat dissipating structure design. The topology optimization of an optimal two-material heat-dissipating structure, illustrated in Figure 6, is also considered. Though this problem has been solved by different approaches, it is interesting to demonstrate the effectiveness of the element stacking method in two-material heat dissipating structure design problems. For the optimization, both normal and side convection phenomena are taken into account.

To solve this problem, Equations (4a)–(4f) can be used as long as Equation (4b) is replaced by

$$[\mathbf{K}_T(\boldsymbol{\gamma}) + \mathbf{K}_h(\boldsymbol{\gamma})]\mathbf{u} = \mathbf{f} + \hat{\mathbf{f}}. \tag{8}$$

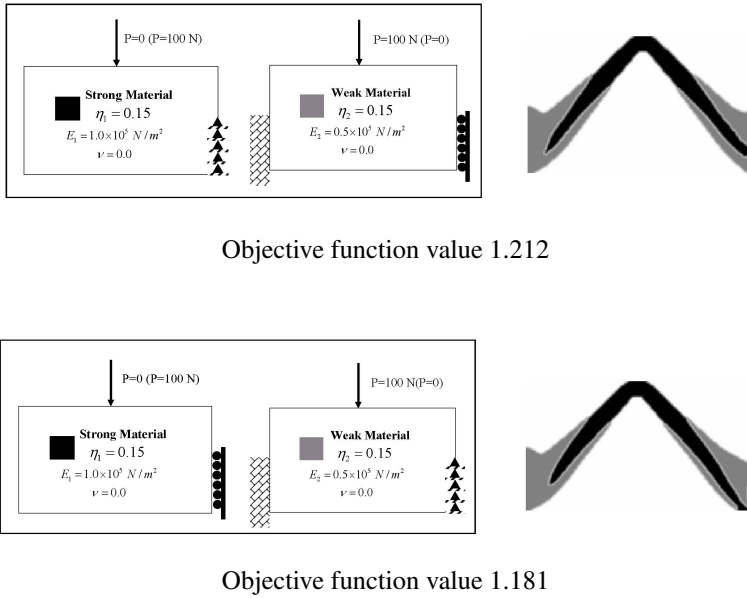


Figure 5. Compliance minimization problems involving material-dependent boundary conditions—Case 2. The boundary conditions for problems shown here in top and bottom are different. (The values of $p = 5$ and $q = 1$ were used.)

For the present problem, the symbols in Equation (4) and Equation (8) should be interpreted as

- $\mathbf{K}_T(\boldsymbol{\gamma})$: stiffness matrix of conductivity,
- $\mathbf{K}_h(\boldsymbol{\gamma}) = \mathbf{K}_{h_n}(\boldsymbol{\gamma}) + \mathbf{K}_{h_s}(\boldsymbol{\gamma})$: stiffness matrix of convection
= normal convection matrix + side convection matrix,
- $\hat{\mathbf{f}}$: nodal point heat flow input vector,
- \mathbf{f} : nodal vector due to the convection boundary condition,
- \mathbf{u} : nodal temperature vector.

Since the procedure to construct \mathbf{K}_T (all $\gamma_i = 1$), \mathbf{K}_h (all $\gamma_i = 1$), $\hat{\mathbf{f}}$ and \mathbf{f} is well known [Bathe 1996], it will not be given here. The formulation in Equation (3) is used to interpolate the element-level conductivity and convection matrices. Especially for the side convection interpolation, the amount of side convection occurring in the i th stacked element of the e th pixel is assumed to be proportional to its own participation factor $\phi_i^e(\boldsymbol{\gamma}^e)$, to facilitate sensitivity analysis; see Figure 7 (top). Figure 7 (bottom) shows a specific case. If the values of the variables are same for the stacked elements having the same material property, the net convection will vanish.

The optimized result for $k_1 = 10$, $k_2 = 1$, $h = 0.002$, $T_\infty = 0$ (room temperature), and $\hat{f} = 0.5$ is shown in Figure 8. The appearance of Material 1 near the heat input boundary physically makes sense because Material 1 has a higher conductivity.

Let us compare the optimized results for one-material optimization and the above two-material optimization. The results are compared in Figure 9. Note that the optimized result using Material 1 alone and the result using Material 2 alone are different because the ratio of the convection coefficient to the conductivity is different depending on the selected material. It is apparent that the performance of the optimized two-material structure behaves somewhere between that of Material 1 and that of Material 2.

Example 4: Design-dependent pressure-loaded problem. The design-dependent pressure-loaded problem is an interesting problem that has received some attention in the topology optimization community [Hammer and Olhoff 2000; Sigmund and Clausen 2007; Yoon et al. 2006]. Figure 10 (top) depicts the problem under consideration. The objective is to find an optimal structural layout in the design domain under pressure load. This can be solved as a material-selection problem [Sigmund and Clausen 2007; Yoon et al. 2006], but it is considered to demonstrate that the element stacking method is capable of handling different material element types. Thus, two different elements, one a mixed finite element capable of simulating incompressible fluid and the other a structural element, will be juxtaposed on the same pixel.

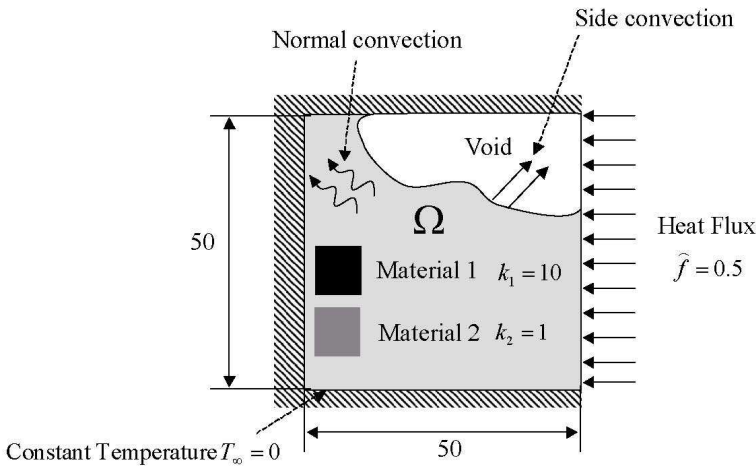


Figure 6. Problem definition for the two-material topology optimization of a heat dissipating structure. (Meshed by 50 by 50 finite elements. The materials are assumed to have different thermal conductivities k_i , but the same convection coefficient h . Heat flux input along the right side is $\hat{f} = 0.5$.)

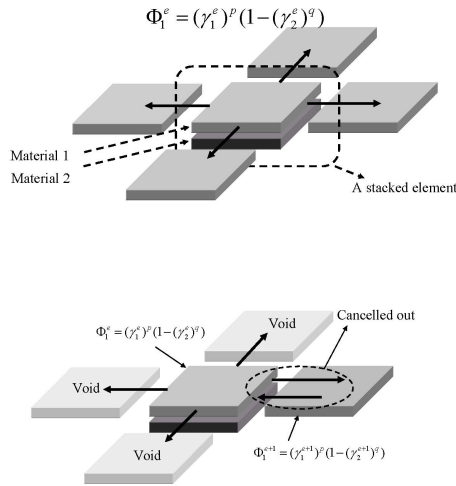


Figure 7. Side convection phenomenon modeled by the participation factor $\phi_i^e(\boldsymbol{\gamma}^e)$. Modeling concept (top), and a specific case where a stacked element in the center is interfaced with three void elements and one nonvoid element (bottom). In the bottom diagram, if γ_i^e are close to γ_i^{e+1} , the net side convection will virtually vanish.

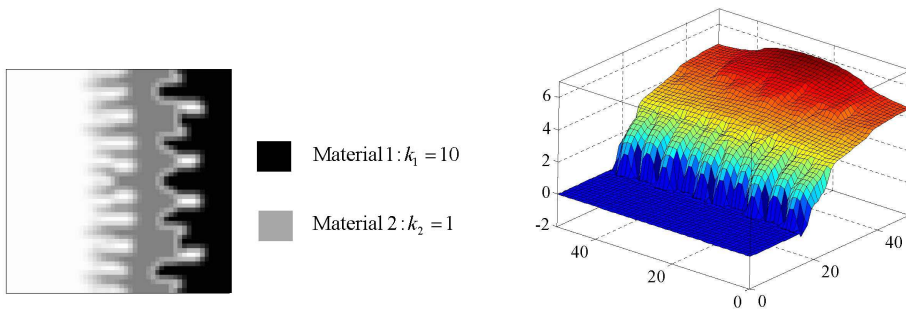


Figure 8. Optimized result for Problem 3 ($k_1 = 10$, $k_2 = 1$, $h = 0.002$, $T_\infty = 0$, $\hat{f} = 0.5$). Optimal distribution of two materials (top), and the temperature distribution of the optimized structure (bottom).

A mixed displacement-pressure element to simulate incompressible fluid ⁴ is the element used in Sigmund and Clausen 2007 and Yoon et al. 2006, which uses bilinear displacements field and constant pressure field. The shape functions in the natural coordinates are illustrated in Figure 11 (left). The structural element employed is a nonconforming element whose six shape functions are plotted in Figure 11 (right). Though other element types can be used, the stacking procedure may be best described with

⁴Any element expressing an incompressible fluid element can be used; we simply use the mixed element available from earlier works [Yoon et al. 2006].

these elements because they have different degrees of freedom. Equation (3) is also used to interpolate

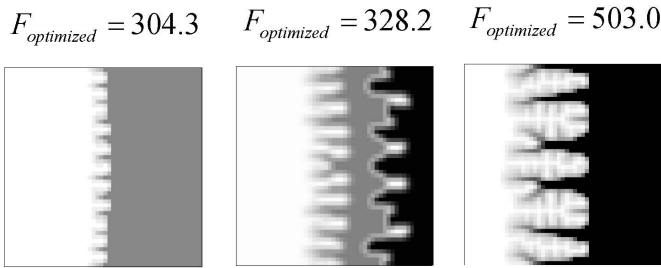


Figure 9. Comparison of the optimized results for Problem 3 using Left: only Material 1 ($k_1 = 1, \eta_1 = 50\%$); middle: both Material 1 ($k_1 = 10, \eta_1 = 25\%$) and Material 2 ($k_2 = 1, \eta_2 = 25\%$); and right: only Material 2 ($k_2 = 10, \eta_2 = 50\%$).

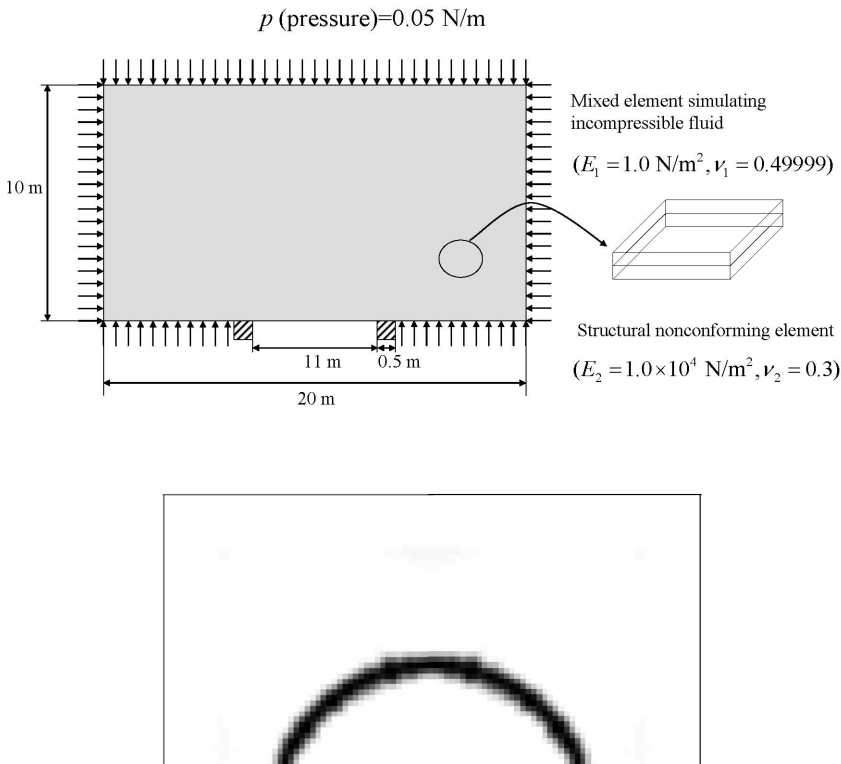


Figure 10. The pressure loaded structure design using the element stacking method. Top: problem description: discretization by 200×100 pixels, 5% structural mass constraint ratio; bottom: an optimization result.

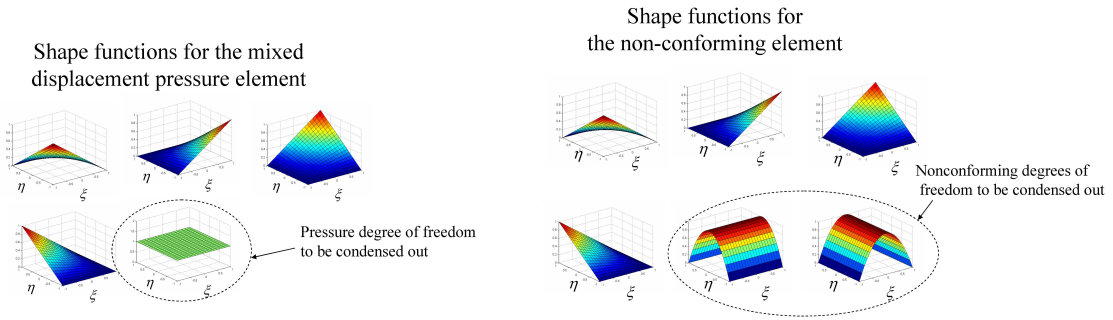


Figure 11. The employed shape functions in the local coordinators for the pressure loaded problem. Left: shape functions used for the mixed displacement-pressure element. Right: shape functions for the nonconforming element. (ξ, η : natural coordinates.)

the element stiffness matrices with the participation factor in Equation (10), as

$$k^e(\gamma^e) = \sum_{i=1}^2 \phi_i^e(\gamma^e) \bar{k}_i^e \tag{9}$$

- \bar{k}_1^e : stiffness matrix of the structural element,
- \bar{k}_2^e : stiffness matrix of the incompressible fluid element.

The participation factors $\phi_i^e(\gamma^e)$ in Equation (9) are given by

$$\phi_1^e(\gamma^e) = \frac{\gamma_1^e}{1 + (1 - \gamma_1^e)\alpha}, \quad \phi_2^e(\gamma^e) = 1 - \phi_1^e(\gamma^e), \tag{10}$$

where α is a penalization factor ($\alpha = 200$ was used in this work).

Because different degrees of freedom are used in the mixed element and the nonconforming element, the degrees of freedom not directly associated with nodes are condensed before the assembly procedure in Equation (9). Figure 10 (bottom) shows the optimized result by the element stacking method. Except for element stacking, no special numerical treatment was conducted to obtain the result. Though not explicitly shown, the result agrees well with results obtained earlier by other methods [Hammer and Olhoff 2000; Sigmund and Clausen 2007; Yoon et al. 2006].

4. Conclusions

A method to stack multiple elements on the same discretization pixel was developed to deal with topology optimization involving material-dependent boundary conditions. By making nodal degrees of freedom of the stacked elements on the same pixel independent, material-dependent boundary conditions were handled in the topology optimization setting. The usefulness of the stacking idea was demonstrated in a two-material heat dissipating structure design problem and also in a design-dependent pressure load problem. The latter problem was solved by simple stacking of an incompressible fluid element and an

elastic solid element with internal degree-of-freedom condensation. The stacking idea can be useful for topology optimization problems involving multiphase problems involving more than one physical principle.

References

- [Bathe 1996] K. J. Bathe, *Finite element procedures*, Prentice-Hall, New Jersey, 1996.
- [Bendsøe and Kikuchi 1988] M. P. Bendsøe and N. Kikuchi, “Generating optimal topologies in structural design using a homogenization method”, *Comput. Methods Appl. Mech. Eng.* **71**:2 (1988), 197–224.
- [Bendsøe and Sigmund 1999] M. P. Bendsøe and O. Sigmund, “Material interpolation schemes in topology optimization”, *Arch. Appl. Mech.* **69**:9-10 (1999), 635–654.
- [Bendsøe and Sigmund 2003] M. P. Bendsøe and O. Sigmund, *Topology optimization: theory, methods and applications*, Springer-Verlag, New York, 2003.
- [Hammer and Olhoff 2000] V. B. Hammer and N. Olhoff, “Topology optimization of continuum structures subjected to pressure loading”, *Struct. Multidiscip. O.* **19**:2 (2000), 85–92.
- [Mei and Wang 2004] Y. Mei and X. Wang, “A level set method for structural topology optimization and its applications”, *Adv. Eng. Softw.* **35**:7 (2004), 415–441.
- [Sigmund 2001] O. Sigmund, “Design of multiphysics actuators using topology optimization — part II: two-material structures”, *Comput. Methods Appl. Mech. Eng.* **190**:49-50 (2001), 6605–6627.
- [Sigmund and Clausen 2007] O. Sigmund and P. M. Clausen, “Topology optimization using a mixed formulation: an alternative way to solve pressure load problems”, *Comput. Methods Appl. Mech. Eng.* **196**:13–16 (2007), 1874–1889.
- [Stegmann and Lund 2005] J. Stegmann and E. Lund, “Discrete material optimization of general composite shell structures”, *Int. J. Numer. Methods Eng.* **62**:14 (2005), 2009–2027.
- [Svanberg 1987] K. Svanberg, “The method of moving asymptotes — a new method for structural optimization”, *Int. J. Numer. Methods Eng.* **24**:2 (1987), 359–373.
- [Yin and Ananthasuresh 2002] L. Yin and G. K. Ananthasuresh, “A novel topology design scheme for the multi-physics problems of electro-thermally actuated compliant micromechanisms”, *Sens. Actuators A Phys.* **97-98** (2002), 599–609.
- [Yoon and Kim 2005a] G. H. Yoon and Y. Y. Kim, “Element connectivity parameterization for topology optimization of geometrically nonlinear structures”, *Int. J. Solids Struct.* **42**:7 (2005), 1983–2009.
- [Yoon and Kim 2005b] G. H. Yoon and Y. Y. Kim, “The element connectivity parameterization formulation for the topology design optimization of multiphysics systems”, *Int. J. Numer. Methods Eng.* **64**:12 (2005), 1649–1677.
- [Yoon et al. 2006] G. H. Yoon, J. S. Jensen, and O. Sigmund, “Topology optimization of acoustic-structure interaction problems using a mixed finite element formulation”, *Int. J. Numer. Methods Eng.* (2006).

Received 19 May 2006. Accepted 27 Jan 2007.

GIL HO YOON: ghy@mek.dtu.dk

Department of Mechanical Engineering, Solid Mechanics, Nils Koppels Allé, Building 403, DK-2800 Kgs. Lyngby, Technical University of Denmark, Denmark

YONG KEUN PARK: ykpark@mit.edu

Department of Mechanical Engineering, Massachusetts Institute of Technology, 77 Massachusetts Avenue, Cambridge, MA 02139-4307, United States

YOON YOUNG KIM: yykim@snu.ac.kr

Multiscale Design Center and Integrated Design & Analysis of Structures Laboratory, School of Mechanical and Aerospace Engineering, Seoul National University, Kwanak-Gu San 56-1, Seoul 151-742, Korea

EXACT SOLUTIONS OF AFM SCANNING PROBES SUBJECTED TO TIP-SAMPLE FORCES

SHUEEI-MUH LIN, SEN-YUNG LEE AND KUEN-WEY LIN

In this study, an analytical method for the static deflection of an AFM nonuniform probe subjected to tip-sample forces is presented. The effects of the Lennard-Jones and electrostatic noncontact forces and a contact force on the deflection of a cantilever are investigated. The contact force is simulated by the Derjaguin–Muller–Toporov model. In general, when an atomic force microscopy is used to measure a sample's topography and properties, a jump phenomenon of a cantilever usually exists. Unfortunately, there is a lack of a complete and precise description about this jump phenomenon. This proposed analytical method is helpful to investigate precisely the jump phenomenon. Moreover, the effects of several parameters on the jump phenomenon are studied. Finally, several simple and general relations between the deflection of beam and the tip-sample distance are presented.

1. Introduction

Atomic force microscopy (AFM) force-distance curves have become a fundamental tool in several fields in research, such as surface science, material engineering, biochemistry and biology [Cappella and Dietler 1999]. Nanoscale wires are usually coated on a substrate as a semiconductor. The materials of wire and substrate are different. Therefore, the contact potential differences between the tip and a sample's surfaces are also different. Because of it, an electrostatic force exists between the tip and the sample's surface, which will result in error when measuring a sample's topography. Kelvin probe force microscopy (KPFM) is a powerful measuring technique on a nanometer scale; it uses an atomic force microscopy with an electrostatic force. It is currently used to image proteins [Rossell et al. 2003] and the contact potential difference on a large variety of samples, such as semiconductors [Shikler et al. 1999; Katano et al. 2002]. The electrostatic force in a Kelvin probe force microscopy results commonly from the tip-sample potential difference and a compensated voltage between tip and sample. Sadewasser et al. [2003; 2004] investigated the resolution of KPFM and the influence of uncompensated electrostatic force on a sample's surface height measurements. They found that the accuracy of the measured step height was strongly dependent on the compensated d.c. voltage between tip and sample.

Several authors have investigated the electrostatic force between a tip and a sample's surface. Belaidi et al. [1997] calculated the electrostatic force acting on the tip of AFM by using the model of equivalent charge distribution. They compared the equivalent charge model with several analytical models simulating the electrostatic forces. They recommended the use of two approximate models for the tip-plane interaction: the spherical model for small and large distance and the perfect cone model or uniformly

Keywords: AFM, exact solution, contact force.

The support of the National Science Council of Taiwan, R. O. C., is gratefully acknowledged (Grant number: Nsc94-2212-E168-003).

charged line for intermediate distances. Further, Belaidi et al. [1998] used the finite element method to simulate the electrostatic force between two conducting parts placed at different voltages. Law and Rieutord [2002] investigated various electrostatic models describing the relation between a polarized atomic force microscopy tip and a sample. They found that the model by Hudlet et al. [1998] provided an excellent description of the experimental data. In our study this model is used to investigate the response of an AFM beam subjected to an electrostatic force.

When the tip-sample distance is in the order of interatomic spacing, chemical bonding can occur. This bond is usually modeled by a phenomenological Lennard-Jones potential. The corresponding Lennard-Jones force is composed of a repulsive force and a van der Waals force. It is a noncontact force. If the tip penetrates a sample's surface, a contact force occurs. When the cantilever approaches the surface, the cantilever becomes unstable and jumps onto a sample's surface. It is referred to as the jump-to-contact discontinuity. When the cantilever retracts from a sample's surface, a jump phenomenon happens also. That's referred to as the jump-off-contact discontinuity. The difference in path between approach and withdrawal curves is usually called *force-displacement curve hysteresis*. Theoretically, the necessary condition of the jump phenomenon is that the tip-sample force gradient is larger than the effective elastic constant of a cantilever. Unfortunately, no complete mathematical theorem of the system has ever been derived. Obviously, a rigorous theorem is needed to investigate the jump phenomenon. Moreover, the corresponding analytical solutions can help to determine the functional relationships between operational parameters and the physical tip-sample force.

So far, due to the complexity no analytical solution for the response of a nonuniform probe subjected to the Lennard-Jones and electrostatic noncontact forces and a contact force exists. Moreover, the jump phenomenon in measurement of a general system has not been investigated yet. In this study, the exact solution of an AFM nonuniform probe subjected to noncontact and contact forces is derived. Moreover, we investigate the jump phenomenon in measurement of a general system.

2. Governing equation and boundary conditions

The static response of a nonuniform probe with elastic root, subjected to the weights of beam and the non-contact Lennard-Jones and electrostatic forces and a contact force is investigated, as shown in Figure 1. Generally, the length and thickness of an AFM beam are approximately 100 and 2 μm , respectively. The deformation is less than approximately 100 nm. Therefore, the Bernoulli–Euler theory is suitable for the AFM probe.

In this study, the following dimensionless quantities are considered:

$$b(\xi) = \frac{E(x)I(x)}{E(0)I(0)}, \quad c_{v1} = \frac{H_1 RL^3}{E(0)I(0)L_c^9}, \quad c_{v2} = \frac{H_2 RL^3}{E(0)I(0)L_c^3}, \quad c_e = \frac{\pi \varepsilon_0 (V - V_0)^2 L^3}{EIL_c},$$

$$\bar{D}_0 = \frac{D_0}{L_c}, \quad f_b = \frac{m_t g L^3}{E(0)I(0)L_c}, \quad f_c = \bar{k}_{\text{eff}} \bar{R}^{1/2} \bar{D}^{3/2} - 2\pi \bar{S}_e \bar{R}, \quad f_l = \frac{c_{v1}}{180(\bar{D}_0 - w)^8} - \frac{c_{v2}}{6(\bar{D}_0 - w)^2},$$

$$f_e = c_e \bar{F}, \quad \bar{k}_{\text{eff}} = \frac{4}{3\pi^2} \frac{L^3 L_c}{I(0)} \left[\frac{1-\nu_t^2}{E_t/E_t(0)} + \frac{1-\nu_s^2}{E_s/E_t(0)} \right]^{-1}, \quad p(\xi) = \frac{P(x)L^4}{E(0)I(0)L_c}, \quad \bar{R} = \frac{R}{L_c},$$

$$\bar{S}_e = \frac{S_e L^3 L_c}{EI}, \quad w(\xi) = \frac{W(x)}{L_c}, \quad \beta_1 = \frac{K_\theta L}{E(0)I(0)}, \quad \beta_2 = \frac{K_T L^3}{E(0)I(0)},$$

$$\gamma_{11} = \frac{\beta_1}{1+\beta_1}, \quad \gamma_{12} = \frac{1}{1+\beta_1}, \quad \gamma_{21} = \frac{\beta_2}{1+\beta_2}, \quad \gamma_{22} = \frac{1}{1+\beta_2}, \quad \xi = \frac{x}{L},$$

where A is the cross sectional area, D_0 the initial distance between the tip and the sample without deformation, E the Young’s modulus, f_b the dimensionless tip weight, f_e the dimensionless interacting force, g the gravity acceleration, I the area moment of inertia, K_T the translational spring constant at the left end, K_θ the rotational spring constants, L the length of beam, L_c the characteristic length, m_t the tip mass, P the beam weight per unit length, W the flexural displacement, x the coordinate along the beam, ρ the mass density per unit volume. Because the length of beam is more than $10 \mu\text{m}$ and the deformation of a cantilever is less than 20 nm , their scale orders are greatly different. For the dimensionless expression of deformation and avoiding the numerical transaction error, one introduces a characteristic length L_c , which is in the scale order as that of deformation, for example, $L_c = 10 \text{ nm}$.

In terms of the above dimensionless quantities, the governing differential equation of the Euler–Bernoulli beam subjected to its weight $p(\xi)$ is

$$\frac{d^2}{d\xi^2} \left[b(\xi) \frac{d^2 w}{d\xi^2} \right] = p(\xi). \tag{1}$$

The boundary conditions of an elastic root of beam at $\xi = 0$ are expressed as

$$\gamma_{12} \frac{d^2 w}{d\xi^2} - \gamma_{11} \frac{dw}{d\xi} = 0, \quad \gamma_{22} \frac{d}{d\xi} \left[b(\xi) \frac{d^2 w}{d\xi^2} \right] + \gamma_{21} w = 0. \tag{2}$$

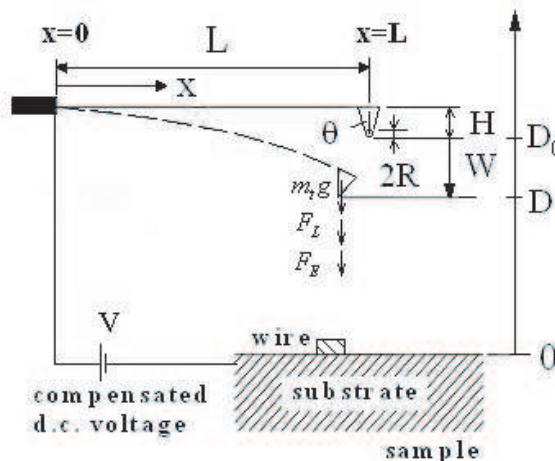


Figure 1. Geometry and coordinate system of a microprobe.

There are a number of forces acting at the tip: the tip weight, the Lennard-Jones force and the electrostatic force. However, no moment acts at the tip of a beam. Boundary conditions at $\xi = 1$ are expressed as

$$\frac{d^2w}{d\xi^2} = 0, \quad \frac{d}{d\xi} \left[b(\xi) \frac{d^2w}{d\xi^2} \right] = -f_b + f_{is}, \tag{3}$$

where f_{is} is the dimensionless tip-sample interacting force. The noncontact force between the tip and the sample by a combination of a longrange electrostatic force f_e and a shortrange (Lennard-Jones) force f_l . The contact force f_c is usually described by macroscopic continuum theories using Derjaguin–Muller–Toporov (DMT) model [Hudlet et al. 1998]. The tip-sample force is composed of the noncontact and contact forces and can be expressed as

$$f_{is} = \begin{cases} f_l + f_e, & D > D_c, \\ f_c, & D < D_c, \end{cases} \tag{4}$$

where D_c is the point of contact [Hölscher 2003]. These forces are described below.

It is well known that when the tip-sample distance is decreased to the nanometer scale, a longrange attractive force between a tip and a sample exits. When the tip-sample distance is further decreased, a shortrange repulsive force exits. These forces are usually modeled by a phenomenological Lennard-Jones force which is composed of a repulsive force and a van der Waals force. The Lennard-Jones force F_L is [Belaidi et al. 1998]

$$F_L = \frac{H_1 R}{180D^8} - \frac{H_2 R}{6D^2},$$

where the first term on the righthand side is a repulsive force and the second term is the van der Waals force, H_i the Hamaker constant, D the tip-sample distance, R the tip radius.

In addition to the van der Waals attractive force, there may be an electrostatic force due to a potential difference between the working functions of a tip and a sample. If the sample is made of only one material, it is possible to measure the sample’s topography correctly. But if nanoscale wires are coated on a substrate, the materials of the wire and the substrate are different. Therefore, the contact potential differences V_0 between the tip and wires are also different from that between the tip and the substrate. These electrostatic forces will induce different deformations of a cantilever. Neglecting the effects of these electrostatic forces will results in an error when measuring a sample’s topography. In order to get an accurate topography of the sample, one usually applies a d.c. voltage V between the tip and a sample’s surface to compensate for the contact potential difference. If $V = V_0$, one obtains accurate topography of the sample. The electrostatic force F_E can be expressed as [Law and Rieutord 2002]

$$F_E = \pi \epsilon_0 (V - V_0)^2 \bar{F}(D),$$

where the parameter $\bar{F}(D)$ depends on the geometry of a tip. In this study, we consider the model by Hudlet et al. [1998]. The parameter $\bar{F}(D)$ for a tip as a spherical apex and cone is expressed as

$$\bar{F}(D) = -K^2 \left[\ln \left(\frac{H}{D + R(1 - \sin \theta)} \right) - 1 + \frac{R \cos^2 \theta / \sin \theta}{D + R(1 - \sin \theta)} \right] - \frac{R^2(1 - \sin \theta)}{D[D + R(1 - \sin \theta)]},$$

where H is the height of tip and $K = 1/\ln(\tan(\theta/2))$.

The static tip-sample interactions are usually described by macroscopic continuum theories such as Hertzian, Johnson–Kendall–Roberts (JKR) and Derjaguin–Muller–Toporov (DMT) contact models [Hölscher 2003]. In this study, we consider the DMT model. Note that the other models can be easily solved by using the proposed method. The tip-sample interaction in the DMT model is

$$F_c = k_{\text{eff}} R^{1/2} |D|^{3/2} - 2\pi S_e R,$$

where S_e is the surface energy and $k_{\text{eff}} = 4[(1 - \nu_s^2)/E_s + (1 - \nu_t^2)/E_t]^{-1}/3\pi^2$ in which $\{\nu_s, E_s\}$ and $\{\nu_t, E_t\}$ are the Poisson ratios and Young’s modulus of sample and tip, respectively.

3. Solution method

In general, it is difficult to derive the analytical solution of a system with nonlinear boundary conditions. Nevertheless, the following method is proposed to derive its exact solution. First, one chooses a relation among the displacement w and two new variables s and v . Upon substituting the relation into the original nonlinear system, the original system will be transformed into two linear independent subsystems in terms of s and v . The solutions s and v of the two linear subsystems can be easily derived. Finally, substituting these solutions back into the relation and letting the relation in Equation (5) satisfy the tip displacement condition, one obtains the general solution. It should be noted that the tip displacement condition is an implicit function. However, one can easily determine its solution by numerical methods.

3.1. Change of variable. The relation among the displacement w and two new variables s and v is chosen as [Lee and Lin 1996]

$$w(\xi) = v(\xi) - (f_b - f_{ts})s(\xi), \tag{5}$$

where $s(\xi)$ is a shifting function, chosen to satisfy the following differential equation

$$\frac{d^2}{d\xi^2} \left[b(\xi) \frac{d^2 s}{d\xi^2} \right] = 0 \tag{6}$$

subject to boundary conditions

$$\gamma_{12} \frac{d^2 s}{d\xi^2} - \gamma_{11} \frac{ds}{d\xi} = 0, \quad \gamma_{22} \frac{d}{d\xi} \left[b(\xi) \frac{d^2 s}{d\xi^2} \right] + \gamma_{21} s = 0, \quad \text{at } \xi = 0, \tag{7}$$

$$\frac{d^2 s}{d\xi^2} = 0, \quad \frac{d}{d\xi} \left[b(\xi) \frac{d^2 s}{d\xi^2} \right] = 1, \quad \text{at } \xi = 1. \tag{8}$$

After substituting Equations (5)–(8) into Equations (1)–(4), one obtains differential equations in terms of $v(\xi, \tau)$. The transformed governing equation is

$$\frac{d^2}{d\xi^2} \left[b(\xi) \frac{d^2 v}{d\xi^2} \right] = p(\xi), \tag{9}$$

and the associated homogeneous boundary conditions are

$$\gamma_{12} \frac{d^2v}{d\xi^2} - \gamma_{11} \frac{dv}{d\xi} = 0, \quad \gamma_{22} \frac{d}{d\xi} \left[b(\xi) \frac{d^2v}{d\xi^2} \right] + \gamma_{21} v = 0, \quad \text{at } \xi = 0, \tag{10}$$

$$\frac{d^2v}{d\xi^2} = 0, \quad \frac{d}{d\xi} \left[b(\xi) \frac{d^2v}{d\xi^2} \right] = 0, \quad \text{at } \xi = 1. \tag{11}$$

The corresponding exact solutions $v(\xi)$ and $s(\xi)$ are to be derived in the following sections. Substituting these solutions into Equation (5), the general solution $w(\xi)$ is obtained. It should be noted that f_i and f_e are the function of the tip deflection $w(1)$. In other words, Equation (5) is an implicit function. However, it is very easy to determine the exact solution $w(\xi)$ of Equation (5) by numerical methods [Lin 1999].

3.2. Shifting functions. The shifting function $s(\xi)$ of Equation (6) can be written as

$$\begin{aligned} \frac{d}{d\xi} \left[b(\xi) \frac{d^2s}{d\xi^2} \right] = c_1 &\Rightarrow b \frac{d^2s}{d\xi^2} = c_1 \xi + c_2 \Rightarrow \frac{ds}{d\xi} = \int \frac{c_1 \xi + c_2}{b(\xi)} d\xi + c_3, \\ &\Rightarrow s = \iint \frac{c_1 \xi + c_2}{b(\xi)} d\xi + c_3 \xi + c_4. \end{aligned} \tag{12}$$

Substituting Equation (12) into the boundary conditions (7) and (8), one obtains the constants c_i as well as the shifting function

$$s(\xi) = \iint \frac{\xi - 1}{b(\xi)} d\xi - \frac{1}{\gamma_{11}} \left(\gamma_{12} + \gamma_{11} \int \frac{\xi - 1}{b(\xi)} d\xi \right)_{\xi=0} \xi - \frac{1}{\gamma_{21}} \left(\gamma_{22} + \gamma_{21} \iint \frac{\xi - 1}{b(\xi)} d\xi \right)_{\xi=0}.$$

If the cross section of beam is uniform, the dimensionless bending rigidity $b = 1$ and $s(\xi)$ becomes

$$s(\xi) = \frac{1}{6} \xi^3 - \frac{1}{2} \xi^2 - \frac{\gamma_{12}}{\gamma_{11}} \xi - \frac{\gamma_{22}}{\gamma_{21}}.$$

Further, if a uniform cantilever is considered, the shifting function becomes $s(\xi) = \frac{1}{6} \xi^3 - \frac{1}{2} \xi^2$, that is the same as that given by Lee and Lin [1996].

3.3. Transformed solution. The transformed solution $v(\xi)$ of Equations (9)–(11) can be written as

$$v(\xi) = V_p(\xi) + \sum_{i=1}^4 D_i V_i(\xi), \tag{13}$$

where $V_p(\xi)$ is the particular solution. D_i is the constant to be determined. $V_i(\xi)$ are the four linearly independent fundamental solutions of Equation (9), which satisfy the following normalized condition

$$\begin{bmatrix} V_1(0) & V_2(0) & V_3(0) & V_4(0) \\ V_1'(0) & V_2'(0) & V_3'(0) & V_4'(0) \\ V_1''(0) & V_2''(0) & V_3''(0) & V_4''(0) \\ V_1'''(0) & V_2'''(0) & V_3'''(0) & V_4'''(0) \end{bmatrix} = \begin{bmatrix} 1 & 0 & 0 & 0 \\ 0 & 1 & 0 & 0 \\ 0 & 0 & 1 & 0 \\ 0 & 0 & 0 & 1 \end{bmatrix}. \tag{14}$$

The particular solution V_p and the fundamental solutions V_i can be derived easily by using the method proposed by Lee and Lin [1996].

Note that the proposed method can be used to solve the static measurement problem of a probe with arbitrary cross section and made of any material. It is well known that a conventional probe has a uniform or *V*-type cross-section. In the following sections we derive the analytical solutions for these conventional probes.

4. V-typed beam

The material properties and the height of the beam are assumed to be constant, while the width of the beam varies linearly with the taper ratio λ . If the taper ratio is negative, the geometry of the probe is *V*-typed. Consequently, the dimensionless bending rigidity $b = (1 + \lambda\xi)$ and the dimensionless body force $p = p_0(1 + \lambda\xi)$ where $p_0 = \rho A_0 g L^4 / [E(0)I(0)L_c]$. Therefore, the transformed governing differential Equation (9) becomes

$$\frac{d^2}{d\xi^2} \left((1 + \lambda\xi) \frac{d^2 v}{d\xi^2} \right) = p_0(1 + \lambda\xi). \tag{15}$$

The particular solution of Equation (15) is easily obtained as

$$V_p = \frac{p_0}{18\lambda} \xi^3 + \frac{p_0}{72} \xi^4.$$

Obviously, the homogeneous differential Equation (15) can be expressed as

$$(1 + \lambda\xi) \frac{d^4 v}{d\xi^4} + 2\lambda \frac{d^3 v}{d\xi^3} = 0. \tag{16}$$

The four normalized fundamental solutions of Equation (16) are:

$$V_1(\xi) = 1, \quad V_2(\xi) = \xi, \quad V_3(\xi) = \frac{1}{2}\xi^2, \quad V_4(\xi) = \frac{\xi}{\lambda^2} + \frac{\xi^2}{2\lambda} - \frac{1 + \lambda\xi}{\lambda^3} \ln(1 + \lambda\xi). \tag{17}$$

These fundamental solutions in Equation (17) satisfy the normalized condition in Equation (14). If $\lambda = 0$, the corresponding fourth fundamental solution $V_4(\xi) = \xi^3/6$.

Upon substituting the solutions (13) and (17) into the boundary conditions (10) and (11), the coefficients D_j are derived

$$D_1 = \frac{-\gamma_{22} p_0 (\lambda^2 + 5\lambda - 6)}{6\gamma_{21}}, \quad D_2 = \frac{\gamma_{12} p_0 (3\lambda + 1)}{6\gamma_{11}}, \quad D_3 = \frac{p_0 (3\lambda + 1)}{6}, \quad D_4 = \frac{-p_0 (1 + \lambda)^3}{3\lambda}.$$

Meanwhile, the shifting function is

$$s = \frac{1}{2\lambda} \xi^2 - \left(1 + \frac{1}{\lambda}\right) \frac{(1 + \lambda\xi)}{\lambda^2} [\ln(1 + \lambda\xi) - 1] - \frac{\gamma_{12}}{\gamma_{11}} \xi - \frac{\gamma_{22}}{\gamma_{21}} - \left(1 + \frac{1}{\lambda}\right) \frac{1}{\lambda^2}. \tag{18}$$

Substituting the solutions (17) and (18) into the relation (5) and letting $\xi = 1$, the solution of tip deflection becomes

$$w(1) = p_0 \bar{V}_1 - (f_b - f_{ts})s(1), \tag{19}$$

where

$$\bar{V}_1 = \frac{1}{18\lambda} + \frac{1}{72} - \frac{\gamma_{22}}{6\gamma_{21}}(\lambda^2 + 5\lambda - 6) + \frac{(3\lambda + 1)}{6} \left(\frac{\gamma_{12}}{\gamma_{11}} + \frac{1}{2} \right) - \frac{(1 + \lambda)^3}{3\lambda} \left(\frac{1}{\lambda^2} + \frac{1}{2\lambda} - \frac{1 + \lambda}{\lambda^3} \ln(1 + \lambda) \right),$$

$$s(1) = \frac{1}{2\lambda} - \left(1 + \frac{1}{\lambda} \right) \frac{(1 + \lambda)}{\lambda^2} [\ln(1 + \lambda) - 1] - \frac{\gamma_{12}}{\gamma_{11}} - \frac{\gamma_{22}}{\gamma_{21}} - \left(1 + \frac{1}{\lambda} \right) \frac{1}{\lambda^2}.$$

Because the force f_{ts} depends on the tip deflection $w(1)$, Equation (19) is an implicit function. Using the numerical method proposed by [Lin 1999], the exact solution $w(1)$ of Equation (19) can be easily determined.

If consider only the van der Waals force, Equation (19) is reduced to be

$$r^3 - 2dr^2 + d^2r + \frac{1}{6}c_{v2}s(1) = 0,$$

where the dimensionless undeformed tip-sample distance $d = \bar{D}_0 - w_s$ and deformed distance $r = w(1) - w_s$. Here w_s denotes the tip deflection due to the weight of probe $w_s = p_0\bar{V}_1 - f_b s(1)$. One can also derive another relation given by

$$d = \sqrt{\frac{-c_{v2}s(1)}{6r}} + r. \tag{20}$$

It tell us that the deformed tip-sample distance can be directly predicted via the relation (20). Moreover, the sensitivity of measurement depends on the dimensionless coefficient c_{v2} and the shifting function $s(1)$. When r is large, d approaches r . When r is very small, d will be very large.

5. Uniform beam

For a uniform beam the bending rigidity $b = 1$ and the taper ratio $\lambda = 0$. The governing differential Equation (15) becomes

$$\frac{d^4 v}{d\xi^4} = p. \tag{21}$$

The four normalized fundamental solutions and the particular solution of Equation (21) are

$$V_1(\xi) = 1, \quad V_2(\xi) = \xi, \quad V_3(\xi) = \frac{1}{2}\xi^2, \quad V_4(\xi) = \frac{1}{6}\xi^3, \quad V_p = \frac{p}{24}\xi^4.$$

The transformed solution v and the shifting function s are, respectively,

$$v(\xi) = p \left(\frac{\gamma_{22}}{\gamma_{21}} + \frac{\gamma_{12}}{2\gamma_{11}}\xi + \frac{1}{4}\xi^2 - \frac{1}{6}\xi^3 + \frac{1}{24}\xi^4 \right), \quad s(\xi) = \left(\frac{1}{6}\xi^3 - \frac{1}{2}\xi^2 - \frac{\gamma_{12}}{\gamma_{11}}\xi - \frac{\gamma_{22}}{\gamma_{21}} \right). \tag{22}$$

Substituting Equation (22) into the relation (5), one obtains the deflection of beam

$$w(\xi) = p \left(\frac{\gamma_{22}}{\gamma_{21}} + \frac{\gamma_{12}}{2\gamma_{11}}\xi + \frac{1}{4}\xi^2 - \frac{1}{6}\xi^3 + \frac{1}{24}\xi^4 \right) - (f_b - f_{ts}) \left(\frac{1}{6}\xi^3 - \frac{1}{2}\xi^2 - \frac{\gamma_{12}}{\gamma_{11}}\xi - \frac{\gamma_{22}}{\gamma_{21}} \right).$$

The corresponding tip deflection due to the beam weight is found as

$$w_s = p \left(\frac{\gamma_{22}}{\gamma_{21}} + \frac{\gamma_{12}}{2\gamma_{11}} + \frac{1}{8} \right) + f_b \left(\frac{1}{3} + \frac{\gamma_{12}}{\gamma_{11}} + \frac{\gamma_{22}}{\gamma_{21}} \right).$$

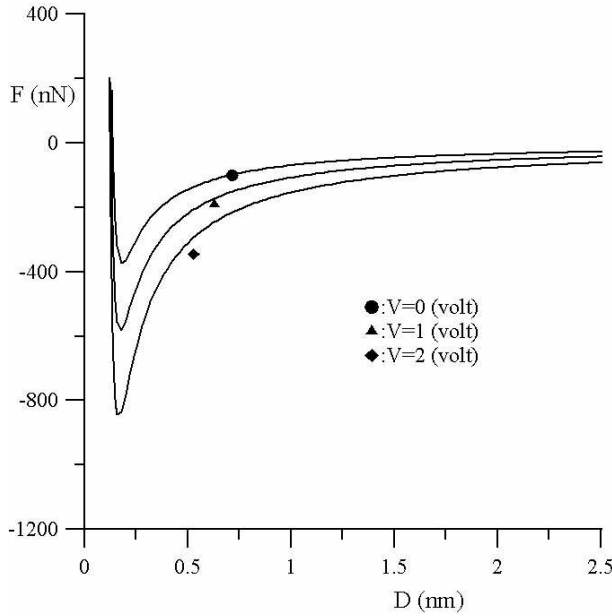


Figure 2. Force-distance curve ($H_1 = 10^{-76}$ Joule, $H_2 = 10^{-19}$ Joule, $H = 6 \mu\text{m}$, $R = 150 \text{ nm}$, $\theta = 12^\circ$, $V_0 = 0$).

Further, if we apply only the van der Waals force to a uniform beam, the relation (20) becomes

$$d = \sqrt{\frac{c_v 2 \left(\frac{1}{3} + \frac{\gamma_{12}}{\gamma_{11}} + \frac{\gamma_{22}}{\gamma_{21}} \right)}{6r}} + r.$$

6. Numerical results and discussion

In this section we investigate the effects of the parameters on the deflection of a probe. Figure 2 shows the relation between the interacting force and the tip-sample distance. A probe is considered to be subjected to both the Lennard-Jones and electrostatic noncontact interacting forces. The influence of the d.c. voltage V on the interacting tip-sample force is presented. For large distances ($D > 2 \text{ nm}$), these two kinds of forces are small. Decreasing the distance dramatically increases the attractive force especially under a larger d.c. voltage V . When the tip-sample distance is very small, the repulsive force becomes dominant.

Figure 3 shows the relation between the undeformed tip-sample distance D_0 and the deformed distance D . If the tip is far from the sample, the attractive force to the probe is small and the deflection of the probe is small. Therefore, the tip-sample distance D is large. In other words, the larger D_0 is, the larger D is. It is shown in Figure 3 that when D_0 is large, the relation between D_0 and D is one-to-one. In other words, there is only one root D of Equation (19) in the domain $D_0 > D_{c2}$. If $D_{c1} < D_0 < D_{c2}$, there are three roots $\{D_1, D_2, D_3\}$ of Equation (19) in this domain. If $D_0 < D_{c1}$, there is only one root D of Equation (19). What it means is that when the probe reaches the sample at a distance approaching the critical distance D_{c2} , the jump-to-contact phenomenon will occur. On the other hand when the probe is

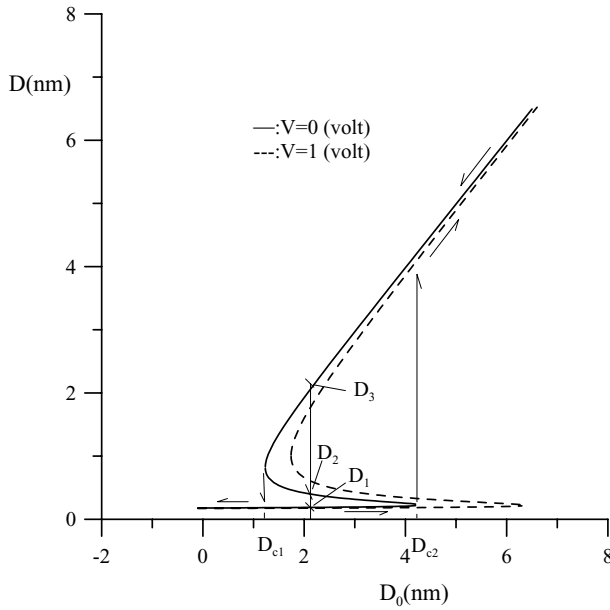


Figure 3. The relation between the undeformed distance and the tip-sample distance ($b = 45 \mu\text{m}$, $h = 4.5 \mu\text{m}$, $L = 200 \mu\text{m}$, $L_c = 10 \text{nm}$, $E = 70.3 \times 10^9 \text{Pa}$, $H_1 = 10^{-76} \text{Joule}$, $H_2 = 10^{-19} \text{Joule}$, $H = 6 \mu\text{m}$, $p = 0$, $R = 150 \text{nm}$, $\rho = 2.5 \times 10^3 \text{kg/m}^3$, $\theta = 12^\circ$, $V_0 = 0$).

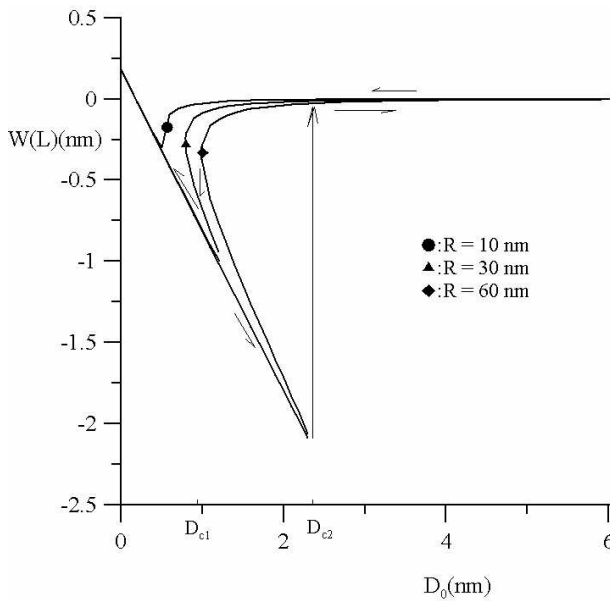


Figure 4. The influence of the radius of tip on the deflection of probe ($b = 45 \mu\text{m}$, $h = 3.5 \mu\text{m}$, $L = 170 \mu\text{m}$, $L_c = 10 \text{nm}$, $E = 70.3 \times 10^9 \text{Pa}$, $H_1 = 10^{-76} \text{Joule}$, $H_2 = 10^{-19} \text{Joule}$, $H = 6 \mu\text{m}$, $p = 0$, $\rho = 2.5 \times 10^3 \text{kg/m}^3$, $\theta = 12^\circ$, $V = V_0 = 0$).

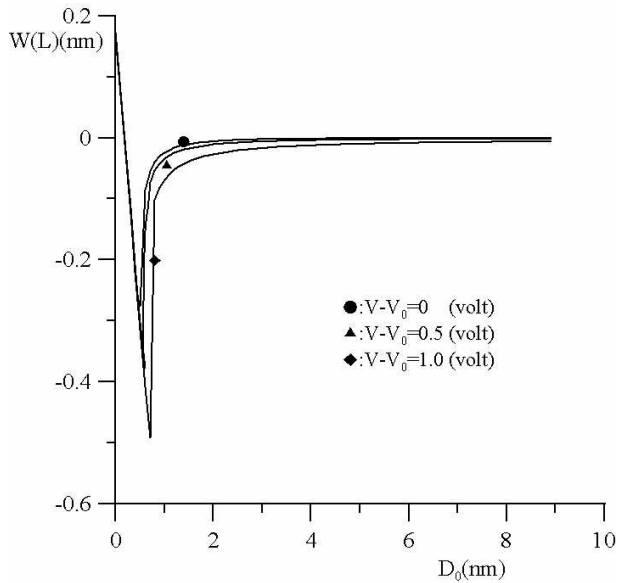


Figure 5. The influence of the d.c. voltage on the deflection of probe ($b = 45 \mu\text{m}$, $h = 4.5 \mu\text{m}$, $L = 170 \mu\text{m}$, $L_c = 10 \text{ nm}$, $E = 70.3 \times 10^9 \text{ Pa}$, $H_1 = 10^{-76} \text{ Joule}$, $H_2 = 10^{-19} \text{ Joule}$, $H = 6 \mu\text{m}$, $p = 0$, $R = 20 \text{ nm}$, $\rho = 2.5 \times 10^3 \text{ kg/m}^3$, $\theta = 12^\circ$, $V_0 = 0$).

pulled off to the critical distance D_{c1} , the jump-off-contact phenomenon will also occur. In other words, if D_0 is in the domain $[D_{c1}, D_{c2}]$, the jump phenomenon will happen. Moreover, one sees from Figure 3 that increasing the contact potential difference ($V - V_0$) increases the domain $[D_{c1}, D_{c2}]$.

Figure 4 shows the influence of the radius of tip on the deflection. It is observed from the case with $R = 60 \text{ nm}$ that when the probe approaches a sample's surface, the attractive tip-sample force pulls the probe down gradually. If the undeformed tip-sample distance D_0 is decreased to the critical value D_{c2} , the jump-to-contact phenomenon occurs. The probe will be pulled down instantly. When the undeformed distance D_0 is decreased further, the repulsive tip-sample force pushes the probe up. The tip deflection of the probe is decreased. When the probe is pulled away from a sample to the critical value D_{c1} , the jump-off-contact phenomenon occurs. The probe will be pulled up instantly. We learn from Figure 4 that increasing the radius of tip R increases the jump domain $[D_{c1}, D_{c2}]$. Moreover, when the radius of tip is decreased to 10 nm , the jump phenomenon disappears.

Figure 5 shows the influence of the contact potential difference ($V - V_0$) on the jump phenomenon and the tip deflection. We find that increasing the contact potential difference enhances the jump phenomenon. Figure 6 shows the influence of the elastic constant k of a probe on the jump phenomenon and the tip deflection. We learn that given $k = 4.612 \text{ N/m}$, the jump phenomenon happens with the jump domain $[D_{c1}, D_{c2}]$. Moreover, increasing the elastic constant k will decrease the jump domain. When the elastic constant k is increased over a critical value, the jump phenomenon disappears. Finally, the effect of a contact force simulated in the DTM model on the tip deflection is investigated. Figure 7 shows the relation among the radius of tip and the tip deflection and the penetrative distance denoted as $-D$. The

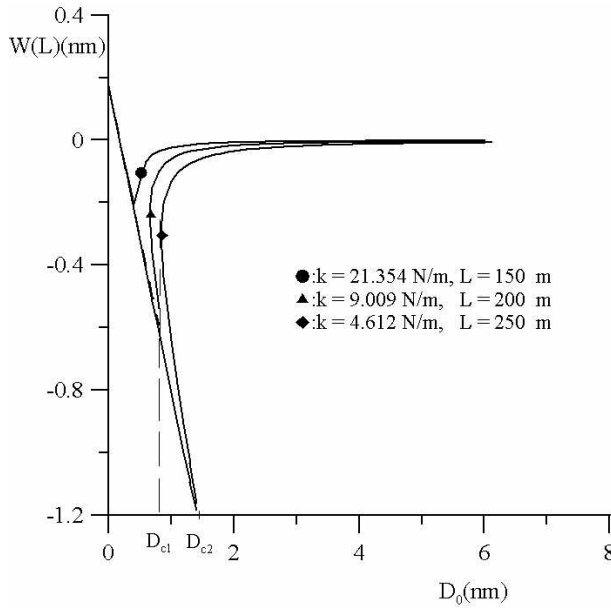


Figure 6. The influence of the elastic constant on the deflection of probe ($b = 45 \mu\text{m}$, $h = 4.5 \mu\text{m}$, $L_c = 10 \text{nm}$, $E = 70.3 \times 10^9 \text{Pa}$, $H_1 = 10^{-76} \text{Joule}$, $H_2 = 10^{-19} \text{Joule}$, $H = 6 \mu\text{m}$, $p = 0$, $R = 20 \text{nm}$, $\rho = 2.5 \times 10^3 \text{kg/m}^3$, $\theta = 12^\circ$, $V = 0.5 \text{volt}$, $V_0 = 0$).

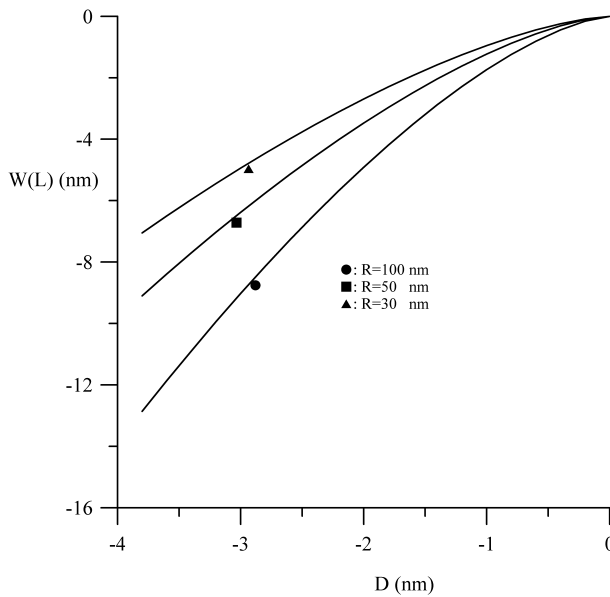


Figure 7. The relation among the penetrative distance, the radius of tip and the deflection of beam subjected to a contact force ($b = 45 \mu\text{m}$, $D_c = 0.37 \text{nm}$, $h = 4.5 \mu\text{m}$, $E_s = E_t = 70.3 \times 10^9 \text{Pa}$, $v_s = v_t = 0.2$, $H = 6 \mu\text{m}$, $p = 0$, $S_e = 0$, $\rho = 2.5 \times 10^3 \text{kg/m}^3$, $\theta = 12^\circ$, $V = V_0 = 0$; $k = 9.009 \text{N/m}$, $L = 200 \mu\text{m}$).

penetrative distance is a distance that the tip penetrates through a sample's surface. We observe that increasing the penetrative distance and the radius of tip increases the deflection of beam.

7. Conclusion

In this paper we study the static measurement of an AFM by using the Bernoulli–Euler beam theory. Its boundary conditions involve several nonlinear tip-sample noncontact and contact forces. The static analytical solution of a general system can be easily derived by the proposed method. We conclude that if only the van der Waals force is considered, the tip-sample distance d is proportional to the van der Waals coefficient c_{v2} and the shifting function $s(1)$. When the tip radius r is large, the magnitude of d is close to r . The effects of several parameters on the jump phenomenon are investigated. To sum up, we have discovered several trends as follows:

- (1) increasing the radius of tip R increases the jump domain $[D_{c1}, D_{c2}]$. If the radius of tip is small enough, the jump phenomenon disappears;
- (2) increasing the contact potential difference $(V - V_0)$ enhances the jump phenomenon;
- (3) increasing the elastic constant k of a probe decreases the jump phenomenon.

References

- [Belaïdi et al. 1997] S. Belaïdi, P. Girard, and G. Leveque, “Electrostatic forces acting on the tip in atomic force microscopy: modelization and comparison with analytic expressions”, *J. Appl. Phys.* **81**:3 (1997), 1023–1030.
- [Belaïdi et al. 1998] S. Belaïdi, F. Lebon, P. Girard, G. Leveque, and S. Pagano, “Finite element simulations of the resolution in electrostatic force microscopy”, *Appl. Phys. A* **66**:supplement 1 (1998), s239–s243.
- [Cappella and Dietler 1999] B. Cappella and G. Dietler, “Force-distance curves by atomic force microscopy”, *Surf. Sci. Rep.* **34**:1-3 (1999), 1–104.
- [Hölscher 2003] H. Hölscher, “Analysis of microscopy and spectroscopy experiments”, pp. 349–369 in *Noncontact atomic force microscopy*, edited by S. Morita et al., Springer, 2003.
- [Hudlet et al. 1998] S. Hudlet, M. Saint Jean, C. Guthmann, and J. Berger, “Evaluation of the capacitive force between an atomic force microscopy tip and a metallic surface”, *Eur. Phys. J. B* **2** (1998), 5–10.
- [Katano et al. 2002] Y. Katano, T. Doi, H. Ohno, and K. Yoh, “Surface potential analysis on doping superlattice by electrostatic force microscope”, *Appl. Surf. Sci.* **188**:3-4 (2002), 399–402.
- [Law and Rieutord 2002] B. M. Law and F. Rieutord, “Electrostatic forces in atomic force microscopy”, *Phys. Rev. B* **66** (2002), #035402.
- [Lee and Lin 1996] S. Y. Lee and S. M. Lin, “Dynamic analysis of non-uniform beams with time dependent elastic boundary conditions”, *J. Appl. Mech. (Trans. ASME)* **63** (1996), 474–478.
- [Lin 1999] S. M. Lin, “Dynamic analysis of rotating nonuniform Timoshenko beams with an elastically restrained root”, *J. Appl. Mech. (Trans. ASME)* **66** (1999), 742–749.
- [Rossell et al. 2003] J. P. Rossell, S. Allen, M. C. Davies, C. J. Roberts, S. J. B. Tendler, and P. M. Williams, “Electrostatic interactions observed when imaging proteins with the atomic force microscope”, *Ultramicroscopy* **96**:1 (2003), 37–46.

[Sadewasser et al. 2003] S. Sadewasser, T. Glatzel, R. Shikler, Y. Rosenwaks, and M. C. Lux-Steiner, “Resolution of Kelvin probe force microscopy in ultrahigh vacuum: comparison of experiment and simulation”, *Appl. Surf. Sci.* **210**:1-2 (2003), 32–36.

[Sadewasser et al. 2004] S. Sadewasser, P. Carl, T. Glatzel, and M. C. Lux-Steiner, “Influence of uncompensated electrostatic force on height measurements in non-contact atomic force microscopy”, *Nanotechnology* **15**:2 (2004), s14–s18.

[Shikler et al. 1999] R. Shikler, T. Meoded, N. Fried, and Y. Rosenwaks, “Potential imaging of operating light-emitting devices using Kelvin force microscopy”, *Appl. Phys. Lett.* **74**:20 (1999), 2972–2974.

Received 16 Jun 2006. Accepted 10 Feb 2007.

SHUEEI-MUH LIN: smlin@mail.ksu.edu.tw

Mechanical Engineering Department, Kun Shan University, Tainan 710-03, Taiwan

SEN-YUNG LEE: sylee@mail.ncku.edu.tw

Mechanical Engineering Department, National Cheng Kung University, Tainan 701, Taiwan

KUEN-WEY LIN: evanlin@itri.org.tw

Mechanical Engineering Department, National Cheng Kung University, Tainan 701, Taiwan

INFLUENCE OF THE ELASTIC PARAMETERS OF A FLUTTERING PLATE ON ITS POST-CRITICAL BEHAVIOR

SILVANO TIZZI

A computational work to determine the post-critical flutter behavior of orthotropic and isotropic panels, according to the Von Karman's large deflection plate theory and quasisteady linearized aerodynamic theory, has been performed. Three different numerical schemes, based on Galerkin, Ritz and finite element method, have been employed for the integration over the panel surface, to reduce the mathematical problem to a system of differential equations in time. These can be integrated by appropriate algorithms to derive the vibrating plate behavior over time. Thus, it has been possible to determine a permanent solution in post-critical conditions. The paper focuses on the influence of the elastic parameters on the limit cycle solution of the vibrating plate under a high supersonic flow. Comparisons between the results obtained by panels with different elastic properties have been mandatory to characterize their effects on the post-critical flutter stationary solution. Particular attention has been given to the limit cycle amplitude, which is a fundamental parameter indicative of the fluttering panel resistance to a high supersonic airflow. Thus it has been possible to state an evaluation criterion of the hierarchic importance of the plate elastic parameters, based on their influence on the panel resistance to the post-critical flutter phenomenon. The reliability of our analysis can be guaranteed through the good agreement between the results of the three methods.

Notation

Roman letters

A_x, A_y	extensional rigidity parameters of the orthotropic plate
$A_r = A_{x,is} = A_{y,is}$	extensional rigidity parameter of the isotropic reference plate
a, b	rectangular plate dimensions
a_1, b_1	nondimensional parameters
$a_{i\psi}$	coefficients of the nondimensional Airy function series expansion
$D_r = D_{x,is} = D_{y,is}$	flexural rigidity modulus of the reference isotropic plate
D_x, D_y, D_t	flexural and torsional rigidity moduli of the orthotropic plate
$E_{\downarrow}, E_{\leftarrow}$	Young's moduli of the orthotropic plate along the fibers direction and the perpendicular one, respectively
E_x, E_y	Young's moduli of the orthotropic plate along the axes x and y , resp.
E_r	Young's modulus of the isotropic reference plate

Keywords: influence, elastic, parameters, plate, fluttering, post-critical, behavior.

$G_{xy} = G_{\downarrow\leftarrow}$	in-plane shear rigidity modulus of the orthotropic plate
$G_r = G_{xy, is}$	in-plane shear rigidity modulus of the isotropic reference plate
h	plate thickness
k_{ij}	stiffness matrix elements
k_{ij}^*	elements of the linear structural-aerodynamic resultant forces matrix
L_a	nondimensional parameter L/a
L, L_w	in-plane and plate thickness reference lengths
M_{ach}	Mach number
m_{ij}	mass matrix elements
N	whole number of the Lagrangian d.o.f.
N_x, N_y, N_{xy}	in-plane membrane forces
t	time symbol
U_a	supersonic flow speed
U, V, W	nondimensional displacements along the axes x, y, z respectively
U_{iU}, V_{iV}, W_{iW}	coefficients of the nondimensional displacements U, V, W series expansions
u, v, w	displacements along the axes x, y, z , respectively
x, y, z	plate reference system axes

Greek symbols

$\alpha_1, \beta_1, \gamma_1$	flexural and torsional rigidity nondimensional parameters
β	nondimensional parameter equal to $\sqrt{M_{ach}^2 - 1}$
γ	geometric nondimensional parameter
δ_{ij}	Kronecker's delta
ζ_{ij}	utilized matrix elements
ϑ	nondimensional parameter in the flutter vibration equation
λ	nondimensional dynamic pressure
$\nu_{xy}, \nu_{yx}, \nu_{\downarrow\leftarrow}, \nu_{\leftarrow\downarrow}$	Poisson's moduli of the orthotropic plate
ν_r	Poisson's modulus of the reference isotropic plate
ξ, η	nondimensional in-plane coordinates
τ	nondimensional time
Φ	Stress Airy function
$\varphi_{i\psi}$	generic element in the nondimensional Airy function series expansion
$\chi_{iU} \chi_{iV} \chi_{iW}$	generic elements of the displacements series expansions
ψ	nondimensional Airy function

Special symbols

∂	partial differentiation
$\mathfrak{d}_{ijk}^{(3)}, \mathfrak{d}_{ijkl}^{(4)}, e_{ijkl}, h_{ijk}$	tensor elements
$I_{...}^{(\cdot)}$	generic integral
$[D^{(4)}][E][H][T][O]$	utilized matrices
$[K^{(op)}][M^{(op)}]$	out-of-plane stiffness and mass matrices
$[K^{(op)}]^*$	out-of-plane linear structural-aerodynamic forces matrix
$[Q^{(op)}]$	out-of-plane Lagrangian degrees of freedom column vector
$[Q^{(op,3)}]$	column vector containing the triple products of the out-of-plane Lagrangian degrees of freedom
$[W]$	utilized column vector of the displacement W series expansions coefficients
$[W^{(3)}]$	utilized column vector containing the triple products between coefficients of W series expansion
$\sin(\) \cos(\) \tan(\)$	trigonometric functions
$\mathcal{T}(\)$	nondimensional kinetic energy expression
$\mathfrak{u}_l^{(\cdot)} \mathfrak{u}_m^{(\cdot)} \mathfrak{u}_{nl}^{(\cdot)}$	nondimensional strain energy expressions due to linear, mixed and nonlinear structural forces

Subscripts

i, j	subscripts with generic meaning
$\dots, is; r$	subscripts referring to the isotropic plate
$i_U j_U k_U, i_V j_V k_V$	subscripts referring to U, V, W , respectively, in the series expansions
$i_W j_W k_W$	subscripts referring to the series expansions
j_{Wc2}, j_{Wc3}	contraction indices
l, m, nl	subscripts referring to the linear, mixed and nonlinear structural forces
\Downarrow, \Leftarrow	subscripts referring to the fibers direction and its perpendicular one

Superscripts

(in)	in-plane situation
(op)	out-of-plane situation

Abbreviations and acronyms

d.o.f.	degree(s) of freedom
FEM	finite element method

1. Introduction

Post-critical flutter behavior of plates and shells exposed to a high supersonic flow has been a subject of major interest and wide research because of its outstanding importance in the aerospace field. In fact the life expectancy and survivability of fluttering panels on high supersonic aircraft depend substantially on their resistance to this phenomenon.

Von Karman's large deflection theory [Bolotin 1963], which takes into account the presence of nonlinear structural forces, together with the assumption of quasisteady first-order high supersonic theory [Bisplinghoff 1962], has been employed by most researchers in the field. The Galerkin method [Kantorowich and Krylov 1964; Mikhlin 1964] was utilized by Dowell [1966; 1967], and by Shiau and Lu [1992], and the Rayleigh-Ritz method [Reddy 1986] was used by Ketter [1967] and Eastep and McIntosh [1971] for the integration over the panel surface. By these methods it was possible to reduce the mathematical problem to a system of nonlinear ordinary differential equations in time, which was solved by numerical integration. Other researchers utilized the finite element method (FEM) [Kikuchi 1986; Reddy et al. 1988] to integrate over the plate or shell surface and to derive a system of ordinary differential equations in-time [Xue and Mei 1993; Dixon and Mei 1993; Zhou et al. 1994; Zhou et al. 1995; Zhou et al. 1996]. The Galerkin method was also used by [Abbas et al. 1993] to examine the problem of nonlinear aerothermoelasticity of panels in supersonic airflow.

A large amount of research was also conducted in the field of piezoelectric actuators to suppress large amplitude limit-cycle flutter [Zhou et al. 1995; Zhou et al. 1996]. Accurate dynamic analysis with actuators present was performed by the use of FEM. Furthermore, the effects of thermal loads were taken into account by some of the above mentioned authors [Xue and Mei 1993; Zhou et al. 1994; Zhou et al. 1995; Zhou et al. 1996; Abbas et al. 1993].

However, none of these authors has developed a particularized study on the influence of the elastic parameters of orthotropic and isotropic plates on the post-critical flutter behavior. One would expect that it would be of fundamental importance to know the role of each one of these parameters related to this phenomenon. For this reason, the main purpose of the present work focuses on their influence on the limit cycle stationary solution of the fluttering panel, whose amplitude determines its resistance to a high supersonic airflow.

First, the classical Galerkin method has been utilized, as in the Dowell's model. Then a Lagrangian functional expression has been formed to apply FEM and Ritz procedures [Tizzi 1994;1997; 2003a], and a system of ordinary differential equations in time has been obtained by the virtual work variational principle [Pars 1968], which has been integrated by appropriate algorithms.

Cases with different in-plane boundary conditions have been considered. For this reason two different models have been utilized with the Galerkin method. The first employs the Airy stress function to arrive at the classical von Karman's equations [Bolotin 1963]; the second one considers the in-plane displacements as unknown variables [Santini 1973].

A single model with the presence of a particular parameter can be employed instead, when FEM or Ritz procedures are utilized; this parameter takes into account the in-plane geometric boundary conditions in the in-plane clamped plate borders case [Tizzi 2003b].

The use of three different numerical schemes, giving very close results, can be helpful in guaranteeing the validity of the developed analysis.

The knowledge of the flutter behavior of a vibrating plate is useful also for multilayer composite laminates. In fact it is well known that the dynamic analysis of a nearly symmetric and balanced vibrating composite structure, angle-ply laminate $\pm\theta$ type, can be simulated by an equivalent orthotropic plate, with appropriate values for thickness and elastic parameters [Crivelli Visconti 1975; Tizzi 1999].

Consequently the present numerical analysis is useful also to characterize the resistance of a panel formed by a generic angle-ply composite laminate $\pm\theta$ with many component layers to air flowing at supersonic speed.

2. Mathematical formulations

Mathematical formulations have been developed for all three procedures treated in the paper.

A generic orthotropic plate, aligned with an x, y, z system of rectangular coordinates and exposed to a high supersonic airflow along the x axis, is considered and shown in Figure 1.

The Galerkin method has been utilized, then FEM and Ritz procedures have been used for the plate dynamic analysis.

The Einstein's summation convention for repeated indices has been adopted in all the forthcoming relations.

2.1. The Galerkin method. The out-of-plane vibration governing equation of a plate undergoing both extension and bending throughout its surface, combined with the transverse constitutive relations of orthotropic plates [Crivelli Visconti 1975], according to the Kirchhoff's hypothesis [Santini 1973], yields the second von Karman's governing equation of the flutter vibration, properly modified for an orthotropic

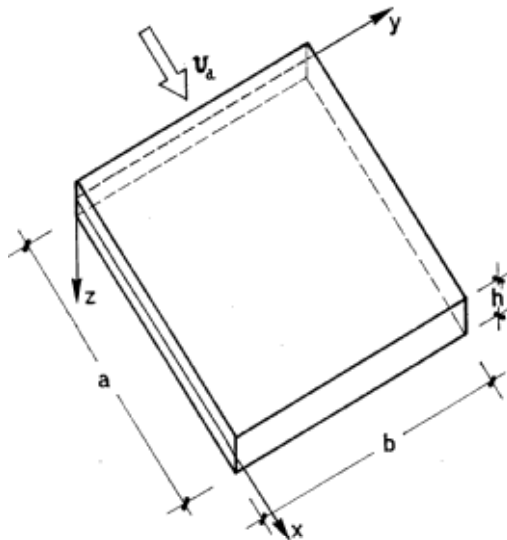


Figure 1. Plate exposed to an airflow at high supersonic speed.

plate:

$$D_x \frac{\partial^4 w}{\partial x^4} + 2(\nu_{xy} D_y + 2D_t) \frac{\partial^4 w}{\partial x^2 \partial y^2} + D_y \frac{\partial^4 w}{\partial y^4} + p_z + \mu \frac{\partial^2 w}{\partial t^2} - N_x \frac{\partial^2 w}{\partial x^2} - 2N_{xy} \frac{\partial^2 w}{\partial x \partial y} - N_y \frac{\partial^2 w}{\partial y^2} = 0, \quad (1)$$

where $w(x, y, t)$ is the transverse displacement, N_x, N_y, N_{xy} are the membrane forces per unit length, and p_z is the aerodynamic loading pressure, which, within the framework of the quasisteady linearized “Piston Theory” of the high supersonic aerodynamics [Bisplinghoff 1962], is given by:

$$p_z = \frac{2q}{\beta} \left(\frac{\partial w}{\partial x} + \frac{1}{U_a} \frac{\beta^2 - 1}{\beta^2} \frac{\partial w}{\partial t} \right). \quad (2)$$

In Equation (2), $\beta^2 = M_{ach}^2 - 1$, U_a is the high supersonic flow speed, and $q = \rho U_a^2 / 2$ is the air flowing dynamic pressure. Finally, the orthotropic plate flexural and torsional rigidity parameters are defined in the customary manner as:

$$D_x = \frac{E_x h^3}{1 - \nu_{xy} \nu_{yx}}, \quad D_y = \frac{E_y h^3}{1 - \nu_{xy} \nu_{yx}}, \quad D_t = G_{xy} \frac{h^3}{12}. \quad (3)$$

Since two different cases of the in-plane boundary conditions are considered, separate Galerkin procedures are utilized for the plate dynamic analysis.

Case 1. First, a simply supported plate for the out-of-plane behavior is considered, having the in-plane borders free—that is the membrane forces vanish on the limit edges:

$$\begin{aligned} N_x = 0 & \quad \text{and} \quad N_{xy} = 0 & \quad \text{at} \quad x = 0, a \\ N_y = 0 & \quad \text{and} \quad N_{xy} = 0 & \quad \text{at} \quad y = 0, a. \end{aligned} \quad (4)$$

The in-plane coordinates and the transverse displacement have been reformulated in nondimensional form:

$$\xi = \frac{x}{a}, \quad \eta = \frac{y}{b}, \quad W = \frac{w}{L_w}, \quad (5)$$

where L_w is the plate thickness reference length, and a, b are the rectangular plate dimensions.

The nondimensional transverse displacement is written in terms of a series expansion:

$$W(\xi, \eta, \tau) = W_{i_w}(\tau) \chi_{i_w}(\xi, \eta), \quad i_w = 1, 2, \dots, N_w, \quad (6)$$

where each element $\chi_{i_w}(\xi, \eta)$ satisfies the boundary conditions of a simply supported plate, and can be defined as:

$$\chi_{i_w}(\xi, \eta) = \sin(i_{W_x} \pi \xi) \sin(i_{W_y} \pi \eta), \quad (7)$$

$$i_{W_x} = 1, 2, \dots, N_{W_x}, \quad i_{W_y} = 1, 2, \dots, N_{W_y}, \quad i_w = (i_{W_x} - 1)N_{W_y} + i_{W_y}, \quad (8)$$

$$i_w = 1, 2, \dots, N_w, \quad N_w = N_{W_x} N_{W_y}. \quad (9)$$

Since the in-plane inertia is being neglected, in this particular case it is better to utilize the Airy stress function to describe the in-plane static behavior and hence to satisfy easily the natural boundary conditions in Equations (4).

This Airy function $\Phi(x, y, t)$ can be reformulated in nondimensional form:

$$\psi = \frac{\Phi}{E_r h L^2}, \tag{10}$$

where L is the in-plane reference length, E_r is the Young’s modulus of the reference isotropic plate, and h is the plate thickness.

A series expansion for $\psi(\xi, \eta, \tau)$ in terms of function elements can be chosen:

$$\psi(\xi, \eta, \tau) = a_{i_\psi}(\tau)\varphi_{i_\psi}(\xi, \eta), \quad i_\psi = 1, 2, \dots, N_\psi, \tag{11}$$

where the generic function element $\varphi_{i_\psi}(\xi, \eta)$ is equal to:

$$\begin{aligned} \varphi_{i_\psi}(\xi, \eta) &= \varphi_{i_{\psi x}}(\xi)\varphi_{i_{\psi y}}(\eta), \\ i_{\psi x} &= 1, 2, \dots, N_{\psi x}, \\ i_{\psi y} &= 1, 2, \dots, N_{\psi y}, \\ i_\psi &= (i_{\psi x} - 1)N_{\psi y} + i_{\psi y}, \\ i_\psi &= 1, 2, \dots, N_\psi, \\ N_\psi &= N_{\psi x}N_{\psi y}, \end{aligned} \tag{12}$$

and further, $\varphi_{i_{\psi x}}(\xi), \varphi_{i_{\psi y}}(\eta)$ are nearly orthonormal describing functions, which vanish with their first normal derivatives at the plate borders. Thus, for the membrane forces with dependence on the stress function, the natural boundary conditions in Equations (4) are satisfied. These are treated in the Appendix.

The in-plane compatibility relation [Santini 1973], by virtue of the in-plane kinematic and constitutive equations of an orthotropic plate [Crivelli Visconti 1975], together with the dependence of the membrane forces on the stress function, lead to the classical von Karman’s first equation, properly modified for an orthotropic plate [Tizzi 2003b].

In view of the same membrane forces’ dependence on the stress function, the flutter governing Equation (1), combined with the in-plane von Karman’s first equation, through Galerkin operations becomes in nondimensional form:

$$\begin{aligned} \ddot{W}_m + \sqrt{\lambda\vartheta} \dot{W}_m + i_{3W}^4 W_m + 4\lambda L_a I_{mjw}^{(\chi\chi)} W_{jw} \\ - \frac{4}{\pi^4} h L^2 a_1^2 b_1^2 \frac{\sqrt{E_x E_y}}{E_r} I_{mi_\psi i_w}^{(\chi\varphi\chi)} \zeta_{i_\psi j_w c_2} W_{i_w} W_{j_w} W_{k_w} = 0 \quad m = 1, 2, \dots, N_W, \end{aligned} \tag{13}$$

where

$$\begin{aligned} i_{3W}^4 &= \alpha_1^4 i_{W_x}^4 + \gamma_1^4 i_{W_x}^2 i_{W_y}^2 + \beta_1^4 i_{W_y}^4, \\ \dot{W}_{i_w} &= \frac{\partial W_{i_w}}{\partial \tau}, \\ \ddot{W}_{i_w} &= \frac{\partial^2 W_{i_w}}{\partial \tau^2}, \\ I_{mjw}^{(\chi\chi)} &= \int_{\Sigma} \chi_m \frac{\partial \chi_{jw}}{\partial \xi} d\Sigma, \end{aligned} \tag{14}$$

$$I_{mi\psi iw}^{(\chi\varphi\chi)} = \int_{\Sigma} \chi_m \left[\frac{\partial^2 \varphi_{i\psi}}{\partial \eta^2} \frac{\partial^2 \chi_{iw}}{\partial \xi^2} - 2 \frac{\partial^2 \varphi_{i\psi}}{\partial \xi \partial \eta} \frac{\partial^2 \chi_{iw}}{\partial \xi \partial \eta} + \frac{\partial^2 \varphi_{i\psi}}{\partial \xi^2} \frac{\partial^2 \chi_{iw}}{\partial \eta^2} \right] d\Sigma. \tag{15}$$

Further, we have introduced in Equations (13) and (14) the following nondimensional parameters:

$$a_1 = \sqrt[4]{\frac{E_r}{E_y} \frac{L}{a}}, \quad b_1 = \sqrt[4]{\frac{E_r}{E_x} \frac{L}{b}}, \quad \gamma = \frac{L_w}{L}, \tag{16}$$

$$\alpha_1^4 = \frac{D_x L^4}{D_r a^4}, \quad \beta_1^4 = \frac{D_y L^4}{D_r b^4}, \quad \gamma_1^4 = \frac{2(v_{xy} D_y + 2D_t)}{D_r} \frac{L^4}{a^2 b^2}, \quad L_a = \frac{L}{a}, \tag{17}$$

$$\lambda = \frac{2qL^3}{\beta\pi^4 D_r}, \quad \vartheta = \left(\frac{\beta^2 - 1}{\beta^2} \right)^2 \frac{2qL}{\beta\mu U_a^2}, \quad \tau = \sqrt{\frac{D_r \pi^4}{\mu L^4}} t, \tag{18}$$

where E_r is the Young’s modulus of the isotropic reference plate, and $D_r = E_r h^3 / 12(1 - \nu_r^2)$ is the flexural rigidity modulus of the same fluttering reference plate.

Finally, the coefficients $\zeta_{i\psi jwc2}$ in Equation (13) are matrix elements, connecting the coefficients $a_{i\psi}$ of the series in Equation (11), with the double product of the out-of-plane bending displacement series expansion coefficients in Equation (6):

$$a_{i\psi} = \zeta_{i\psi jwc2} W_{jw} W_{kw}. \tag{19}$$

In Equation (19) $jwc2$ is the contraction of the two indices jw and kw .

Detailed explanations of the analytical developments which, starting from the flutter Equation (1) and the in-plane static equilibrium von Karman’s relation, allow us to derive, through Galerkin operations, the governing Equation (13) and the relation (19), are shown in [Tizzi 2003b]. These developments are very similar to those in the analytical studies carried out by other authors [Dowell 1966; Dowell 1967; Shiau and Lu 1992; Abbas et al. 1993].

Equation (13) can be transformed into its equivalent matrix form:

$$[\ddot{\mathbf{W}}] + \sqrt{\lambda} \vartheta [\dot{\mathbf{W}}] + i_3^4 [\mathbf{W}] + [\mathbf{H}][\mathbf{W}] - [\mathbf{O}][\mathbf{W}^{(3)}] = 0, \tag{20}$$

where $[\mathbf{W}]$ is the column vector having dimensions N_W , whose elements are the series expansions coefficients of the transverse displacement in Equation (6); $[\mathbf{W}^{(3)}]$ is the column vector with dimensions N_W^3 , whose elements are the triple products of the same coefficients $p_{jwc3}^{(3)} = W_{iw} p_{jwc2}^{(2)} = W_{iw} W_{jw} W_{kw}$ ($jwc3$ is the contraction of the three indices i_w, j_w, k_w or $i_w, jwc2$); $[\mathbf{H}]$ and $[\mathbf{O}]$ are matrices, having dimensions $N_W \times N_W$ and $N_W \times N_W^3$, respectively, whose elements are:

$$h_{mjw} = 4\lambda L_a I_{mjw}^{(\chi\chi)}, \quad o_{mjwc3} = 4hL^2 a_1^2 b_1^2 \frac{\sqrt{E_x E_y}}{E_r} I_{mi\psi iw}^{(\chi\varphi\chi)} \zeta_{i\psi jwc2}. \tag{21}$$

In the second of Equations (21) the summation convention for the repeated index $i\psi$ has been utilized.

Thus, a reduced system of nonlinear differential equations is derived, with a single independent variable W . For the integration in time, an algorithm based on the Kutta-Merson procedure is utilized, with variable control of the step integration [Merson 1957; Lambert 1991].

Case 2. We then analyze a second case of a plate, likewise simply supported at the borders for the transverse behavior but clamped at the four edges for the in-plane displacements. In place of Equations (4) there are the following boundary conditions for in-plane displacements:

$$u = 0 \quad \text{and} \quad v = 0 \quad \text{at} \quad x = 0, a \quad \text{and} \quad y = 0, b. \tag{22}$$

In this case it is not convenient to use the Airy function, but to set-up the in-plane governing equations by means of the membrane displacements functions over the mid-plane panel surface.

Like the transverse displacement $W = w/L_w$, as in the third of Equations (5), the in-plane displacements u, v have also been reformulated in nondimensional form:

$$U = \frac{u}{a} \frac{1}{\gamma_a^2}, \quad V = \frac{v}{b} \frac{1}{\gamma_b^2}. \tag{23}$$

Notice that the order of magnitude of the in-plane displacements u, v is the same as that of w^2 ; thus the same order of magnitude corresponds to U, V, W .

Appropriate series expansions have been chosen for the nondimensional in-plane displacements:

$$U = U_{i_U}(\tau) \chi_{i_U}(\xi, \eta), \quad V = V_{i_V}(\tau) \chi_{i_V}(\xi, \eta), \quad i_U, i_V = 1, 2, \dots, N_U, N_V, \tag{24}$$

where each function element of the series is defined as

$$\begin{aligned} \chi_{i_U}(\xi, \eta) &= \sin(i_{U_x} \pi \xi) \sin(i_{U_y} \pi \eta) \\ \chi_{i_V}(\xi, \eta) &= \sin(i_{V_x} \pi \xi) \sin(i_{V_y} \pi \eta) \end{aligned} \tag{25}$$

$$\begin{aligned} i_{U_x}, i_{V_x} &= 1, 2, \dots, N_{U_x}, N_{V_x}, \\ i_{U_y}, i_{V_y} &= 1, 2, \dots, N_{U_y}, N_{V_y}, \\ i_U, i_V &= (i_{U_x}, i_{V_x} - 1)N_{U_y}, N_{V_y} + i_{U_y}, i_{V_y}, \\ i_U, i_V &= 1, 2, \dots, N_U, N_V, \\ N_U, N_V &= N_{U_x}, N_{V_x} \times N_{U_y}, N_{V_y} \end{aligned} \tag{26}$$

which satisfy the boundary conditions in Equations (22).

Also, in this case, the in-plane inertia effects are being neglected. The static equilibrium equations along the x and y axes, for the in-plane kinematic and constitutive relationships of an orthotropic plate, expressed in terms of the membrane displacements [Santini 1973; Crivelli Visconti 1975], can be determined [Tizzi 2003b].

The von Karman’s flutter vibration Equation (1), in view of the same in-plane kinematic and constitutive relations of an orthotropic plate, combined with the two in-plane static equilibrium equations, through Galerkin operations becomes

$$\ddot{W}_m + \sqrt{\lambda \vartheta} \dot{W}_m + i_{3W}^4 W_m + 4\lambda L_a I_{mjw}^{(\chi\chi)} W_{jw} + t_{mjw\epsilon_3} W_{iw} W_{jw} W_{kw} = 0, \quad m = 1, 2, \dots, N_W, \tag{27}$$

where the time derivatives, along with the parameter i_{3W}^4 and the integral $I_{mjw}^{(\chi\chi)}$, have been previously defined in Equations (14), and the meaning of the nondimensional parameters λ and ϑ is explained in Equations (18).

Furthermore t_{mjwc3} are matrix elements, where j_{wc3} is the contraction of the three indices i_w, j_w, k_w , as stated after Equation (20).

Detailed explanations of the analytical developments, which, starting from the flutter Equation (1), and combined with the two in-plane static equilibrium relations, allow us to find the governing Equation (27) through Galerkin operations, are given in [Tizzi 2003b].

Introducing the matrix $[T]$, having elements t_{mjwc3} and dimensions $N_W \times N_W^3$, allows Equation (27) to take its equivalent matrix form:

$$[\ddot{W}] + \sqrt{\lambda\vartheta}[\dot{W}] + i_{3W}^4[W] + [H][W] - [T][W^{(3)}] = 0, \tag{28}$$

where the same column vector $[W^{(3)}]$, previously defined after Equation (20), and the same matrix $[H]$, whose elements have been defined in the first of Equations (21), are utilized. The same algorithm, applying the Kutta-Merson procedure with variable step control for the integration in time, is utilized, as it is for the differential relations system in Equation (20).

2.2. Ritz and FEM procedures. Procedures built both on the Rayleigh-Ritz method and on FEM [Tizzi 1994; 1997; 2003a] have been employed to extract the requested results. These arise from differential operations on an energetic functional, whose stationary conditions lead to the dynamic governing equations. Since with FEM or Ritz method one is not obliged to satisfy the natural boundary conditions in the free in-plane edges case, as in Equation (4), the same model can be utilized for the two cases with different in-plane conditions at the panel borders. It is only sufficient to introduce a parameter which takes into account the geometric in-plane boundary conditions in the in-plane clamped plate edges case.

The strain energy expression, due to the in-plane and transverse linear structural forces only, can be stated as:

$$U_l^{(in)} = \frac{1}{2}k_{ij}^{(in)}q_i^{(in)}q_j^{(in)}, \quad U_l^{(op)} = \frac{1}{2}k_{ij}^{(op)}q_i^{(op)}q_j^{(op)}, \tag{29}$$

where

- (1) $k_{ij}^{(in)}$ and $k_{ij}^{(op)}$ are the in-plane and out-of-plane stiffness matrix elements of the orthotropic plate, respectively, which have been previously evaluated both for Ritz and for FEM procedure,
- (2) $q_i^{(in)}, q_j^{(in)}$ and $q_i^{(op)}, q_j^{(op)}$ are the in-plane and out-of-plane transverse degrees of freedom (d.o.f.), respectively, of both methods.

In the Ritz procedure, these stand for the coefficients of the polynomial series expansions of the in-plane and transverse displacements, respectively, as in Equations (24) and (6), whereas in the FEM, these correspond to the same displacements and their first order derivatives in the in-plane coordinates on the grid points of the chosen mesh [Tizzi 2003b].

Also the contribution of the mixed and nonlinear structural forces to the in-plane strain energy can be evaluated and expressed as:

$$\mathcal{U}_m^{(in)} = \frac{1}{2}\mathfrak{d}_{ijk}^{(3)}q_i^{(in)}q_j^{(op)}q_k^{(op)}, \quad \mathcal{U}_{nl}^{(in)} = \frac{1}{2}\mathfrak{d}_{ijkl}^{(4)}q_i^{(op)}q_j^{(op)}q_k^{(op)}q_l^{(op)}, \tag{30}$$

where $\mathfrak{d}_{ijk}^{(3)}$ and $\mathfrak{d}_{ijkl}^{(4)}$ are tensor elements, previously determined in the Ritz and FEM procedures [Tizzi 2003b].

The in-plane and transverse kinetic energy expressions can be stated in the classical form:

$$\mathcal{T}^{(in)} = \frac{1}{2} m_{ij}^{(in)} \dot{q}_i^{(in)} \dot{q}_j^{(in)}, \quad \mathcal{T}^{(op)} = \frac{1}{2} m_{ij}^{(op)} \dot{q}_i^{(op)} \dot{q}_j^{(op)}, \quad (31)$$

where $\dot{q}_i, \dot{q}_j = \partial[q_i, q_j]/\partial\tau$, and $m_{ij}^{(in)}, m_{ij}^{(op)}$ are the in-plane and out-of-plane mass matrix elements, respectively. Also these have been previously evaluated for a fluttering orthotropic plate using both procedures [Tizzi 2003b]. Since the in-plane inertia effects have been neglected, the component $\mathcal{T}^{(in)}$ of the kinetic energy is not considered, and consequently only the elements $m_{ij}^{(op)}$ of the mass matrix are taken into account.

The Lagrangian \mathcal{L}_a functional can be introduced:

$$\mathcal{L}_a = \mathcal{T}^{(op)} - \mathcal{U}_l^{(in)} - \mathcal{U}_l^{(op)} - \mathcal{U}_m^{(in)} - \mathcal{U}_{nl}^{(in)}. \quad (32)$$

The differential principle of virtual work, applied to the $i - th$ in-plane (in) or out-of-plane (op) d.o.f, leads to the classical Lagrange equation [Pars 1968]:

$$\frac{d(\partial\mathcal{L}_a/\partial\dot{q}_i^{(in,op)})}{d\tau} - \frac{\partial\mathcal{L}_a}{\partial q_i^{(in,op)}} = 0. \quad (33)$$

This gives the in-plane or out-of-plane governing equations, depending on whether the generic degree of freedom refers to in-plane $q_i^{(in)}$ or the out-of-plane $q_i^{(op)}$ behavior.

Combining the two equations, and taking into account the aerodynamic generalized force presence in the out-of-plane governing equation, leads to:

$$m_{ij}^{(op)} \ddot{q}_j^{(op)} + f_{ij}^{(t)} \dot{q}_j^{(op)} + (k_{ij}^{(op)})^* q_j^{(op)} + e_{iklm} q_k^{(op)} q_l^{(op)} q_m^{(op)} + 2\mathfrak{d}_{ijkl}^{(4)} q_j^{(op)} q_k^{(op)} q_l^{(op)} = 0, \quad (34)$$

where the elements:

$$(k_{ij}^{(op)})^* = k_{ij}^{(op)} + f_{ij}^{(x)} \quad (35)$$

collect both the linear out-of-plane structural and aerodynamic coupling forces [Tizzi 1994]. Furthermore, the coefficients $f_{ij}^{(x)}$ and $f_{ij}^{(t)}$ appear in the expressions of the two components of the generalized aerodynamic force:

$$F_i^{(a)} = F_i^{(a,x)} + F_i^{(a,t)} \quad F_i^{(a,x)} = f_{ij}^{(x)} q_j^{(op)}, \quad F_i^{(a,t)} = f_{ij}^{(t)} \dot{q}_j^{(op)}. \quad (36)$$

The component $F_i^{(a,x)}$, containing the transverse displacement derivative in the x coordinate, is responsible for the coupling between different natural vibrating modes, while the damping component $F_i^{(a,t)}$, contains the transverse displacement time derivative, according to the linearized Piston Theory.

Detailed explanations of the way in which Equation (34) is derived, starting from the two in-plane and out-of-plane governing equations, are given in [Tizzi 2003b], where the meaning of the tensor elements e_{iklm} is sufficiently illustrated. The other tensor elements $\mathfrak{d}_{ijkl}^{(4)}$ are the same as in the second of Equations (30).

The out-of-plane mass matrix $[M^{(op)}]$, having elements $m_{ij}^{(op)}$, and the linear structural-aerodynamic forces matrix $[K^{(op)}]^*$, having elements $(k_{ij}^{(op)})^*$, are introduced, together with the nonlinear structural forces matrices $[E]$ and $[D^{(4)}]$, having tensor elements e_{ijc_3} and $\mathfrak{d}_{ijc_3}^{(4)}$, respectively (j_{c_3} is the contraction

index of the three indices k, l, m or j, k, l). The column vectors $[\mathbf{Q}^{(op)}]$, having elements the out-of-plane d.o.f. $q_i^{(op)}$, and $[\mathbf{Q}^{(op,3)}]$, containing the triple products

$$p_{jc3}^{(3)} = q_k^{(op)} q_l^{(op)} q_m^{(op)} \quad \text{or} \quad p_{jc3}^{(3)} = q_j^{(op)} q_k^{(op)} q_l^{(op)}$$

are also introduced. The elements $f_{ij}^{(t)}$ of the aerodynamic damping forces are proportional to the out-of-plane mass matrix elements $m_{ij}^{(op)}$ [Tizzi 2003a; 2003b]:

$$f_{ij}^{(t)} = \gamma_d m_{ij}^{(op)}. \tag{37}$$

Hence, the matrix having elements $f_{ij}^{(t)}$ would be coincident with the out-of-plane mass matrix $[\mathbf{M}^{(op)}]$, but for a coefficient γ_d , both for Ritz and for FEM methods.

This allows Equation (34) to take its equivalent matrix form:

$$[\ddot{\mathbf{Q}}^{(op)}] + \gamma_d [\dot{\mathbf{Q}}^{(op)}] + [\mathbf{M}^{(op)}]^{-1} [\mathbf{K}^{(op)}] * [\mathbf{Q}^{(op)}] + [\mathbf{M}^{(op)}]^{-1} \{[\mathbf{E}] + 2[\mathbf{D}^{(4)}]\} [\mathbf{Q}^{(op,3)}] = 0. \tag{38}$$

A nonlinear equations system is obtained, similar to the one in Equation (28), which likewise can be integrated by an algorithm utilizing the Kutta-Merson procedure with variable integration step.

3. Applications and results

The introduced numerical approaches have been applied to different cases of orthotropic and isotropic plates. In all the considered cases the following geometric characteristics of the rectangular plates are supposed:

$$L = a = b = 100L_w = 100h, \tag{39}$$

and concerning the nondimensional parameter ϑ in the second of Equations (18), it has been assumed that

$$\vartheta = 0.1. \tag{40}$$

The in-plane and out-of-plane boundary conditions of the reference vibrating isotropic plate are the same as those for the fluttering orthotropic plate in every considered case.

The amplitude W_A of the flutter vibration displacement is evaluated in the point with maximum value of the transverse deflection $w(x, y, t)$, which verifies at about 3/4 of the central side parallel to the airflow direction, starting from the leading edge. This is a parameter of great importance; in fact the smaller this amplitude is, the higher is the resistance of the fluttering plate under the effects of air flowing at supersonic speed.

In the first two cases an orthotropic plate of composite u.d. materials, made of glass fibers and eposidic resin, is used, having the following elastic properties [Crivelli Visconti 1975]:

$$E_{\Downarrow} = 45 \text{ GPa}, \quad E_{\Leftarrow} = 14 \text{ GPa}, \quad G_{\Downarrow\Leftarrow} = 6 \text{ GPa}, \quad \nu_{\Downarrow\Leftarrow} = 0.24, \quad \nu_{\Leftarrow\Downarrow} = 0.0746, \tag{41}$$

where E_{\Downarrow} is the Young's modulus along the fibers direction, E_{\Leftarrow} is the Young's modulus along the perpendicular direction, $G_{\Downarrow\Leftarrow}$ is the shear rigidity modulus between the two directions, and $\nu_{\Downarrow\Leftarrow}, \nu_{\Leftarrow\Downarrow}$ denote the two Poisson's moduli. These are equal to ν_{xy}, ν_{yx} if the fibers are oriented in the airflow direction, and ν_{yx}, ν_{xy} if the fibers are oriented in the perpendicular direction.

λ	1.47	2.0	3.78	4.0	5.21	6.0	8.0	10.0	12.0	14.0	16.0
$E_x < E_y = E_r$	0	2.53		8.56		11.57	13.24	14.42	15.16	15.47	15.57
$E_x = E_r > E_y$			0	0.43		3.15	4.63	5.66	6.53	7.26	7.79
isotropic					0	0.70	2.01	2.84	3.47	4.0	4.42

Table 1. Values of the post-critical limit cycle amplitude W_A versus the nondimensional dynamic pressure λ in the first case.

In the first case considered, for a significant comparison of the results obtained, a reference isotropic plate is utilized having Young’s modulus E_r equal to the higher of the two of the orthotropic plate and a Poisson’s modulus $\nu_r = 0.3$. The plate is simply supported for the out-of-plane flutter dynamics, but with free in-plane boundary conditions, as in Equation (4).

The behavior of the limit cycle highest amplitude W_A versus the nondimensional dynamic pressure λ in Figure 2, corresponds to the post-critical dynamics of the orthotropic plate with the fibers oriented in the perpendicular direction to the airflow. In this subcase the Young’s modulus along the x axis (direction of the airflow) is lower than the corresponding one along the perpendicular axis y ($E_x < E_y = E_r$), because $E_x = E_{\downarrow}$ and $E_y = E_{\uparrow}$. The lowest amplitude graph corresponds to the flutter of the reference isotropic vibrating plate. The middle amplitude curve of the flutter oscillations corresponds to the limit cycle of the orthotropic plate, with the fibers oriented in the airflow direction. In this second subcase, the Young’s modulus along the x axis is higher than the corresponding one along the perpendicular direction ($E_x = E_r > E_y$), because $E_x = E_{\uparrow}$ and $E_y = E_{\downarrow}$.

The data points, which in Figure 2 appear as dots, are summarized in Table 1.

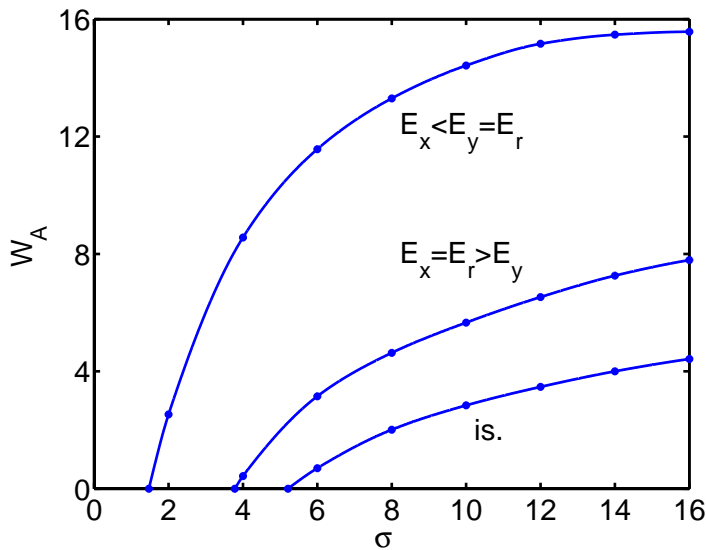


Figure 2. Behavior of the post-critical limit cycle amplitude W_A versus the nondimensional dynamic pressure λ in the first considered case.

λ	4.26	4.89	6.0	12.0	12.31	18.0	24.0	30.0	36.0	42.0	48.0
$E_x = E_r < E_y$	0		2.28	7.79		11.05	12.98	14.00	14.63	15.15	15.47
isotropic		0	0.8	3.68		5.26	6.42	7.16	7.79	8.30	8.84
$E_x > E_y = E_r$					0	2.95	4.57	5.47	6.31	7.05	7.68

Table 2. Values of the post-critical limit cycle amplitude W_A versus the nondimensional dynamic pressure λ in the second case.

In the second case, the same vibrating orthotropic plate of the previous case is considered, with the same in-plane and out-of-plane boundary conditions, but the Young’s modulus E_r of the reference isotropic plate is equal to the smaller of the two ones of the orthotropic plate. Since the dynamic pressure has been reformulated in nondimensional form by dividing by the flexural rigidity modulus D_r of the isotropic plate (see the first of Equations (18)), which is lower than the corresponding one in the previous case, higher values of λ , compared to those in Figure 2, are noticed (see Figure 3).

In the same Figure 3, the curve of the highest amplitude behavior versus λ corresponds to the orthotropic plate with the fiber direction perpendicular to that of the airflow ($E_x = E_r < E_y$), whereas the lowest flutter amplitude chart corresponds to the fiber orientation in the airflow direction ($E_x > E_y = E_r$). The graphic curve of the limit cycle amplitude behavior versus λ of the isotropic plate, with lower Young’s and equal Poisson’s modulus with respect to the same parameter values of the previous case, is located between the two ones of the orthotropic plate.

The data points, which in Figure 3 appear as dots, are written in Table 2.

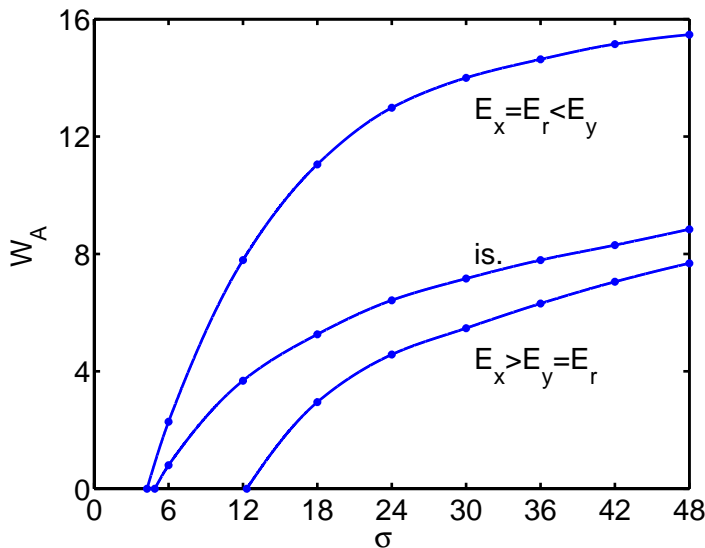


Figure 3. Behavior of the post-critical limit cycle amplitude W_A versus the nondimensional dynamic pressure λ in the second considered case.

λ	0.94	2.0	3.43	4.0	5.37	6.0	8.0	10.0	12.0	14.0	16.0
$E_x < E_y = E_r$	0	3.59		10.0		15.0	18.91	21.87	24.06	25.31	26.25
$E_x = E_r > E_y$			0	2.19		6.65	9.06	11.25	12.97	14.69	16.25
isotropic					0	0.94	2.45	2.90	3.20	3.62	3.91

Table 3. Values of the post-critical limit cycle amplitude W_A versus the nondimensional dynamic pressure λ , in the third case.

The third case refers to an orthotropic plate of composite u.d. materials, made of carbon fibers and epoxy resin type C3, and having the following elastic parameters [Crivelli Visconti 1975]:

$$E_{\downarrow} = 107 \text{ GPa}, \quad E_{\leftarrow} = 7 \text{ GPa}, \quad G_{\downarrow\leftarrow} = 6 \text{ GPa}, \quad \nu_{\downarrow\leftarrow} = 0.24, \quad \nu_{\leftarrow\downarrow} = 0.0157. \quad (42)$$

The in-plane and out-of-plane boundary conditions are the same as in the previous cases. In Figure 4 the curve of the highest amplitude behavior versus λ corresponds to the orthotropic plate with the fibers lined up in the perpendicular direction to the airflow, i.e. $E_x = E_{\leftarrow}$ and $E_y = E_{\downarrow}$ ($E_x < E_y = E_r$). The lowest amplitude graph corresponds to the flutter limit cycle of the isotropic plate, with the Young’s modulus equal to the higher of the two Young’s moduli of the orthotropic plate, and likewise $\nu_r = 0.3$. The graphic curve located between the two previous ones corresponds to the orthotropic plate with the fibers aligned along the airflow direction, i.e. $E_x = E_{\downarrow}$ and $E_y = E_{\leftarrow}$ ($E_x = E_r > E_y$).

The data points, which in Figure 4 appear as dots, are shown in Table 3.

The fourth case refers to the same orthotropic plate of the previous case, but with the Young’s modulus E_r of the isotropic reference plate equal to the lower of E_x and E_y .

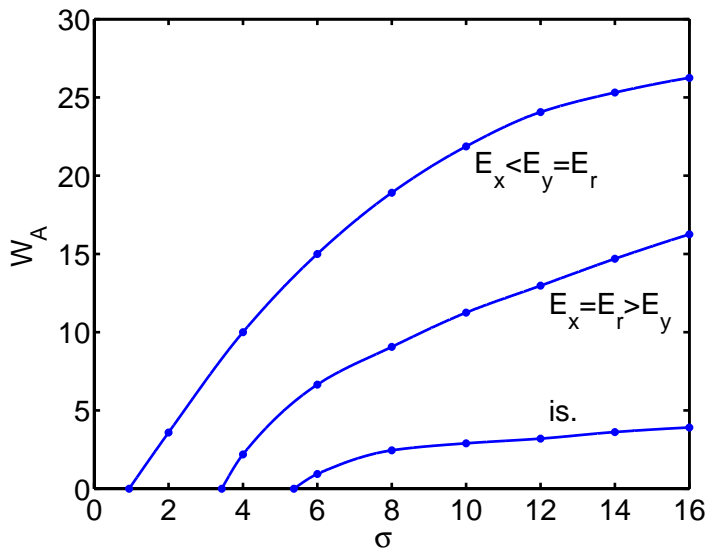


Figure 4. Behavior of the post-critical limit cycle amplitude W_A versus the nondimensional dynamic pressure λ in the third case considered.

λ	14.06	20.62	30.0	52.45	60.0	90.0	120.0	150.0	180.0	210.0	240.0
$E_x = E_r < E_y$	0		3.58		9.98	14.96	18.85	21.78	23.92	25.15	26.06
isotropic		0	2.19		6.43	9.52	11.76	13.34	14.78	15.95	17.03
$E_x > E_y = E_r$				0	2.18	6.63	9.02	11.17	12.82	14.45	16.00

Table 4. Values of the post-critical limit cycle amplitude W_A versus the nondimensional dynamic pressure λ , in the fourth case.

Figure 5 shows:

- (1) the highest amplitude graphic line, corresponding to the orthotropic plate with the fibers aligned along the perpendicular direction to the airflow ($E_x = E_r < E_y$);
- (2) the middle amplitude graph, corresponding to the isotropic reference plate;
- (3) the lowest amplitude chart line, corresponding to the orthotropic plate with the fibers aligned in the airflow direction ($E_x > E_y = E_r$), as in the second case.

The reason for which the values of λ in Figure 5 differ from those in Figure 4, though they refer to the same orthotropic plate, is the same as that explained above for the second case.

The data points, which in Figure 5 appear as dots, are summarized in Table 4.

The orthotropic fluttering plate described in the two last cases is the same as that of the first two cases, but there are different in-plane boundary conditions, with rectangular edges clamped for the in-plane displacements, whereas the same simply supported plate boundary conditions are supposed for the out-of-plane flutter behavior.

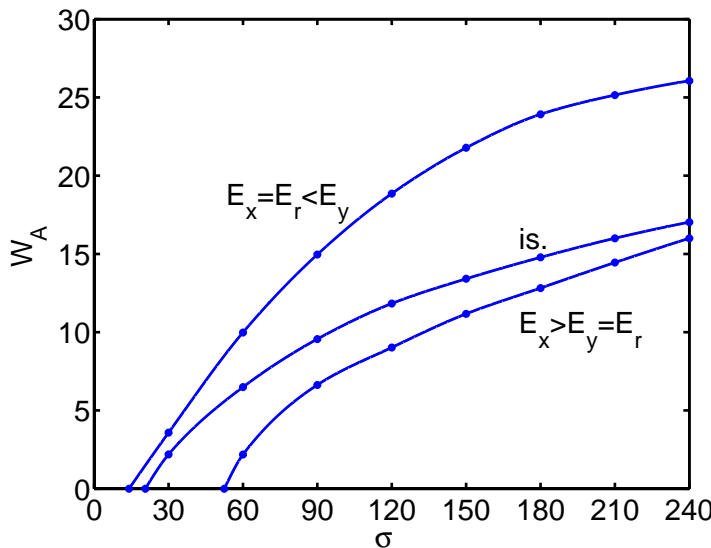


Figure 5. Behavior of the post-critical limit cycle amplitude W_A versus the nondimensional dynamic pressure λ in the fourth case considered.

λ	1.69	2.0	4.0	5.56	6.0	8.0	10.0	12.0	14.0	16.0
$E_x < E_y = E_r$	0	0.37	2.16		3.53	4.49	5.12	5.53	5.75	5.875
$E_x = E_r > E_y$			0		0.56	0.79	0.92	1.00	1.07	1.13
isotropic				0	0.18	0.62	0.75	0.81	0.875	0.91

Table 5. Values of the post-critical limit cycle amplitude W_A versus the nondimensional dynamic pressure λ , in the fifth case.

The fifth case refers to the isotropic plate with the Young’s modulus E_r equal to the higher of E_x and E_y , as in the first and third cases. Figure 6 exhibits the behavior versus λ of the limit cycle amplitude of the orthotropic plate both for $E_x < E_y = E_r$ and for $E_x = E_r > E_y$, respectively, and also of the isotropic plate with the smallest limit cycle amplitude values, as in Figures 2 and 4.

The data points, which in Figure 6 appear as dots, are written in Table 5.

Figure 7 shows the behavior versus λ of the flutter modal amplitude of the same orthotropic plate described in the fifth case, but with the Young’s modulus of the reference isotropic plate equal to the lower of E_x and E_y , as in the second and fourth cases. In this last sixth case, the graph of the lowest amplitude behavior versus λ corresponds to the orthotropic plate with fibers aligned along the airflow direction ($E_x > E_y = E_r$). The highest amplitude curve corresponds to the orthotropic plate with the fibers aligned along the perpendicular direction ($E_x = E_r < E_y$). The chart line of the isotropic plate is located between the two previous ones, as in Figure 3 and Figure 5. Also in this last case, as in the second and fourth cases, higher values of λ can be pointed out with respect to the previous case for the same above illustrated reason.

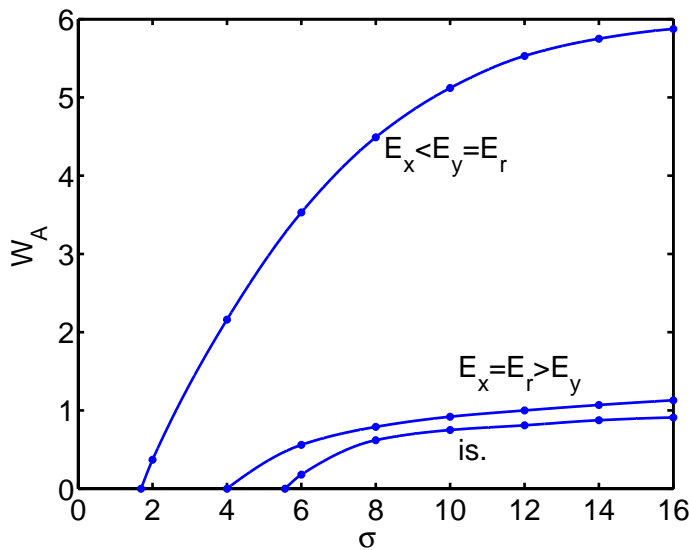


Figure 6. Behavior of the post-critical limit cycle amplitude W_A versus the nondimensional dynamic pressure λ in the fifth considered case.

λ	4.89	5.68	6.0	7.0	9.0	12.0	12.63	18.0	24.0	30.0	36.0	42.0	48.0
$E_x = E_r < E_y$	0.		0.33			2.05		3.37	4.32	5.0	5.45	5.71	5.87
isotropic		0.	0.16	0.42	0.65	0.79		0.97	1.08	1.18	1.26	1.30	1.33
$E_x > E_y = E_r$							0.	0.53	0.78	0.86	0.94	1.00	1.03

Table 6. Values of the post-critical limit cycle amplitude W_A versus the nondimensional dynamic pressure λ , in the sixth case.

The data points, which in Figure 7 appear as dots, are shown in Table 6.

To compare the amplitude values for limit cycles thus obtained with those found by other authors who use similar numerical schemes to find post-critical flutter solutions, one must take into account that our expression for the nondimensional dynamic pressure (first equation in (18)) differs from its nearest equivalent in those authors' works by the presence of π^4 in the denominator. Thus their values should be divided by approximately 100 ($\sim \pi^4$) for comparison with ours. With this precaution, we see that our limit cycles amplitudes are indeed comparable to those in the literature [Eastepe and McIntosh 1971; Shiau and Lu 1992; Xue and Mei 1993].

Table 7 shows the frequencies values versus the nondimensional dynamic pressure, in the last considered case. Similar dependence verifies in the previous considered cases.

Also, the obtained frequency values are comparable with those obtained by the other authors. If we look at the expression of the nondimensional time τ in the third of Equations (18), we notice that it would be the same as that utilized by the other above-mentioned authors, but for the presence of a coefficient π^2 . This means that the time τ values should be divided by about 10, and the corresponding nondimensional

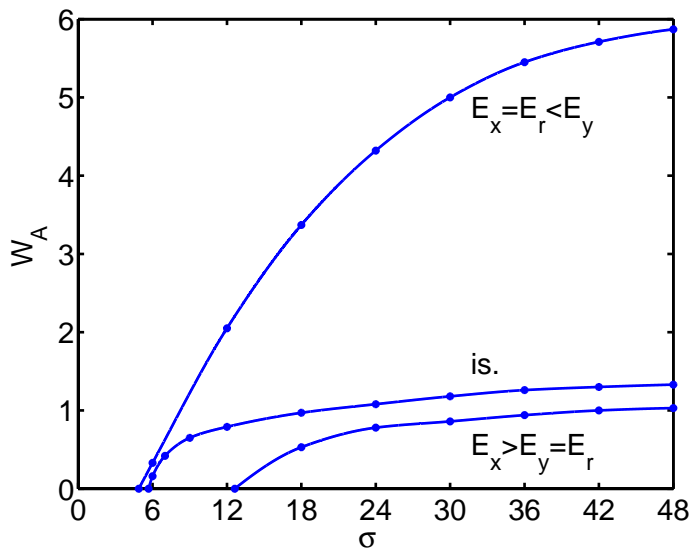


Figure 7. Behavior of the post-critical limit cycle amplitude W_A versus the nondimensional dynamic pressure λ in the sixth considered case.

λ	4.89	5.68	6.0	7.0	9.0	12.0	12.63	18.0	24.0	30.0	36.0	42.0	48.0
$E_x = E_r < E_y$	0.46		0.48			0.69		0.88	1.05	1.22	1.39	1.53	1.70
isotropic		0.70	0.72	0.9	1.3	1.85		2.95	4.0	4.76	5.85	6.75	7.48
$E_x > E_y = E_r$							3.3	4.9	6.35	7.70	9.01	10.31	11.40

Table 7. Values of the frequencies of the post-critical limit cycle versus the nondimensional dynamic pressure λ , in the sixth case.

Numerical parameters	Ritz	Ritz	Galerkin	Galerkin	FEM	FEM	FEM
N	30	42	36	64	80	120	168
W_A	5.838	5.872	5.856	5.872	5.941	5.903	5.881
ω	1.688	1.703	1.69	1.702	1.735	1.712	1.708
N	30	42	36	64	80	120	168
W_A	0.998	1.031	1.020	1.030	1.062	1.042	1.034
ω	11.383	11.402	11.398	11.401	11.443	11.421	11.410

Table 8. Values of amplitude and frequency in the sixth case for $\lambda = 48$, with $E_x = E_r < E_y$ (top) and $E_x > E_y = E_r$ (bottom), obtained by the three different methods with various values of the number N of the Lagrangian d.o.f.

frequency multiplied by the same coefficient for a significant comparison with the same parameter values obtained by the other authors. Thus it is reasonable to conclude that these derived frequency values are comparable with those shown in the graphs in [Ketter 1967; Eastep and McIntosh 1971].

Table 8 gives the values of the frequency and amplitude in the last case considered, corresponding to $\lambda = 48$ and for $(E_x > E_y = E_r)$ and $(E_x = E_r < E_y)$, and obtained by the three methods with different numbers of Lagrangian degrees of freedom. It is possible to evince the higher convergence rate of Ritz and Galerkin method with respect to the FEM, and the convergence of FEM results towards those of the two other methods, as the number of degrees of freedom grows indefinitely. It is evident enough that the amplitude values obtained by the three different methods are very close, and that the same chart lines would be derived by each method. The same is true for the previous cases considered, and the comparisons performed in this last case are sufficiently illustrative of the good agreement between the results obtained by the three different numerical schemes.

The meaning of the Table 9 is explained in the Appendix.

4. Discussion and conclusion

Concerning the post-critical flutter behavior of the vibrating panel, a significant effect of the plate elastic parameters on the amplitude of the limit cycle stationary solution has been detected. The importance of this amplitude value is fundamental, because, as mentioned earlier, it is a significant parameter of the vibrating panel resistance under the effects of a supersonic airflow.

i_{ψ_x}, i_{ψ_y}	$P_{i_{\psi_x}}, P_{i_{\psi_y}}$	N_d	N_p
1	4.712389	3.829886	
2	7.853982		17.923313
3	10.995574	86.324865	
4	14.137167		415.2424
5	17.278760	1997.5148	
6	20.420352		9608.99
7	23.561945	46223.87	
8	26.703538		222358.8966

Table 9. Values of $P_{i_{\psi_x}}, P_{i_{\psi_y}}$ and N_d, N_p versus i_{ψ_x}, i_{ψ_y} .

Furthermore, even a cursory examination of the obtained results is sufficient to conclude that the importance of the elastic Young’s modulus in the flow direction is predominant with respect to the one in the perpendicular direction, as far as the flutter phenomenon is concerned.

In every case of the orthotropic fluttering plate if $E_x > E_y$, the amplitude of the post-critical limit cycle, is lower than the corresponding one with $E_x < E_y$. This fact is consistent with the results of [Shiau and Lu 1992], who found that the alignment of the fibers of a multilayer angle-ply laminate with the airflow direction diminishes the limit cycle amplitude, and consequently that the panel resistance to the flutter phenomenon grows. It is obvious that the smaller the angle between fibers and a reference axis in each lamina, the higher the Young’s modulus of the equivalent orthotropic plate of the multilayer laminate along the same axis. Thus, with the increasing value of this modulus E_x along the flow direction, the vibration amplitude diminishes, and consequently it can be considered an elastic parameter of paramount importance as far as the limit cycle post-critical solution is concerned.

However the Poisson’s moduli are also elastic parameters, which, after the above-mentioned one, play an important role in the considered phenomenon, because a remarkable effect of their values on the flutter amplitude can be evinced. (See Figures 3, 5 and 7.) In the corresponding cases considered, the Young’s modulus of the isotropic reference plate is equal to the lower of the two Young’s moduli of the orthotropic plate. The graphic curve of its flutter amplitude behavior versus λ lies between the two curves of the orthotropic plate. It means that the limit cycle amplitude of the isotropic plate is lower than the corresponding one of the orthotropic plate with $E_x = E_r < E_y$, although its Young’s modulus E_r is equal to the smaller of E_x and E_y .

This fact bears further analysis. To this end it is necessary to recall the flexural rigidity moduli, introduced in Equation (3):

$$D_x = \frac{E_x h^3}{1 - \nu_{xy}\nu_{yx}}, \quad D_y = \frac{E_y h^3}{1 - \nu_{xy}\nu_{yx}}. \tag{43}$$

It is evident that the Poisson’s moduli ν_{xy}, ν_{yx} influence these out-of-plane rigidity parameters, because the higher their product is, the larger these parameters are. In these subcases with $E_x = E_r < E_y$ the Young’s modulus E_r of the isotropic reference plate is equal to the lower one E_x of the orthotropic plate, but the Poisson’s modulus $\nu_r = 0.3$ of the isotropic plate is larger than the two corresponding ones of the

orthotropic plate, as shown in Equations (41) and (42). Thus, although $E_r = E_x$, a value of this stiffness bending parameter $D_{x,is} = D_r$ along the x axis is obtained for the isotropic plate bigger than the one D_x of the orthotropic plate:

$$D_{x,is} = D_r = \frac{E_x h^3}{1 - \nu_r^2} > D_x = \frac{E_x h^3}{1 - \nu_{xy} \nu_{yx}}, \quad 1 - \nu_r^2 < 1 - \nu_{xy} \nu_{yx}. \tag{44}$$

This means that there is a higher flexural rigidity along the airflow direction (coincident with the x axis direction) in the isotropic panel.

On the contrary, along the perpendicular y axis direction the Young’s modulus E_y of the orthotropic plate is higher enough than E_r , so the flexural rigidity parameter D_y of the orthotropic plate is much larger than the corresponding one $D_{y,is} = D_r$ of the isotropic plate, in spite of the higher value of the Poisson’s modulus ν_r with respect to both ν_{xy} and ν_{yx} :

$$D_{y,is} = D_{x,is} = D_r = \frac{E_r h^3}{1 - \nu_r^2} < D_y = \frac{E_y h^3}{1 - \nu_{xy} \nu_{yx}}, \quad E_r = E_x \ll E_y. \tag{45}$$

Also, the modulus of mixed flexural rigidity between the two directions is important because, as in Equation (1), it influences the fluttering dynamics. This increases more than D_x when we pass from the orthotropic to the isotropic plate:

$$D_{xy,is} = \nu_r D_r = \nu_r \frac{E_r h^3}{1 - \nu_r^2} > D_{xy} = \nu_{xy} D_y = \nu_{xy} \frac{E_y h^3}{1 - \nu_{xy} \nu_{yx}}, \tag{46}$$

although, as above mentioned, E_y is much higher than $E_x = E_r$, but the product $\nu_r E_r$ is bigger than $\nu_{xy} E_y$ for both considered orthotropic panels, as seen from Equations (41) and (42). Furthermore this inequality is true also for the same other reason illustrated in Equation (44): $1 - \nu_r^2 < 1 - \nu_{xy} \nu_{yx}$.

Precisely the same holds for the extensional rigidity parameter $A_x = E_x h / (1 - \nu_{xy} \nu_{yx})$ along the flow direction, which is smaller than the corresponding one $A_{x,is} = A_r = E_r h / (1 - \nu_r^2)$ of the isotropic plate, although the Young’s modulus E_r of the reference plate is equal to the lower of the two ones of the orthotropic plate, for the same reason stated earlier concerning the Poisson’s moduli. A much higher value of $A_y = E_y h / (1 - \nu_{xy} \nu_{yx})$ along the perpendicular direction corresponds to the orthotropic plate. The same thing is also true for the mixed extensional rigidity parameter, which is much higher for the isotropic plate.

The resulting effect is that the limit cycle amplitude is lower if the isotropic plate is employed with respect to the one of the orthotropic plate with fibers oriented in the perpendicular direction to the airflow, even if $E_r = E_x < E_y$, although the bending and extensional stiffness along the y axis direction of the orthotropic plate is much larger. In particular, increasing the flexural and extensional rigidity parameters in the airflow direction, along with the corresponding ones of the mixed rigidity, has an enhancing effect on the panel resistance to the flutter phenomenon much higher than increasing the same rigidity parameters in the perpendicular direction. This means that a much higher value of the Young’s modulus of the orthotropic plate along the direction perpendicular to the airflow has lower influence on the considered phenomenon than a larger value of the Poisson’s moduli—that is, the importance of these moduli ν_{xy} , ν_{yx} is predominant with respect to E_y .

If one looks carefully at Figures 3, 5 and 7, a further remark can be highlighted. For small values of the limit cycle amplitude, the $W_A - \lambda$ graphic curve of the isotropic plate is very near to the one of the orthotropic plate with $E_x = E_r < E_y$, but with the increasing dynamic pressure this curve tends to the one of the orthotropic plate with $E_x > E_y = E_r$, characterized by a higher resistance to the flutter phenomenon. This means that increasing the values of the Poisson's moduli correspondingly improves the resistance to the flutter phenomenon as the dynamic pressure grows.

Concerning the shear rigidity modulus $G_{xy} = G_{\downarrow\leftarrow}$, no particular remarkable influence on the fluttering plate dynamics has been detected. In fact, in all the cases considered with $E_x = E_r < E_y$ this modulus is smaller for the isotropic plate. In the first considered orthotropic panel, whose elastic coefficients are defined in Equations (41), the value of this parameter of the reference isotropic plate is $G_{xy, is} = G_r = E_r/2(1 + \nu_r) = 5.38$ GPa, because $E_r = E_x = E_{\leftarrow} = 14$ GPa, which is smaller than the corresponding one of the orthotropic plate $G_{\downarrow\leftarrow} = 6$. But we have a much lower value of this parameter for the isotropic reference plate if the Young's modulus of the second considered orthotropic panel is assumed (see Equations (42)). In fact, $G_{xy, is} = G_r = E_r/2(1 + \nu_r) = 2.69$ GPa because $E_r = E_x = E_{\leftarrow} = 7$ GPa, and we have the same value of $G_{\downarrow\leftarrow} = 6$. The resistance of the reference isotropic plate to the flutter phenomenon is higher than the one of both considered orthotropic panels, with the fibers aligned along the direction perpendicular to the airflow, even if $E_r = E_x < E_y$, for the above illustrated reason concerning the Poisson's moduli. Therefore decreasing the in-plane shear rigidity modulus has a quite negligible effect.

The use of three different numerical schemes to achieve the requested results, can offer a sufficient guarantee of the validity of the present numerical analysis, considering the good concordance between the results derived by the three methods. However, in some more complicated cases it could be difficult to apply the Galerkin method; in these more difficult circumstances, it would be useful to observe the slower convergence of the FEM results toward those of the Ritz procedure with the increasing number of d.o.f.; see [Tizzi 1994; 1999; 2003a].

Our analysis of flutter has been limited within the framework of the linearized piston theory. Yet it would seem relevant to know the influence of the nonlinear contribution to the aerodynamic forces on the permanent post-critical solution of the fluttering panel, confining attention to the limit cycle amplitude, which is particularly important for the reasons explained above. At a recent Italian congress (2005), we have presented evidence that also in post-critical conditions, if the dynamic pressure doesn't exceed overly much its critical value, limited effects of the nonlinear contributions to the aerodynamic forces can be seen. This would always be true but for the presence of particular initial conditions (such as those induced by a gust), which can instigate instability and chaos even before the critical value of the dynamic pressure is reached [Dessi et al. 2002]. Also, the presence of shock waves in transonic flight could instigate instability in the flutter phenomenon. It is indispensable to take into account the nonlinear contributions to aerodynamic forces in such cases, and this will undoubtedly be the focus of continued research.

Appendix

Functions utilized with Galerkin method in the free in-plane boundary conditions case. The functional elements of the nondimensional Airy function $\psi(\xi, \eta)$ series expansion in Equations (11) and (12), are

formed by two separate components, depending on ξ and η , respectively:

$$\varphi_{i\psi}(\xi, \eta) = \varphi_{i\psi_x}(\xi)\varphi_{i\psi_y}(\eta),$$

where both components $\varphi_{i\psi_x}(\xi)$ and $\varphi_{i\psi_y}(\eta)$ vanish at the rectangular edges, along with their first normal derivatives:

$$\begin{aligned} \varphi_{i\psi_x}(0) = (\varphi_{i\psi_x})'(0) = \varphi_{i\psi_x}(1) = (\varphi_{i\psi_x})'(1) = 0, \quad ()' &= \frac{\partial()}{\partial\xi}, \\ \varphi_{i\psi_y}(0) = (\varphi_{i\psi_y})'(0) = \varphi_{i\psi_y}(1) = (\varphi_{i\psi_y})'(1) = 0, \quad ()' &= \frac{\partial()}{\partial\eta}, \end{aligned} \tag{A.1}$$

because, taking into account the membrane stresses dependence on the Airy function [Santini 1973], the in-plane boundary conditions in Equation (4) are satisfied. For convenience, functions are utilized which satisfy further conditions:

$$\begin{aligned} \frac{d^4\varphi_{i\psi_x}}{d\xi^4} &= p_{i\psi_x}^4 \varphi_{i\psi_x}, & \frac{d^4\varphi_{i\psi_y}}{d\eta^4} &= p_{i\psi_y}^4 \varphi_{i\psi_y}, \\ \int_0^1 \varphi_{i\psi_x} \varphi_{j\psi_x} d\xi &\cong \delta_{i\psi_x j\psi_x}, & \int_0^1 \varphi_{i\psi_y} \varphi_{j\psi_y} d\eta &\cong \delta_{i\psi_y j\psi_y}. \end{aligned}$$

Consequently the expressions of $\varphi_{i\psi_x}$ can be written as

$$\varphi_{i\psi_x}(\xi) = \frac{1}{N_d} \left\{ \cos\left(\frac{p_{i\psi_x}}{2}\right) \cosh\left[p_{i\psi_x}\left(\xi - \frac{1}{2}\right)\right] - \cosh\left(\frac{p_{i\psi_x}}{2}\right) \cos\left[p_{i\psi_x}\left(\xi - \frac{1}{2}\right)\right] \right\}, \quad i\psi_x = 1, 3, 5, \dots,$$

$$\varphi_{i\psi_x}(\xi) = \frac{1}{N_p} \left\{ \sin\left(\frac{p_{i\psi_x}}{2}\right) \sinh\left[p_{i\psi_x}\left(\xi - \frac{1}{2}\right)\right] - \sinh\left(\frac{p_{i\psi_x}}{2}\right) \sin\left[p_{i\psi_x}\left(\xi - \frac{1}{2}\right)\right] \right\}, \quad i\psi_x = 2, 4, 6, \dots,$$

where

$$p_{i\psi_x} = (2i\psi_x + 1) \frac{\pi}{2}$$

and

$$N_d^2 = \left[\cosh\left(\frac{p_{i\psi_x}}{2}\right) \right]^2 \left[\frac{1}{2} - \frac{\cos\left(\frac{p_{i\psi_x}}{2}\right) \sin\left(\frac{p_{i\psi_x}}{2}\right)}{p_{i\psi_x}} \right] + \left[\cos\left(\frac{p_{i\psi_x}}{2}\right) \right]^2 \left[\frac{1}{2} - \frac{\cosh\left(\frac{p_{i\psi_x}}{2}\right) \sinh\left(\frac{p_{i\psi_x}}{2}\right)}{p_{i\psi_x}} \right],$$

$$N_p^2 = \left[\sinh\left(\frac{p_{i\psi_x}}{2}\right) \right]^2 \left[\frac{1}{2} - \frac{\cos\left(\frac{p_{i\psi_x}}{2}\right) \sin\left(\frac{p_{i\psi_x}}{2}\right)}{p_{i\psi_x}} \right] + \left[\sin\left(\frac{p_{i\psi_x}}{2}\right) \right]^2 \left[\frac{1}{2} - \frac{\cosh\left(\frac{p_{i\psi_x}}{2}\right) \sinh\left(\frac{p_{i\psi_x}}{2}\right)}{p_{i\psi_x}} \right],$$

and similarly for $\varphi_{i\psi_y}$, with $p_{i\psi_y}$ in place of $p_{i\psi_x}$ and η in place of ξ . The conditions in Equation (A.1) referring to the first derivatives are satisfied if it is taken into account that

$$\tan\left(\frac{p_{i\psi_x}, p_{i\psi_y}}{2}\right) \cong 1$$

for the values of $p_{i\psi_x}$ and $p_{i\psi_y}$ used.

The values of $p_{i\psi_x}, p_{i\psi_y}$ connected with $i\psi_x, i\psi_y$, together with N_d, N_p , are summarized in Table 9, for $i\psi_x, i\psi_y = 1, 2, \dots, 8$.

References

- [Abbas et al. 1993] J. F. Abbas, R. A. Ibrahim, and R. F. Gibson, “Nonlinear flutter of orthotropic composite panel under aerodynamic heating”, *AIAA J.* **31**:8 (1993), 1478–1488.
- [Bisplinghoff 1962] R. L. Bisplinghoff, *Principles of aeroelasticity*, Wiley, New York, 1962.
- [Bolotin 1963] V. V. Bolotin, *Nonconservative problems of the theory of elastic stability*, MacMillan, New York, 1963.
- [Crivelli Visconti 1975] I. Crivelli Visconti, *Materiali compositi – tecnologie e progettazione*, Tamburini, Milano, 1975.
- [Dessi et al. 2002] D. Dessi, F. Mastroddi, and L. Morino, “Limit-cycle stability reversal near a Hopf bifurcation with aeroelastic applications”, *J. Sound Vib.* **256**:2 (2002), 347–365.
- [Dixon and Mei 1993] I. R. Dixon and C. Mei, “Finite element analysis of large-amplitude panel flutter of thin laminates”, *AIAA J.* **31**:4 (1993), 701–707.
- [Dowell 1966] E. H. Dowell, “Nonlinear oscillations of a fluttering plate”, *AIAA J.* **4**:7 (1966), 1267–1275.
- [Dowell 1967] E. H. Dowell, “Nonlinear oscillations of a fluttering plate, II”, *AIAA J.* **5**:10 (1967), 1856–1862.
- [Eastep and McIntosh 1971] F. E. Eastep and S. C. McIntosh, Jr., “Analysis of nonlinear panel flutter and response under random excitation or nonlinear aerodynamic loading”, *AIAA J.* **9**:3 (1971), 411–418.
- [Kantorowich and Krylov 1964] L. V. Kantorowich and V. I. Krylov, *Approximate methods of higher analysis*, Interscience, New York, 1964.
- [Ketter 1967] D. J. Ketter, “Flutter of flat, rectangular, orthotropic panels”, *AIAA J.* **5**:1 (1967), 116–124.
- [Kikuchi 1986] N. Kikuchi, *Finite element methods in mechanics*, Cambridge University Press, Cambridge, 1986.
- [Lambert 1991] J. D. Lambert, *Numerical methods for ordinary differential systems*, Wiley, Chichester, UK, 1991.
- [Merson 1957] R. H. Merson, “An operational method for the study of integration processes”, pp. 110–125 in *Proc. Symp. Data Processing* (Salisbury, S. Australia, 1957), Weapons Res. Establ. Salisbury, 1957.
- [Mikhlin 1964] S. G. Mikhlin, *Variational methods in mathematical physics*, Pergamon Press, Oxford, 1964.
- [Pars 1968] L. A. Pars, *A treatise on analytical dynamics*, Heinemann Educational Books, Ltd., London, 1968.
- [Reddy 1986] J. N. Reddy, *Applied functional analysis and variational methods in engineering*, McGraw-Hill, New York, 1986.
- [Reddy et al. 1988] J. N. Reddy, C. S. Krishnamoorthy, and K. N. Seetharamu, *Finite element analysis for engineering design*, Springer, Berlin, 1988.
- [Santini 1973] P. Santini, *Introduzione alla teoria delle strutture*, Tamburini Editore, Milano, 1973.
- [Shiau and Lu 1992] L. C. Shiau and L. T. Lu, “Nonlinear flutter of two-dimensional simply supported symmetric composite laminated plates”, *J. Aircr.* **29**:1 (1992), 140–145.
- [Tizzi 1994] S. Tizzi, “A numerical procedure for the analysis of a vibrating panel in critical flutter conditions”, *Comput. Struct.* **50**:3 (1994), 299–316.
- [Tizzi 1997] S. Tizzi, “Numerical procedure for the dynamic analysis of three-dimensional aeronautical structures”, *J. Aircr.* **34**:1 (1997), 120–130.
- [Tizzi 1999] S. Tizzi, “Free frequencies and modal shapes of cylindrical vibrating composite structures”, *Comput. Struct.* **73**:6 (1999), 629–653.
- [Tizzi 2003a] S. Tizzi, “Influence of non-linear forces on beam behaviour in flutter conditions”, *J. Sound Vib.* **267**:2 (2003), 279–299.
- [Tizzi 2003b] S. Tizzi, “Three numerical procedures for the post-critical flutter of an orthotropic plate”, preprint, Aerospace and Astronautics Engineering Department, Università di Roma “La Sapienza”, June 2003. Available at the web page for this paper.
- [Xue and Mei 1993] D. Y. Xue and C. Mei, “Finite element nonlinear panel flutter with arbitrary temperatures in supersonic flow”, *AIAA J.* **31**:1 (1993), 154–162.
- [Zhou et al. 1994] R. C. Zhou, D. Y. Xue, and C. Mei, “Finite element time domain—modal formulation for nonlinear flutter of composite panels”, *AIAA J.* **32**:10 (1994), 2044–2052.

[Zhou et al. 1995] R. C. Zhou, Z. Lai, D. Y. Xue, J. K. Huang, and C. Mei, "Suppression of nonlinear panel flutter with piezoelectric actuators using finite element method", *AIAA J.* **33**:6 (1995), 1098–1105.

[Zhou et al. 1996] R. C. Zhou, C. Mei, and J. K. Huang, "Suppression of nonlinear panel flutter at supersonic speeds and elevated temperatures", *AIAA J.* **34**:2 (1996), 347–354.

Received 9 Jul 2006. Revised 30 Nov 2006. Accepted 15 Feb 2007.

SILVANO TIZZI: s.tizzi@caspur.it

Aerospace and Astronautics Engineering Department, University of Rome "La Sapienza", Via Eudossiana 16, 00184 Rome, Italy

MICROMECHANICAL APPROACH TO TRANSFORMATION TOUGHENING IN ZIRCONIA-ENRICHED MULTIPHASE COMPOSITES

HIDEAKI TSUKAMOTO AND ANDREI KOTOUSOV

A micromechanical model based on the mean-field approach was developed to investigate the effect of the mismatch in material properties of the constituents on the transformation toughening in zirconia enriched multiphase composites. Important results have been obtained for SiC/Al composites, which have a large potential for application in lightweight automotive structures.

1. Introduction

The phenomenon of stress transformation in zirconia-enriched composites was first reported by Garvie et al. [1975]. Some of the early experimental investigations on zirconia composites were performed by Gupta et al. [1978], Evans and Heuer [1980], Lange [1982], and others. In accordance with these investigations, the unconstrained phase transformation of zirconia particles results in approximately 4% dilatation and 16% shear strain. However, the particles embedded in a composite transform with twin bands of an alternative character so that the overall change in shear strain is very small [Simha and Truskinovsky 1994]. Therefore, the strain changes due to stress-induced phase transformation in composites are usually assumed to be dilatant.

When the particles surround a stable or a growing crack, the high stress concentration near the crack tip will trigger the transformation of zirconia particles near the crack tip. The typical transformation zone sizes found experimentally are on the order of 20 μm or less [Casellas et al. 2001]. The dilatant transformation will induce closure tractions on/along the crack faces. The overall stress concentration near the crack tip is, therefore, reduced; hence, the fracture toughness of the composite is enhanced, since a higher remote stress must be applied to reach the critical conditions at the crack tip.

The stress-induced transformation toughening mechanism has been successfully used to increase the fracture toughness of brittle ceramics [Kelly and Rose 2002; Basu et al. 2004]. In recent years, the demand for the development of super high temperature resistant and lightweight materials applied to aerospace structures has stimulated intensive research on the transformation toughening of brittle intermetallics composites, particularly with molybdenum or nickel aluminide matrices [Sbaizero et al. 2003]. The transformation toughening mechanism is now regarded as the most effective way to enhance the fracture toughness of ceramics and ceramic matrix composites [Kelly and Rose 2002; Basu et al. 2004; Cesari et al. 2006].

The continuum models of the phenomenon were developed by Lange [1982], McMeeking and Evans [1982], Budiansky et al. [1983], and Stump and Budiansky [1989]. All of these models are based on the assumption of effectively homogeneous composite material, where only macroscopic aspects of the

Keywords: transformation toughening, micromechanics, multiphase composites, crack, zirconia particles, continuum model, dilatant strain.

material deformation are considered. Strictly speaking, these theories are only applicable to a composite with the same material properties in all constituent phases, which have to be equal to the material properties of zirconia. However, in a real composite, the effect of the mismatch in material properties of the constituent phases on the transformation toughening mechanism can be significant. Consider, for example, a limiting case—a two-phase composite with rigid matrix and soft transformable particles. In such a composite the stress induced transformation in the particles will not affect the dilatation of the representative volume element (RVE) of the composite [Hill 1963] and, in its turn, the high stress concentration in the RVE in the vicinity of the crack tip will generate much less stress in the particles, reducing the size of the transformation zone. Both mechanisms will lead to a greatly reduced toughening effect in comparison with that predicted assuming homogeneous material with effective properties of the composite (continuum models). It can be shown that the opposite situation to that described above takes place for a composite with a soft matrix and rigid particles. When a multiphase composite is enriched with zirconia particles, the final effect of the mismatch in the material properties of the constituent phases is difficult to envisage.

A number of numerical studies have reported a significant influence of local stress concentration, particle size, shape and microstructure on the transformation toughening mechanism. Some of these factors were recently analyzed using a hybrid finite element method [Zeng et al. 2004; Alfano et al. 2006] and a micromechanical approach [Tsukamoto and Kotousov 2006]. The previous studies focused primarily on two-phase composite systems. For multiphase composites, in addition to the factors discussed above, a strong influence of the nontransforming dispersed phases on the transformation toughening mechanism is also expected. This was confirmed by results of some experimental investigations [Chen et al. 2000; Chen and Tuan 2001]. However, it seems that so far there have been no attempts to study theoretically the toughening effect in multiphase composites [Zeng et al. 2004].

In this paper, a micromechanical model is developed and incorporated into the continuum model of transformation toughening of Stump and Budiansky [1989], to investigate the effect of the mismatch of the constituent phases on the transformation toughening mechanism in multiphase composites. This model is based on the mean-field theory of Wakashima and Tsukamoto [1991]. It was reported in the literature that among the averaging methods [Hill 1963; Bui et al. 1972], the Wakashima–Tsukamoto estimate provides the closest prediction to numerical calculations in terms of the effective material properties of the composite [Miyamoto et al. 1999]. Similar methods were discussed in some other works, for example, [Ponte-Castaneda and Willis 1995; Cho and Ha 2001].

2. Continuum theory of transformation toughening

For the sake of completeness of this paper a brief introduction of the continuum model of transformation toughening [Stump and Budiansky 1989] will be presented next. Assume that a transformation zone surrounding the crack tip has undergone an irreversible transformation dilatation of strength $f^{(1)}\theta$ where $f^{(1)}$ is the zirconia particle volume fraction and θ is the unconstrained particle dilatation (Figure 1). Since typical transformation zone sizes are on the order of $20\ \mu\text{m}$ or less, the small scale zone size approximation can be invoked. Then, the stress field in the vicinity of the crack tip can be described as

$$\sigma_{ik} = \frac{K}{\sqrt{2\pi r}} F_{ik}(\phi), \quad (1)$$

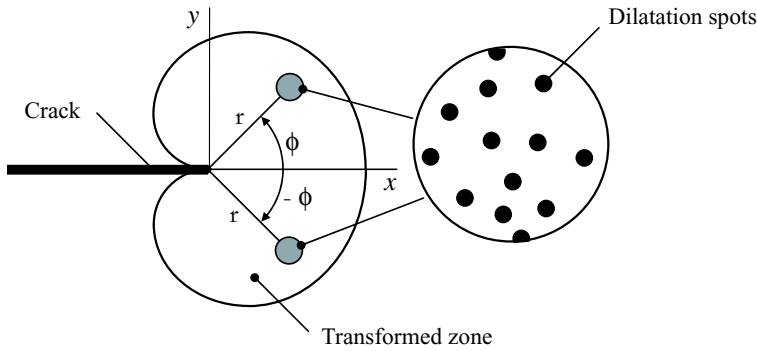


Figure 1. Symmetrically placed dilatant spots at a crack tip.

where K is the stress intensity factor at the crack tip, r is the distance from the crack tip, and $F_{ik}(\phi)$ is the well known trigonometric function.

The mean stress due to dilatation can be calculated using Hutchinson’s solution for two small circular spots of dilatation of area dA located at $z_0 = x_0 + iy_0$ and $\bar{z}_0 = x_0 - iy_0$ (Figure 1) [Hutchinson 1974] as

$$\sigma_m = \frac{E f^{(1)} \theta}{18\pi} \frac{1 + \nu}{1 - \nu} \operatorname{Re} \left\{ \frac{1}{\sqrt{z z_0} (\sqrt{z} + \sqrt{z_0})} + \frac{1}{\sqrt{z \bar{z}_0} (\sqrt{z} + \sqrt{\bar{z}_0})} \right\} dA, \tag{2}$$

where E is Young’s modulus and ν is Poisson’s ratio.

The equation for the zone boundary, $z = R(\phi)e^{i\phi}$, is then obtained by adding the near field mean stress of Equation (1) to the zone contribution calculated by integrating Equation (2) over the upper half of the transformed zone, and equating the sum to σ_m^c as

$$\sigma_m^c = \frac{K(1 + \nu)}{3} \sqrt{\frac{\pi R}{2}} \cos(\phi/2) + \int_A F(z, z_0) dA, \tag{3}$$

where σ_m^c is the critical value for mean stress corresponding to the phase transformation, and $F(z, z_0)$ is given by Equation (2).

The stress intensity factor at the crack tip, K , is equal to the sum of the applied stress intensity factor K_{ap} and that induced by the presence of the transformed zone. Once the transformed zone is found, K as a function of K_{ap} can be obtained by integrating the change of the stress intensity factor ΔK due to the two small circular spots of dilatation, as

$$\Delta K = \frac{E f^{(1)} \theta}{6\sqrt{2\pi}(1 - \nu)} \operatorname{Re} \{ z_0^{-3/2} + \bar{z}_0^{-3/2} \} dA \tag{4}$$

over the upper half of the transformed zone

$$K = K_{ap} + \int_A \Delta K(z, z_0) dA. \tag{5}$$

A similar procedure can be adapted to the growing crack case as well. Details can be found in Stump and Budiansky [1989]. The final result of the calculation of the fracture toughening of the composite for a stable and a growing crack is shown in Figure 2.

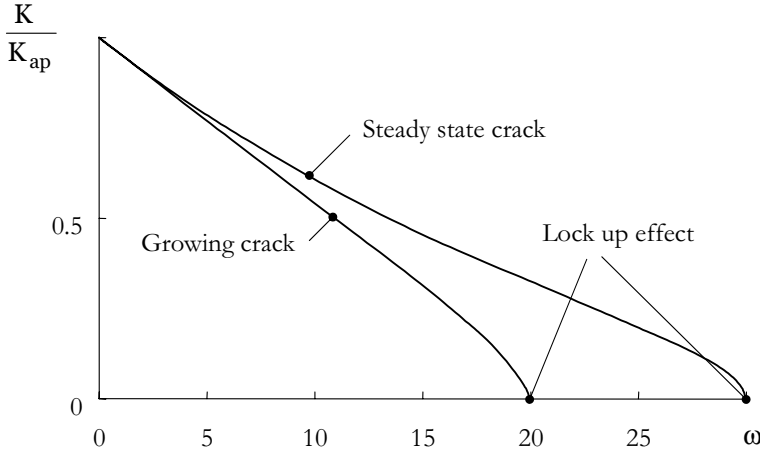


Figure 2. Fracture toughening versus the strength of transformation, ω .

In Figure 2 the nondimensional measure of the strength of the transformation, ω , is defined by

$$\omega = \frac{E f^{(1)} \theta}{\sigma_m^c} \frac{1 + \nu}{1 - \nu}. \tag{6}$$

The toughening effect increases with the increase of the strength of the transformation. The most notable feature of Figure 2 is the existence of the *lock-up* effect, that is, infinite toughening of the composite, which was discovered by Rose [1986]. It occurs at $\omega \approx 30$ for the steady state case, and at $\omega \approx 20.2$ for the growing crack.

3. Mean-field micromechanical model

In this section, a composite consisting of N types of inclusions uniformly and randomly distributed in an isotropic continuum matrix is considered. Let us introduce a representative volume element (RVE) of the general heterogeneous media. When the RVE is subjected to macrostress $\bar{\sigma}_{ik}$ (corresponding to the traction vector $t_i = \bar{\sigma}_{ik} n_k$), the volume average of the induced microstress, σ_{ik}^{ap} , over RVE is equal to the macrostress $\bar{\sigma}_{ik}$ such that

$$\frac{1}{V^R} \int_{V^R} \sigma_{ik}^{ap} dV = \bar{\sigma}_{ik}, \tag{7}$$

where V^R is the volume of RVE. The volume average of the internal stress, σ_{ik}^{in} , due to the presence of eigenstrain, ε_{ij}^* , which was introduced by Mura [1982], is equal to zero, that is,

$$\frac{1}{V^R} \int_{V^R} \sigma_{ik}^{in} dV = 0. \tag{8}$$

For the system under consideration, the potential energy, Φ , is defined as

$$\Phi = \frac{1}{2} \int_{V^R} (\sigma_{ik}^{ap} + \sigma_{ik}^{in}) \cdot (\varepsilon_{ik}^{ap} + \varepsilon_{ik}^{in} - \varepsilon_{ik}^*) dv - \int_{S^R} (\sigma_{ik}^{ap} n_k) \cdot (u_i^{ap} + u_i^{in}) ds, \quad (9)$$

where S^R is the surface of the RVE, and the repeated indexes assume the usual summation convention.

Equation (9) can be rewritten in terms of summations of piecewise uniform quantities as

$$\Phi = -\frac{1}{2} \bar{\sigma}_{ik} \sum_{r=0}^N f^{(r)} M_{iklm}^{(r)} \bar{\sigma}_{lm}^{ap(r)} - \frac{1}{2} \sum_{r=0}^N f^{(r)} \varepsilon_{ik}^{*(r)} \cdot \bar{\sigma}_{ik}^{in(r)} - \sum_{r=0}^N f^{(r)} \varepsilon_{ik}^{*(r)} \cdot \bar{\sigma}_{ik}^{ap(r)}, \quad (10)$$

where the superscript (r) is the number identifying the constitutive phases and r runs from $0-N$, 0 denotes the matrix, and $1-N$ denotes the corresponding dispersed particle phase. $M_{iklm}^{(r)}$ is the elastic compliance tensor of r -th phase, and $\varepsilon_{ik}^{*(r)}$ is the eigenstrain in r -th phase. $\bar{\sigma}_{ik}^{ap(r)}$ and $\bar{\sigma}_{ik}^{in(r)}$ are the volumetric average of the microstresses in phase (r) due to external loading and internal factors such as thermal expansion, plastic deformations and the like, respectively. Hill [1963] reported that $\bar{\sigma}_{ik}^{ap(r)}$ is proportional to the applied macrostress, $\bar{\sigma}_{ik}$. This can be written mathematically as

$$\bar{\sigma}_{ik}^{ap(r)} = B_{iklm}^{(r)} \bar{\sigma}_{lm}, \quad (11)$$

where $B_{iklm}^{(r)}$ is the stress concentration factor tensor. Equations (7) and (11) lead to the following relation:

$$\sum_{r=0}^N f^{(r)} B_{iklm}^{(r)} = I_{iklm}, \quad (12)$$

where I_{iklm} is the fourth order identity tensor.

According to the mean-field micromechanical theory [Wakashima and Tsukamoto 1991], which is based on Eshelby's equivalent inclusion method [Eshelby 1957; 1959; 1961] and Mori-Tanaka's mean-field approximation [Mori and Tanaka 1973], the following algebraic relations for $B_{iklm}^{(r)}$ can be derived:

$$B_{iklm}^{(r)} = C_{ikop}^{(r)} \left\{ \sum_{s=0}^N f^{(s)} C_{oplm}^{(s)} \right\}^{-1}, \quad (13)$$

$$C_{iklm}^{(r)} = \{ I_{iklm} + P_{ikop}^{(r)} (M_{oplm}^{(r)} - M_{oplm}^{(0)}) \}^{-1}, \quad (14)$$

$$P_{iklm}^{(r)} = L_{ikop}^{(0)} (I_{oplm} - S_{oplm}^{(r)}), \quad (15)$$

where $L_{ikop}^{(0)}$ is the elastic stiffness tensor of the matrix, and $S_{oplm}^{(r)}$ are the Eshelby's tensors for the (r) phase. Details of the derivation of these expressions are given in Appendix A. Further, the internal stress for each phase $\bar{\sigma}_{ik}^{in(r)}$ is also related to the eigenstrain, $\varepsilon_{ik}^{*(r)}$, and the stress concentration tensor, $B_{iklm}^{(r)}$, as

$$\bar{\sigma}_{ik}^{in(r)} = D_{iklm}^{(r)} \Delta \varepsilon_{lm}^{*(r)} - B_{ikop}^{(r)} \sum_{s=0}^N f^{(s)} D_{oplm}^{(s)} \Delta \varepsilon_{lm}^{*(s)}, \quad (16)$$

with

$$D_{oplm}^{(r)} = -C_{opik}^{(r)} P_{iklm}^{(r)}, \tag{17}$$

$$\Delta \varepsilon_{lm}^{*(r)} = \varepsilon_{lm}^{*(r)} - \varepsilon_{lm}^{*(0)}. \tag{18}$$

The macro strain $\bar{\varepsilon}_{ik}$ can be related to macro stress $\bar{\sigma}_{ik}$ using the potential energy Φ as

$$\bar{\varepsilon}_{ik} = -\frac{\partial \Phi}{\partial \bar{\sigma}_{ik}}. \tag{19}$$

Thus, from Equations (10), (11), (16), and (19) the constitutive relation of the composites can be written as

$$\bar{\varepsilon}_{ik} = \sum_{r=0}^r f^{(r)} M_{ikop}^{(r)} B_{oplm}^{(r)} \bar{\sigma}_{lm} + \sum_{r=0}^r f^{(r)} B_{iklm}^{(r)T} \varepsilon_{lm}^{*(r)}. \tag{20}$$

The effective elastic properties (bulk modulus and shear modulus) of multiphase composites with randomly distributed spherical particles can be derived by substituting the Eshelby’s tensor for the spherical inclusions [Eshelby 1957]:

$$S_{iklm} = \frac{1 + \nu^{(0)}}{3(1 - \nu^{(0)})} \delta_{ik} \delta_{lm} + \frac{8 - 10\nu^{(0)}}{15(1 - \nu^{(0)})} (\delta_{il} \delta_{km} + \delta_{im} \delta_{kl} - \frac{2}{3} \delta_{ik} \delta_{lm}) \tag{21}$$

into Equations (15), and from Equations (13), (14), (15), and (20). In Equation (21) $\nu^{(0)}$ is Poisson’s ratio of the matrix. Finally, the effective bulk and shear modulus can be written as

$$k^c = \frac{\sum_{r=0}^N f^{(r)} \xi_{B0}^{(r)}}{\sum_{r=0}^N \frac{f^{(r)} \xi_{B0}^{(r)}}{k^{(r)}}}, \tag{22}$$

$$\mu^c = \frac{\sum_{r=0}^N f^{(r)} \eta_{B0}^{(r)}}{\sum_{r=0}^N \frac{f^{(r)} \eta_{B0}^{(r)}}{\mu^{(r)}}}, \tag{23}$$

respectively, with

$$\xi_{B0}^{(r)} = \frac{k^{(r)} (3k^{(0)} + 4\mu^{(0)})}{3k^{(0)} (3k^{(r)} + 4\mu^{(0)})}, \tag{24}$$

$$\eta_{B0}^{(r)} = \frac{\mu^{(r)} (\mu^{(0)} + \chi^{(0)})}{\mu^{(0)} (\mu^{(r)} + \chi^{(0)})}, \tag{25}$$

and

$$\chi^{(0)} = \frac{\mu^{(0)} (9k^{(0)} + 8\mu^{(0)})}{6 (k^{(0)} + 2\mu^{(0)})}.$$

In the above equations δ_{ij} is the Kronecker delta. $f^{(r)}$ is the volume fraction, $k^{(r)}$ the bulk modulus, and $\mu^{(r)}$ the shear modulus of phase r . k^c and μ^c are overall effective bulk modulus and shear modulus of the multiphase composites, respectively.

Now, consider the unconstrained dilatational strain of the composite, Θ , corresponding to the unconstrained dilatational strain of the particles, $\theta^{(r)}$. The relation between Θ and $\theta^{(r)}$ is given as

$$\Theta \delta_{ik} = \sum_{r=1}^n f^{(r)} B_{iklm}^{(r)T} \delta_{lm} \theta^{(r)}. \quad (26)$$

In the same way as the effective elastic constants were derived above, the relation between the dilatational strain component Θ of the composite and the dilatational strain of the unconstrained transformable particle $\theta^{(r)}$ can be also written as

$$\Theta = \sum_{r=1}^n f^{(r)} \xi_B^{(r)} \theta^{(r)}, \quad (27)$$

where

$$\xi_B^{(r)} = \xi_{B0}^{(r)} / \sum_{r=0}^N f^{(r)} \xi_{B0}^{(r)}. \quad (28)$$

Further, in order to take into account the stress concentration effect on the stress transformation criterion, let us consider the mean stress in the particles. The mean stress in each phase, $\sigma_m^{(r)}$, is given as

$$\sigma_m^{(r)} = \frac{\bar{\sigma}_{ii}^{(r)}}{3} = \frac{B_{iikl}^{(r)} \bar{\sigma}_{kl}}{3}. \quad (29)$$

Similarly, the following relations are derived:

$$\sigma_m^{(r)} = \xi_B^{(r)} \bar{\sigma}_m. \quad (30)$$

Here, $\xi_B^{(r)}$ is the stress concentration factor, which is shown in Equation (28). Consequently, using these equations, one can calculate the effective elastic constants, microstress in each phase, and unconstrained dilatation Θ of the composite due to dilatation of each phase $\theta^{(r)}$.

4. Micromechanical model of transformation toughening

Consider the toughening effect in a multiphase composite enriched with partially stabilized spherical zirconia particles. The micromechanical model developed above can be directly incorporated into the continuum model [Stump and Budiansky 1989] by replacing the corresponding material constants, dilatation, and critical stress with those derived from the micromechanical model, Equations (22), (23), (28) and (30). Such substitution will not affect the fracture-toughening curve as shown in Figure 2; however the strength of the transformation will be modified as

$$\omega_m = \xi^2 \frac{E^c f^{(t)} \theta}{\sigma_m^c} \frac{1 + \nu^c}{1 - \nu^c}, \quad (31)$$

where ξ is the stress concentration factor, which corresponds to the transforming particles and can be calculated using Equations (28) and (24), and $f^{(t)}$ is the volume fraction of the transforming particles. Young's modulus E^c and Poisson's ratio ν^c are related to the bulk modulus k^c and shear modulus μ^c (Equations (22) and (23)), of the composite by well-known relationships.

The strength of the transformation ω_m calculated based on the micromechanical model differs from that obtained from the continuum model by factor ξ^2 . This parameter reflects the effect of the mismatch in the constituent material properties on the toughening mechanism. The mismatch in the material properties of the constituent phases results in two effects: the first influences the unconstrained dilatation of the composite, and the second influences the average stress in the particles. Both effects produce the same factor ξ in the strength of the transformation parameter Equation (31) and both act in the same direction, increasing or decreasing the stress transformation parameter depending on the combination of material properties of the constituents.

5. Case study

As an application of the developed theory, a SiC/Al composite will be considered next. Such composites have a significant potential for application in lightweight automotive structures, forgings for suspension, chassis, drive train, and vehicle structures, as well as automotive rolled products and semiproducts for the manufacture of advanced automotive components [Fang et al. 1997; Tung and McMillan 2004]. The greatest interest in aluminum metal-matrix composites is in their ability to provide high specific strength and stiffness. This translates into weight savings by producing lighter components capable of withstanding the required loads, for example, space frames and sheet panels, which is of particular interest in the modern transportation industry. One of the major concerns regarding widespread application in the automotive industry is the relatively high brittleness of this composite in comparison with traditional materials [Ma et al. 2003; Agrawal and Sun 2004].

An estimation of a potential benefit from the enrichment of the SiC/Al composite with zirconia particles, as calculated using the developed model and previously reported results (Figure 2), is shown in Figure 3.

Figure 3 demonstrates a very significant influence of the microstructure on toughening of the composite as the theory under consideration differentiates the matrix phase from the dispersed particle phases. In the case when a crack is located in an SiC matrix, the toughening effect of the stress transformation of partially stabilized zirconia particles is significant and reaches a maximum in the vicinity of 15% of volume fraction of SiC (or 55% of Al). In the case when crack is located in an Al matrix, the toughening effect is not so significant for small volume fractions of SiC. However at large volume fractions of SiC the toughening effect becomes stronger than in the case when SiC is the matrix. It is interesting that the toughening effect can decrease or increase when increasing the volume fraction of SiC, depending on the microstructure of the composite. Consequently, in engineering and toughening such composites special attention should be paid to the microstructure of the composite.

The results obtained for SiC/Al indicate that the stress-induced mechanism of toughening of multiphase composites is pretty effective and visible for these composites. For a multiphase composite the toughening effect can be tailored in accordance with the desired profile based on the developed theory. A greater toughening effect may be expected by increasing the volume fraction of ZrO_2 , and theoretically the strength of transformation, ω_m , could reach the lock-up values (Figure 2). It should be mentioned that the present theory is based on a small scale approximation and neglects the actual sizes of the component. At high values of ω_m , the transformation zone could be very large to justify the application of the small scale approximation.

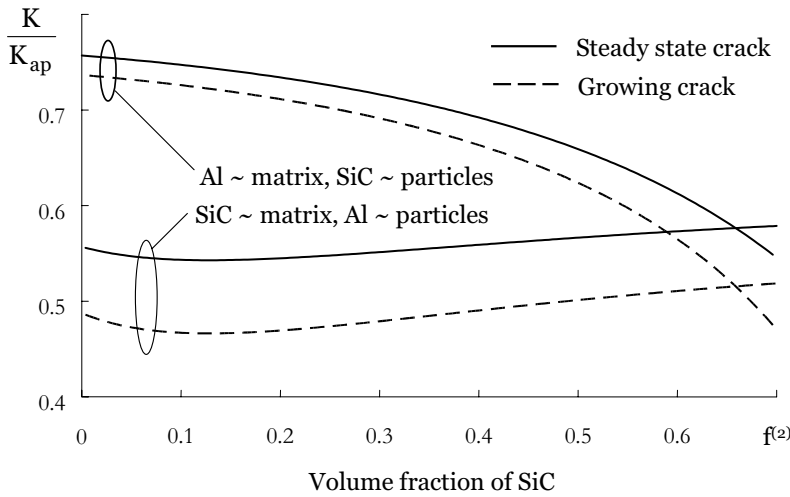


Figure 3. Toughening effect of adding ZrO_2 particles to SiC/Al composite. Material properties: Al $E^{(0)} = 70 \text{ GPa}$, $\nu^{(0)} = 0.3$ [Simmons and Wang 1971], ZrO_2 : $E^{(1)} = 200 \text{ GPa}$, $\nu^{(1)} = 0.3$, $\sigma_m^c = 500 \text{ MPa}$ [Pace et al. 1969; Zeng et al. 2004], SiC: $E^{(2)} = 430 \text{ GPa}$, $\nu^{(2)} = 0.17$ [Jackson 2005]. The volume fraction of ZrO_2 particles is set at 30% for each composite.

6. Conclusion

A micromechanical model was developed to investigate the possibility of fracture toughening of multiphase composites using the stress transformation mechanism of partially stabilized zirconia particles. Results obtained within this model demonstrate a very strong influence of the material properties of constituent phases and microstructure on the toughening mechanism. The toughening of SiC/Al composites, which have a significant potential for application in lightweight automotive structures, were studied in detail. A high level of the toughening effect can be reached by adding ZrO_2 particles to the composite. Based on the developed theory the toughening effect for multiphase composites can also be tailored by varying the phase composition in a pre-determined profile. It is recognized that extensive experimental work is needed to validate the developed theory and include other important effects.

Notation

K	Stress intensity factor
r	Distance from the crack tip
E	Young's modulus
ν	Poisson's ratio
σ_m^c	Critical value of mean stress for the stress-induced phase transformation in transformable particles
K_{ap}	Stress intensity factor due to remote applied loading

ΔK	Change of the stress intensity factor due to presence of the transformed zone
ω	Non-dimensional measure of the strength of the transformation, defined by continuum model
V^R	Volume of RVE
S^R	Surface of RVE
n_i	Outward unit vector normal to the surface S of RVE
$\bar{\sigma}_{ik}, \bar{\varepsilon}_{ik}$	Macrostress and macrostrain
$\sigma_{ik}^{ap}, \varepsilon_{ik}^{ap}, u_i^{ap}$	Microstress, microstrain and microdisplacement due to applied loading, respectively
$\sigma_{ik}^{in}, \varepsilon_{ik}^{in}, u_i^{in}$	Microstress, microstrain and displacement due to the presence of inclusions
Φ	Potential energy
$f^{(r)}$	Volume fraction of the r th phase
$\varepsilon_{ik}^{*(r)}$	Eigenstrain in the r th phase
$P_{iklm}^{(r)}$	Fourth-rank tensor defined by Equation (15)
$\bar{C}_{iklm}, \bar{C}_{iklm}^{(r)}$	Fourth-rank tensor defined by Equations (A.11), (A.12)
I_{iklm}	Fourth rank identity tensor
$L_{iklm}^{(r)}, M_{iklm}^{(r)}$	Elastic stiffness and compliance, respectively
$\bar{\sigma}_{ik}^{ap(r)}, \bar{\sigma}_{ik}^{in(r)}$	Average microstress in the r th phase due to applied loading and internal stress, respectively
$k^{(r)}$	Bulk modulus of the r th phase
$\mu^{(r)}$	Shear modulus of the r th phase
$S_{iklm}^{(r)}$	Eshelby's tensor
$B_{iklm}^{(r)}$	Stress concentration factor tensor of the r th phase
$\xi_B^{(r)}$	Stress concentration factor of the r th phase
$\xi_{B0}^{(r)}, \eta_{B0}^{(r)}$	Parameters for the r th phase defined by Equation (24) and (25)
Θ	Unconstrained dilatation strain of the composite
$\theta^{(r)}$	Unconstrained dilatation strain of the r th phase
ω_m	Modified strength of the stress-induced phase transformation derived from the micromechanical model

Appendix A

The mean-field micromechanical approach reformulated by Wakashima and Tsukamoto [1991], which stems from Eshelby's equivalent inclusion method [Eshelby 1957; 1959; 1961] and Mori–Tanaka's

mean-field approximation [Mori and Tanaka 1973] will be mentioned briefly here. Based on Eshelby's equivalent inclusion concept, we can replace the microinhomogeneous material by the homogeneous comparison material (HCM), with the equivalent inclusions and the fictitious eigenstrain distribution to represent the disturbance of stress field in the microinhomogeneous material. The HCM has exactly the same microgeometry as the multiphase composite. For the microinhomogeneous material Hooke's law can be written as

$$\bar{\varepsilon}_{ik}^{ap(r)} = M_{iklm}^{(r)} \bar{\sigma}_{lm}^{ap(r)}, \quad (\text{A.1})$$

while for the homogeneous comparison material (HCM) it can be written as,

$$\bar{\varepsilon}_{ik}^{ap(r)} = M_{iklm}^{(r)} \bar{\sigma}_{lm}^{ap(r)} + \varepsilon_{ik}^{**(r)}, \quad (\text{A.2})$$

where $\varepsilon_{ik}^{**(r)}$ is a uniform fictitious eigenstrain, defined in the equivalent inclusions corresponding to the r -th phase. From Equations (A.1) and (A.2) it follows that

$$\varepsilon_{ik}^{**(r)} = (M_{iklm}^{(r)} - M_{iklm}^{(0)}) \bar{\sigma}_{lm}^{ap(r)}, \quad (\text{A.3})$$

where

$$\varepsilon_{ik}^{**(0)} = 0. \quad (\text{A.4})$$

According to the Eshelby's solution [Eshelby 1957], the following relation is derived:

$$\bar{\sigma}_{ik}^{ap(r)} - \bar{\sigma}_{ik} = -P_{iklm}^{(r)} \varepsilon_{lm}^{**(r)}, \quad (\text{A.5})$$

where

$$P_{iklm}^{(r)} = L_{ikop}^{(0)} (I_{oplm} - S_{oplm}^{(r)}). \quad (\text{A.6})$$

$S_{oplm}^{(r)}$ denotes Eshelby's tensor, whose components are dimensionless and dependent on the axial ratios of the elliptical inclusions and Poisson's ratio of the matrix, which is assumed to be isotropic. This scheme is only applicable to the case when the discrete phases are dilute. To overcome this limitation, the Mori-Tanaka concept will be used. Equation (A.5) is replaced by the following equation:

$$\bar{\sigma}_{ik}^{ap(r)} - \bar{\sigma}_{ik}^{ap(0)} = -P_{iklm}^{(r)} \varepsilon_{lm}^{**(r)}. \quad (\text{A.7})$$

From Equations (A.3) and (A.7), the following relation can be derived:

$$\bar{\sigma}_{ik}^{ap(r)} = C_{iklm}^{(r)} \bar{\sigma}_{lm}^{ap(0)}, \quad (\text{A.8})$$

where

$$C_{iklm}^{(r)} = \{I_{iklm} + P_{ikop}^{(r)} (M_{oplm}^{(r)} - M_{oplm}^{(0)})\}^{-1}. \quad (\text{A.9})$$

By considering Equation (7), the sum of the microstress can be written as

$$\bar{\sigma}_{ik} = \sum_{r=0}^N f^{(r)} \bar{\sigma}_{ik}^{ap(r)}. \quad (\text{A.10})$$

Therefore, the stress concentration factor $B_{ijkl}^{(r)}$ is calculated as

$$B_{iklm}^{(r)} = C_{ikop}^{(r)} \bar{C}_{oplm}^{-1}, \quad (\text{A.11})$$

where

$$\bar{C}_{iklm} = \sum_{r=0}^N f^{(r)} C_{iklm}^{(r)}. \quad (\text{A.12})$$

Next, the internal stress in the microinhomogeneous material will be considered. For the internal strain in the microinhomogeneous material,

$$\bar{\varepsilon}_{ik}^{in(r)} = M_{iklm}^{(r)} \bar{\sigma}_{lm}^{in(r)} + \varepsilon_{ik}^{*(r)}. \quad (\text{A.13})$$

In accordance with the last Equation (A.13), in the equivalent homogeneous material

$$\bar{\varepsilon}_{ik}^{in(r)} = M_{iklm}^{(0)} \bar{\sigma}_{lm}^{in(r)} + \varepsilon_{ik}^{*(r)} + \varepsilon_{ik}^{** (r)}, \quad (\text{A.14})$$

where $\varepsilon_{ik}^{** (r)}$ is the fictitious eigenstrain, which is found from (A.13) and (A.14) as

$$\varepsilon_{ik}^{** (r)} = (M_{iklm}^{(r)} - M_{iklm}^{(0)}) \bar{\sigma}_{lm}^{in(r)}. \quad (\text{A.15})$$

Using the Mori–Tanaka concept, the following equation can be written:

$$\bar{\sigma}_{ik}^{in(r)} - \bar{\sigma}_{ik}^{in(0)} = -P_{iklm}^{(r)} (\Delta \varepsilon_{lm}^{*(r)} + \varepsilon_{lm}^{** (r)}), \quad (\text{A.16})$$

where $\Delta \varepsilon_{kl}^{*(r)}$ is defined by Equation (18). From Equations (A.15) and (A.16), it follows that

$$\bar{\sigma}_{ik}^{in(r)} = B_{iklm}^{0(r)} (\bar{\sigma}_{lm}^{in(0)} - P_{lmop}^{(r)} \Delta \varepsilon_{op}^{*(r)}). \quad (\text{A.17})$$

The sum of the internal stress must be equal to zero,

$$\sum_{r=0}^N f^{(r)} \bar{\sigma}_{ik}^{in(r)} = 0, \quad (\text{A.18})$$

and therefore,

$$\bar{\sigma}_{ik}^{in(0)} = \bar{C}_{iklm}^{-1} \sum_{r=0}^N f^{(r)} C_{lmop}^{(r)} P_{opvw}^{(r)} \Delta \varepsilon_{vw}^{*(r)}. \quad (\text{A.19})$$

By comparing Equation (A.19) with Equation (16), $D_{ijkl}^{(r)}$ is obtained as given in Equation (17) as

$$D_{ijkl}^{(r)} = -C_{ikop}^{(r)} P_{oplm}^{(r)}. \quad (\text{A.20})$$

References

- [Agrawal and Sun 2004] P. Agrawal and C. T. Sun, “Fracture in metal-ceramic composites”, *Compos. Sci. Technol.* **64**:9 (2004), 1167–1178.
- [Alfano et al. 2006] M. Alfano, F. Furguele, and C. Maletta, “Stress intensity factor in alumina-zirconia composites”, *Key Eng. Mater.* **324-325** (2006), 1135–1138.
- [Basu et al. 2004] B. Basu, J. Vleugels, and O. V. Biest, “Toughness tailoring of yttria-doped zirconia ceramics”, *Mater. Sci. Eng. A* **380**:1-2 (2004), 215–221.
- [Budiansky et al. 1983] B. Budiansky, J. W. Hutchinson, and J. C. Lambropoulos, “Continuum theory of dilatant transformation toughening in ceramics”, *Int. J. Solids Struct.* **19**:4 (1983), 337–355.

- [Bui et al. 1972] H. D. Bui, A. Zaoui, and J. Zarka, "On the elastoplastic and viscoplastic behavior of single crystals and metallic polycrystals of face centered cubic structure", pp. 50–75 in *Proc. Int. Symp. on Foundations of Plasticity*, edited by A. Sawczuk, Warsaw, 1972. Preprint, (Groningen 1973).
- [Casellas et al. 2001] D. Casellas, F. L. Cumbrera, F. S. Sánchez Bajo, W. Forsling, L. Llanes, and M. Anglada, "On the transformation toughening of Y–ZrO₂ ceramics with mixed Y–TZP/PSZ microstructures", *J. Eur. Ceram. Soc.* **21**:6 (2001), 765–777.
- [Cesari et al. 2006] F. Cesari, L. Esposito, F. M. Furgiuele, C. Maletta, and A. Tucci, "Fracture toughness of alumina-zirconia composites", *Ceram. Int.* **32**:3 (2006), 249–255.
- [Chen and Tuan 2001] R. Z. Chen and W. H. Tuan, "Toughening alumina with silver and zirconia inclusions", *J. Eur. Ceram. Soc.* **21**:16 (2001), 2887–2893.
- [Chen et al. 2000] R. Z. Chen, Y. T. Chiu, and W. H. Tuan, "Toughening alumina with both nickel and zirconia inclusions", *J. Eur. Ceram. Soc.* **20**:12 (2000), 1901–1906.
- [Cho and Ha 2001] J. R. Cho and D. Y. Ha, "Averaging and finite-element discretization approaches in the numerical analysis of functionally graded materials", *Mater. Sci. Eng. A* **302**:2 (2001), 187–196.
- [Eshelby 1957] J. D. Eshelby, "The determination of the elastic field of an ellipsoidal inclusion, and related problems", *P. Roy. Soc. Lond. A Mat.* **241**:1226 (1957), 376–396.
- [Eshelby 1959] J. D. Eshelby, "The elastic field outside an ellipsoidal inclusion", *P. Roy. Soc. Lond. A Mat.* **252**:1271 (1959), 561–569.
- [Eshelby 1961] J. D. Eshelby, "Elastic inclusions and inhomogeneities", *Prog. Solid Mech.* **2** (1961), 89–140.
- [Evans and Heuer 1980] A. G. Evans and A. H. Heuer, "Transformation toughening in ceramics: martensitic transformations in crack-tip stress fields", *J. Am. Ceram. Soc.* **63**:5-6 (1980), 241–248.
- [Fang et al. 1997] Q. Fang, P. Sidky, and M. G. Hocking, "Erosive wear behaviour of aluminium based composites", *Mater. Des.* **18**:4-6 (1997), 389–393.
- [Garvie et al. 1975] R. C. Garvie, R. H. Hannink, and R. T. Pascoe, "Ceramic steel", *Nature* **258**:5537 (1975), 703–704.
- [Gupta et al. 1978] T. K. Gupta, F. F. Lange, and J. H. Bechtold, "Effect of stress-induced phase transformation on the properties of polycrystalline zirconia containing metastable tetragonal phase", *J. Mater. Sci.* **13**:7 (1978), 1464–1470.
- [Hill 1963] R. Hill, "Elastic properties of reinforced solids: some theoretical principles", *J. Mech. Phys. Solids* **11**:5 (1963), 357–372.
- [Hutchinson 1974] J. W. Hutchinson, "On steady quasi-static crack growth", Report DEAP S-8, Harvard University Report, Division of Applied Sciences, April 1974.
- [Jackson 2005] K. M. Jackson, "Fracture strength, elastic modulus and Poisson's ratio of polycrystalline 3C thin-film silicon carbide found by microsample tensile testing", *Sens. Actuators A Phys.* **125**:1 (2005), 34–40.
- [Kelly and Rose 2002] P. M. Kelly and L. R. F. Rose, "The martensitic transformation in ceramics: its role in transformation toughening", *Prog. Mater. Sci.* **47**:5 (2002), 463–557.
- [Lange 1982] F. F. Lange, "Transformation toughening, 4: fabrication, fracture toughness and strength of Al₂O₃-ZrO₂ composites", *J. Mater. Sci.* **17**:1 (1982), 247–254.
- [Ma et al. 2003] T. Ma, H. Yamaura, D. A. Koss, and R. C. Voigt, "Dry sliding wear behavior of cast SiC-reinforced Al MMCs", *Mater. Sci. Eng. A* **360**:1-2 (2003), 116–125.
- [McMeeking and Evans 1982] R. M. McMeeking and A. G. Evans, "Mechanics of transformation toughening in brittle materials", *J. Am. Ceram. Soc.* **65**:5 (1982), 242–246.
- [Miyamoto et al. 1999] Y. Miyamoto, W. A. Kaysser, B. H. Rabin, A. Kawasaki, and R. G. Ford, *Functionally graded materials: design, processing and applications*, Kluwer Academic Publishers, 1999.
- [Mori and Tanaka 1973] T. Mori and K. Tanaka, "Average stress in matrix and average elastic energy of materials with misfitting inclusions", *Acta Metall.* **21** (1973), 571–574.
- [Mura 1982] T. Mura, *Micromechanics of defects in solids*, Martinus Nijhoff, The Hague, 1982.
- [Pace et al. 1969] N. G. Pace, G. A. Saunders, Z. Sümengen, and J. S. Thorp, "The elastic constants and interatomic binding in yttria stabilised zirconia", *J. Mater. Sci.* **4**:12 (1969), 1106–1110.

- [Ponte-Castaneda and Willis 1995] P. Ponte-Castaneda and J. R. Willis, "The effect of spatial distribution on the effective behavior of composite materials and cracked media", *J. Mech. Phys. Solids* **43**:12 (1995), 1919–1951.
- [Rose 1986] L. R. F. Rose, "The size of the transformed zone during steady-state cracking in transformation-toughened materials", *J. Mech. Phys. Solids* **34**:6 (1986), 609–616.
- [Sbaizero et al. 2003] O. Sbaizero, S. Roitti, and G. Pezzotti, "R-curve behavior of alumina toughened with molybdenum and zirconia particles", *Mater. Sci. Eng. A* **359**:1-2 (2003), 297–302.
- [Simha and Truskinovsky 1994] N. Simha and L. Truskinovsky, "Shear induced transformation toughening in ceramics", *Acta Metall. Mater.* **42** (1994), 3827–3836.
- [Simmons and Wang 1971] G. Simmons and H. Wang, *Single crystal elastic constants and calculated aggregate properties: a handbook*, 2nd ed., MIT Press, Cambridge, MA, 1971.
- [Stump and Budiansky 1989] D. M. Stump and B. Budiansky, "Crack-growth resistance in transformation-toughened ceramics", *Int. J. Solids Struct.* **25**:6 (1989), 635–646.
- [Tsukamoto and Kotousov 2006] H. Tsukamoto and A. Kotousov, "Transformation toughening in zirconia-enriched composites: micromechanical modeling", *Int. J. Fract.* **139**:1 (2006), 161–168.
- [Tung and McMillan 2004] S. C. Tung and M. L. McMillan, "Automotive tribology overview of current advances and challenges for the future", *Tribol. Int.* **37**:7 (2004), 517–536.
- [Wakashima and Tsukamoto 1991] K. Wakashima and H. Tsukamoto, "Mean-field micromechanics model and its application to the analysis of thermomechanical behaviour of composite materials", *Mater. Sci. Eng. A* **146**:1-2 (1991), 291–316.
- [Zeng et al. 2004] D. Zeng, N. Katsube, and W. O. Soboyejo, "Discrete modeling of transformation toughening in heterogeneous materials", *Mech. Mater.* **36**:11 (2004), 1057–1071.

Received 2 Aug 2006. Accepted 20 Feb 2007.

HIDEAKI TSUKAMOTO: hideaki.tsukamoto@mecheng.adelaide.edu.au
School of Mechanical Engineering, The University of Adelaide, SA 5005, Australia

ANDREI KOTOUSOV: andrei.kotousov@adelaide.edu.au
School of Mechanical Engineering, The University of Adelaide, SA 5005, Australia

THE SIMULATION OF RESIDUAL STRESSES IN FRICTION STIR WELDS

ZHAO ZHANG AND HONGWU ZHANG

A numerical model is developed to investigate energy dissipations and residual stress distributions in friction stir welds. Results indicate that the maximum longitudinal residual stress can be increased with the increase of the translational velocity of the pin. But the variation of the angular velocity of the pin does not significantly affect the residual stress distributions. Energy dissipation in friction is increased with the increase of the angular velocity of the pin. However, with the increase of the translational velocity of the pin the plastic dissipation of energy is increased and the frictional dissipation is decreased.

1. Introduction

Friction stir welding (FSW) is a new solid-state joining technology invented by the Welding Institute (TWI) in 1991 [Thomas et al. 1991]. Compared with conventional welding processes, FSW has many advantages such as no melting, low defects, and low distortion, and can even join thin and thick sections. This new technique has been successfully applied to the aerospace, automobile, and shipbuilding industries.

Temperatures near the rotating pin never reach the melting point in FSW [Tang et al. 1998], and quite complicated flow was observed in welds [Murr et al. 1998; Xu et al. 2001]. Colligan [1999] studied the material flow in 6061 and 7075 aluminum by imbedding small steel balls as tracers into grooves cut into the work piece parallel to the weld line. Murr et al. [1999] and Li et al. [1999] found that dynamic recrystallization plays a key role in material movement. The joining of Al 6061 alloy to AISI 1018 steel by the combined effect of fusion and solid state welding was investigated by Chen and Kovacevic [2004]. It was found that the intermetallic phases $Al_{13}Fe_4$ and Al_5Fe_2 exist in the weld zone.

The temperature field in friction stir welding was studied by Song and Kovacevic [2003] and Chen and Kovacevic [2003] using a finite element method. It was shown that the preheating into the work piece is beneficial to FSW. Dalle Donne et al. [2000] found that the residual stress of the weld affects the fatigue properties. Webster et al. [2001] reported the measurement of residual stress in FSW by the X-ray technique and found that the longitudinal residual stress varies in the range from 60 to 140 MPa. Sutton et al. [2002] investigated the residual stress in 2024-T3 aluminum friction stir butt welds using the neutron diffraction technique. The results show that the highest stress occurs near the crown side of the weld over the entire FSW region. Peel et al. [2003] further gave the results of microstructure, mechanical property and residual stress of four aluminum AA5083 friction stir welds produced under varying conditions.

Keywords: friction stir welding, residual stress, finite element method, energy dissipation.

This work is supported by the National Natural Science Foundation of China (nos. 10302007, 10421202, and 10225212), the Program for Changjiang Scholars and the Innovative Research Team in the University of China (PCSIRT) and the National Key Basic Research Special Foundation of China (no. 2005CB321704).

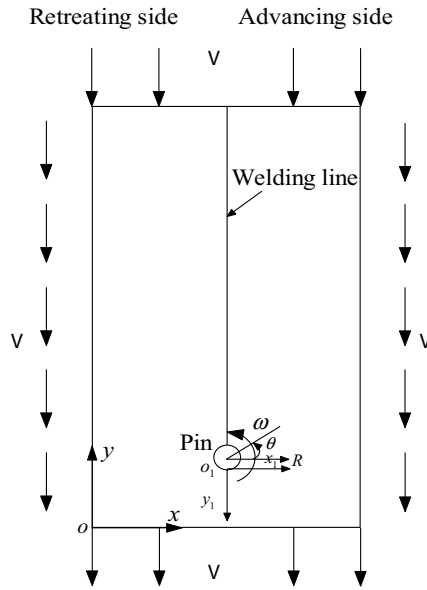


Figure 1. The geometry model and boundary conditions of FSW.

Zhu and Chao [2004] reported the transient temperature and residual stresses of 304L stainless steel. The distribution and the influence of residual stresses on fatigue in FSW were investigated by James et al. [2004]. Reynolds et al. [2003] reported the residual stress distribution of 304L steel under different angular velocities. A two dimensional modeling of FSW, based on the Arbitrary Lagrangian–Eulerian (ALE) finite element formulation, was reported by Deng and Xu [2001]. The method was further extended to analyze the three dimensional material flow by Xu and Deng [2002]. In the numerical models established by Deng and Xu, rate-independent material was used to model the friction stir welding process. It was found that the rate-independent material is appropriate enough to model the material behaviors in FSW process.

So far, there are no successful in-depth numerical reports on residual stress distributions in friction stir welds in different process parameters, including welding speed and angular velocity. A new numerical method, that is, transferring the results from a dynamic solver into a static one to obtain the residual stress on the friction stir weld after the FSW process, is herein proposed to investigate the residual stress distributions in the present research. Two approaches are needed to reduce the computational costs: one is to use the experimental data of the temperature field in the friction stir welds; the other is to increase the boundary conditions by 1000 times. Comparison with experimental tests on residual stresses in friction stir welds in the existing literature can validate the numerical model developed.

2. Model description

In FSW the material of the work piece in front of the tool is pushed aside by the pin and is forced to flow by the action of the pin, around which large plastic flow develops. In order to model the contact surface properly and handle mesh distortion during large plastic deformation, a thermo-mechanical

finite element method, based on the Arbitrary Lagrangian–Eulerian (ALE) formulation and the adaptive remeshing technique, is employed. By means of ALE, material surfaces can be tracked with the accuracy characteristic of the Lagrangian methods and the interior mesh can be fixed in some directions so as to avoid element distortion and entanglement. The mesh should be prescribed so that the boundaries and interfaces remain at least partially Lagrangian.

The radius of the pin R_0 is 3 mm, and the dimensions of the two plates are 100 mm in length (along the welding line) and 30 mm in width (see Figure 1). Such a small welding plate has been proven to precisely predict the material behaviors [Deng and Xu 2004; Zhang et al. 2005b] by tracing the material particles near the rotating tool and the tool forces applied on the shoulder [Ulysse 2002]. The main advantage of such a small welded plate is that the computational cost can be greatly reduced. The same size welded plate is used in the present research for the investigation on material velocity field near the rotating pin and the residual stress distribution on the friction stir weld. The two dimensional geometry is discretized into four-node quadrilateral elements. Reduced integration with hourglass control is used to avoid the mesh-locking problems associated with large incompressible plastic deformation. The mesh consists of 11717 elements and 11986 nodes. The material of the plate is AL 6061-T6, as a rate independent elasto-plastic material. However, the effect of temperature on yielding is considered explicitly. The properties of the material at different temperatures are shown in Table 1 [Brown et al. 1993].

The constitutive relations are given by the von Mises yield criterion and the associated flow rule. The von Mises yield condition can be expressed as

$$F_d(\sigma_{ij}, \bar{\varepsilon}) = \frac{1}{2} \sigma'_{ij} \sigma'_{ij} - \frac{1}{3} \sigma_s^2(\bar{\varepsilon}), \quad (1)$$

where σ' is the deviatoric part of Kirchhoff stress. $\bar{\varepsilon}$ represents the equivalent plastic strain and σ_s is the yield stress of the material.

For an associate flow, the direction of the plastic flow n_s is normal to the flow potential F_d as

$$n_s = \frac{\partial F_d / \partial \sigma}{\|\partial F_d / \partial \sigma\|} = \frac{\mathbf{D}_p}{\|\mathbf{D}_p\|}, \quad (2)$$

where \mathbf{D}_p represents the inelastic rate of deformation, and $\|\mathbf{D}_p\| = (\mathbf{D}_p : \mathbf{D}_p)^{1/2}$.

T (°C)	E (GPa)	σ_u (MPa)	ν
25.00	66.94	278.12	0.330
100.00	63.21	260.68	0.334
148.89	61.32	251.24	0.335
204.44	56.80	221.01	0.336
260.00	51.15	152.26	0.338
315.56	47.17	73.87	0.360
371.11	43.51	36.84	0.400
426.67	28.77	21.58	0.410
482.22	20.20	10.49	0.420

Table 1. Temperature-dependent material properties of AL6061-T6.

The flow rule has the form

$$\mathbf{D}^p = \dot{\lambda} \frac{3\boldsymbol{\sigma}'}{2\bar{\sigma}}, \quad (3)$$

where $\dot{\lambda}$ denotes the scalar measuring of the rate of inelastic flow, and $\bar{\sigma}$ denotes the equivalent stress, $\bar{\sigma} = [\frac{3}{2}\boldsymbol{\sigma}' : \boldsymbol{\sigma}']^{1/2}$.

The Jaumann rate of the Kirchhoff stress tensor is given as

$$\boldsymbol{\sigma}^{\nabla J} = \dot{\boldsymbol{\sigma}} - \mathbf{W} \cdot \boldsymbol{\sigma} + \boldsymbol{\sigma} \cdot \mathbf{W}, \quad (4)$$

where the additive decomposition of the rate of deformation tensor \mathbf{D} into elastic and plastic components is implied, that is, $\mathbf{D} = \mathbf{D}^e + \mathbf{D}^p$. \mathbf{W} is the rate of spin tensor. The rate of deformation is defined as the symmetric part of the velocity gradient, $\mathbf{D} = \frac{1}{2}((\nabla \mathbf{v})^T + \nabla \mathbf{v})$, and the rate of spin tensor is the skew symmetric part, $\mathbf{W} = \frac{1}{2}((\nabla \mathbf{v})^T - \nabla \mathbf{v})$.

2.1. Definition of contact. The frictional contact model is used. The interface may experience frictional contact described by a modified Coulomb friction law. The Coulomb friction law is modified so that there exists a maximum critical frictional stress, above which the frictional stress stays constant and is no longer equal to the product of the friction coefficient and the contact pressure. A reasonable upper bound $\tau_{\max} = \sigma_s / \sqrt{3}$ is used.

2.2. Boundary conditions. At the boundaries of the plates, material particles move with a constant speed \mathbf{v} relative to the pin, as shown in Figure 1. The pin rotates with an angular velocity ω . It has been proved that the FSW process is in a steady state [Deng and Xu 2004; Zhang et al. 2005b]. So FSW can be treated as a quasistatic problem and the loading speed can be increased to save computational costs. In the present research, both the translational velocity and the angular velocity are increased 1000 times to accelerate convergence. In my previous work, the material flow patterns during the friction stir welding process have been investigated in detail [Zhang et al. 2005a; 2005b; Zhang and Zhang 2005] and the results can correlate well with the experimental tests [Guerra et al. 2002]. The computational results obtained in my previous work [Zhang et al. 2005b] are transferred from ABAQUS/Explicit to ABAQUS/Standard in the present research. The obtained results from the dynamic solver are transferred to the static solver and then are treated as a static problem to obtain the residual stress distributions in the friction stir weld. In this process, the fixtures are released and the temperature is reduced to room temperature.

2.3. Integration method. The simplest operator that provides unconditional stability for integration equations is the backward Euler method. The strain rate decomposition is integrated over a time increment as

$$\Delta \boldsymbol{\varepsilon} = \Delta \boldsymbol{\varepsilon}^{el} + \Delta \boldsymbol{\varepsilon}^{pl}, \quad (5)$$

where $\Delta \boldsymbol{\varepsilon}$ is defined by central difference operator

$$\Delta \boldsymbol{\varepsilon} = \text{sym} \left[\frac{\partial \Delta \mathbf{x}}{\partial (x_t + \frac{1}{2} \Delta x)} \right].$$

During the solution, the elasticity relationship and the integrated rate decomposition are satisfied exactly, so that

$$c_{\sigma} = -D^{el} : c_{\boldsymbol{\varepsilon}}, \quad (6)$$

where c_σ is the correction to the stress, c_ε is the correction to the plastic strain increments, and $D^{el} = \frac{\partial^2 U}{\partial \varepsilon^{el} \partial \varepsilon^{el}}$ is the tangent elasticity matrix.

If hardening laws are considered, then

$$c_\alpha = h_\alpha c_\lambda + \Delta\lambda \left(\frac{\partial h_\alpha}{\partial \sigma} : c_\sigma + \frac{\partial h_\alpha}{\partial H_\beta} c_\beta \right), \quad (7)$$

where c_α is the correction to ΔH_α , and c_λ is the correction to $\Delta\lambda$.

The flow rule is not satisfied exactly until the following solution has been found

$$c_\varepsilon - c_\lambda \frac{\partial g}{\partial \sigma} - \Delta\lambda \left(\frac{\partial^2 g}{\partial \sigma \partial \sigma} : c_\sigma + \frac{\partial^2 g}{\partial \sigma \partial H_\alpha} c_\alpha \right) = \Delta\lambda \frac{\partial g}{\partial \sigma} - \Delta \boldsymbol{\varepsilon}^{pl}. \quad (8)$$

The Newton–Raphson iteration method is applied until the flow equation and yield constraints are satisfied.

2.4. Temperature field. The heat generated at the interface between the shoulder and the work piece in FSW is the driving force to make FSW successful [Chao et al. 2003]. The heat flux must keep the maximum temperature in the work piece high enough so that the material is sufficiently soft to be stirred but low enough so that the material does not melt. The maximum temperature created by FSW ranges from 80% to 90% of the melting temperature of the welding material, as measured by Tang et al. [1998] and Colegrove et al. [2000].

The limitation of the PC computing power makes a fully thermo-mechanical analysis difficult to be completed in a reasonably short time [Deng and Xu 2001; Xu and Deng 2002]. To compensate for the lack of a predicted temperature field, actual temperature values from the practical FSW test [McClure et al. 1999] will be used to construct an approximate temperature field for the FSW process simulation, as shown in Figure 2. A tool rotation of 400rpm and a translational velocity of 2 mm/s are used in this experiment. Due to the limitation of the melting point of the material, the temperature fields near the pin under different cases do not have significant differences. So the same temperature field is used to model the friction stir welding process under different cases in the present analysis.

To show the reasonableness of the predicted temperature field, Figure 3 shows the predicted temperature field when the rotational velocity is 400 rpm before the translational movement of the pin. The maximum temperature occurs on the pin-plate interface. This is a quasistatic temperature field and the temperature distribution in the longitudinal direction perpendicular to the welding line scarcely varies with time. When the approximate temperature field is constructed, the pin starts to move along the welding line.

3. Results and discussion

Figure 4 shows the distribution of the residual stresses in the direction perpendicular to the welding line at $y_1 = 1$ mm, $y_1 = 2$ mm, and $y_1 = 3$ mm when $v = 2$ mm/s and $\omega = 390$ RPM. The maximum of the longitudinal residual stress occurs near $(R_0 + 1)$ mm away from the welding line. The longitudinal residual stress ranges from -100 MPa to about 100 MPa. The results can be validated in [Dalle Donne et al. 2001; Hornbach et al. 2003; Staron et al. 2004]. It seems that the maximum longitudinal residual stress occurs in the location where the equivalent plastic strain is decreased suddenly, as shown in Figure

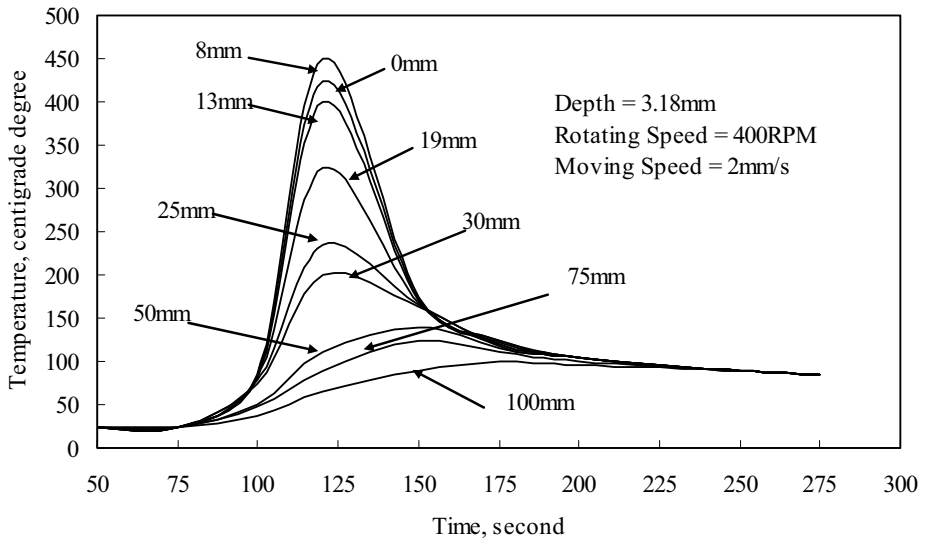


Figure 2. Fitted temperature history at various distances from the weld line.

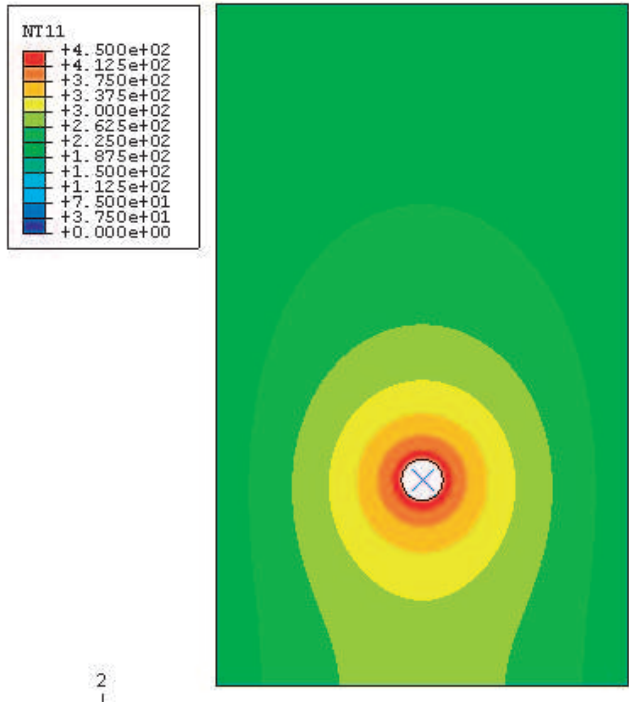


Figure 3. Predicted temperature field according to the experimental data.

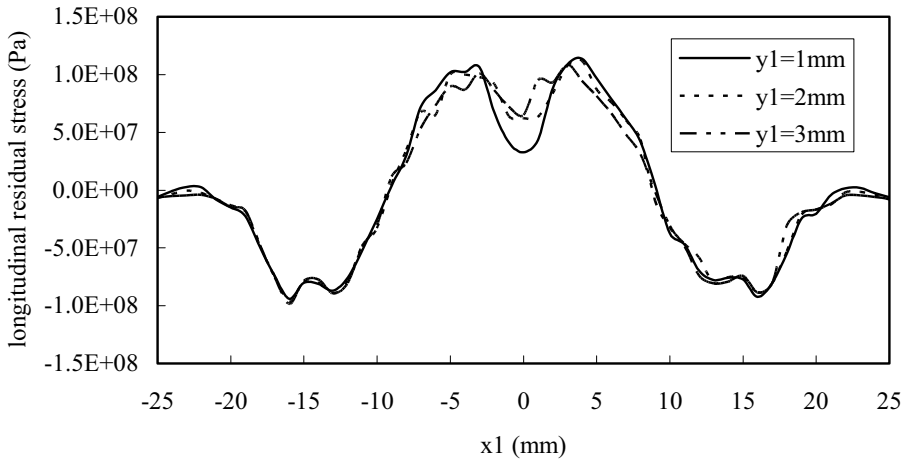


Figure 4. The distributions of the longitudinal residual stress in the direction perpendicular to the welding line ($v = 2 \text{ mm/s}$, $\omega = 390 \text{ RPM}$).

5. The region of large tensile residual stress can correlate well with that of large equivalent plastic strain. It is found that in the region where the equivalent plastic strain is decreasing, longitudinal residual stress is also decreasing. When away from the extraction point of the pin, the longitudinal residual stress in the welding line is slightly increasing. But after about 2 mm, distribution of the longitudinal residual stress remains steady. This means that the distributions of the longitudinal residual stress are not affected by the extraction of the pin after 2 mm away from the extraction point. The ratio of the maximum longitudinal residual stress to the initial yield stress is only about 39%, which is much lower than the one obtained in the welds produced by the traditional welding techniques. The residual stresses are not symmetric to the welding line because the deformations are clearly unsymmetric. When the fixtures are released and the temperature is reduced to room temperature, the material in the nugget zone tends to recover. But the material in the heat affected zone has smaller deformation and will prevent the recovery process in the nugget zone. So the maxima of longitudinal residual stress occur in the boundaries of the heat affected zone with a minimum in the nugget zone. The deformations on the retreating side and the advancing side differ, causing the recovery processes to differ too. So the residual stress cannot be symmetric to the welding line.

Figure 6 shows the distributions of the longitudinal residual stress under different translational velocities in the direction perpendicular to the welding line. It is clear that the longitudinal residual stress is increased with the increase of the translational velocity in the tensile region, which can correlate well with the observations from experiments [Peel et al. 2003]. But at points where $x_1 = \pm 16 \text{ mm}$, the longitudinal residual stress is not affected by the increase of the translational velocity. In the compressive region, it is difficult to judge the effect of the increase of the translational velocity. But in fact, the region of the large tensile stress is much more interesting since it is much closer to the welding line. Compared with the results in Figure 4, the maximum of the longitudinal residual stress occurs only near $(R_0 + 1) \text{ mm}$, which is about 140 MPa. The ratio of the maximum longitudinal residual stress to the initial yield stress

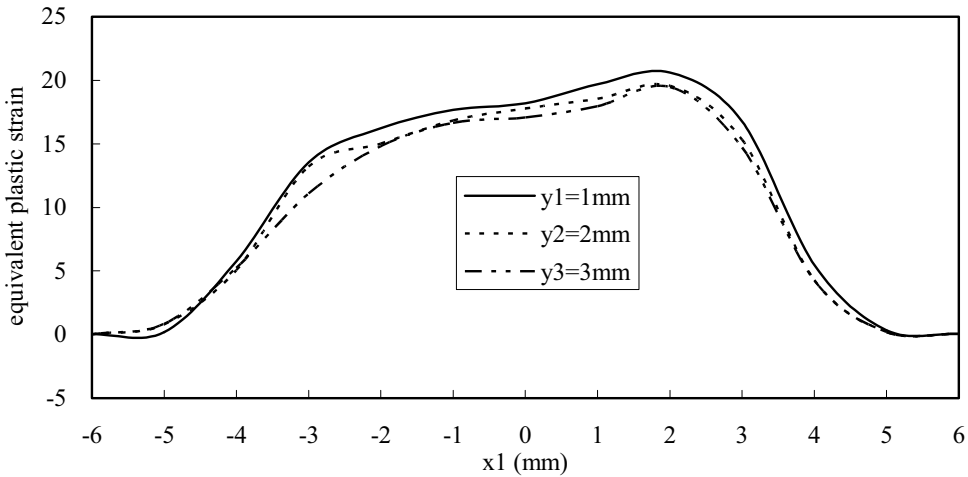


Figure 5. The distributions of the equivalent plastic strain in the direction perpendicular to the welding line ($v = 2 \text{ mm/s}$, $\omega = 390 \text{ RPM}$).

is also increased approximately from 41% to 50% when the translational velocity of the pin is increased from 4 mm/s to 10 mm/s.

Figure 7 shows the distributions of the longitudinal residual stress under different angular velocities in the direction perpendicular to the welding line. With the increase of the angular velocity, the large tensile region is moved to the advancing side. By experiments, Dalle Donne et al. [2001] found that the maximum longitudinal residual stress occurs on the advancing side. Both the numerical modeling in the present research and Dalle Donne's experiment lead to the same conclusion, that is, that the maximum longitudinal residual stress can occur at the advancing side instead of the retreating side, which can

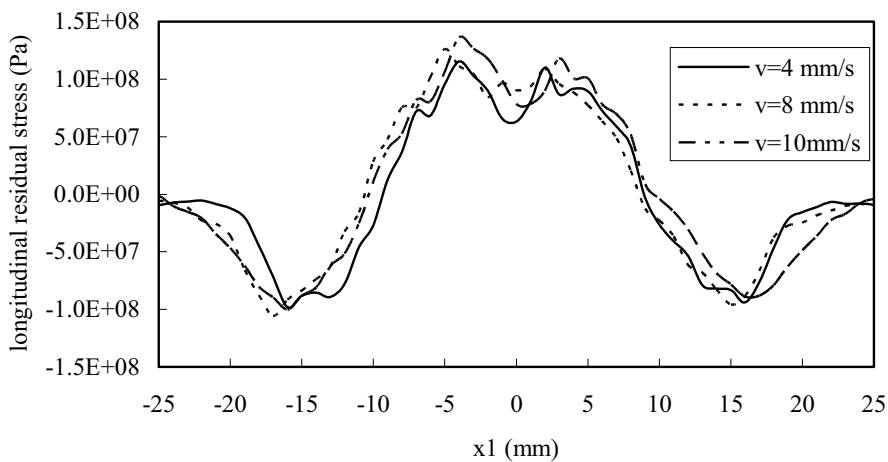


Figure 6. The distributions of the longitudinal residual stress under different translational velocities in the direction perpendicular to the welding line ($\omega = 390 \text{ RPM}$).

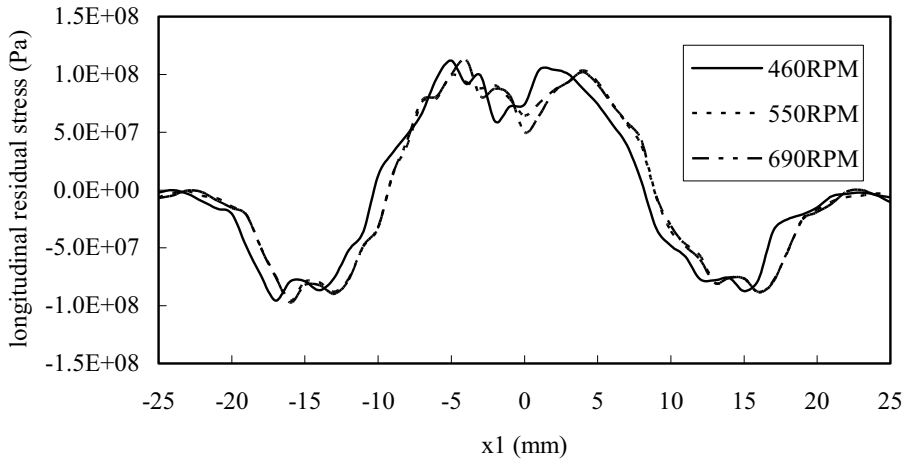


Figure 7. The distributions of the longitudinal residual stress under different angular velocities in the direction perpendicular to the welding line ($v = 2 \text{ mm/s}$).

validate the numerical model established. There is a concave point near the welding line. The change of the angular velocity can affect the location of the concave point. With the increase of the angular velocity, the concave point can be moved to the advancing side. In summary, the effect of the change of the angular velocity on the longitudinal residual stress is not clear, which can be fitted well with experiments on residual stress in friction stir welding [Reynolds et al. 2003]. So, the variation of the angular velocity does not significantly affect the ratio of maximum longitudinal residual stress to the initial yield stress.

When the translational velocity of the pin is smaller, the maximum longitudinal residual stress on the retreating side and the one on the advancing side are similar, as shown in Figure 4. But with the increase of the translational velocity of the pin, the maximum longitudinal residual stress on the retreating side becomes higher than that on the advancing side. The maximum longitudinal residual stress can be increased from 100 MPa to about 140 MPa when the translational velocity is increased to 10 mm/s.

Remark. The residual stress distributions of friction stir welds have been studied by experiments reported in [Dalle Donne et al. 2001; Hornbach et al. 2003; Reynolds et al. 2003; Staron et al. 2004]. It was found that the curve of the longitudinal residual stress has a feature of a double peak. The maxima of the residual stress occur in the boundaries of the heat affected zone. The distributions of the longitudinal residual stress obtained from the present numerical model can correlate well with those in the experiments. The longitudinal residual stresses of 6XXX alloys range from -60 MPa to $+100 \text{ MPa}$ [Dalle Donne et al. 2001], which are very similar to those obtained in the present research, as shown in Figure 8. The residual stresses can differ due to the different measurement method. It should be noted that this is a weak comparison due to the differences between experimental and numerical conditions. In particular, the shoulder effect is not considered in the present research. To reveal the residual stress distributions correctly, a three-dimensional model of FSW is needed for further investigation of residual stresses.

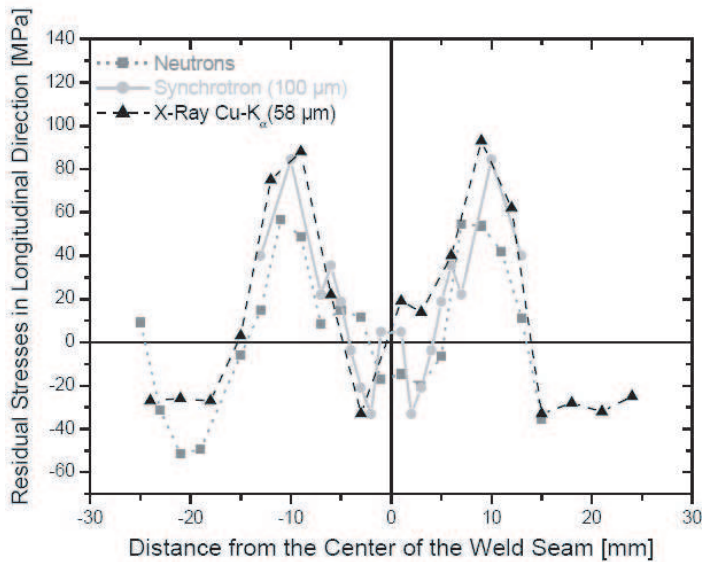


Figure 8. Longitudinal residual stresses measured by different published methods [Dalle Donne et al. 2001].

For better understanding of the mechanism of FSW, it is necessary to study the energy dissipations in FSW under different cases. It is known that the major energy dissipations in FSW are frictional ones and plastic ones. The energy dissipations under different process parameters are shown in Figure 9. It can be seen that the frictional dissipation of energy increases with the increase of the angular velocity of the pin. A possible explanation is that more revolutions are performed for the same length of the weld seam when the angular velocity of the pin is increased. For instance, the frictional dissipation is about 7×10^4 J at $t = 3.1 \times 10^{-3}$ s when $\omega = 460$ RPM, while the dissipation at the same t is 8.5×10^4 J when $\omega = 550$ RPM. The dissipation can be increased to 10.5×10^4 J at $t = 3.1 \times 10^{-3}$ s when $\omega = 690$ RPM. But the increase of the angular velocity of the pin does not affect the plastic dissipation which remains the same in Figures 9a–c.

The increase of the translational velocity of the pin does have an apparent effect on the plastic dissipation in FSW. The plastic dissipation can be increased with the increase of the translational velocity of the pin, but at the same time the frictional dissipation of energy is decreased, as shown in Figures 9d–f. The possible explanation is that with the increase of the translational velocity, the material deformation becomes more severe in the same time interval. So the plastic deformation of the material in the weld plates absorbs more energy. For instance, the frictional dissipation is 1.4×10^4 J and the plastic dissipation is 0.8×10^4 J at $t = 0.8 \times 10^{-3}$ s when $v = 4$ mm/s. When $v = 8$ mm/s, the frictional dissipation is 1.02×10^4 J and the plastic dissipation is 1.2×10^4 J at $t = 0.8 \times 10^{-3}$ s. When $v = 10$ mm/s, the frictional dissipation is 0.98×10^4 J and the plastic dissipation is 1.3×10^4 J at $t = 0.8 \times 10^{-3}$ s.

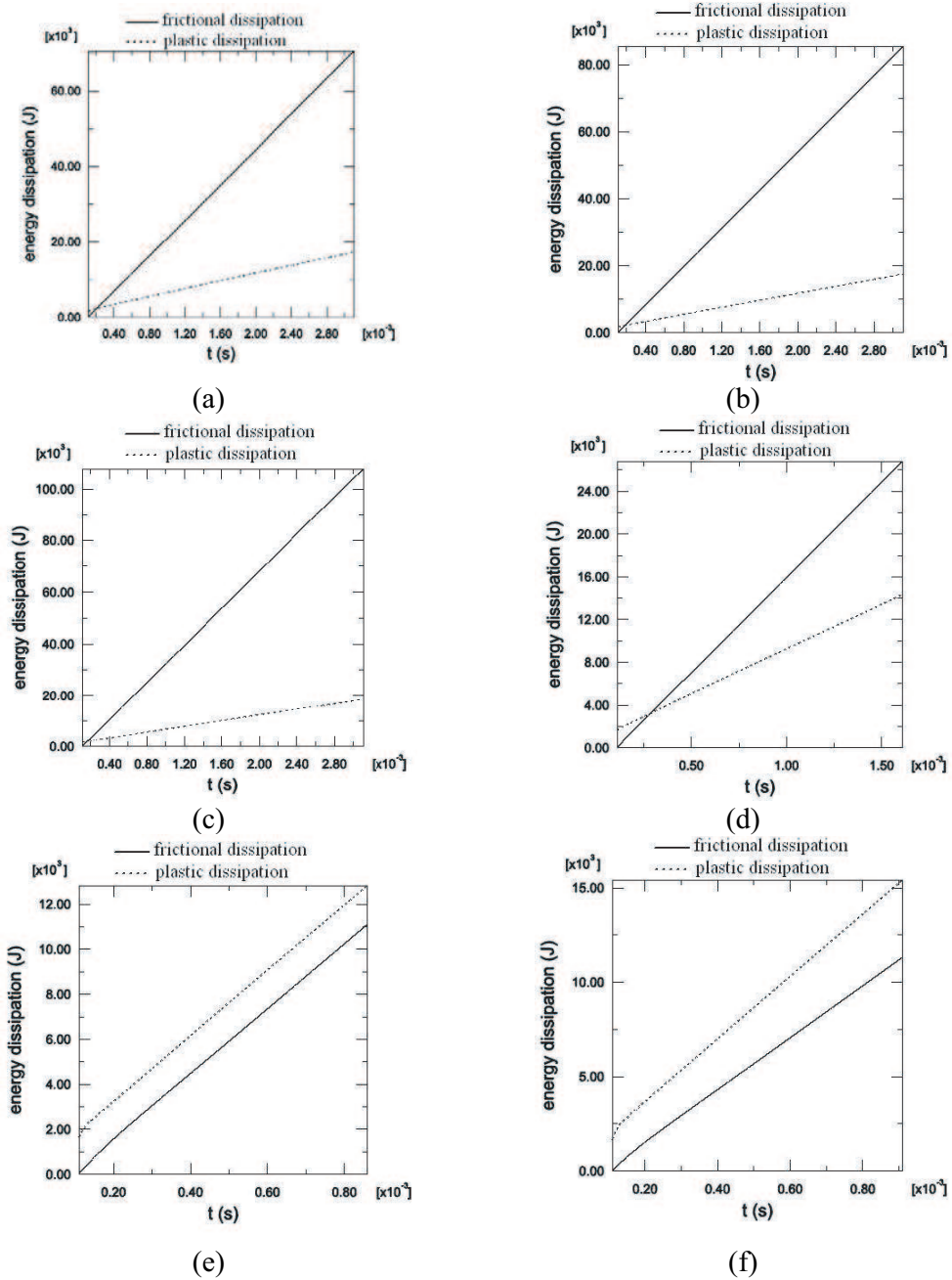


Figure 9. The energy dissipations in FSW under different cases: (a) $v = 2$ mm/s, $\omega = 460$ RPM, (b) $v = 2$ mm/s, $\omega = 550$ RPM, (c) $v = 2$ mm/s, $\omega = 690$ RPM, (d) $v = 4$ mm/s, $\omega = 390$ RPM, (e) $v = 8$ mm/s, $\omega = 390$ RPM, (f) $v = 10$ mm/s, $\omega = 390$ RPM.

4. Conclusions

The finite element method can be successfully applied to the modeling of residual stress distributions in friction stir welds. The results obtained in this paper are as follows:

- (1) The maximum of the longitudinal residual stress occurs in the location where the equivalent plastic strain is decreased.
- (2) The maximum longitudinal residual stress can be increased with the increase of the translational velocity of the pin, but the rotational velocities do not significantly affect the magnitude of the longitudinal residual stresses.
- (3) The energy dissipation on friction is increased with the increase of the angular velocity of the pin. However, with the increase of the translational velocity of the pin the plastic dissipation is increased and the frictional dissipation is decreased.

Acknowledgments

The authors would like to thank Prof. X. M. Deng and Dr. S. W. Xu at the University of South Carolina for their helpful suggestions regarding the present research.

References

- [Brown et al. 1993] W. F. Brown, H. Jr. Mindlin, and C. Y. Ho, *Aerospace structural metals handbook*, CINDAS/Purdue University, 1993.
- [Chao et al. 2003] Y. J. Chao, X. Qi, and W. Tang, "Heat transfer in friction stir welding – experimental and numerical studies", *J. Manuf. Sci. Eng. (Trans. ASME)* **125**:1 (2003), 138–145.
- [Chen and Kovacevic 2003] C. M. Chen and R. Kovacevic, "Finite element modeling of friction stir welding – thermal and thermomechanical analysis", *Int. J. Mach. Tools Manuf.* **43**:13 (2003), 1319–1326.
- [Chen and Kovacevic 2004] C. M. Chen and R. Kovacevic, "Joining of Al 6061 alloy to AISI 1018 steel by combined effects of fusion and solid state welding", *Int. J. Mach. Tools Manuf.* **44**:11 (2004), 1205–1214.
- [Colegrove et al. 2000] P. Colegrove, M. Painter, D. Graham, and T. Miller, "3 dimensional flow and thermal modeling of the friction stir welding process", in *Second international symposium on friction stir welding* (Gothenburg, Sweden), TWI, Cambridge, 2000.
- [Colligan 1999] K. Colligan, "Material flow behavior during friction stir welding of aluminum", *Weld. J.* (July 1999), 229–237 (supplement, *Welding Research*).
- [Dalle Donne et al. 2000] C. Dalle Donne, G. Biallas, T. Ghidini, and G. Raimbeaux, "Effect of weld imperfections and residual stresses on the fatigue crack propagation in friction stir welded joints", in *Second international symposium on friction stir welding* (Gothenburg, Sweden), TWI, Cambridge, 2000.
- [Dalle Donne et al. 2001] C. Dalle Donne, E. Lima, J. Wegener, A. Pyzalla, and T. Buslaps, "Investigation of residual stresses in friction stir welds", in *Third international symposium on friction stir welding* (Kobe, Japan), TWI, Cambridge, 2001.
- [Deng and Xu 2001] X. Deng and S. Xu, "Solid mechanics simulation of friction stir welding process", *Trans. NAMRI/SME, SME* **XXIX** (2001), 631–638.
- [Deng and Xu 2004] X. M. Deng and S. W. Xu, "Two-dimensional finite element simulation of material flow in the friction stir welding process", *J. Manuf. Process.* **6**:2 (2004), 125–133.
- [Guerra et al. 2002] M. Guerra, C. Schmidt, J. C. McClure, L. E. Murr, and A. C. Nunes, "Flow patterns during friction stir welding", *Mater. Charact.* **49**:2 (2002), 95–101.

- [Hornbach et al. 2003] D. Hornbach, M. Mahoney, P. Prevey, D. Waldron, and J. Cammett, “Low plasticity burnishing of friction stir welds in 2219 aluminum to increase corrosion fatigue life”, pp. 302–306 in *Trends in welding research, proceedings of the 6th international conference* (Phoenix, 2002), edited by S. A. David et al., ASM International, Materials Park, OH, 2003.
- [James et al. 2004] M. N. James, D. G. Hattingh, D. J. Hughes, L. W. Wei, E. A. Patterson, and J. Quinta Da Fonseca, “Synchrotron diffraction investigation of the distribution and influence of residual stresses in fatigue”, *Fatigue Fract. Eng. Mater. Struct.* **27**:7 (2004), 609–622.
- [Li et al. 1999] Y. Li, L. E. Murr, and J. C. McClure, “Flow visualization and residual microstructures associated with the friction stir welding of 2024 and 6061 aluminum”, *Mater. Sci. Eng. A* **271**:1-2 (1999), 213–223.
- [McClure et al. 1999] J. C. McClure, Z. Feng, W. Tang, J. E. Gould, L. E. Murr, and X. Guo, “A thermal model of friction stir welding”, pp. 590–596 in *Trends in welding research, proceedings of the 5th international conference* (Pine Mountain, GA, 1998), edited by J. M. Vitek et al., ASM International, Materials Park, OH, 1999.
- [Murr et al. 1998] L. E. Murr, Y. Li, and R. D. Flores, “Intercalation vortices and related microstructural features in the friction stir welding of dissimilar metals”, *Mater. Res. Innov.* **2**:3 (1998), 150–163.
- [Murr et al. 1999] L. E. Murr, E. A. Trillo, Y. Li, R. D. Flores, B. M. Nowak, and J. C. McClure, “Solid-state flow associated with the friction stir welding of dissimilar metals”, pp. 31–36 in *Fluid flow phenomena in metals processing* (San Diego, 1999), edited by N. El-Kaddah et al., Warrendale, PA, 1999.
- [Peel et al. 2003] M. Peel, A. Steuwer, M. Preuss, and P. J. Withers, “Microstructure, mechanical properties and residual stresses as a function of welding speed in aluminium AA5083 friction stir welds”, *Acta Mater.* **51**:16 (2003), 4791–4801.
- [Reynolds et al. 2003] A. P. Reynolds, W. Tang, T. Gnaupel-Herold, and P. H., “Structure, properties and residual stress of 304L stainless steel friction stir welds”, *Scr. Mater.* **48**:9 (2003), 1289–1294.
- [Song and Kovacevic 2003] M. Song and R. Kovacevic, “Thermal modeling of friction stir welding in a moving coordinate system and its validation”, *Int. J. Mach. Tools Manuf.* **43**:6 (2003), 605–615.
- [Staron et al. 2004] P. Staron, M. Kocak, S. Williams, and A. Wescott, “Residual stress in friction stir-welded Al sheets”, *Physica B Condens. Matter* **350**:1-3 (2004), e491–e493.
- [Sutton et al. 2002] M. A. Sutton, A. P. Reynolds, D. Q. Wang, and C. R. Hubbard, “A study of residual stresses and microstructure in 2024-T3 aluminum friction stir butt welds”, *J. Eng. Mater. Technol. (Trans. ASME)* **124**:2 (2002), 215–221.
- [Tang et al. 1998] W. Tang, X. Guo, J. C. McClure, and L. E. Numes, “Heat input and temperature distribution in friction stir welding”, *J. Mater. Process. Manuf. Sci.* **7**:2 (1998), 163–172.
- [Thomas et al. 1991] W. M. Thomas, E. D. Nicholas, J. C. Needham, M. G. Murch, P. Templesmith, and C. J. Dawes, “Friction stir welding”, International Patent Application No. PCT/GB92102203 and Great Britain Patent Application No. 9125978.8, 1991.
- [Ulysse 2002] P. Ulysse, “Three-dimensional modeling of the friction stir welding process”, *Int. J. Mach. Tools Manuf.* **42**:14 (2002), 1549–1557.
- [Webster et al. 2001] P. J. Webster, L. Djapic Oosterkamp, P. A. Browne, D. J. Hughes, W. P. Kang, P. J. Withers, and G. B. M. Vaughan, “Synchrotron X-ray residual strain scanning of a friction stir weld”, *J. Strain Anal. Eng. Des.* **36**:1 (2001), 61–70.
- [Xu and Deng 2002] S. Xu and X. Deng, “A three-dimensional model for the friction stir welding process”, pp. 699–704 in *Proceedings of the 21st Southeastern Conference on Theoretical and Applied Mechanics (SECTAM XXI)*, 2002.
- [Xu et al. 2001] S. Xu, X. Deng, A. P. Reynolds, and T. U. Seidel, “Finite element simulation of material flow in friction stir welding”, *Sci. Technol. Weld. Joining* **6**:3 (2001), 191–193.
- [Zhang and Zhang 2005] Z. Zhang and H. W. Zhang, “The 3D simulation of friction stir welding process”, pp. 1338–1342 in *International conference on mechanical engineering and mechanics* (Nanjing, China), 2005.
- [Zhang et al. 2005a] H. W. Zhang, Z. Zhang, and J. T. Chen, “Effect of angular velocity of the pin on material flow during friction stir welding”, *Acta Metall. Sin.* **41** (2005), 853–869. In Chinese.
- [Zhang et al. 2005b] H. W. Zhang, Z. Zhang, and J. T. Chen, “The finite element simulation of the friction stir welding process”, *Mater. Sci. Eng. A* **403**:1-2 (2005), 340–348.

[Zhu and Chao 2004] X. K. Zhu and Y. J. Chao, "Numerical simulation of transient temperature and residual stresses in friction stir welding of 304L stainless steel", *J. Mater. Process. Technol.* **146**:2 (2004), 263–272.

Received 8 Aug 2006. Revised 7 Nov 2006. Accepted 27 Feb 2007.

ZHAO ZHANG: zhangz@dlut.edu.cn

Department of Engineering Mechanics, State Key Laboratory of Structural Analysis for Industrial Equipment, Dalian University of Technology, Dalian 116024, China

HONGWU ZHANG: zhanghw@dlut.edu.cn

Department of Engineering Mechanics, State Key Laboratory of Structural Analysis for Industrial Equipment, Dalian University of Technology, Dalian 116024, China

NUMERICAL AND EXPERIMENTAL ANALYSIS OF THE STATIC COMPLIANCE OF CHIRAL TRUSS-CORE AIRFOILS

ALESSANDRO SPADONI AND MASSIMO RUZZENE

This paper presents an innovative wing profile featuring an internal truss-like structure of chiral topology. The chiral design is selected because of its unique deformation characteristics, which produce a theoretical, in-plane Poisson's ratio of -1 . Such a Poisson's ratio yields a very high shear modulus, which in principle does not require the wing profile to be defined by a closed section or stressed-skin configuration. In addition, the peculiar deformation mechanism of the chiral configuration allows large decambering deflections to occur, with all the members of assembly behaving within the linear range of the material. Hence the proposed design combines large chordwise compliance and large in-plane shear stiffness. Such conflicting mechanical properties can be achieved through the proper selection of a limited number of geometric parameters defining the core configuration. The objective of the paper is to investigate the compliance characteristics of the airfoil. Two-dimensional profiles, designed according to results from previous investigations, are manufactured and tested to assess compliance and evaluate decambering deflection limits. The experimental analysis is guided by numerical models that account for deviations from the ideal configuration due to manufacturing limitations. Numerical and experimental results demonstrate the influence of core geometry on the compliance and confirm the ability of chiral-core airfoils to sustain large deflections while not exceeding yield strain limits.

1. Introduction

Since the first attempts of powered flight, researchers have tried to devise techniques to implement morphing as a form of flight control. Most notably, the Wright brothers utilized controlled warping of the wings of Wright Flyer to achieve lateral control [Culik 2003]. More recently, the introduction of smart structures and adaptive technologies in the aerospace field has offered opportunities to implement novel structural morphing concepts [McGowan et al. 2003]. In general, morphing requires structural compliance which often conflicts with stiffness requirements for carrying prescribed aerodynamic loads. Among the various configurations investigated, the *belt rib concept* [Campanile and Sachau 2000] allows the achievement of continuous camber variations by transferring the stroke of an actuator to a geometric shape change of the airfoil through a closed belt and an internal structural network. A similar, remarkable solution for camber variation is the *finger concept* [Monner et al. 2000], where the airfoil features a flexible rib composed of plate-like elements connected through revolute joints. Tension-torsion coupling has been employed as an effective means to actively control camber in helicopter blades [Büter et al. 2001], while other design solutions have considered inflatable airfoil structures [Cadogan et al. 2004],

Keywords: morphing airfoils, aeroelastic tailoring, chiral topology, truss-core airfoils.

The authors wish to thank the Army Research Office (ARO) for the support provided for this work under the grant 45518-EG.

variable-span morphing wings [Trenker 2003; Bae et al. 2004], and hingeless flexible leading and trailing edges actuated using shape memory alloys [Kudva 2004].

Cellular materials are applied for the design of structural components with superior mechanical properties and multifunctional characteristics. Their properties are topology dependent, that is, they are a function of the geometry and of the shape of the elementary cell composing the assembly. Cell shape and geometry can be tailored to satisfy requirements of a given application or to achieve various functionalities. The chiral geometry, introduced in [Lakes 1991] and studied extensively in [Prall and Lakes 1997], is a configuration whose negative in-plane Poisson's ratio leads to a very high shear modulus, while featuring some degree of in-plane bending compliance. From a continuum point of view, a structural component defined by periodic structure whose unit cell is the chiral honeycomb may be able to carry higher torsional and shear loads, if compared to the same component made of solid material such as aluminum, which usually possesses a Poisson's ratio of 0.33. This unusual mechanical behavior can be exploited for the design of sandwich structures with chiral truss core as presented in [Spadoni and Ruzzene 2006; Spadoni et al. 2006]. The chiral structure can be accommodated within an airfoil, so that its compliant characteristics can be used to achieve chordwise bending. The deformation mechanisms of chiral structures allow continuous deformations of the airfoil to occur with all the individual members undergoing strains within the linear range of the material. The ability to sustain large deformations without exceeding yield conditions is required to achieve repeatability, while smooth deformations are required for aerodynamic efficiency.

The objective of this paper is to investigate the compliance of the proposed configuration. The work continues previous investigations presented in [Spadoni and Ruzzene 2006], where a coupled-physics model, comprised of weakly-coupled CFD and linear, elastostatic structural analyses, was developed to investigate the influence of the core configuration on the static aeroelastic behavior of the airfoil. Results in [Spadoni and Ruzzene 2006] showed that significant changes in the bending compliance can be achieved through the variation of the geometric parameters defining the core layout. The results of [Spadoni and Ruzzene 2006] are used to select three airfoil designs to be manufactured and tested. The experiments are guided by a numerical analysis performed using nonlinear FE models, which account for deviations in geometry from the ideal configuration introduced by the manufacturing process.

The paper is organized as follows. This introduction is followed by a section describing the motivation for this work, the concept under investigation and the main parameters considered in the analysis. Section 3 presents the airfoil design process and the numerical investigations performed to extend the work in [Spadoni and Ruzzene 2006]. Section 4 describes experimental set-up, procedures and results, and finally Section 5 summarizes the work and provides recommendation for future investigations.

2. Motivations and objectives

2.1. Overview. The design of deformable systems may be driven by kinematic or mechanical considerations, according to the manner in which the system's deformations take place. Deformations may be desired to alleviate structural stresses, they may be passive in nature and arise from low structural stiffness, or they may be actively induced, as in the case of structural mechanisms. Often, the ability of a structural system to deform is coupled with strength requirements, which often arise in applications for which weight considerations drive the design. Aircraft are a prime example of such requirements. Given

the state-of-the-art, it is common practice to select an aircraft configuration based on the most frequent conditions encountered during a mission. For a passenger aircraft, for example, cruise conditions dictate the design. The lifting surfaces may be optimized to maximize the lift-to-drag ratio (L/D) at cruise conditions, but they also need to operate properly even for off-design conditions. Such requirements are satisfied by wing reconfiguration, which is often justified in terms of efficiency, while it is in fact required to sustain flight. The deformations to which lifting surfaces are subjected can be divided into passive, due to aeroelastic phenomena, and active, due to the actuation of mechanisms for reconfiguration such as flaps and slats. Elastic deformations may be further differentiated into span-wise and chord-wise directions. Span-wise deformations may be of torsional, bending or shearing nature. Spanwise bending is usually sought to relieve wing-root stresses, while spanwise torsion is to be avoided as it is one of the major causes of aeroelastic divergence, aileron reversal, and flutter [Hodges and Pierce 2002]. Chordwise deformations are currently avoided as they alter wing section aerodynamic characteristics, and, more importantly, the spanwise characteristics of a wing [Ghiringhelli and Mantegazza 1994; Hodges and Pierce 2002], while highly coupling the design of reconfiguration mechanisms with elastic phenomena. However, exploiting elastic deformations for control and aeroelastic tailoring purposes could yield enormous reductions in complexity and weight.

2.2. Geometry of chiral layout. The proposed wing design exploits the mechanical characteristics of the chiral topology shown in Figure 1 [Lakes 1991; Prall and Lakes 1997]. The layout consists of circular elements acting as nodes, connected by ribs or ligaments tangent to the nodes. The parameters defining the geometry are R , L , β , t , and θ , which in turn define the distance between the node centers, the rib length, the angle between the imaginary line connecting circles centers and a rib, the wall thickness, and the angle defining unit cell's width to height ratio. The following relations hold [Prall and Lakes 1997]:

$$\tan(\beta) = \frac{2r}{L} \tag{1}$$

$$\sin(\beta) = \frac{2r}{R} \tag{2}$$

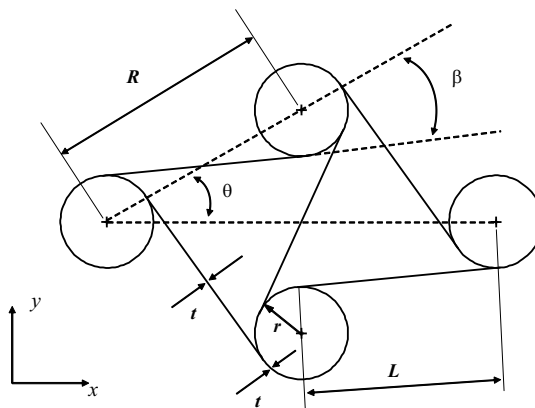


Figure 1. Chiral configuration and parameters defining the unit configuration.

$$\sin(\theta) = \frac{R}{R/2} \quad (3)$$

The resulting cellular structure is characterized by a nonclassical mechanical behavior due to its negative in-plane Poisson's ratio theoretically ≈ -1 [Prall and Lakes 1997], in addition to the ability to undergo large displacements while operating in the elastic range of the constituent material [Prall and Lakes 1997]. Such unusual Poisson's ratio leads to unique deformation characteristics [Prall and Lakes 1997], which include rotational degrees of freedom (DOF) in addition to translational DOF's, and in principle provides the assembly with a very high in-plane shear modulus. A negative Poisson's ratio also affects the dynamics response of assemblies [Lakes 1991]. Moreover, its properties can be altered through variations of geometric parameters such as the ratio of rib length L to node radius R . Examples of configurations with different L/R ratios are shown in Figure 2.

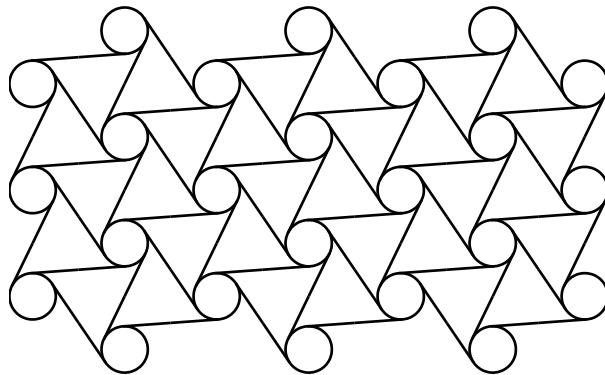
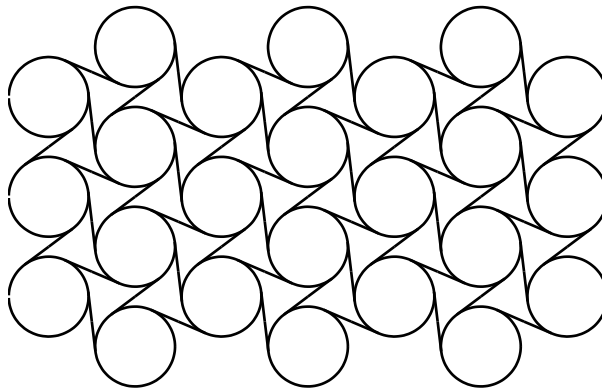
(a) $L/R = 0.90$ (b) $L/R = 0.60$

Figure 2. Variation of chiral lattice characteristics with L/R ratio.

2.3. Objectives and relation to previous investigations. Initial investigations on the application of the chiral geometry to morphing can be found in [Bornengo et al. 2005], where the performance of a conformable race car wing is analyzed through a numerical model. In [Bornengo et al. 2005], the airfoil core is modeled as a homogeneous material with the mechanical properties of a homogenized chiral assembly. This implicitly assumes that the unit cell size is much smaller than the dimensions of the wing. Subsequent studies [Spadoni and Ruzzene 2006; Spadoni et al. 2006] have instead considered configurations where the cell has dimensions of the order of those of the structure (Figure 3). Both in [Bornengo et al. 2005] and in [Spadoni and Ruzzene 2006], an Eppler 420 profile is considered. Such a highly cambered airfoil is chosen to demonstrate the compliance of the assembly, as the deformations that are sought involve decambering effects. In [Spadoni and Ruzzene 2006] the compliance of the core airfoil, in terms of de-cambering deformations due to aerodynamic loads, was investigated through weakly coupled CFD and linear, elastostatic FE models. The results showed the strong influence of the core configuration, and specifically how number of cells and L/R ratio can be selected to achieve desired levels of de-cambering deformations for assigned flow conditions.

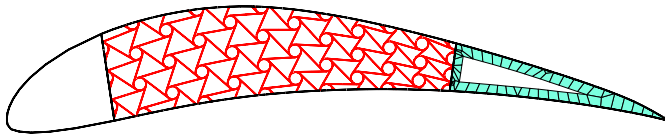


Figure 3. Truss-core airfoil configuration.

The main objective of the current paper is to investigate the properties of the chiral core airfoil experimentally. While in [Spadoni and Ruzzene 2006], the loads applied to the FE models were distributed pressures of aerodynamic nature, the experimental tests on the manufactured airfoil samples involve a simplified scenario whereby mechanical point-loads are employed to promote bending. Specifically, the de-cambering deformations of the airfoil as a result of increasing mechanical loads are measured while monitoring the strain at selected locations. The purpose of the tests is to verify the strong influence of core design on airfoil compliance and to estimate maximum deflections achievable in the elastic range of the material. The tests are guided by a numerical model, which is used to predict load values to be considered in the experiments. The model is significantly different from the one used in previous investigations [Spadoni and Ruzzene 2006]. First, material nonlinearities are introduced to enable the prediction of loads causing the material to enter the plastic range. In addition, the geometry of the structure is modified to reflect variations from the ideal geometry due to the water jet manufacturing process employed for the fabrication of the samples. In particular, a perfect tangency condition between nodes and ligaments cannot be reproduced. Fillets between nodes and ligaments are included in the FE model in an attempt to reproduce the geometry of the test specimens. The presence of fillets is important as it may in fact modify the bending behavior of the ligaments, which is the leading mechanism of deformation of the chiral structure [Lakes 1991].

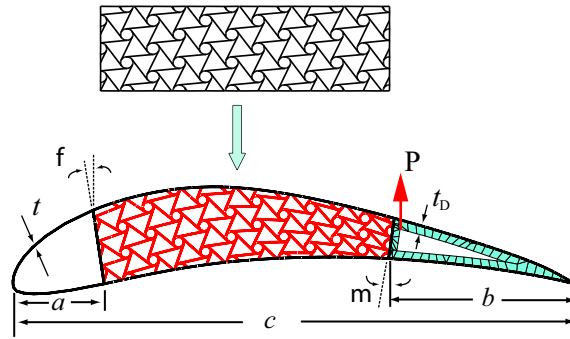


Figure 4. Mapped chiral-core configuration.

3. Design, manufacturing and modeling

3.1. Airfoil configurations. The configuration of the core is defined by selecting a periodic, two-dimensional chiral lattice with specified number of cells and L/R ratio. The resulting geometry is then mapped into the airfoil profile (Eppler 420) through a simple coordinate transformation. The procedure is depicted schematically in Figure 4. The configurations considered for the analysis are depicted in Figure 5. Such geometries, selected on the basis of results from [Spadoni and Ruzzene 2006], are respectively defined by 2 cells across the thickness and $L/R = 0.60$ (Figure 5a), 3 cells across the thickness and $L/R = 0.60$ (Figure 5b), and 3 cells across the thickness and $L/R = 0.94$ (Figure 5c). In the remainder of the paper, the airfoil of Figure 5a will be referred to as configuration *a*, the one depicted in Figure 5b will

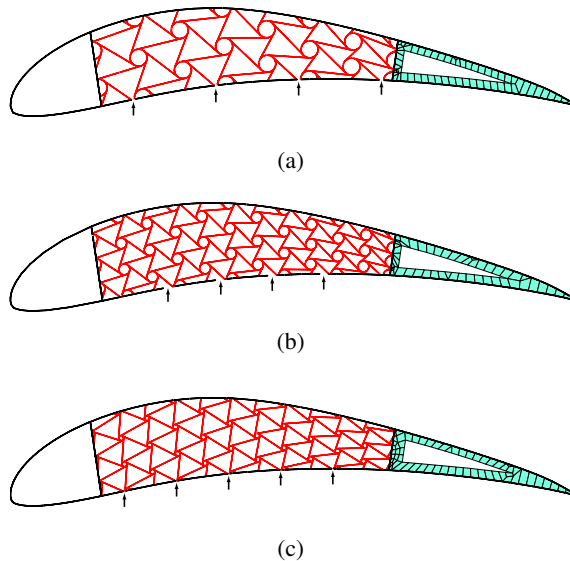


Figure 5. Mapped chiral-core configurations.

be referred to as configuration b , and the one depicted in Figure 5c will be denoted as configuration c . The following wing dimensions are selected on the basis of manufacturing constraints: chord $c = 0.7$ m, angle $\phi = 8.58^\circ$, angle $\mu = 8.0^\circ$, lengths a and b respectively equal to 11 and 23.5 cm, and wall nominal thickness of core structure and skins $t = 0.76$ mm. The out-of-plane thickness of the structure is 1.9 cm. The shaded area in the trailing-edge region (Figure 4) is obtained by offsetting the trailing-edge profile by 2.54 cm. The resulting thickness on the upper and lower trailing-edge boundaries, t_D is then 2.54 cm.

In an attempt to maximize deflections, the lower skin of each airfoil configuration has been cut at the locations indicated by arrows in Figure 5. In the proposed design, the skin has been found to act as an obstacle to the decambering deformation. The ability to carry shear loads illustrated in [Spadoni and Ruzzene 2006] and the potential torsional rigidity of the chiral design due to its negative Poisson's ratio suggest that the classic closed section with stressed skin may not be necessary. In fact the core itself may provide sufficient torsional and shear-loads carrying capacity, that the skins would only be used to provide the surface continuity dictated by aerodynamic requirements. Additional developments of the concept would therefore require the investigation of the application of flexible skins, able to conform to the airfoil, to allow de-cambering deflections, while maintaining smoothness of the airfoil surface. For simplicity of manufacturing, the airfoil is cut out of a solid aluminum plate so that the entire assembly is made of a single material. This leads to skins that are unnecessarily stiff. The decision to cut them at selected locations is simply motivated by the need to reduce the complexity of manufacturing and to avoid the issue of the skin design, which is currently under investigation. Finally, although the proposed design may present complexities that currently outweigh the choice of conventional wing assemblies over their truss-core counterparts, the aim is to demonstrate a concept of a multifunctional and adaptable wing which does not require control surfaces, and may offer optimal aerodynamic characteristics on a wide range of flight regimes.

3.2. Manufacturing. Three truss-core airfoils matching the configurations of Figure 5 have been manufactured using an OMAX[®] water-jet cutting machine out of a plate of aluminum 1.9 cm thick. The resulting test specimens are shown in Figure 6. Manufacturing constraints imposed the presence of fillets at the locations where ligaments join with nodes. The radius of such fillets was estimated to be of the order of 0.13 mm. In addition, the thickness of the ligaments, nominally designed to be 0.76 mm, was found upon measurement to vary between 0.66 and 0.80 mm.

3.3. Numerical model. A structural FE model is developed to investigate the ability of the airfoil to undergo large chord-wise deformations while within the linear range of the material. The model includes material nonlinearity to allow the estimation of load limits for the onset of plastic deformations. Such limits are used as guidelines during the experiments. In the model, developed using the commercially available software ANSYS[®], the material behavior is described by a bilinear stress-strain relation, which approximates the behavior of the selected material (Aluminum 6061 T651: Young's modulus $E = 69$ GPa, density $\rho = 2700$ Kg/m³, Poisson's ratio $\nu = 0.33$, yield stress $\sigma_y = 276$ MPa, and tangent modulus $E_t = 100$ MPa) [Herbert et al. 2006]. In the model, the leading edge region is considered completely clamped and therefore it is not modeled. The trailing-edge regions are made of solid material, while the remaining portions of the wing feature beam-like components. The resulting two-dimensional FE model includes bilinear, 4-node, plane elements and beam elements with both axial and transverse degrees of freedom. The plane element used is PLANE42 [ANSYS 2005], which features 4 nodes and 2 DOF per

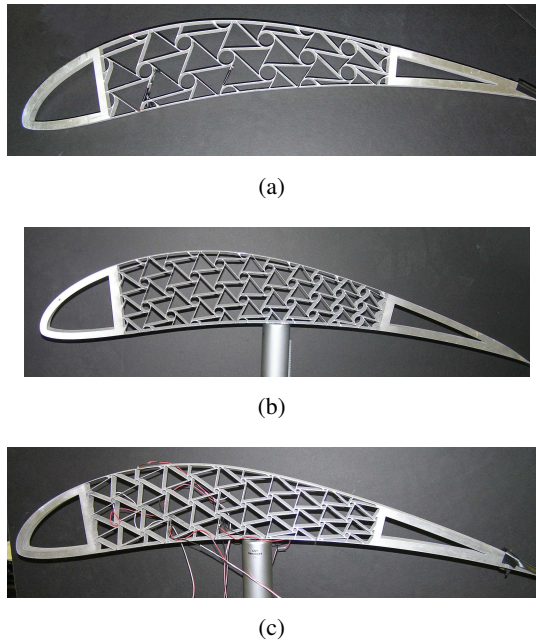


Figure 6. Manufactured truss-core airfoils.

node to describe the in-plane displacements. The beam element (BEAM23 [ANSYS 2005]), features axial and transverse DOF's to describe axial, bending and shear deformations. Both BEAM23 and PLANE42 elements have plastic deformation capabilities. In addition, PLANE42 elements are added in the filleted regions shown in Figure 7. The ligaments discretization is also refined in an attempt to better capture stress concentrations expected at the aforementioned locations. Finally, the presence of

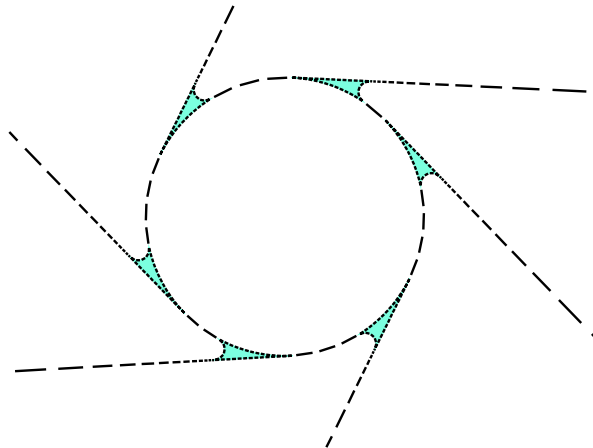


Figure 7. Detail of core discretization with fillets at the nodes/ligaments joints.

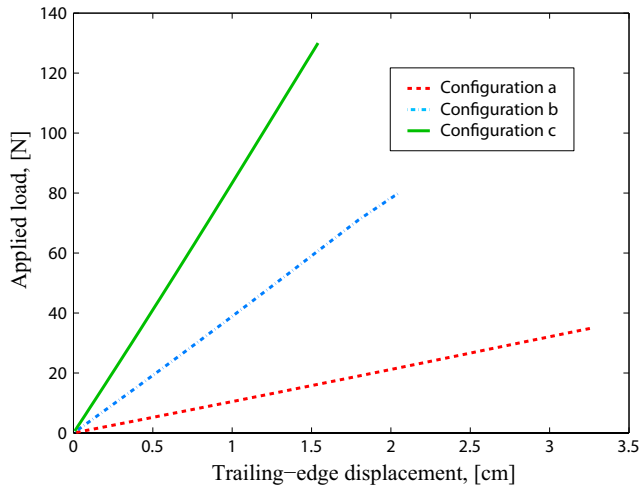


Figure 8. Load, trailing-edge displacement relationship for the considered configurations.

thickness irregularities in the test samples is reproduced by randomly assigning the wall thickness t of each beam element in the interval $[0.66, 0.80]$ mm.

4. Results

4.1. Numerical results.

4.2. Experimental set-up. The deflections of the wing profile are induced by a concentrated mechanical load applied at the location shown in Figure 4. This loading configuration reproduces the one considered experimentally as described in Section 3. The numerical model is used to evaluate the compliance of the three considered configurations, and to identify load ranges to be used during the experiments. Load/displacement curves for the three configurations are plotted in Figure 8, which shows, in adherence with the results of [Spadoni and Ruzzene 2006], that configuration *a* is the most compliant, while configuration *c* is the least compliant. The maximum load applied to each airfoil is selected in order to obtain clear onset of plastic deformations in parts of the structure: for configuration *a*, the maximum load is 35 N, for configuration *b* is 80 N, while for configuration *c* is 130 N. Figure 9 shows the von Mises stress distribution immediately before the onset of plastic deformations. In all cases, the highest stresses appear within the core, and in particular, where ligaments join nodes. It is interesting to note that the locations of highest stress are different for each configuration. Such disparities may be attributed to the different deformation mechanisms that arise by varying the geometry of the honeycomb core by modifying the ratio L/R . The maximum von Mises stress within the considered assemblies follows the stress-strain curve of the constitutive material, as shown in Figure 10.

The experimental setup is depicted in Figure 11. It consists of a Linear Variable Displacement Transducer (LVDT) from RDP[®] (Model DCTH) and associated power supply (Agilent[®], Model E3641A), to measure the trailing edge deflection. The strain in selected structural members is measured by a set of strain gages (VISHAY[®] CEA-13-125UN-120). The strain gages are applied to the ligaments within the

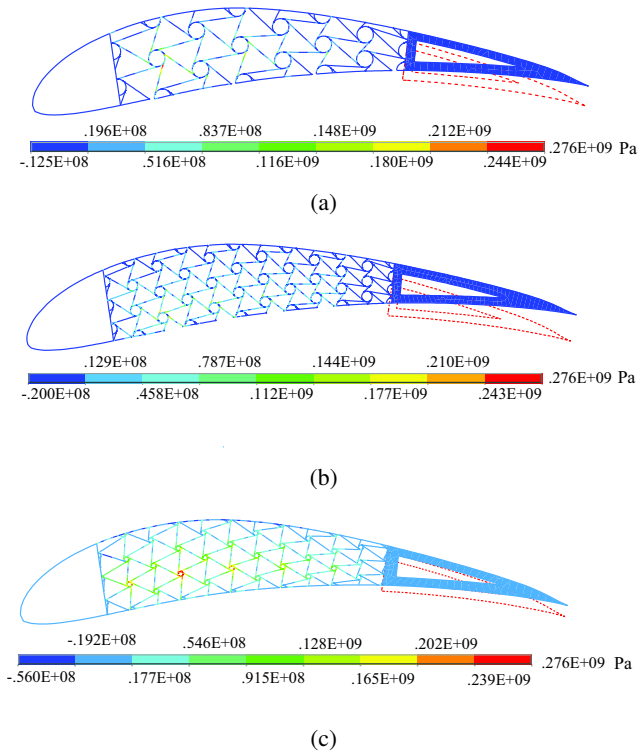


Figure 9. Von Mises stress distribution of considered configurations.

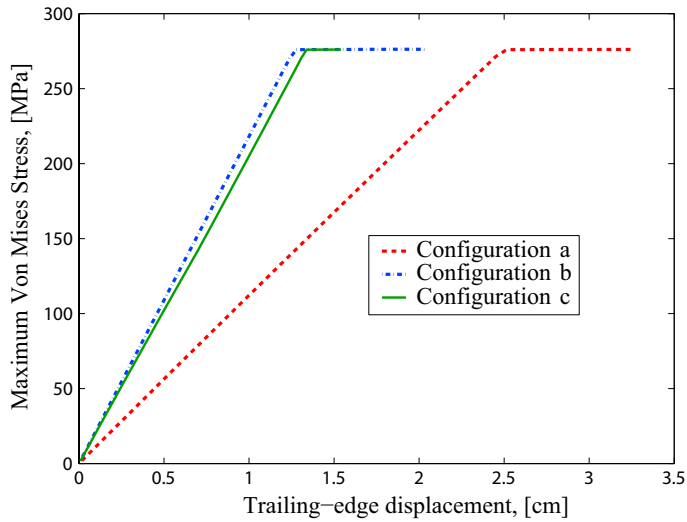


Figure 10. Maximum von Mises stress, trailing-edge displacement relationship for the considered configurations.

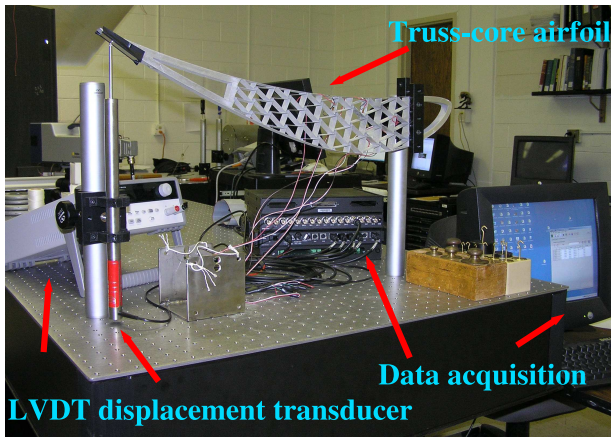


Figure 11. Experimental setup.

truss core and on the airfoil profile based on the stress distribution observed from numerical simulations. The selected locations for the strain gages are depicted in Figure 12, which also shows point of load application and location of the LVDT. The stress distribution within a ligament can be estimated from the linear-elastic deformation mechanism proposed by [Prall and Lakes 1997] and depicted in Figure 13.

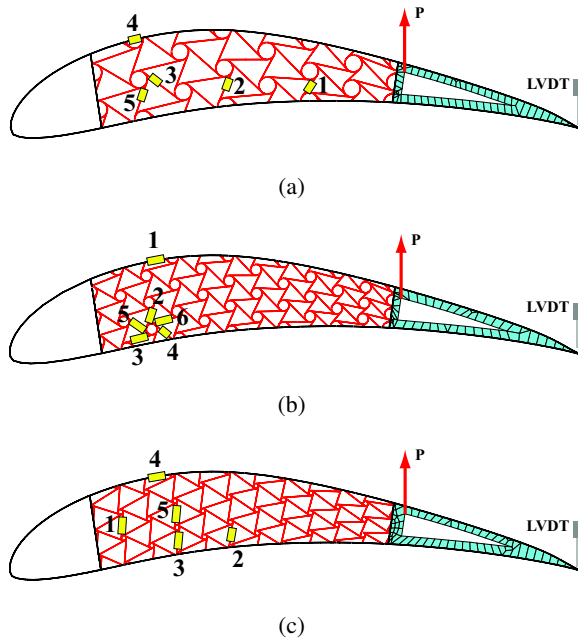


Figure 12. Strain gage, load and LVDT locations.

Loading of the chiral lattice causes rotation of the nodes and bending of the ligaments as depicted in Figure 13. Neglecting shear deformations, the resulting axial strain distribution within a ligament varies linearly along the length from a negative to a positive value, so that, at mid span, the axial strain is approximately 0. The highest axial strain is then expected at the location where ligaments join nodes in a tangential fashion. Consequently, the strain gages are placed on the ligaments, as close to the nodes as possible.

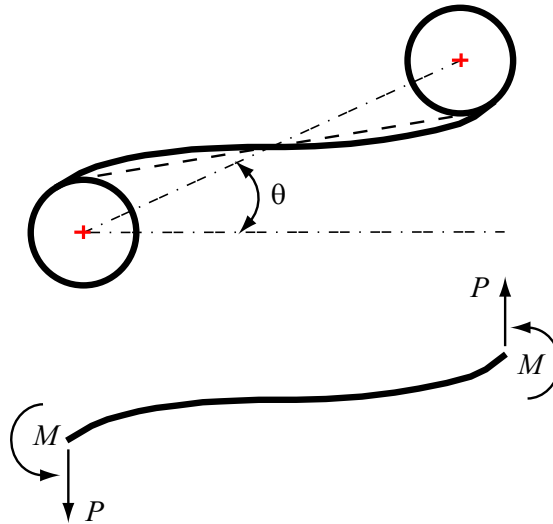


Figure 13. Deformation mechanism proposed by [Prall and Lakes 1997].

4.3. Results and comparison with numerical predictions. The truss-core airfoils depicted in Figure 6 are loaded as described in the previous section. In the experiments, each specimen is subjected to a loading/unloading cycle to observe deviations from linearity, hysteresis and the presence of residual deformations upon unloading. To preserve the integrity of the manufactured samples for future tests, the maximum applied load is maintained below the value which numerical results indicate capable of producing plastic deformations. The numerical analysis in certain circumstances, however, lacks the ability to accurately predict stress concentrations, even with very refined meshes. This is certainly the case for the models presented in the current work, where thin, beam-like members are connected to much more rigid nodes. The load/trailing edge displacement variation for configuration *a* is shown in Figure 14, which directly compares experimental measurements and numerical predictions. The plot shows good agreement and indicates the presence of some hysteresis. Such hysteresis can be associated to friction at the airfoil/LVDT contact region, and internal to the LVDT itself. In addition, a residual displacement is observed upon unloading. The strain recorded at location 5 (see Figure 12) shown in Figure 15 also indicates the presence of a residual strain upon unloading. Figure 15 presents for completeness the strain predicted at location 4, whose variation highlights a discrepancy between numerical and experimental strain. Such a discrepancy may be attributed to the fact that strain gages may not have been placed

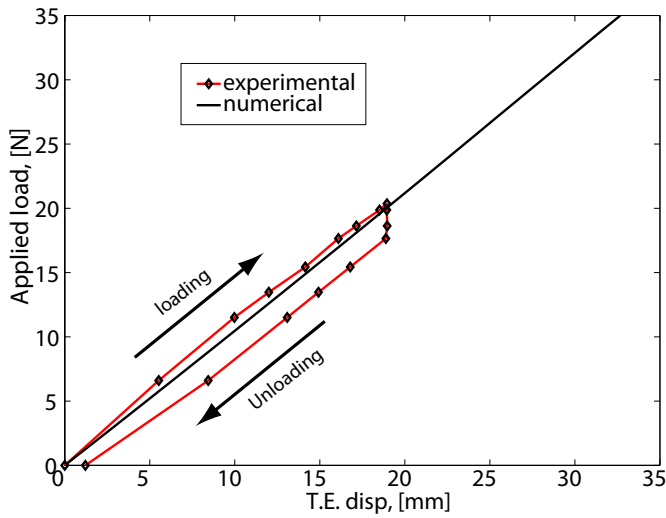


Figure 14. Numerical and experimental trailing-edge displacement for configuration *a*.

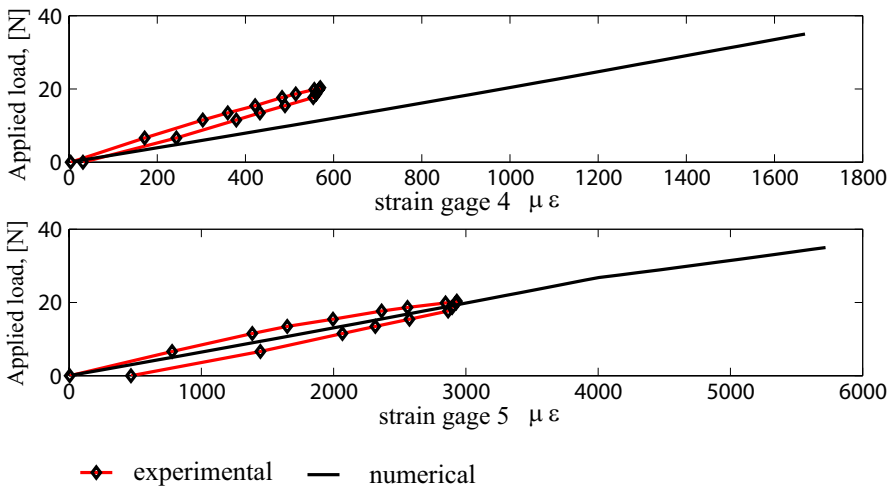


Figure 15. Numerical and experimental strain for configuration *a*.

exactly on the location of maximum strain, and that the strain is averaged over the gage area, while a point, nodal value is extracted from the FE results.

The results for configuration *b* presented in Figure 17 show an excellent agreement between measurements and numerical predictions. As opposed to the previous case, no residual displacement is observed, indicating that, for configuration *b*, all trailing edge displacement is recovered upon unloading. The absence of plastic deformations in the material is confirmed by the strain variation at location 5 (see Figure 12) shown in Figure 16. The strain variation at another location (location 2) does not show the same level of agreement, but confirms the absence of residual strains. It should be observed that the

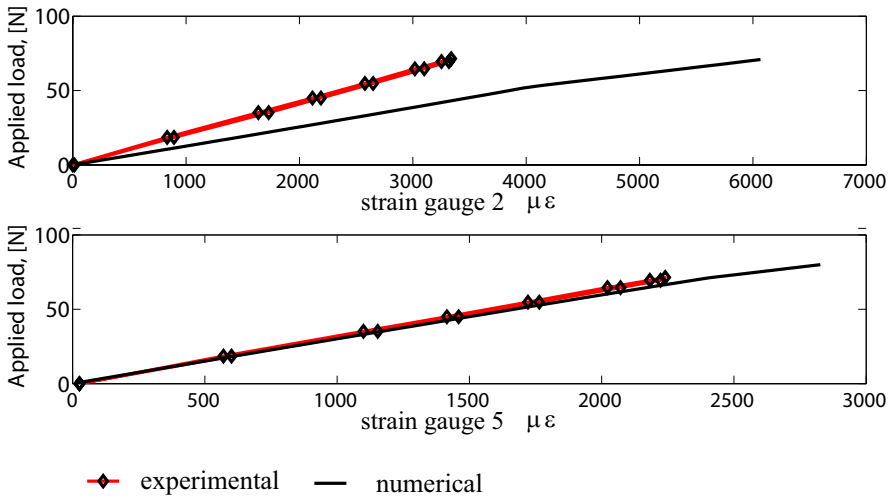


Figure 16. Numerical and experimental strain for configuration *b*.

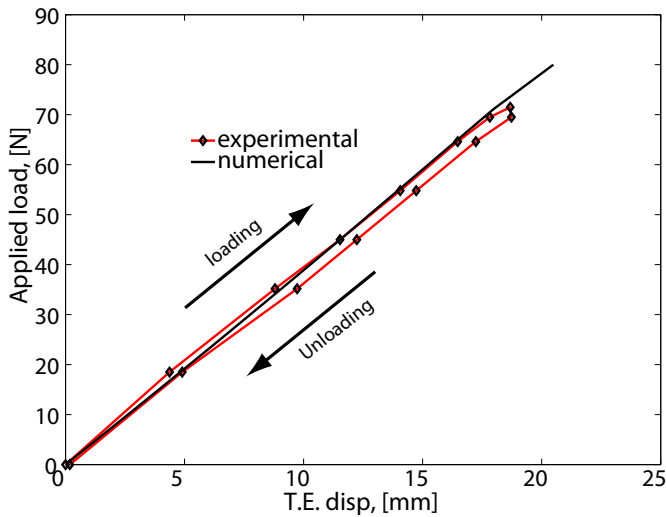


Figure 17. Numerical and experimental trailing-edge displacement for configuration *b*.

application of strain gages on configuration *b* was made more difficult by the smaller size of the unit cell and correspondingly of the ligaments on which strain gages needed to be applied.

Similarly to configurations *a* and *b*, the numerical model for configuration *c* is able to capture the trailing edge displacement variation for increasing applied loads (Figure 18). As in the case of configuration *b*, no residual displacements are observed. Variations of strain at selected locations do not show as good of an agreement as in the previous two cases, but clearly confirm the absence of nonlinear trends in the curve, and of residual strains upon unloading (Figure 19). The lack of agreement on strains in

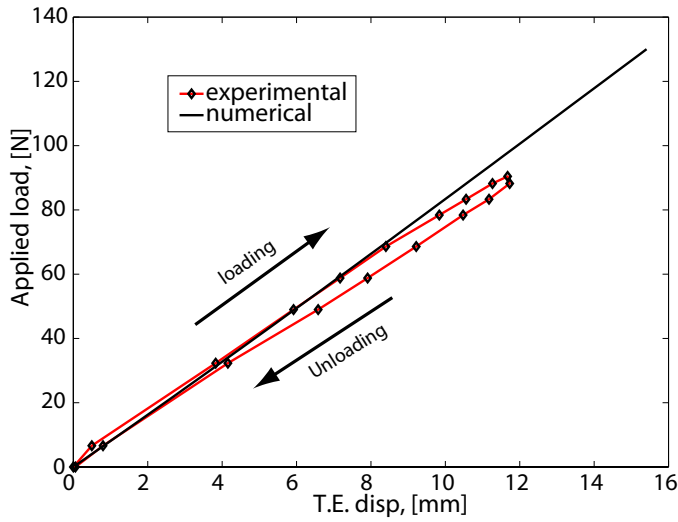


Figure 18. Numerical and experimental trailing-edge displacement for configuration *c*.

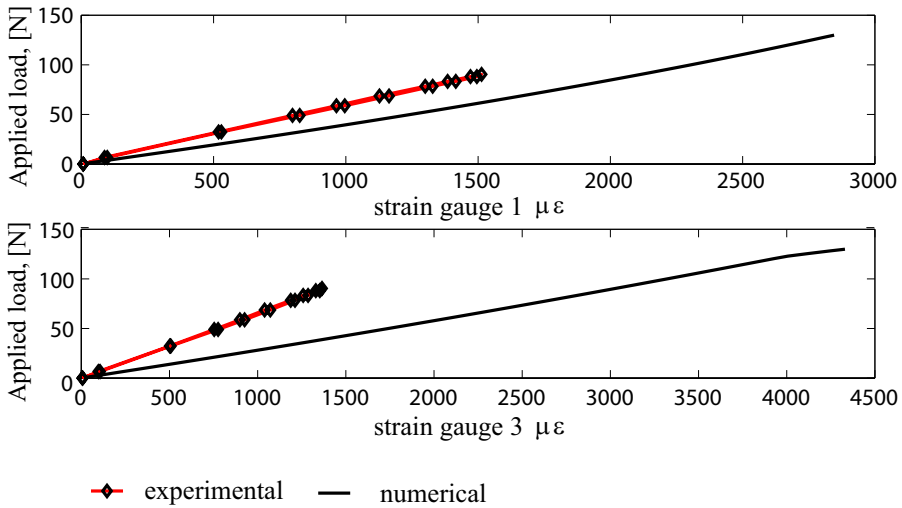


Figure 19. Numerical and experimental strain for configuration *c*.

this and in the previous two cases may indicate shortcomings in the FE model, and a lack in accuracy in the strain gage positioning. It is interesting to note, however, that the numerical model is able to accurately reproduce the displacement/load variation and to show the linear relationships in all three cases. In addition, the experimental results confirm the strong dependence of the airfoil compliance on the core configuration as demonstrated by the direct comparison of trailing edge displacement versus load, experimental and numerical, for the three configurations, which is presented in Figure 20.

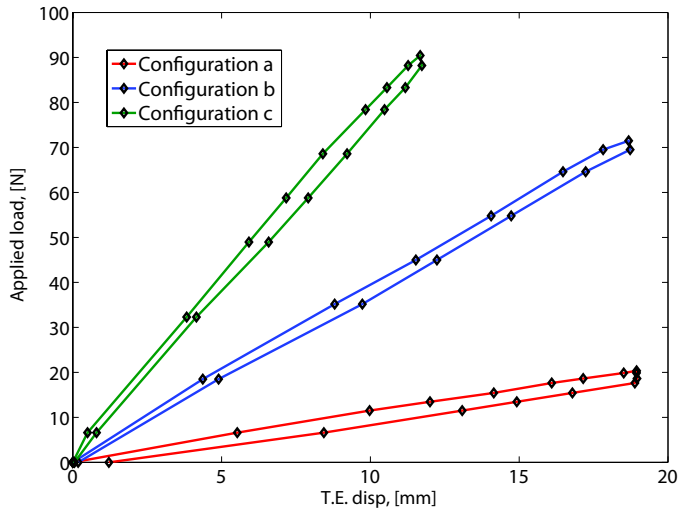


Figure 20. Comparison of trailing-edge displacement for the three considered configurations.

5. Conclusions

This paper presents numerical and experimental investigations performed on a novel airfoil configuration. In the proposed design, a chiral cellular structure is accommodated within the airfoil profile to provide it with chordwise bending compliance, combined with the ability of carrying torsional loads. The compliance characteristics of airfoils with different core designs are investigated with the objective of assessing the ability of the structure to undergo large deflections while remaining in the linear range of the material, and the strong influence of the core design on the overall performance of the airfoil. To this end, three configurations have been designed, manufactured and tested. The tests are guided by numerical investigations performed using nonlinear FE models. A comparison of numerical and experimental results shows that the devised numerical models are overall capable of providing estimates of the onset of plastic deformations and can predict the trailing-edge displacement resulting from assigned loads. Numerical and experimental results also show the ability of the considered airfoil design to undergo significant camber changes. The same analyses suggest the opportunity of achieving significant performance variations through the proper selection of a limited number of parameters which define the core geometry. A natural application for this concept is aeroelastic tailoring. Future investigations will therefore address the performance of three dimensional wings with chiral ribs, or of wings with an internal, three dimensional network which extends the configuration herein investigated. Dynamic characterization of the proposed truss core airfoil should also be performed.

References

- [ANSYS 2005] P. Kohnke (editor), *ANSYS theory reference*, Release 10.0 ed., Canonsburg, PA: ANSYS, 2005, Available at http://www.we.mtu.edu/users/applist/appdocs/ansys/ansys_theory_ref.pdf.
- [Bae et al. 2004] J. S. Bae, T. M. Seigler, D. J. Inman, and I. Lee, “Aerodynamic and aeroelastic considerations of a variable-span morphing wing”, pp. 2378–2396 in *45th AIAA/ASME/ASCE/AHS/ASC Structures, Structural Dynamics and Materials*

- Conference (Palm Springs, CA, 2004), AIAA, Reston, VA, 2004, Available at <http://www.aiaa.org/content.cfm?pageid=2.Paper#2004-1726>.
- [Bornengo et al. 2005] D. Bornengo, F. Scarpa, and C. Remillat, "Evaluation of hexagonal chiral structure for morphing airfoil concept", *Proc. Inst. Mech. Eng. G, J. Aerosp. Eng.* **219**:3 (2005), 185–192.
- [Büter et al. 2001] A. Büter, U. C. Ehlert, D. Sachau, and E. Breitbach, "Adaptive rotor blade concepts: direct twist and camber variation", pp. 1–12 (Section 19) in *Active control technology for enhanced performance operational capabilities of military aircraft, land vehicles and sea vehicles* (Braunschweig, 2000), RTO Meeting Proceedings **51**, NATO Research and Technology Organization, Neuilly-sur-Seine, 2001, Available at <ftp://ftp.rta.nato.int/PubFullText/RTO/MP/RTO-MP-051/MP-051-MSSM-19.PDF>. Report RTO-MP-051.
- [Cadogan et al. 2004] D. Cadogan, T. Smith, F. Uhelsky, and M. MacCusick, "Morphing airfoil wing development for compact package unmanned aerial vehicles", pp. 3205–3217 in *45th AIAA/ASME/ASCE/AHS/ASC Structures, Structural Dynamics and Materials Conference* (Palm Springs, CA, 2004), AIAA, Reston, VA, 2004, Available at <http://www.aiaa.org/content.cfm?pageid=2.Paper#2004-1807>.
- [Campanile and Sachau 2000] L. F. Campanile and D. Sachau, "The belt-rib concept: a structronic approach to variable camber", *J. Intell. Mater. Syst. Struct.* **11**:3 (2000), 215–224.
- [Culik 2003] F. E. C. Culik, "The Wright brothers: first aeronautical engineers and test pilots", *AIAA J.* **41**:6 (2003), 985–1006.
- [Ghiringhelli and Mantegazza 1994] G. Ghiringhelli and P. Mantegazza, "Linear, straight and untwisted anisotropic beam section properties from solid finite elements", *Compos. Eng.* **4**:12 (1994), 1225–1239.
- [Herbert et al. 2006] E. G. Herbert, W. C. Oliver, and G. M. Pharr, "On the measurement of yield strength by spherical indentation", *Philos. Mag.* **86**:33 (2006), 5521–5539.
- [Hodges and Pierce 2002] D. Hodges and G. Pierce, *Introduction to structural dynamics and aeroelasticity*, Cambridge Aerospace Series **15**, Cambridge University Press, New York, 2002.
- [Kudva 2004] J. N. Kudva, "Overview of the DARPA smart wing project", *J. Intell. Mater. Syst. Struct.* **15**:4 (2004), 261–267.
- [Lakes 1991] R. S. Lakes, "Deformation mechanisms in negative Poisson's ratio materials: structural aspects", *J. Mater. Sci.* **26**:9 (1991), 2287–2292.
- [McGowan et al. 2003] A. R. McGowan, D. E. Cox, B. S. Lazos, M. R. Waszak, D. L. Raney, E. J. Siochi, and P. S. Pao, "Biologically inspired technologies in NASA's morphing project", pp. 1–13 in *Smart structures and materials 2003: electroactive polymer actuators and devices (EPAD)* (San Diego, 2003), edited by Y. Bar-Cohen, Proceedings of SPIE **5051**, SPIE, Bellingham, WA, 2003.
- [Monner et al. 2000] H. P. Monner, D. Sachau, and E. Breitbach, "Design aspects of the elastic trailing edge for an adaptive wing", pp. 1–8 (Section 14) in *Structural aspects of flexible aircraft control* (Ottawa, 1999), RTO Meeting Proceedings **36**, NATO Research and Technology Organization, Neuilly-sur-Seine, 2000, Available at <ftp://ftp.rta.nato.int/PubFulltext/RTO/MP/RTO-MP-036/MP-036-14.pdf>. Report RTO-MP-036.
- [Prall and Lakes 1997] D. Prall and R. S. Lakes, "Properties of a chiral honeycomb with a Poisson's ratio of -1 ", *Int. J. Mech. Sci.* **39**:3 (1997), 305–314.
- [Spadoni and Ruzzene 2006] A. Spadoni and M. Ruzzene, "Static aeroelastic behavior of chiral-core airfoils", *J. Intell. Mater. Syst. Struct.* (2006). In press.
- [Spadoni et al. 2006] A. Spadoni, M. Ruzzene, and F. Scarpa, "Dynamic response of chiral truss-core assemblies", *J. Intell. Mater. Syst. Struct.* **17**:11 (2006), 941–952.
- [Trenker 2003] M. Trenker, "Design concepts for adaptive airfoils with dynamic transonic flow control", *J. Aircr.* **40**:4 (2003), 734–740.

Received 30 Nov 2006. Accepted 25 Mar 2007.

ALESSANDRO SPADONI: alessandro@gatech.edu

School of Aerospace Engineering, Georgia Institute of Technology, 270 Ferst Drive, Atlanta, GA, United States

MASSIMO RUZZENE: Massimo.ruzzene@ae.gatech.edu

School of Aerospace Engineering, Georgia Institute of Technology, 270 Ferst Drive, Atlanta, GA, United States

RESONANCE PHENOMENA AT THE INTERFACE OF TWO PERFECTLY BONDED, PRESTRESSED ELASTIC STRIPS

GRAHAM A. ROGERSON AND ANTON V. KRYNKIN

The problem of vibration localized within the vicinity of the interface of two perfectly bonded semi-infinite elastic strips is investigated. The cases of free and forced vibration are both examined in strips composed of prestressed, incompressible elastic material. It is established that the localized interfacial vibration frequencies are functions of an associated interfacial wave speed. A consequence of the prestress is that interfacial waves exist only for certain regimes of primary deformation. For critical values of principal stretches the wave speed may approach either zero, corresponding to quasistatic interfacial deformations, or an associated body wave speed, corresponding to degeneration of the interfacial wave into a body wave. In the case of free vibration, approaching a critical principal stretch value is shown to result in a significant increase in the edge spectrum density. In the forced vibration problem, a corresponding significant decrease in the influence in the resonances is observed. The analysis is carried out within the most general appropriate constitutive framework, and includes a number of numerical illustrations involving neo-Hookean and Varga materials to illustrate the aforementioned phenomena.

1. Introduction

The subject of interfacial waves propagating along the interface of two perfectly bonded elastic half-spaces is a well-studied scientific area of long history. An important property of such waves is that the associated displacement and stress fields are localized within the vicinity of the interface. In the classical linear isotropic elastic case this problem was first studied by Stoneley [1924], with this type of wave later being termed a Stoneley wave. In more recent years, the study of this type of wave has been extended to more constitutively complicated elastic media; see, for example, [Dowaikh and Ogden 1991; Chadwick 1995a; 1995b].

In the case of two perfectly bonded prestressed incompressible elastic half-spaces, the existence criteria for interfacial waves has been investigated with respect to the most general isotropic strain energy function associated with incompressible elasticity [Dowaikh and Ogden 1991]. Within their two-dimensional study, the crucial influence of the principal stretches on the interfacial wave speed was established. A particular feature well worthy of remark is the existence of critical principal stretch values associated with the vanishing of the interfacial wave speed, indicating the existence of interfacial waves only within certain principal stretch domains. A further feature, which has also previously been investigated, is the problem of interfacial waves propagating along the interface of a half-space and a layer of finite thickness. This introduces the effect of dispersion, which is again highly sensitive to changes in the principal stretches. Such dependency has been investigated by Ogden and Sotiropoulos [1995] and Sotiropoulos and Sifniotopoulos [1995].

Keywords: interfacial vibration, prestress, elasticity.

In this present paper we are specifically interested in the type of so-called interfacial vibration that may occur when two layers, each infinite only in one direction, are perfectly bonded along a common boundary. Attention is restricted to a two-dimensional case; the geometrical setup may therefore be thought of as two perfectly bonded semiinfinite strips. In the case of one semiinfinite strip, vibrations localized within the vicinity of a free edge were investigated by Kaplunov et al. [2004], who established a link between the localized free edge vibration frequencies and the associated surface wave speed. These authors also showed that when a load is applied to the edge, various resonance phenomena may be observed. Within the framework of their study, a number of boundary conditions imposed on the upper and lower faces of the semiinfinite strip were considered and shown able to support localized edge vibrations. The problem was also shown to lead to a discrete spectrum of edge vibration frequencies which are in fact functions of the associated surface wave speed. In the case of surface waves, the wave speed is crucially dependent of the normal Cauchy prestress σ_2 . A significant increase in the spectrum density was observed when the value of σ_2 was close to that associated with the vanishing of the surface wave speed.

Our aim is to extend the above investigations to elucidate the existence of localized vibration modes associated with two perfectly bonded, prestressed, semiinfinite incompressible elastic strips. In doing so we establish that localized interfacial vibration modes, associated with free interfacial vibrations, do exist and that their frequencies are functions of an associated interfacial wave speed. Moreover, in the case of vibrations arising from interfacial loading, a discrete spectrum of resonance frequencies is shown to exist, which are again functions of the interfacial wave speed. In contrast to the surface wave speed, the interfacial wave speed is independent of the normal (to the interface) static Cauchy stress. Specifically, we consider a plane problem and focus attention on the case in which both strips have coincident principal prestrain axes, one of which is normal to the interface. In the context of interfacial waves, the analogous problem has been previously investigated, largely for a class of strain energy functions epitomized by the Mooney–Rivlin strain energy function [Ogden 1984].

The layout of this paper is as follows. In Section 2 the specific interfacial vibration problem to be addressed is stated and the governing equations established. In Section 3 it is demonstrated that the discrete spectrum of interfacial vibration frequencies are functions of the associated interfacial wave speed. In Section 4 we review results related to the criteria for the existence of interfacial waves and investigate their consequences for interfacial vibration. In Section 5 the influence of the principal stretches, and in particular the passage towards critical principal stretches, is examined and numerically illustrated.

2. Statement of the problem

Consider two prestressed incompressible elastic plane semiinfinite strips, each of thickness $2h$, which are perfectly bonded along a common boundary. Relative to a Cartesian coordinate system, $\{x_1, x_2, x_3\}$, the two strips are bounded in the x_2 direction, with interface along $x_1 = 0$. A horizontal force of amplitude A acting parallel to x_1 , is applied at the interface; see Figure 1. We also remark that the principal axes of the static primary deformation coincide with the chosen coordinate axes. The mixed boundary conditions applied to the faces $x_2 = \pm h$ will preclude any normal displacement, that is, displacement in the x_2 direction. These strips may therefore be thought of as two-dimensional and forming some sort of frictionless enclosure, terminology apparently first adopted by Kaplunov et al. [2004].

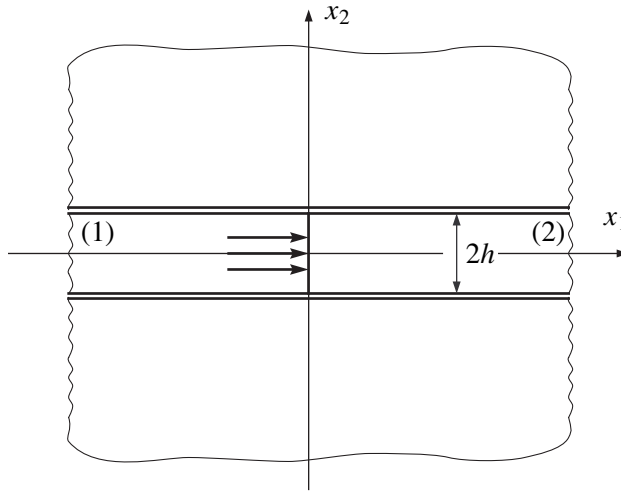


Figure 1. The geometry of the two semiinfinite strips.

Prior to proceeding with the establishment of the appropriate governing equations, it will prove helpful to introduce some notation and conventions. Parameters associated the left and right strips are assigned the superscripts (1) and (2), respectively. We shall also let $\lambda_j^{(i)}$, $i = 1, 2, j = 1, 2, 3$, denote the principal stretches along the x_j axes in the indicated strip. The squares of these principal stretches are the eigenvalues of the left, or right, Cauchy–Green strain tensor. In view of our assumption of incompressibility, the product of the principal stretches within each strip must obey the constraint $\lambda_1^{(i)}\lambda_2^{(i)}\lambda_3^{(i)} = 1$. The strain-energy function in each strip will be assumed to be a function of the three appropriate principal stretches. The subsequent analysis will be carried out within a general theoretical framework. However, for numerical calculations particular cases of the Ogden strain-energy function will be employed. This particularly general strain energy function may be represented in the form

$$W(\lambda_1^{(i)}, \lambda_2^{(i)}, \lambda_3^{(i)}) = \frac{\mu^{(i)}}{s} [(\lambda_1^{(i)})^s + (\lambda_2^{(i)})^s + (\lambda_3^{(i)})^s - 3], \quad s \in \mathbb{R}, \tag{1}$$

with $\mu^{(i)}$ denoting the shear modulus [Ogden 1984]. Through a combination of the problem’s two-dimensional nature and incompressibility, we will also assume that

$$\lambda_3^{(i)} = 1, \quad \lambda_2^{(i)} = 1/\lambda_1^{(i)}, \quad \lambda_1^{(i)} \equiv \lambda^{(i)}. \tag{2}$$

We remark that the two particular cases of the strain energy (1) associated with $s = 1$ and $s = 2$ correspond to what are commonly known as Varga and neo-Hookean materials, respectively. These two strain energy functions will be later employed for the purposes of numerical illustration.

We now consider small time-dependent motions superimposed upon the finite, static primary deformation. In view of the fact that our problem is two-dimensional, we take the infinitesimal displacement v_3 along x_3 to be identically zero and assume that the other two displacement components, v_1 and v_2 , are independent of x_3 . The two nontrivial equations of motion, assuming time variation of the form $\exp(i\omega t)$,

are then given by

$$\begin{aligned} B_{1111}^{(i)} v_{1,11}^{(i)} + (B_{1122}^{(i)} + B_{1221}^{(i)}) v_{2,12}^{(i)} + B_{2121}^{(i)} v_{1,22}^{(i)} - p_{,1}^{(i)} &= -\rho^{(i)} \omega^2 v_1^{(i)}, \\ B_{1212}^{(i)} v_{2,11}^{(i)} + (B_{1122}^{(i)} + B_{1221}^{(i)}) v_{1,12}^{(i)} + B_{2222}^{(i)} v_{2,22}^{(i)} - p_{,2}^{(i)} &= -\rho^{(i)} \omega^2 v_2^{(i)}, \end{aligned} \tag{3}$$

with the corresponding two-dimensional linearised incompressibility condition requiring that

$$v_{1,1}^{(i)} + v_{2,2}^{(i)} = 0. \tag{4}$$

For full details concerning the derivation of these governing equations, the reader is referred to [Dowaikh and Ogden 1991]. In (3), B_{ijkl} denote components of the fourth order elasticity tensor, which possesses the symmetries $B_{ijji} = B_{jii j}$ and $B_{iijj} = B_{jjii}$, with $i, j, k, l = 1, 2, 3$. Additionally, a comma indicates differentiation with respect to the indicated component of \mathbf{x} , ω is the circular frequency and $\rho^{(i)}$, $i = 1, 2$, are the mass densities.

As alluded to briefly earlier in the paper, the problem we will consider involves imposing conditions on the faces $x_2 = \pm h$, together with some possible loading at the interface $x_1 = 0$. The mixed conditions, imposed on the faces of the strips at $x_2 = \pm h$, are prescribed by

$$v_2^{(i)}|_{x_2=\pm h} = 0, \quad \tau_{21}^{(i)}|_{x_2=\pm h} = 0, \tag{5}$$

while the perfectly bonded interface conditions take the form

$$v_j^{(1)}|_{x_1=0} = v_j^{(2)}|_{x_1=0}, \quad \tau_{12}^{(1)}|_{x_1=0} = \tau_{12}^{(2)}|_{x_1=0}, \quad \tau_{11}^{(1)}|_{x_1=0} = \tau_{11}^{(2)}|_{x_1=0} - A\phi(x_2), \tag{6}$$

with traction components

$$\begin{aligned} \tau_{11}^{(i)} &= (B_{1111}^{(i)} + B_{1212}^{(i)} - B_{1221}^{(i)} - \sigma_1^{(i)}) v_{1,1}^{(i)} + B_{1122}^{(i)} v_{2,2}^{(i)} - p^{(i)}, \\ \tau_{12}^{(i)} &= B_{1212}^{(i)} v_{2,1}^{(i)} + (B_{1212}^{(i)} - \sigma_1^{(i)}) v_{1,2}^{(i)}, \quad \tau_{21}^{(i)} = B_{2121}^{(i)} v_{1,2}^{(i)} + (B_{1212}^{(i)} - \sigma_1^{(i)}) v_{2,1}^{(i)}, \end{aligned}$$

where $\sigma_1^{(i)}$ denote the appropriate principal Cauchy stresses along x_1 in the prestressed equilibrium states within each semistrip. The principal Cauchy stress must also be continuous across the interface, namely, $\sigma_1^{(1)} = \sigma_1^{(2)}$ at $x_1 = 0$.

We also note that in the perfectly bonded interface conditions in Equation (6), $A\phi(x_2)$ denotes a force of amplitude A , which, following Kaplunov et al. [2004], we assume to be

$$\phi(x_2) = \pi^2 \left(\frac{1}{3} - \frac{x_2^2}{h^2} \right). \tag{7}$$

Finally, in this section it will prove convenient to introduce the two nondimensional parameters $\epsilon = \mu^{(2)}/\mu^{(1)}$ and $\kappa = \rho^{(2)} \mu^{(1)}/\rho^{(1)} \mu^{(2)}$. These will aid numerical investigation and in particular allow us to easily contrast the relative parameters of both semiinfinite strips.

3. The discrete spectrum of the problem solution

Taking into account the boundary conditions imposed upon the upper and lower faces at $x_2 = \pm h$ — see (5) — the solution of equations (3) together with the incompressibility conditions permits the two

possible forms of linear combinations

$$(v_1^{(i)}, v_2^{(i)}, p^{(i)}) = \sum_{n=1}^{\infty} [V_1^{(i)} \cos(k_n x_2), V_2^{(i)} \sin(k_n x_2), k_n P^{(i)} \cos(k_n x_2)] \times \exp [(-1)^{i+1} q^{(i)} x_1], \quad (8)$$

$$(\tilde{v}_1^{(i)}, \tilde{v}_2^{(i)}, \tilde{p}^{(i)}) = \sum_{n=1}^{\infty} [\tilde{V}_1^{(i)} \sin(\tilde{k}_n x_2), \tilde{V}_2^{(i)} \cos(\tilde{k}_n x_2), \tilde{k}_n \tilde{P}^{(i)} \sin(\tilde{k}_n x_2)] \times \exp [(-1)^{i+1} \tilde{q}^{(i)} x_1], \quad (9)$$

composed of harmonics characterized by two discrete sets of wave numbers $k_n = \Lambda_n/h = \pi n/h$, and $\tilde{k}_n = \tilde{\Lambda}_n/h = \pi(n - \frac{1}{2})/h$, with $n \in \mathbb{N}$, which allow us to define an associated speed of wave propagation using the circular frequency ω as

$$c = \frac{\omega h}{\Lambda_n}, \quad \tilde{c} = \frac{\omega h}{\tilde{\Lambda}_n}. \quad (10)$$

Without loss of generality, the speed given by the first of Equation (10) is used below as the main unknown parameter. It will be further assumed that both the velocity and circular frequency are real-valued.

To reduce the number of similar and relatively routine calculations, we restrict attention to the first harmonic given in Equation (8). The general form of the problem solution, for both the left and right half-strips, may now be substituted into the equations of motion and incompressibility condition, Equations (3) and (4), giving us

$$\alpha^{(i)} - \rho^{(i)} c^2 - (2\beta^{(i)} - \rho^{(i)} c^2) \left(\frac{q^{(i)}}{k_n}\right)^2 + \left(\frac{q^{(i)}}{k_n}\right)^4 \gamma^{(i)} = 0, \quad (11)$$

where

$$\alpha^{(i)} = B_{2121}^{(i)}, \quad \beta^{(i)} = \frac{1}{2}(B_{1111}^{(i)} + B_{2222}^{(i)} - 2B_{1122}^{(i)} - 2B_{1221}^{(i)}), \quad \gamma^{(i)} = B_{1212}^{(i)}.$$

For solutions to be localized close to the interface at $x_1 = 0$, we require decay of the displacement components and incremental pressure, within both strips, as $|x_1| \rightarrow \infty$. As a consequence, the roots of the biquadratic equation (11) must be chosen so that they have positive real parts. Only two roots, denoted by $q_j^{(i)}(c)$, for $i, j = 1, 2$, are able to satisfy this requirement; these may be represented in the explicit forms

$$q_j^{(i)}(c) = k_n \sqrt{\frac{2\beta^{(i)} - \rho^{(i)} c^2 + (-1)^j \sqrt{(2\beta^{(i)} - \rho^{(i)} c^2)^2 - 4\gamma^{(i)}(\alpha^{(i)} - \rho^{(i)} c^2)}}{2\gamma^{(i)}}} \quad (12)$$

defined through

$$(q_1^{(i)})^2 + (q_2^{(i)})^2 = \frac{k_n^2}{\gamma^{(i)}} (2\beta^{(i)} - \rho^{(i)} c^2), \quad (q_1^{(i)} q_2^{(i)})^2 = \frac{k_n^4}{\gamma^{(i)}} (\alpha^{(i)} - \rho^{(i)} c^2). \quad (13)$$

Each harmonic in (8) can now be represented through a two term summation, with the arguments of the exponents taking appropriate roots of (11).

To proceed further, we need to represent the function ϕ , defined in (7), as a Fourier cosine series expanded in terms of $\pi x_2/h$, which is readily shown to take the form

$$\phi(x_2) = \sum_{n=1}^{\infty} \frac{(-1)^{n+1} \cos(\Lambda_n x_2/h)}{n^2}.$$

The continuity conditions in (6) may now be employed to determine the constants in (8) associated with the n -th harmonic. After doing this we arrive at the following form of the solution for displacement components and pressure increment

$$(v_1^{(i)}, v_2^{(i)}, p^{(i)}) = \sum_{n=1}^{\infty} \sum_{j=1}^2 \frac{A(-1)^{n+j} (q_2^{(i)} - q_1^{(i)})(w_j^{(i)} + y_j^{(i)}) e^{(-1)^{j+1} q_j^{(i)} x_1}}{n^2 (q_2^{(1)} - q_1^{(1)})(q_2^{(2)} - q_1^{(2)}) f(c)} \times (k_n^2 \cos(k_n x_2), k_n q_j^{(i)} \sin(k_n x_2), -q_j^{(i)} z_j^{(i)} \cos(k_n x_2)),$$

within which the functions occurring in the numerator are given by

$$\begin{aligned} w_1^{(l)}(c) &= \gamma^{(l)} (q_1^{(l)} q_2^{(l)} + q_1^{(l)} q_2^{(m)} + q_2^{(l)} q_2^{(m)} - k_n^2), & w_2^{(l)}(c) &= \gamma^{(l)} (q_1^{(l)} q_2^{(l)} + q_1^{(m)} q_2^{(l)} + q_1^{(l)} q_1^{(m)} - k_n^2), \\ y_1^{(l)}(c) &= \gamma^{(m)} (k_n^2 + (q_2^{(m)})^2), & y_2^{(l)}(c) &= \gamma^{(m)} (k_n^2 + (q_1^{(m)})^2), \\ z_j^{(l)}(c) &= k_n^2 [B_{1221} - B_{2222} + B_{1122} + B_{1212} (q_j^{(l)}/k_n)^2 + \rho^{(l)} c^2], \end{aligned}$$

with $f(c)$ given by

$$f(c) = \gamma^{(1)2} g^{(1)}(c) - \gamma^{(1)} \gamma^{(2)} \left[2k_n^2 (k_n^2 - q_1^{(1)} q_2^{(1)} - q_1^{(2)} q_2^{(2)}) + 2q_1^{(1)} q_2^{(1)} q_1^{(2)} q_2^{(2)} + (q_1^{(1)} + q_2^{(1)})(q_1^{(2)} + q_2^{(2)})(q_1^{(1)} q_2^{(1)} + q_1^{(2)} q_2^{(2)}) \right] + \gamma^{(2)2} g^{(2)}(c), \tag{14}$$

where $g^{(i)}(c) = k_n^4 - 2q_1^{(i)} q_2^{(i)} k_n^2 - q_1^{(i)} q_2^{(i)} (q_1^{(i)} q_2^{(i)} + (q_1^{(i)})^2 + (q_2^{(i)})^2)$, $l \neq m \in \{1, 2\}$ and $i, j = 1, 2$. In accordance with formulae (12), the wave number k_n can be eliminated from $f(c)$. As a result, Equation (14) essentially becomes the phase speed equation associated with interfacial waves propagating along, and localized close to, the interface of two perfectly bonded incompressible prestressed elastic half-spaces. These two half-spaces have the same geometrical setup and prestressed states as our two semiinfinite strips. A similar equation has previously been derived within the interfacial wave context by Dowaikh and Ogden [1991]. Therefore, by making use of the theory of the interfacial waves we are able to use the existence conditions for the zeros of $f(c)$ interpreting them as free vibrational frequencies or, alternatively, resonance frequencies of our problem with respect to the wave number k_n .

4. Prestressed domain within which resonance exists

Before proceeding to reviewing the existence conditions for interfacial waves, we first note the strong ellipticity conditions, which for the two-dimensional problem considered here take the form

$$\alpha^{(i)} > 0, \quad \gamma^{(i)} > 0, \quad \beta^{(i)} > -\sqrt{\alpha^{(i)} \gamma^{(i)}}. \tag{15}$$

Results relating to the existence of interfacial waves will be stated without proof. For further details the reader is referred to [Dowaikh and Ogden 1991].

Clearly, the solutions of the equation $f(c) = 0$ have to be consistent with the decay conditions $\Re\{q_j^{(i)}(c)\} > 0$. As may readily be established from (12), these inequalities introduce the strict condition that the real part of $q_j^{(i)}$ exists. In order to analyse the domain within which interfacial vibration frequencies, or resonance frequencies, may exist, the two roots given in (12) of the characteristic equation (11) are represented in the form $q_j^{(i)} = k_n(a^{(i)} \pm \sqrt{b^{(i)}})^{1/2}$, within which $a^{(i)}$ and $b^{(i)}$ are readily determined from Equation (12). Investigation of the decay condition above may be carried out with respect to the two cases

$$a^{(i)} > 0, \quad b^{(i)} < 0. \tag{16}$$

Due to the fact that the decay conditions dictate that only real or complex conjugate values of characteristic roots $q_j^{(i)}$ may arise, these inequalities help us to uniquely define the conditions that will guarantee the existence of a positive real part of the solutions for $q_j^{(i)}$. In addition, it is then possible to consider $f(c)$ as a real function, this being readily established by considering the resulting specific forms of (14). As expected, whenever the equation $f(c) = 0$ possesses real solutions, associated free interfacial (or resonance) vibrations will exist.

Within the framework of the incompressibility requirement introduced in (2), conditions (16) may be analysed in terms of regions in the $\lambda^{(1)}\lambda^{(2)}$ -plane. The two inequalities respectively define the two regions as

$$2\beta^{(i)} \geq \alpha^{(i)}, \quad 2\beta^{(i)} < \alpha^{(i)}, \tag{17}$$

where we recall that for specific strain energy functions, α and β are themselves known functions of λ .

The region defined by the first inequality in (17) introduces an upper bound to ensure a nonnegative squared wave speed, hence defining the domain of existence of interfacial vibration frequencies. Using Equation (13) together with the first inequality in (17), the wave speed is bounded as follows

$$0 \leq c \leq \min_{i=1,2} \{c_L^{(i)}\}, \quad c_L^{(i)} = \sqrt{\alpha^{(i)}/\rho^{(i)}}. \tag{18}$$

These are the so-called limiting wave speeds for appropriate half strip. They may also be identified as the plane shear wave speeds at which interfacial waves degenerate into shear waves.

Crucially, the upper bound in (18) may in certain cases be not compatible with the required decay condition for some range of $\alpha^{(i)}$. In such cases the upper bound must be redefined; see [Ogden and Sotiropoulos 1995; Sotiropoulos and Sifniotopoulos 1995] for more details. This leads to the second inequality in (17), where the limit of the wave speed in interval given in Equation (18) must be replaced by zeros of $b^{(i)}$, implying that

$$0 \leq c < \min_{i=1,2} \{c_b^{(i)}\}, \quad c_b^{(i)} = \max_{j=1,2} \left\{ \frac{2\beta^{(i)} - 2\gamma^{(i)} + (-1)^j 2\sqrt{-2\beta^{(i)}\gamma^{(i)} + \gamma^{(i)2} + \gamma^{(i)}\alpha^{(i)}}}{\rho^{(i)}} \right\}^{1/2}, \tag{19}$$

and if the second inequality in (17) holds, then we have $\min_{i=1,2} \{c_b^{(i)}\} < \min_{i=1,2} \{c_L^{(i)}\}$.

The existence of real $c_b^{(i)}$ is in general dependent on both the strain-energy function and the prestress. In the case of linear isotropic, neo-Hookean or Mooney–Rivlin materials, real $c_b^{(i)}$ can never exist. For Varga materials, however, real $c_b^{(i)}$ may exist for certain prestressed states. In passing we remark that

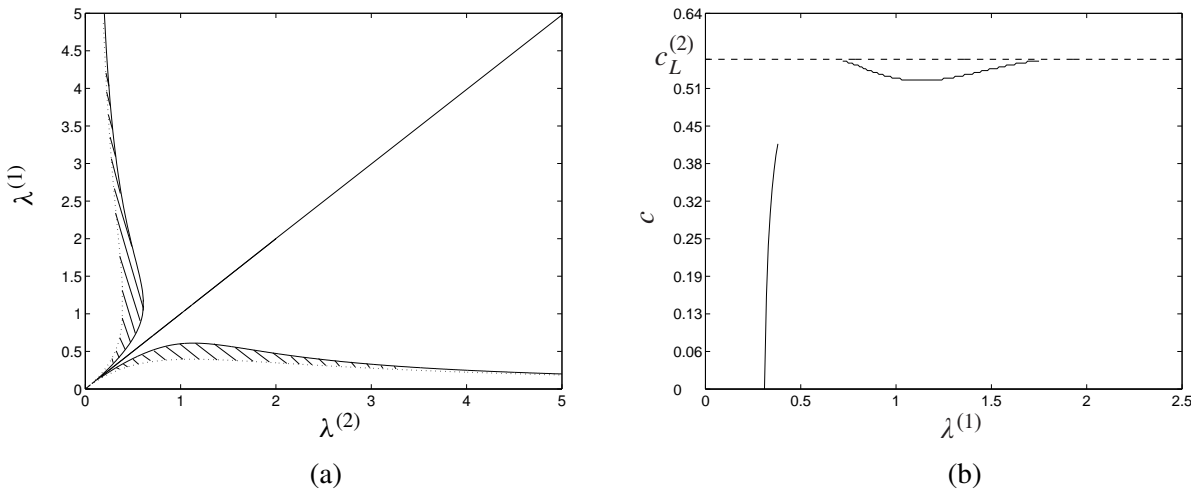


Figure 2. Plots of Equation (14) for a neo-Hookean material with identical material parameters: (a) dependency of $f(c)|_{c=0, c_L^{(i)}} = 0$ on principal stretches $\lambda^{(i)}$, $i = 1, 2$; (b) dependency of $f(c) = 0$ on principal stretch $\lambda^{(1)}$ and velocity c when $\lambda^{(2)} = 0.5$.

the existence of real $c_b^{(i)}$ also indicates that the associated slowness section may be nonconvex. This has important consequences for reflection and transmission of waves [Ogden and Sotiropoulos 1997]. In view of the two speeds given in Equations (18) and (19), the two regions in (17) may be expressed as $2\beta^{(l)} \geq \alpha^{(m)}$ and $2\beta^{(l)} < \alpha^{(m)}$, respectively, with $l, m = 1, 2$.

4.1. Neo-Hookean material: $s=2$. In this section results are presented for the case of a neo-Hookean strain energy function. The main parameters of the problem in this case are given by

$$\alpha^{(i)} = \mu^{(i)}(\lambda^{(i)})^2, \quad \gamma^{(i)} = \frac{\mu^{(i)}}{(\lambda^{(i)})^2}, \quad \beta^{(i)} = \frac{\alpha^{(i)} + \gamma^{(i)}}{2}.$$

These definitions and the strong ellipticity conditions (15) dictate that only the one region, given by the first inequality in (17), need be considered. As a result, the interval of resonance existence is uniquely determined merely by consideration of inequality (18).

Our graph of the $\lambda^{(1)}\lambda^{(2)}$ -plane is similar to plots previously seen in [Dowaikh and Ogden 1991; Sotiropoulos and Sifniotopoulos 1995]. Specifically, the numerical illustrations which we present relate to two different scenarios. The first case, presented in Figure 2, is for identical materials in both half-strips, that is, $\epsilon = 1$, but with differing prestress $\lambda^{(i)}$. Within this figure, the prestressed states associated with resonance are indicated as the shaded regions within the narrow domains that lie between the dotted and solid curves in Figure 2(a). The solid and dotted curves define solutions of the equation $f(0) = 0$ and $f(c_L) = 0$, respectively, where c_L is the smallest value of $c_L^{(i)}$, $i = 1, 2$. The potential resonance existence region may also be confirmed by considering Figure 2 (b), illustrating resonance with respect to $\lambda^{(1)}$ at the fixed value of $\lambda^{(2)} = 0.5$. For this value of $\lambda^{(2)}$ we must take into account both parts of Figure 2(a), that is, that below and above the line $\lambda^{(1)} = \lambda^{(2)}$. The domain $\lambda^{(1)} > \lambda^{(2)}$ is of particular interest in our numerical analysis, where both a decrease and an increase of the resonance velocity, bounded by $c_L^{(2)}$,

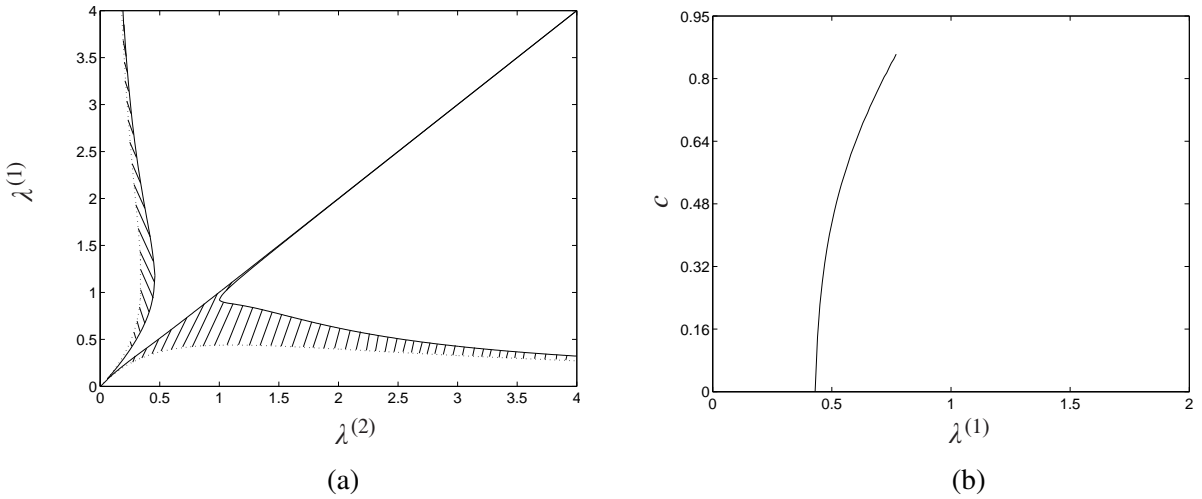


Figure 3. Plots of Equation (14) for a neo-Hookean material with contrasting material parameters ($\epsilon = 0.6$): (a) dependency of $f(c)|_{c=0, c_L^{(i)} = 0}$ on principal stretches $\lambda^{(i)}$, $i = 1, 2$; (b) dependency of $f(c) = 0$ on principal stretch $\lambda^{(1)}$ and velocity c when $\lambda^{(2)} = 0.9$.

may be observed. In fact, the resonance velocity will tend to zero as the principal stretch $\lambda^{(2)}$ approaches the point at which the tangent to the upper curve $f(0) = 0$ is parallel to the $\lambda^{(1)}$ -axis in Figure 2(a).

A contrast case with $\epsilon = 0.6$ and $\kappa = 1$ is presented in Figure 3. The resonance existence characteristics associated with the region below the line $\lambda^{(1)} = \lambda^{(2)}$ in Figure 3(a) differ considerably from the previous example and from those above the line in this example. The upper existence domain is again indicated as a shaded region between the solid and dotted curves, defined by $f(0) = 0$ and $f(c_L) = 0$. However, the lower existence region is bounded above by the line $\lambda^{(1)} = \lambda^{(2)}$, to which the curve $f(c_L^{(1)}) = 0$ asymptotes. In this case along the line $\lambda^{(1)} = \lambda^{(2)}$ we have $c_L^{(1)} = c_L^{(2)}$. We additionally note that the lower existence region is in fact significantly larger in size than both the upper region and the upper and lower regions of the previous example. The lower existence interval is shown in Figure 3(b) for the fixed value $\lambda^{(2)} = 0.9$. The associated velocity approaches that corresponding to the point on the line $\lambda^{(1)} = \lambda^{(2)} = 0.9$ in Figure 3(a), and there exists no other branch of the curve unlike the previous example.

4.2. Varga material: $s=1$. The problem parameters for the case of a Varga material are

$$\alpha^{(i)} = \frac{\mu^{(i)}(\lambda^{(i)})^2}{\lambda^{(i)} + 1/\lambda^{(i)}}, \quad \gamma^{(i)} = \frac{\mu^{(i)}}{(\lambda^{(i)})^2(\lambda^{(i)} + 1/\lambda^{(i)})}, \quad \beta^{(i)} = \sqrt{\alpha^{(i)}\gamma^{(i)}}.$$

For the Varga material, analysis of the secular equation $f(c) = 0$ allows either of the two inequalities in (17). We may therefore expect more complicated existence domains within the $\lambda^{(1)}\lambda^{(2)}$ -plane.

Figure 4 presents an illustration for a noncontrast case, with $\epsilon = 1$ and $\kappa = 1$. Observation of Figure 4(a) clearly shows two types of domains within which resonance may exist. The first of these is a natural analogue of the previously observed neo-Hookean type case. In this case, these two regions are the shaded regions between the dotted and solid curves which approach the origin. The two additional

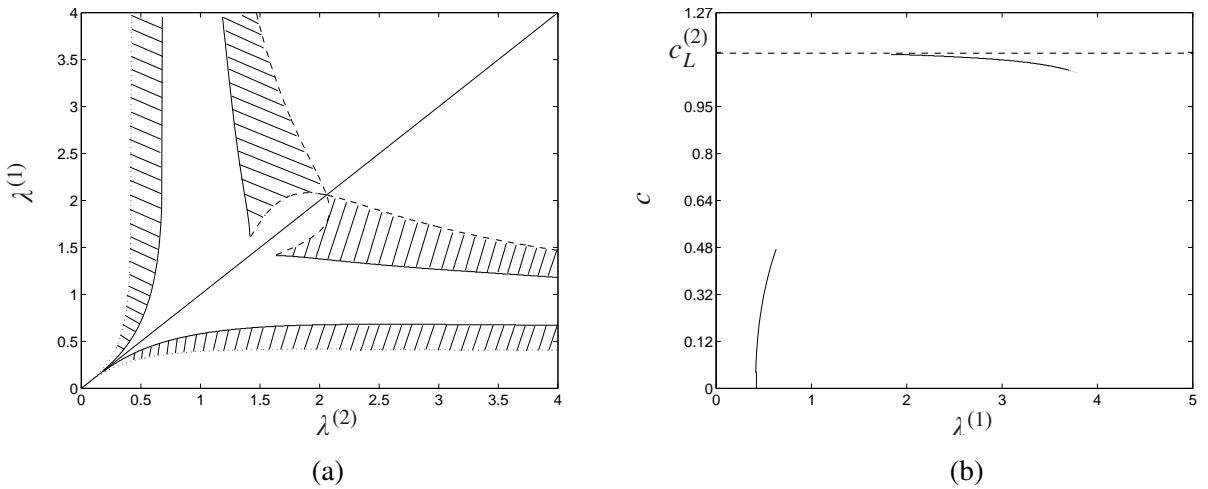


Figure 4. Plots of Equation (14) for a Varga material with identical material parameters: (a) dependency of $f(c)|_{c=0, c_L^{(i)}, c_b^{(i)}} = 0$ on principal stretches $\lambda^{(i)}$, $i = 1, 2$; (b) dependency of $f(c) = 0$ on principal stretch $\lambda^{(1)}$ and velocity c when $\lambda^{(2)} = 1.5$.

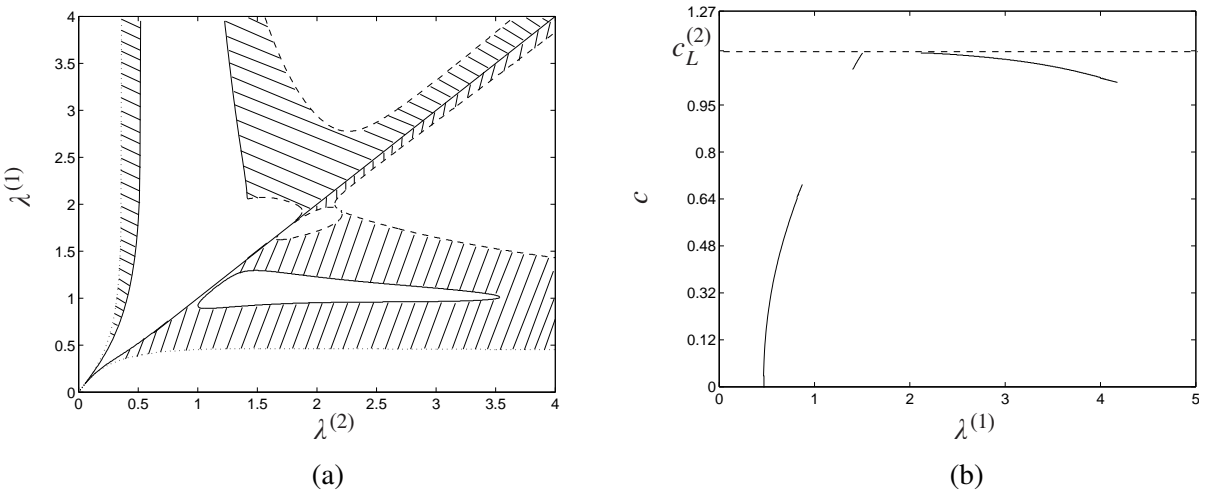


Figure 5. Plots of Equation (14) for a Varga material with contrasting material parameters ($\epsilon = 0.6$): (a) dependency of $f(c)|_{c=0, c_L^{(i)}, c_b^{(i)}} = 0$ on principal stretches $\lambda^{(i)}$, $i = 1, 2$, (b) dependency of $f(c) = 0$ on principal stretch $\lambda^{(1)}$ and velocity c when $\lambda^{(2)} = 1.5$.

shaded areas occur because of the existence of real values for $c_b^{(i)}$. For these domains, their extremities are the solid curve, defined by $f(c_L^{(i)}) = 0$, and the dashed curve, defined by $f(c_b^{(i)}) = 0$.

Figure 4(b) presents the resonances associated with both the above mentioned domain types for the fixed value of $\lambda^{(2)} = 1.5$. As might be expected for this value of $\lambda^{(2)}$, the upper branch emanates from close to the line $c = c_L^{(2)}$, specifically originating at the point $c = c_b^{(2)} \approx 1.13$ and then monotonically decreasing to the value $c = c_b^{(1)}$.

The final numerical example in this section concerns the contrast case $\epsilon = 0.6$ and $\kappa = 1$. As with the immediately previous example, this produces significant changes in the existence characteristics which may be observed in Figure 5(a). In this case a closed solid curve is observed below the line $\lambda^{(1)} = \lambda^{(2)}$. Within this region, the boundary of which corresponds to the solution of $f(c_L^{(1)}) = 0$, resonances may not exist. Moreover, an additional closed curve exists with boundary $f(c_b^{(1)}) = 0$ and represented by a dashed curve. Again, within this region no resonances may exist.

Figure 5(b) presents the resonances associated with both the above mentioned domain types for the fixed value of $\lambda^{(2)} = 1.5$. In this case the upper branch starts at a point associated with the solution of $f(c_L^{(1)}) = 0$ and monotonically increases to a point on the line $\lambda^{(1)} = \lambda^{(2)}$. After this, it monotonically decreases to the lowest possible value of $c_b^{(1)}$ associated with existence of resonances. We also note that for this example the value of $c_b^{(2)}$ is well within 1% of $c_L^{(2)}$.

5. Critical values of stretches

In this section we numerically examine the cases in which the associated interfacial wave either degenerates into a shear wave or a quasistatic interfacial deformation. In the first graph shown in Figure 6 the variation of $v_1^{(2)}$ with velocity is presented for the fixed value of $\lambda^{(2)} = 1.5$ and an appropriate range of $\lambda^{(1)}$. The range of $\lambda^{(1)}$ chosen is that indicated by the lower branch in Figure 4(b). The degeneration of localized interfacial vibration is indicated by the gradual reduction in the width of the resonance spikes as the speed, and corresponding $\lambda^{(1)}$, approach those values associated with degeneration into a shear wave. This is in fact the upper-most point on the lower branch of Figure 4(b).

In Figure 7, a scenario in which the interfacial wave degenerates into quasistatic interfacial deformations is presented. Specifically, these graphs show an appropriate approximation of $v_1^{(2)}$ against scaled frequency Ω over the range from $0 \leq \Omega \leq 1.0$. For all three presented graphs within this figure we take $\lambda^{(2)} = 1.5$ and three specific values of $\lambda^{(1)}$ associated with those approaching the critical state. It is immediately noted that, as the critical state is approached, by moving from (a) to (b) to (c), a significant increase in the interfacial spectrum density is observed.

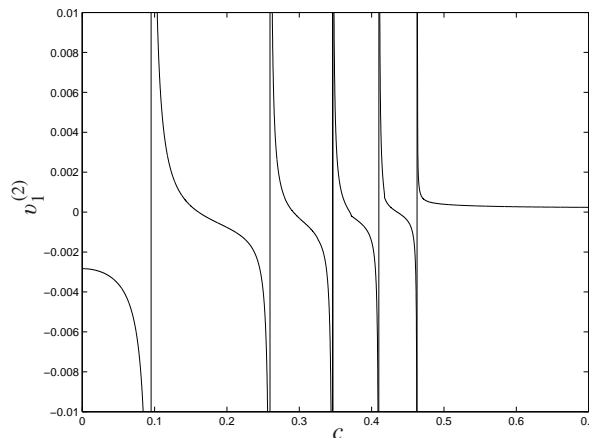


Figure 6. Degeneration of the interfacial resonances for $\lambda^{(1)} \in [0.42, 0.65]$, with $\lambda^{(2)} = 1.5$.

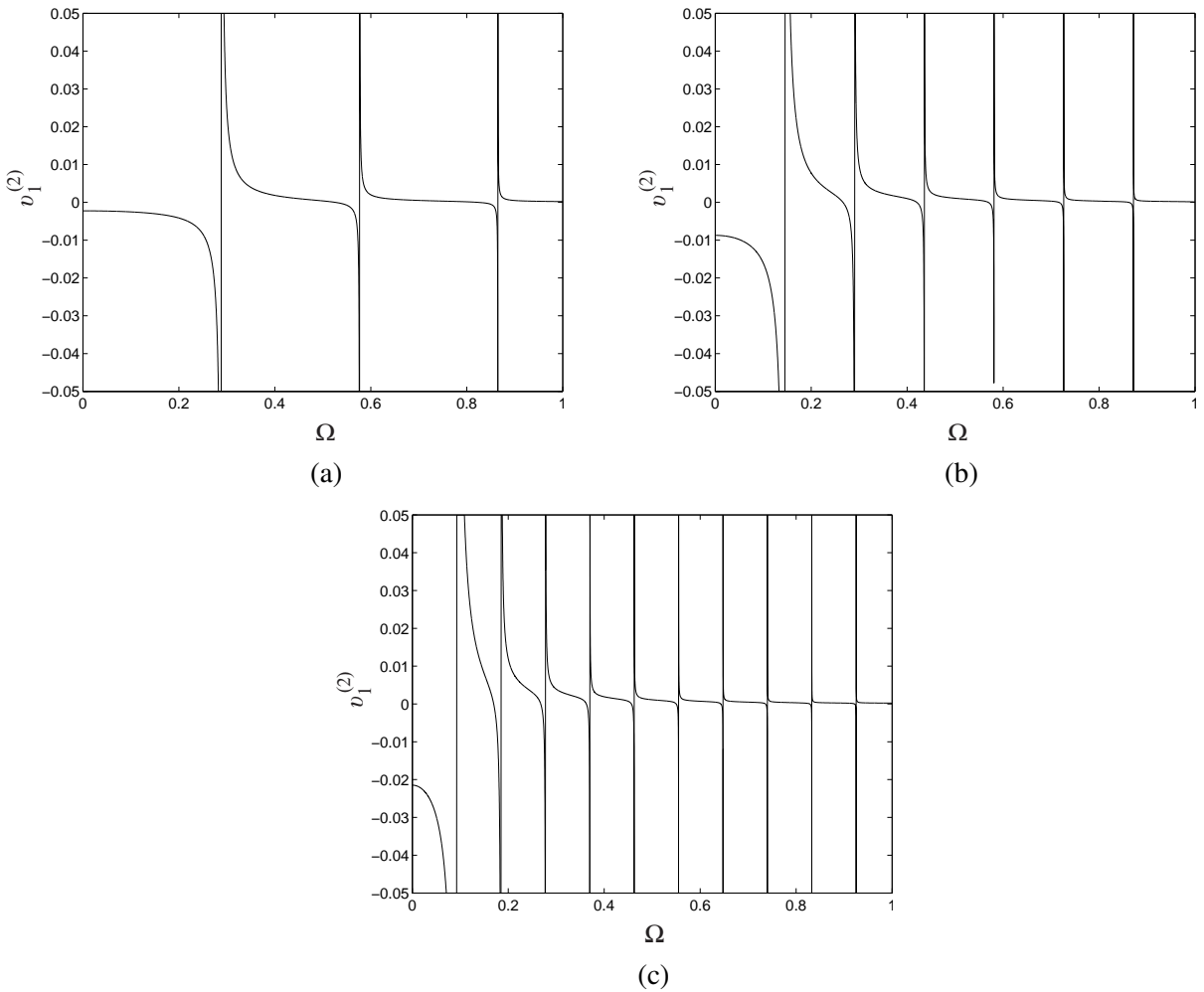


Figure 7. Singularities of displacement v_1 , as functions of frequency $\Omega = c k_n$, for Varga materials with $\lambda^{(2)} = 1.5$: (a) $\lambda^{(1)} = 0.4$, (b) $\lambda^{(1)} = 0.395$, (c) $\lambda^{(1)} = 0.394$.

Finally, in Figure 8, plots of the real and imaginary parts of $v_1^{(i)}$ are presented against x_1 , the in-plane spatial variation, for a number of values of $\lambda^{(1)}$ and fixed $\lambda^{(2)} = 1.5$. These plots clearly show that the displacement is in general localized within the vicinity of the interface $x_1 = 0$, with this localization being least pronounced when the velocity is close to the shear velocity. In particular, we note that it is quite possible to have a situation in which significant localization may occur within one semistrip, with little localization visible in the other. This is particularly the case when $\lambda^{(1)} = 0.62$, in which case there is significant localization in the right strip and little in the left.

6. Conclusion

For certain upper and lower face boundary conditions it has been established that localized vibrations may exist within the vicinity of a common plane boundary of two perfectly bonded semiinfinite strips.

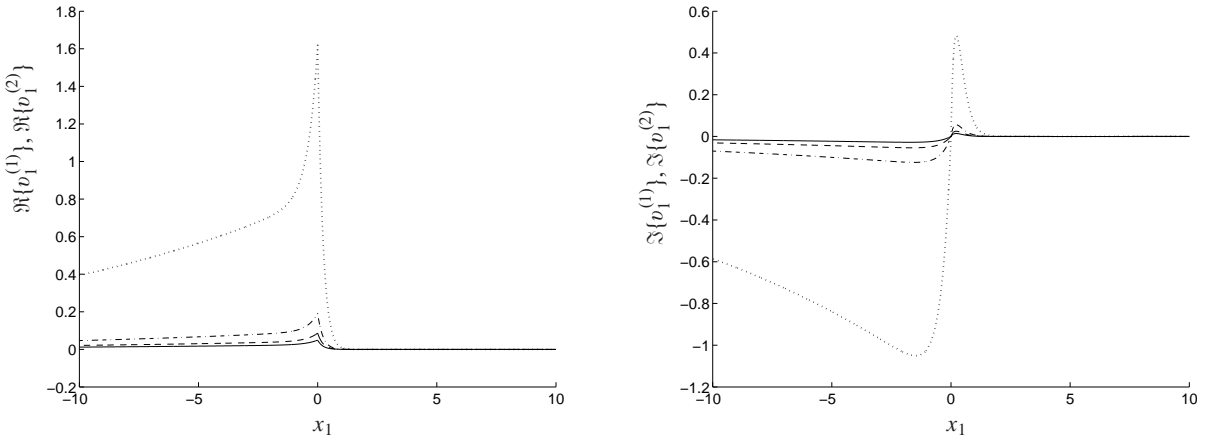


Figure 8. Localisation of the interfacial vibrations, showing displacements $v_1^{(i)}$, $i = 1, 2$, against x_1 as the velocity moves closer to the limiting wave speed $c_L^{(1)}$ for a fixed $\lambda^{(2)} = 1.5$: (a) real part, (b) imaginary part.

The frequencies of these so-called interfacial vibrations have been shown to be functions of the associated interfacial wave speed. The presence of an underlying finite primary deformation makes it quite possible for the interfacial wave speed to either vanish or for an interfacial wave to degenerate into a shear wave. These scenarios have been shown to have important consequences with regard to types of localized interfacial vibrations considered. In the case of the wave speed vanishing, a significant increase in the spectrum density has been observed, whereas degeneration into a body wave has been shown to be associated with the diminishing influence of the resonances within the overall dynamic response.

References

- [Chadwick 1995a] P. Chadwick, "Interfacial and surface waves in pre-strained isotropic elastic media", *Z. Angew. Math. Phys.* **46**:Special Issue (1995), S51–S71. Theoretical, experimental, and numerical contributions to the mechanics of fluids and solids. MR 96j:73033 Zbl 0830.73019
- [Chadwick 1995b] P. Chadwick, "Interfacial waves in an inextensible elastic composite", *Int. J. Eng. Sci.* **33**:9 (1995), 1273–1287.
- [Dowaikh and Ogden 1991] M. A. Dowaikh and R. W. Ogden, "Interfacial waves and deformations in pre-stressed elastic media", *Proc. R. Soc. Lond. A* **433**:1888 (1991), 313–328. MR 92c:73039 Zbl 0726.73020
- [Kaplunov et al. 2004] J. D. Kaplunov, D. A. Prikazhnikov, and G. A. Rogerson, "Edge vibration of a pre-stressed semi-infinite strip with traction-free edge and mixed face boundary conditions", *Z. Angew. Math. Phys.* **55**:4 (2004), 701–719. MR 2005f:74042 Zbl 02106467
- [Ogden 1984] R. W. Ogden, *Nonlinear elastic deformations*, Ellis Horwood, Chichester, 1984. MR 86h:73011 Zbl 0541.73044
- [Ogden and Sotiropoulos 1995] R. W. Ogden and D. A. Sotiropoulos, "On interfacial waves in pre-stressed layered incompressible elastic solids", *Proc. R. Soc. Lond. A* **450**:1939 (1995), 319–341. MR 96d:73022 Zbl 0846.73012
- [Ogden and Sotiropoulos 1997] R. W. Ogden and D. A. Sotiropoulos, "The effect of pre-stress on the propagation and reflection of plane waves in incompressible elastic solids", *IMA J. Appl. Math.* **59**:1 (1997), 95–121. MR 99a:73049 Zbl 0894.73024
- [Sotiropoulos and Sifniotopoulos 1995] D. A. Sotiropoulos and C. G. Sifniotopoulos, "Interfacial waves in pre-stressed incompressible elastic interlayers", *J. Mech. Phys. Solids* **43**:3 (1995), 365–387.

[Stoneley 1924] R. Stoneley, “Elastic waves at the surface of separation of two solids”, *Proc. R. Soc. Lond. A* **106**:738 (1924), 416–428.

Received 8 Feb 2007. Accepted 27 Mar 2007.

GRAHAM A. ROGERSON: g.a.rogerson@keele.ac.uk

Department of Mathematics, University of Keele, Keele, Staffordshire ST5 5BG, United Kingdom

ANTON V. KRYNKIN: a.krynkin@keele.ac.uk

Department of Mathematics, University of Keele, Keele, Staffordshire ST5 5BG, United Kingdom

SUBMISSION GUIDELINES

ORIGINALITY

Authors may submit manuscripts in PDF format on-line. Submission of a manuscript acknowledges that the manuscript is *original and has neither previously, nor simultaneously, in whole or in part, been submitted elsewhere*. Information regarding the preparation of manuscripts is provided below. Correspondence by email is requested for convenience and speed. For further information, write to:

Marie-Louise Steele
Division of Mechanics and Computation
Durand Building, Room 262
Stanford University
Stanford CA 94305

LANGUAGE

Manuscripts must be in English. A brief abstract of about 150 words or less must be included. The abstract should be self-contained and not make any reference to the bibliography. Also required are keywords and subject classification for the article, and, for each author, postal address, affiliation (if appropriate), and email address if available. A home-page URL is optional.

FORMAT

Authors are encouraged to use L^AT_EX and the standard article class, but submissions in other varieties of T_EX, and, exceptionally in other formats, are acceptable. Electronic submissions are strongly encouraged in PDF format only; after the refereeing process we will ask you to submit all source material.

REFERENCES

Bibliographical references should be listed alphabetically at the end of the paper and include the title of the article. All references in the bibliography should be cited in the text. The use of B^IB_T_EX is preferred but not required. Tags will be converted to the house format (see a current issue for examples), however, in the manuscript, the citation should be by first author's last name and year of publication, e.g. "as shown by Kramer, et al. (1994)". Links will be provided to all literature with known web locations and authors are encouraged to provide their own links on top of the ones provided by the editorial process.

FIGURES

Figures prepared electronically should be submitted in Encapsulated PostScript (EPS) or in a form that can be converted to EPS, such as GnuPlot, Maple, or Mathematica. Many drawing tools such as Adobe Illustrator and Aldus FreeHand can produce EPS output. Figures containing bitmaps should be generated at the highest possible resolution. If there is doubt whether a particular figure is in an acceptable format, the authors should check with production by sending an email to:

production@mathscipub.org

Each figure should be captioned and numbered so that it can float. Small figures occupying no more than three lines of vertical space can be kept in the text ("the curve looks like this:"). It is acceptable to submit a manuscript with all figures at the end, if their placement is specified in the text by means of comments such as "Place Figure 1 here". The same considerations apply to tables.

WHITE SPACE

Forced line breaks or page breaks should not be inserted in the document. There is no point in your trying to optimize line and page breaks in the original manuscript. The manuscript will be reformatted to use the journal's preferred fonts and layout.

PROOFS

Page proofs will be made available to authors (or to the designated corresponding author) at a web site in PDF format. Failure to acknowledge the receipt of proofs or to return corrections within the requested deadline may cause publication to be postponed.

JOURNAL OF MECHANICS OF MATERIALS AND STRUCTURES

Volume 2 No. 5 May 2007

-
- Two complementary trios material model and experimental simulations of SAE 4340 and RHA 793
CHEIN-SHAN LIU, HONG-KI HONG AND YA-PO SHIAO
- Geometrically nonlinear effects in the flexural response of masonry walls strengthened with composite materials 829
EHAB HAMED AND ODED RABINOVITCH
- A marching procedure for form-finding for tensegrity structures 857
ANDREA MICHELETTI AND WILLIAM O. WILLIAMS
- Element stacking method for topology optimization with material-dependent boundary and loading conditions 883
GIL HO YOON, YONG KEUN PARK AND YOON YOUNG KIM
- Exact solutions of AFM scanning probes subjected to any of tip-sample forces 897
SHUEEI-MUH LIN, SEN-YUNG LEE AND KUEN-WEY LIN
- Influence of the elastic parameters of a fluttering plate on its post-critical behavior 911
SILVANO TIZZI
- Micromechanical approach to transformation toughening in zirconia-enriched multiphase composites 937
HIDEAKI TSUKAMOTO AND ANDREI KOTOUSOV
- The simulation of residual stresses in friction stir welds 951
ZHAO ZHANG AND HONGWU ZHANG
- Numerical and experimental analysis of the static compliance of chiral truss-core airfoils 965
ALESSANDRO SPADONI AND MASSIMO RUZZENE
- Resonance phenomena at the interface of two perfectly bonded, prestressed elastic strips 983
GRAHAM A. ROGERSON AND ANTON V. KRYNKIN



1559-3959(200705)2:5;1-7